Advances in Sustainability Science and Technology

Sadhan Mahapatra
Muhammad Shahbaz
Alfredo Vaccaro
Valentina Emilia Balas *Editors*

Advances in Energy Technology

Proceedings of ICAET 2020

KES International

Springer

Advances in Sustainability Science and Technology

The book series aims at bringing together valuable and novel scientific contributions that address the critical issues of renewable energy, sustainable building, sustainable manufacturing, and other sustainability science and technology topics that have an impact in this diverse and fast-changing research community in academia and industry.

The areas to be covered are

- Climate change and mitigation, atmospheric carbon reduction, global warming
- Sustainability science, sustainability technologies
- Sustainable building technologies
- Intelligent buildings
- Sustainable energy generation
- Combined heat and power and district heating systems
- Control and optimization of renewable energy systems
- Smart grids and micro grids, local energy markets
- Smart cities, smart buildings, smart districts, smart countryside
- Energy and environmental assessment in buildings and cities
- Sustainable design, innovation and services
- Sustainable manufacturing processes and technology
- Sustainable manufacturing systems and enterprises
- Decision support for sustainability
- Micro/nanomachining, microelectromechanical machines (MEMS)
- Sustainable transport, smart vehicles and smart roads
- Information technology and artificial intelligence applied to sustainability
- Big data and data analytics applied to sustainability
- Sustainable food production, sustainable horticulture and agriculture
- Sustainability of air, water and other natural resources
- Sustainability policy, shaping the future, the triple bottom line, the circular economy

High quality content is an essential feature for all book proposals accepted for the series. It is expected that editors of all accepted volumes will ensure that contributions are subjected to an appropriate level of reviewing process and adhere to KES quality principles.

The series will include monographs, edited volumes, and selected proceedings.

More information about this series at http://www.springer.com/series/16477

Sadhan Mahapatra · Muhammad Shahbaz ·
Alfredo Vaccaro · Valentina Emilia Balas
Editors

Advances in Energy Technology

Proceedings of ICAET 2020

Springer

Editors
Sadhan Mahapatra
Department of Energy
Tezpur University
Tezpur, Assam, India

Alfredo Vaccaro
Department of Engineering
University of Sannio
Benevento, Italy

Muhammad Shahbaz
Department of International Trade and Finance
Bejing Institute of Technology
Bejing, China

Valentina Emilia Balas
Department of Automatics and Applied Software
"Aurel Vlaicu" University of Arad
Arad, Romania

ISSN 2662-6829 ISSN 2662-6837 (electronic)
Advances in Sustainability Science and Technology
ISBN 978-981-15-8699-6 ISBN 978-981-15-8700-9 (eBook)
https://doi.org/10.1007/978-981-15-8700-9

This Springer imprint is published by the registered company Springer Nature Singapore Pte Ltd.
The registered company address is: 152 Beach Road, #21-01/04 Gateway East, Singapore 189721, Singapore

Preface

Energy is the key input for the development process of any country. The conventional fossil fuel-based economy started with the invention of the steam engine in England and oil exploration in the USA. The present day's economy primarily relies upon coal, oil and natural gas. However, all these energy sources availabilities are limited and not uniformly distributed throughout the world. Energy access is crucial for poverty alleviation, economic growth and improved living standards of peoples. However, still a large number of people in sub-Saharan Africa and Southeast Asia do not have access to clean energy. It is also important to note that climate change is primarily due to extensive use of fossil fuel-based energy sources. Energy accounts for two-thirds of total greenhouse gas emission. Renewable energy and energy efficiency are the viable alternatives to mitigate climate change or to reduce the greenhouse gas emissions. The application of most important renewable energy sources like solar, wind, hydro or biomass is in the area of electric power generation. Solar photovoltaic-based micro-grids are slowly becoming the backbone for access to clean energy in the remote villages.

This book contains selected papers presented at the International Conference on Advances in Energy Technology (ICAET 2020) organized by Gandhi Institute for Education and Technology, Baniatangi, Bhubaneswar, India, during 17–18 January 2020. The conference was inaugurated by Prof. (Dr.) Satya Prakash Panda, Honourable Chairman of Gandhi Group of Institutions. This book includes research findings of various researchers from industry, academia and research organizations. Attempts have been made to cover diversified research domains of energy science and engineering. The works are in a wide range of spectrums ranging from theoretical analysis to field study findings. Almost 78 numbers of papers were presented in the conference, and 23 papers are selected for this book. Various aspects of energy conversion, energy management and efficiency, renewable energy, IoT-based energy systems and related topics are covered in this conference. The ICAET 2020 conference was definitely the witness of many presentations by experts on up-to-date information and analysis on renewable energy technologies, power engineering technologies and focuses both theoretical and practical solutions. The researchers as well as participants had an opportunity to acquire

knowledge on energy optimization, control and limitations of different technologies as well as detailed economic study, implementation and management issues. This book represents an intellectual forum for energy engineers, renewable energy experts, professionals and research scholars, students of renewable energy and power generation involved in design, control, management and optimization of energy generation and process engineering.

The editors would like to thank all the authors for paying attention to the quality of the publications. We are also very much thankful to Prof. Jyoti Prakash Mishra, Vice Chairman, Prof. Snigdharani Panda, Secretary, and Dr. Sambit Kumar Mishra, Principal of Gandhi Institute for Education and Technology, Baniatangi, for their encouragement and support to organize this conference. The conference received financial support from TEQIP III, Biju Patnaik University of Technology, Rourkela, Odisha, India. This publication will surely generate a much larger scientific discussion. It is expected that the readers will be benefited from the contributions included in the book. Editors are thankful to all the authors, reviewers and editorial board members for making this effort successful. Special thanks go to the publisher—Springer, for all-round assistance in this unprecedented COVID-19 situation towards the publication of this book.

Tezpur, India — Sadhan Mahapatra
Bejing, China — Muhammad Shahbaz
Benevento, Italy — Alfredo Vaccaro
Arad, Romania — Valentina Emilia Balas

Contents

About the Editors

Dr. Sadhan Mahapatra is currently working as an Associate Professor in the Department of Energy, Tezpur University. He has obtained M.Sc. (Physics) from Visva-Bharati, Shantiniketan, M.Tech. (Energy Science and Technology) from Jadavpur University, Calcutta, and Ph.D. from Indian Institute of Science, Bangalore. The area of the Ph.D. work is Biomass Gasification. He teaches Solar Energy, Wind Energy, Energy Management & Conservation and Energy Efficiect Building in the M.Tech. in Energy Technology Programme. His research interests are biomass gasification, climate responsive buildings, decentralized energy systems, and photovoltaic systems. He has published more than 60 papers in international journals and conference proceedings. He is Member of International Solar Energy Society (ISES), Indian Society for Technical Education (ISTE), Institution of Engineers, Indian Science Congress, etc. He is Reviewer of many international journals including Energy, Applied Energy, Buildings and Environment, Solar Energy, Energy and Buildings, Energy for Sustainable Development, Journal of Cleaner Production, Energy Policy, Indoor and Built Environment, RSC Advances, Energy and Environmental Science, etc.

Dr. Muhammad Shahbaz is a Full Professor at the School of Management and Economics, Beijing Institute of Technology, China. He is also an Affiliated Visiting Scholar at the Department of Land Economy, University of Cambridge, UK, and an Adjunct Professor at COMSATS Institute of Information Technology, Lahore, Pakistan. He previously served as a Chair Professor of Energy and Sustainable Development at Montpellier Business School, France, and Principal Research Officer at COMSATS. He received his Ph.D. in Economics from the National College of Business Administration and Economics, Lahore, Pakistan. His research focuses on financial economics, energy finance, energy economics, environmental economics, development economics, and tourism economics. He has published more than 300 research papers in peer-reviewed international journals, is among the world's top 15 economics authors as ranked by IDEAS, and was selected as one of the top 5 authors on economics in developing countries by David McKenzie,

Chief Economist of the World Bank. Dr. Shahbaz has published papers in various journals, including Applied Economics, Social Indicators Research, Renewable Energy, and the Journal of Cleaner Production.

Dr. Alfredo Vaccaro obtained his master's degree from the University of Salerno and Ph.D. in Electrical and Computer Engineering from the University of Waterloo, Ontario, Canada. Presently, he is associated with the Department of Electric Power Systems Engineering, University of Sannio. Earlier he was associated with the research group of Intelligent Systems and Control at the Department of Automatic Control and System Engineering, University of Sheffield (UK). He also chaired the Research & Development Committee of the Opera21 Group SpA in the field of Advanced Information and Communications Technologies for Smart Grids and also Scientific Director of the bureau of the Research Centre on Pure and Applied Mathematics at the Department of Engineering, University of Sannio. Presently, he is the Chair of the Task Force "Enabling Paradigms for High-performance Computing in Wide Area Monitoring Protective and Control Systems" of the IEEE PSOPE Technologies & Innovation Subcommittee and IEEE PES Awards and Recognition Committee. He published 1 international patent, 3 books, 9 book chapters, 75 journal papers, and 66 conference papers, obtaining 2250 citations and H-index 25 (SCOPUS).

Valentina Emilia Balas is currently a Full Professor in the Department of Automatics and Applied Software at the Faculty of Engineering, "Aurel Vlaicu" University of Arad, Romania. She holds a Ph.D. in Applied Electronics and Telecommunications from Polytechnic University of Timisoara. Dr. Balas is author of more than 350 research papers in refereed journals and international conferences. Her research interests are intelligent systems, fuzzy control, soft computing, smart sensors, information fusion, modeling, and simulation. She is the Editor-in-Chief to the International Journal of Advanced Intelligence Paradigms (IJAIP) and to the International Journal of Computational Systems Engineering (IJCSysE), Editorial Board member of several national and international journals, and evaluator expert for national, international projects, and Ph.D. Thesis. Dr. Balas is the Director of Intelligent Systems Research Centre in Aurel Vlaicu University of Arad and Director of the Department of International Relations, Programs and Projects in the same university. She served as General Chair of the International Workshop Soft Computing and Applications (SOFA) in eight editions 2005–2020 held in Romania and Hungary. Dr. Balas participated in many international conferences as Organizer, Honorary Chair, Session Chair, and member in Steering, Advisory or International Program Committees. She is a member of EUSFLAT and SIAM, a senior member of IEEE, member in TC – Fuzzy Systems (IEEE CIS), Chair of the TF 14 in TC – Emergent Technologies (IEEE CIS), and member in TC – Soft Computing (IEEE SMCS). Dr. Balas was past Vice-President (Awards) of IFSA International Fuzzy Systems Association Council (2013–2015), is a Joint Secretary of the Governing Council of Forum for Interdisciplinary Mathematics (FIM),

A Multidisciplinary Academic Body, India, and recipient of the "Tudor Tanasescu" Prize from the Romanian Academy for contributions in the field of soft computing methods (2019).

Chapter 1
Demonstration and Simulation of Brushless Direct Current Motor

Prakriti Mohanty, Debani Prasad Mishra, Anshuman Behera, and Swati Swarupa Das

Abstract In this paper, the Brushless Direct Current Motor (BLDC) is simulated with the help of the software MATLAB using some basic theories and its practical features and its performance is analyzed. This helps simulate the corresponding model for the BLDC with ease. The output of BLDC motor performance which was obtained in MATLAB can be analyzed for different input parameters, critically in the MATLAB. The precision and practicality of the model can be known by analyzing the output results obtained from simulation with actual BLDC model. The construction of the BLDC Motor is briefly discussed.

Keywords BLDC · MATLAB · PMBLDC · Modeling · Simulation · Construction

1 Introduction

Direct Current motors conventionally contain brushes and commutators which makes their maintenance very difficult and expensive. So brushless Direct current motors have been started being preferred to use. It consists of permanent magnet. It is used in households as well as automobiles. Also, it has its applications in aerospace. It has its applications in military because of the high torque that it produces. It also has very high ratio of output to input also known as efficiency. It is because of these characteristics that the brushless Direct Current motor has found a lot of applications. The information regarding the position of the rotor is required for corresponding values of variation of current or commutations so that the values can be controlled electronically [1, 2].

It has a variety of applications as mentioned above. Apart from those, the brushless Direct Current motor can be implemented in offices, hard drives, robots used for automation, also for automation of offices. It is also used in various drive applications. The main advantages of the motor are its high efficiency, no complex controls, high

P. Mohanty · D. P. Mishra (✉) · A. Behera · S. Swarupa Das
Department of Electrical Engineering, International Institute of Information Technology, Bhubaneswar, India
e-mail: debani@iiit-bh.ac.in

S. Mahapatra et al. (eds.), *Advances in Energy Technology*, Advances in Sustainability Science and Technology, https://doi.org/10.1007/978-981-15-8700-9_1

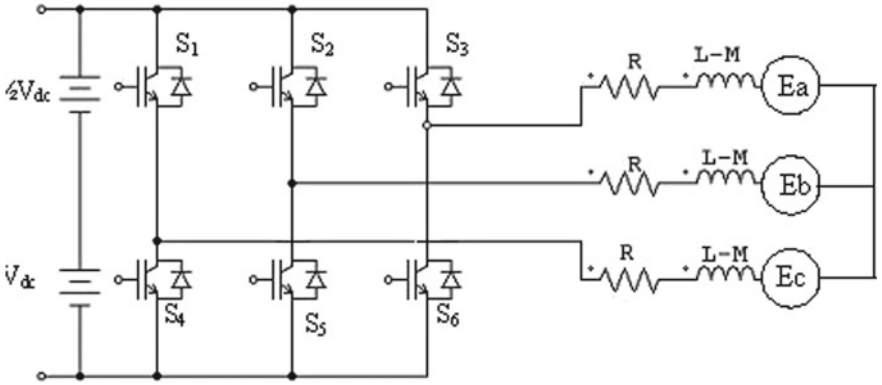

Fig. 1 BLDC motor connected to a converter circuit

ratio of speed to torque. Also, it is portable and compact. The maintenance of brushes is not required anymore. The mechanical and physical wear and tear of the brushes causes a lot of problems which are avoided by using BLDC motor. A diagram showing a typical BLDC motor connected to a converter circuit is given below (Fig. 1).

It can be achieved by changing rotor and stator position. An inverter is required which shall help in the alternating the functions of the used brushes and the commutator. Another essential component utilized is a position sensor which is helpful in detecting the position of the rotor. The software Simulink of MATLAB has been used for the modeling of the motor and for the simulation part as well MATLAB consists of many commands and can be used to solve and simulate different types of problems ranging from power electronics to control systems to power systems or DC machines. It provides quick simulation and also has an interface which is user-friendly so it is preferred to be used for simulation purposes. It also makes it possible to get connected to third-party software such as PSIM or Proteus. We can use the MATLAB and Simulink software to solve a wide variety of problems in an easy and efficient manner [3, 4].

2 Principle and Construction

The Brushless DC motors are categorized based on the shape of the wave of their emf that is induced in it, which are of two types, i.e., trapezoidal and sinusoidal. The permanent magnet synchronous motor comes under sinusoidal type and trapezoidal type s included in PM Brushless dc (BLDC) machine. Synchronous motors are those types of motors in which the stator and the rotor both generate their respective magnetic fields at the same or equal frequency.

Since the BLDC motors do not contain brushes, they do not experience the wear and tear of brushes and also the slip that is found in normal induction motors is

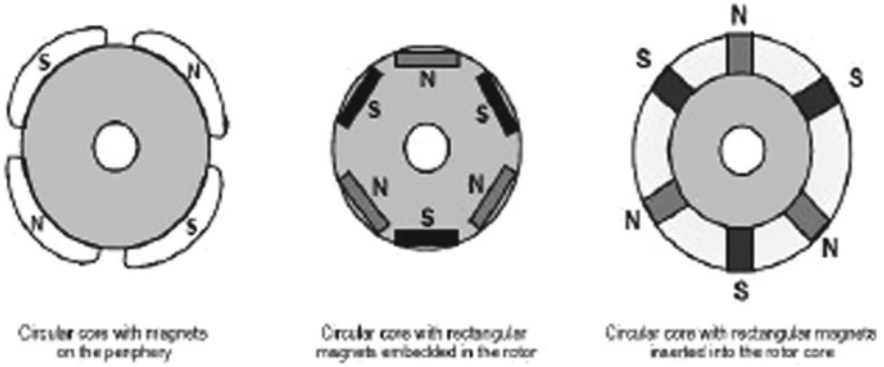

Fig. 2 Construction of a rotor

absent. The BLDC motors are available in various different variants namely one, two, or phases and the number of rotor windings depends on its type. The major components of motor are stator and rotor [5, 6].

2.1 Rotor

The rotor consists of permanent magnets consisting of varying pole pairs, two to eight in number, with South and North in alternating fashion. The material chosen to make the rotor depends on the density of the magnetic field required for rotor. Generally, ferrites or rare earth metals are used. It is because they are cheap, but they have low density of flux corresponding to a given volume. On the contrary alloys have flux density enabling the rotor to get more compressed for the similar values of torque [7].

They also have increased size and weight ratio and they also have the capability to generate a larger amount of torque as compared to their ferrite counterparts possessing similar size. A few constructions have been shown as follows (Fig. 2).

2.2 Stator

The BLDC motor and induction motor has similar constructional features. Brushless Direct motors generally have three stator windings which are generally interconnected in the form of a star. Windings placed are stacked steel in axially cut internal slots placed in the periphery co-axially. The BLDC motor and induction motor has similar constructional features.

Each slot consists of a single or more coil that are connected to one another to form a winding. The rotor is surrounded by windings to form the poles which are

Table 1 Phase sequence of the rotating position of rotor

Hall effect signals			Decoded signals		
H1	H2	H3	h1	h2	h3
0	0	0	0	0	0
0	0	1	0	−1	+1
0	1	0	−1	+1	0
0	1	1	−1	0	+1
1	0	0	+1	−1	0
1	0	1	0	+1	−1
1	1	0	+1	0	−1
1	1	1	0	0	0

even in number. Sinusoidal and trapezoidal are the two variants of stator windings found. It is based on the connection of coils to generate reverse Electromotive Force in the stator winding [8].

2.3 Sensing Position of the Rotor

In a brushed Direct Current motor, the commutation is physical whereas, in brushless, it is electronical. When the windings of the stator are filled with energy, sequentially, the motor shaft rotates. The exact position of the shaft (Rotor) can be sensed through the sensors contained in the stator using Hall effect. It also provides the order of energization of the phase. Mostly BLDC motors contain three sensors which give high signal for North Pole and low signal for South Pole when they pass by the sensors. The combination of phase sequence is determined by the Sensor order [9] (Table 1).

3 Mathematical Modeling

A differential equation of the first order can be used to describe the phase of activity of a motor of Alternating Current type [10, 11]. A voltage equation for any of the phases can be generalized as follows.

$$Vx = Rix + \sum_{k=1}^{n} \frac{\mathrm{d}\Psi kx(\theta, ix)}{\mathrm{d}t}$$

where Vx is voltage of phase, R is Resistance, ix is current of the phase, θ is the position of the rotor, ψ is the linkage of flux, n is the phase number.

The three phase equations are:

$$Va = R(ia) + L\frac{\mathrm{d}(ia)}{\mathrm{d}t} \tag{1}$$

$$Vb = R(ib) + L\frac{\mathrm{d}ib}{\mathrm{d}t} \tag{2}$$

$$Vc = R(ic) + L\frac{\mathrm{d}ic}{\mathrm{d}t} \tag{3}$$

where,

L is the self-induction (H).

R is the resistance of armature (Ω).

Va, Vb, Vc are the voltages at end terminal in per phase (V).

ia, ib, ic are the input currents of the motor (three-phase) (A).

The reverse voltages can be represented in terms of mechanical speed of the rotor, ωm, and the electrical angle of the rotor, θr as follows:

$$ea = Kw(\theta e)w \tag{4}$$

$$eb = Kw(\theta e - 2\pi/3) \tag{5}$$

$$ec = Kw(\theta e + 2\pi/3) \tag{6}$$

The rotor angle θr determines the coefficients ke_a, ke_b, and ke_c. This model assumes an ideal waveform in the form of a trapezoid.

The equation for mechanical torque is:

$$J \,.\, \frac{\mathrm{d}\omega m}{\mathrm{d}t} = T\mathrm{em} - B.\omega m - T\mathrm{load}$$
$$\frac{\mathrm{d}\theta r}{\mathrm{d}t} = (P/2).\omega m$$

where B refers to coefficient, Tload refers to torque of the given load, and P refers to the number of poles. The mechanical time constant and moment of inertia J help in calculation of coefficient B given as:

$$B = J/\tau\mathrm{mech}$$

4 BLDC in Simulation Environment

Figure 3 shows the simulation diagram of BLDC motor with PID controller and Hall Effect sensor. Figure 4 shows the circuit which has been used to implement commutation logic. Figure 5 shows the electromagnetic torque of the BLDC motor under no-load condition and closed-loop system. Figure 6 shows the Hall Effect Signal for the BLDC motor under no-load condition and closed-loop system. It is obtained from the sensors which sense the rotor speed of the motor. Figure 7 shows the Stator Current of the Brushless DC motor under no-load condition and in closed-loop system. Figure 8 shows the Output-Rotor Speed of the Brushless DC motor

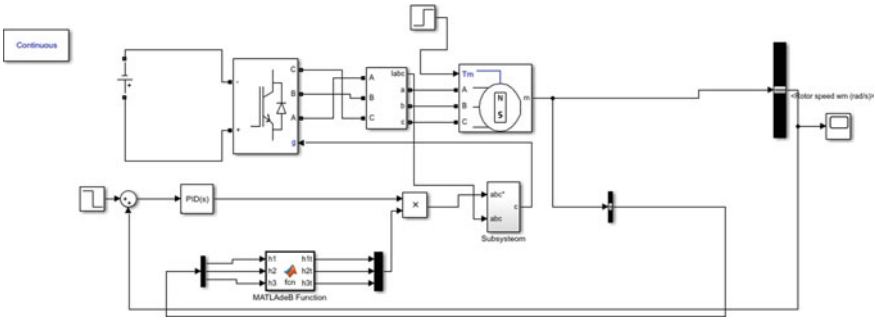

Fig. 3 Simulation diagram of BLDC motor with PID controller

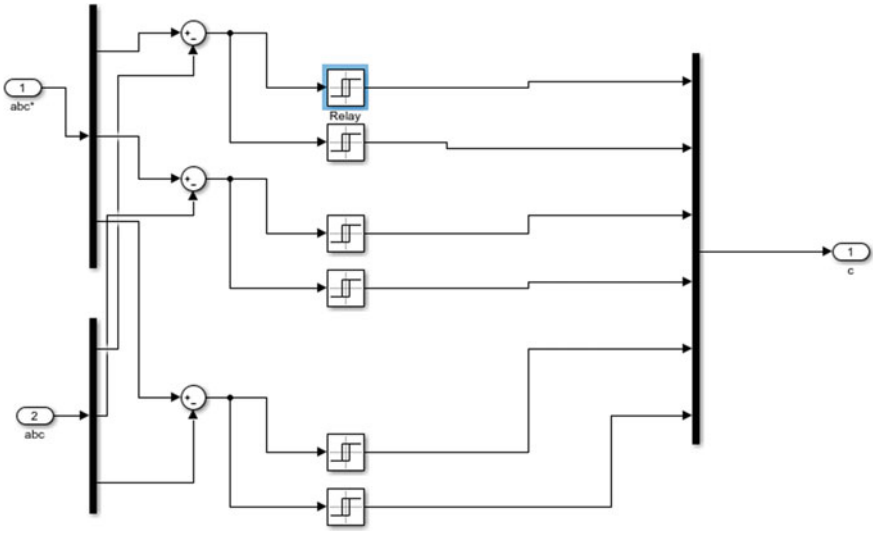

Fig. 4 Subsystem

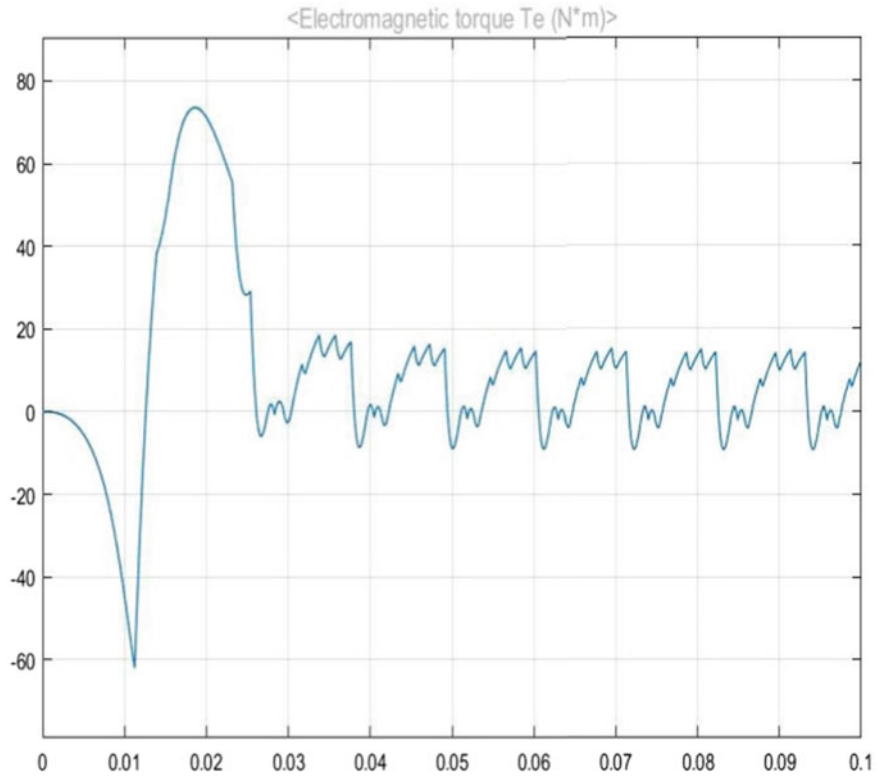

Fig. 5 Electromagnetic torque

under no load condition and in closed loop system. This speed is sensed by the Hall Effect sensor and thus determines conduction of winding commutation of each phase.

5 Conclusion

The working and construction of the Brushless Direct Current motor were studied successfully. The motor model was simulated using MATLAB in which different characteristics like rotor speed, electromagnetic torque, Hall Effect signal, stator current of the motor were analyzed. The speed and load torque were varied and various results were obtained. The result of the simulation helps in building real-time model and helps in saving manpower and reduces cost.

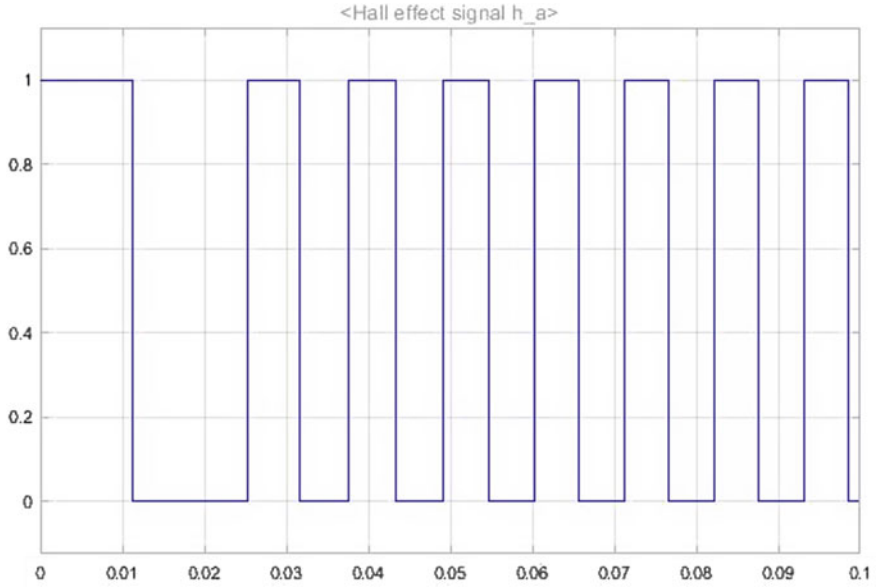

Fig. 6 Hall effect signal for one-phase

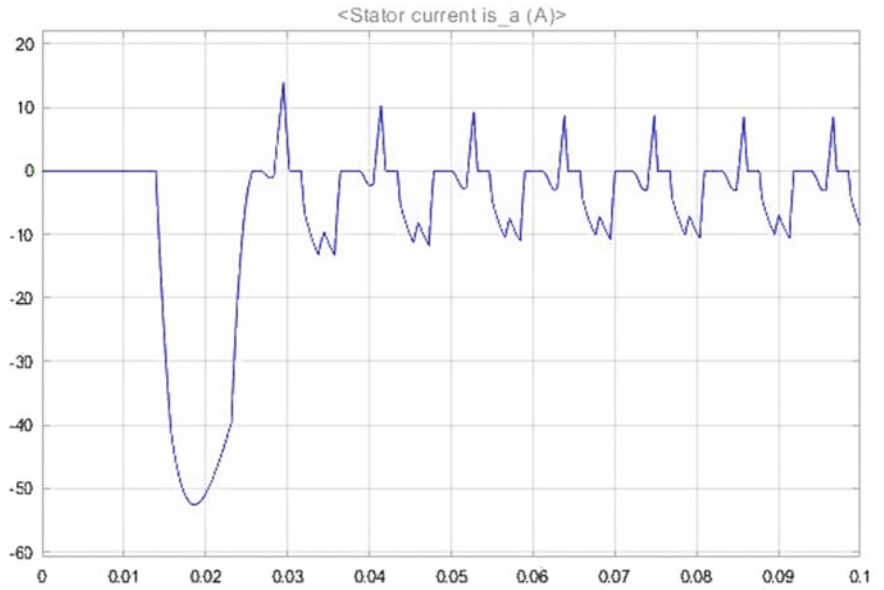

Fig. 7 Stator current

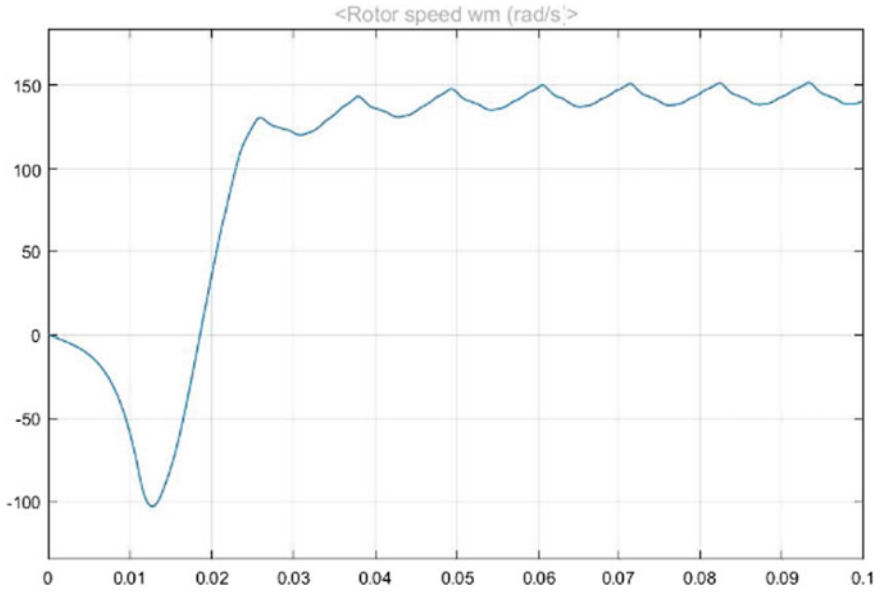

Fig. 8 Output-rotor speed

References

1. Kim JH, Jung IS, Ha GS (2015) Design and manufacturing of ultra small actuator. IEEE 3rd international conference on mechatronics, pp 23–26
2. Mishra DP, Sarangi JP (2019) Identification and analysis of different parameters for eddy current braking system along with its applications. IJRTER, 5(11):23–29
3. Mishra RN, Mohanty KB, Ray P, Mishra DP (2016) A reduced MF-based self-tuned robust neuro-fuzzy control of a decoupling linearized IM drive. ICNGIS-2016, 1st–3rd Sep 2016, Rajiv Gandhi Institute of Technology, pp 1–6
4. Alanson Sample P, Meyer DA, Smith JR (2016) Analysis, experimental results, and brushless DC motor speed control based on PID controller with 2-DOF and anti-windup techniques, vol 58, no. 2
5. Etacheri V, Marom R, Elazari R, Salitra G, Aurbach D (2018) Research on speed control system of brushless DC motor based on neural network: a review. Science 4(9):3243–3262
6. Kainan C, Zhengming Z (2013) Modelling and simulation methods for brushless DC motor drives IEEE. J Emerg Sel Topics Power Electron 1(2):114–121
7. Puqi N, Miller JM, Onar OC, White CP (2013) Brusless DC motor controlled by using IOT. In: Proceedings of IEEE ECCE, pp 3629–3634
8. Lukic S, Pantic Z (2013) Brushless DC motor speed control using proportional integral and fuzzy controller. IEEE Electrific Mag 1(1):57–64
9. Budhia M, Boys JT, Covic GA, Chang-Yu H (2013) Rapid control prototyping approach to fuzzy speed control of brushless DC Motor. IEEE Trans Ind Electron 60(1):318–328
10. Yiming Z, Zhengming Z, Kainan C (2014) Speed performance evaluation of BLDC motor based on dynamic wavelet neural network and PSO algorithm. IEEE Trans Power Electron 29(3):1058–1063
11. Mishra DP, Ray P (2018) Fault detection, location and classification of a transmission line. Neural Comput Appl 30(5):1377–1424

Chapter 2
Speed Control of DC Servomotor Using Chopper-Based PI Controller

Tejeswararao Lakkoju and Prasadarao Bobbili

Abstract In industry, the most commonly used control strategy is PID. The effectiveness of PI controller is increased by tuning of it (Ziegler-Nicholas Method). Using PID and Ziegler-Nichols controllers, speed control of industrial applications is not controlled in suggested manner. Fuzzy controller is enhanced than Ziegler-Nichols controller but rise time is high. In this research, DC servomotor speed control is governed by chopper-based PI controller that monitors time-domain variables like as rise time, settling time, peak amplitude, over shoot, and oscillations. Simulation results of speed control of DC servomotor using PI, Ziegler-Nicholas controller, fuzzy controller, chopper-based PI controller are demonstrated.

Keywords Ziegler-Nicholas controller · Fuzzy controller · DC servomotor · Chopper-based PI controller

1 Introduction

Industrial systems which are having high performance and efficiency are playing pivotal role in robot technology. Because of the need of robot technology had made to research and developed control techniques during previous years. Robot manipulation is main pillar of the core fields in industrial manufacturing and healthcare sectors. It works in unforeseeable, risky, and difficult to live in conditions where human cannot survive as in the chemical and nuclear sectors [1].

The best example for robot manipulator is DC servomotor. DC servomotor is treated as heart of the industrial applications. They are used in automatic doors, disk drives, and precise control applications. These motors are extensively used and various control logics have been developed to improve their efficiency but they are suffering from nonlinear parameters varying the overall system efficiency. Changing

T. Lakkoju (✉) · P. Bobbili
Department of Electrical and Electronics Engineering, Vignan's Institute of Information & Technology (A), Visakhapatnam, Andhrapradesh 530049, India
e-mail: tejeswararaolakkoju@gmail.com

S. Mahapatra et al. (eds.), *Advances in Energy Technology*, Advances in Sustainability Science and Technology, https://doi.org/10.1007/978-981-15-8700-9_2

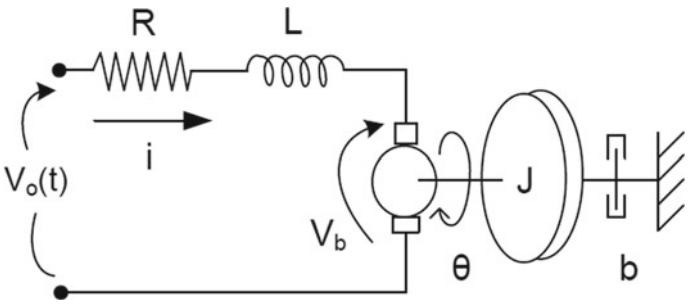

Fig. 1 DC servomotor circuit diagram

the load connected to the motor or further unexpected change in working condition may introduce more complexity to the application [2].

DC servomotor is used as actuators in servomechanisms. DC servomotor is used in robotic technology because of ability to operate at high torque at any speed. It can hold at any instant static position which play Levant role in robotic mechanism and servomechanism. These motors can change the direction of rotation quickly. As AC servo motor is more complex than DC servomotor, speed-controlled DC drive is more economical than speed-controlled AC drive [3].

In this work, performance of DC servomotor is performed and observed in Simulink/MATLAB environment. For performing the operation of DC servomotor, modelling of the motor is done in this work. DC servomotor is simulated under different controllers. For PI controller, steady-state error of the system is reduced but less stable. For PID controller, the parameters like rise time and steady-state error are controlled. Here, uncontrolled parameter is overshoot. For Ziegler-Nicholas controller, rise time of the system is more but problem occurs with oscillatory response. Could not find overshoot and stable operation for fuzzy logic controller yet rise time varied high. But chopper-based PI controller controls almost all time-domain specifications (Fig. 1).

2 Modelling of DC Servomotor

DC servomotors are more preferable for extensive speed varying control and are available for a lot of variable speed drives. Simulation for this, Fig. 2 depicts a variant of the DC servomotor. Table 1 displays parameters and values calculated and estimated (For practical conditions) for motor simulation [1].

Input voltage in Laplace transform is

$$E_a(s) = L \cdot s \cdot I_a(s) + R_a \cdot I_a(s) + E_b(s)$$
$$E_a(s) = (L \cdot s + R_a) \cdot I_a(s) + E_b(s)$$
$$E_a(s) - E_b(s) = (L \cdot s + R_a) \cdot I_a(s)$$

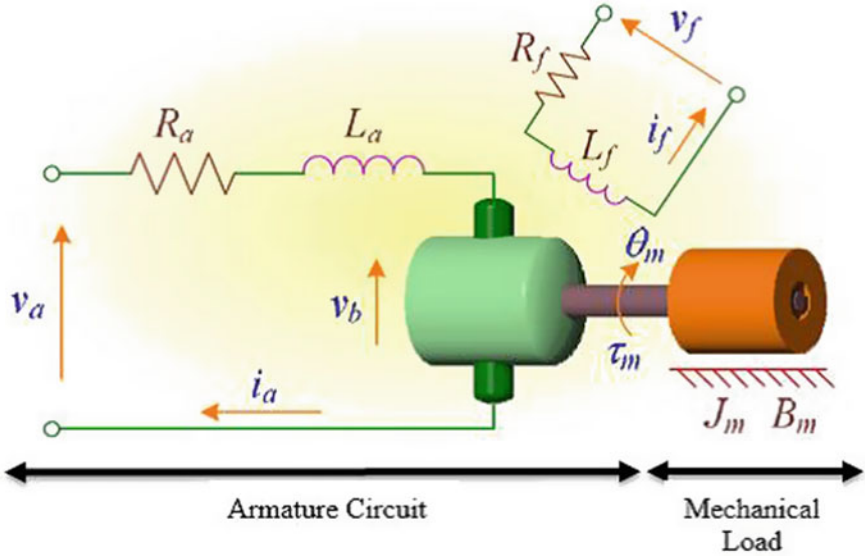

Fig. 2 Circuit diagram of DC servomotor

Table 1 Parameters and values for DC servomotor

Parameter	Value
Moment of inertia (J_m)	0.000052 kg m^2
Friction coefficient (B_m)	0.01 N ms
Back EMF constant (K_b)	0.235 V/rad s^{-1}
Torque constant (K_a)	0.235 Nm/A
Electric resistance (R_a)	2 Ω
Electric inductance (L_a)	0.23 H

$$I_a(s) = \left[\frac{1}{L \cdot s + R_a}\right][E_a(s) - E_b(s)]$$

Equation for output mechanical system is

$$T(t) = J_m \cdot \frac{\mathrm{d}\omega_m(t)}{\mathrm{d}t} + B_m \cdot \omega_m(t)$$

Apply Laplace transform to above equation

$$T(s) = [J_m \cdot s + B_m] \cdot \Omega_m(s)$$
$$\Rightarrow \Omega_m(s) = \left[\frac{1}{J_m \cdot s + B_m}\right] \cdot T(s)$$

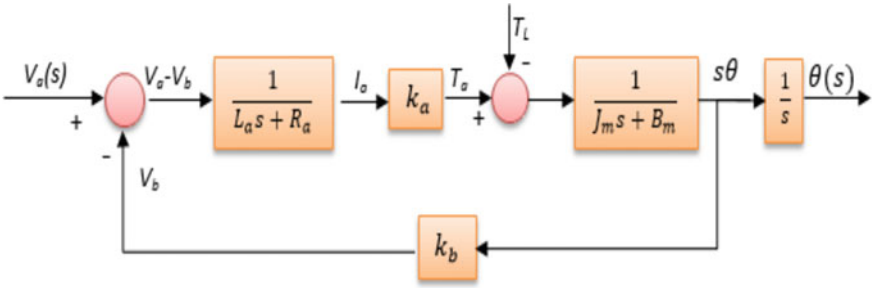

Fig. 3 Block diagram of DC servomotor

DC servomotor block diagram is shown in Fig. 3 With zero-load torque (*TL*)

Modeling the DC servomotor is intended to mimic the idealistic DC servomotor. Summing up the parameters to the transfer function equation, we can get the DC servomotor transfer function for monitoring position.

$$G(\text{position}) = \frac{\theta(s)}{V_a(s)} = \frac{19640}{s^3 + 201s^2 + 6290s}$$

3 Control Techniques Comparison

3.1 PI Controller

The proportional plus integral controller specifies two terms for an output signal: one is proportional to the error signal, while the other is proportional to the error signal integral. Figure 4 depicts the block diagram of PI controller of DC servomotor.

It is known from the closed-loop transfer function that the PI controller adds zero into the system and changes the order by one. Lifting the order of the system results in less stable system than the comparative one because higher orders are less reliable than lower order systems.

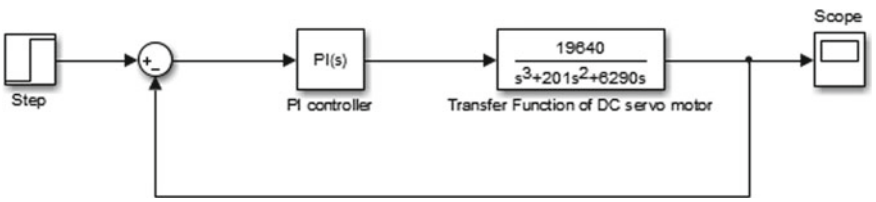

Fig. 4 Simulink diagram of PI controller of DC servomotor

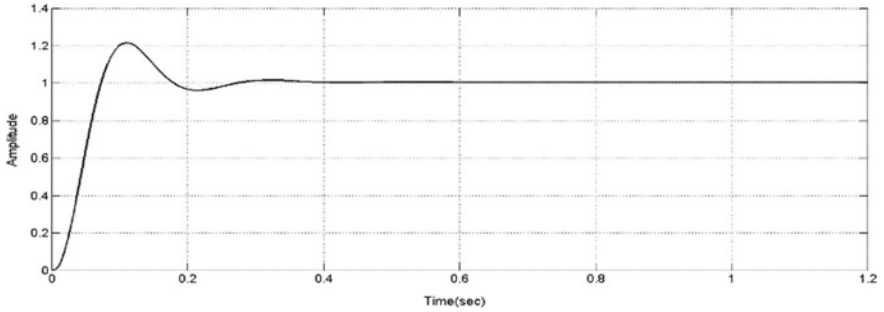

Fig. 5 PI controller-speed response of DC servomotor

From the loop transfer function, the PI controller is found to increase the number of the type by one. The increase in the number of type results in a decrease of the error of the steady state. Figure 5 depicts the speed response of DC servomotor using PI controller.

3.2 PID Controller

The best choice of three fundamental relationships: proportional, integral, and derivative can improve the performance of the system in all aspects. Figure 6 depicts Simulink block diagram of PID controller to the DC servomotor.

The proportional controller stabilizes the gain but maintains a steady error in the process. The integral controller decreases the steady-state error or eliminates it. The derivative controller gradually diminishes the rate of change of error. Figure 7 depicts speed response of DC servomotor using PID controller (Fig. 8).

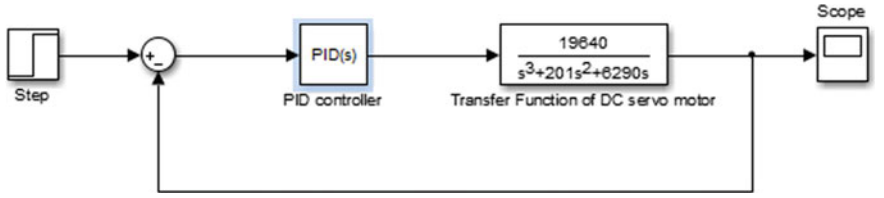

Fig. 6 Simulink diagram of PID controller of DC servomotor

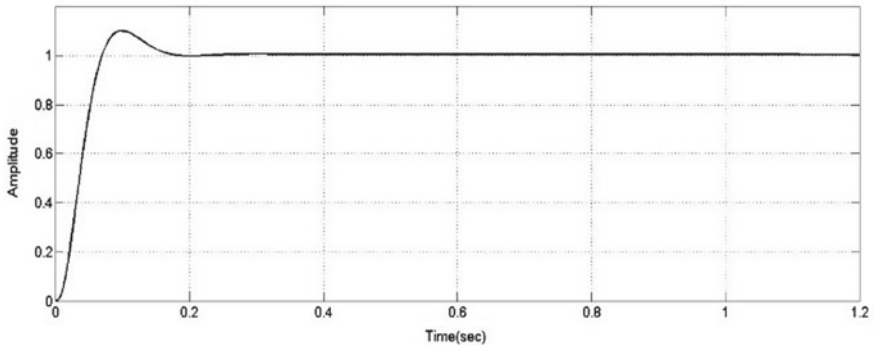

Fig. 7 PID controller-speed response of DC servomotor

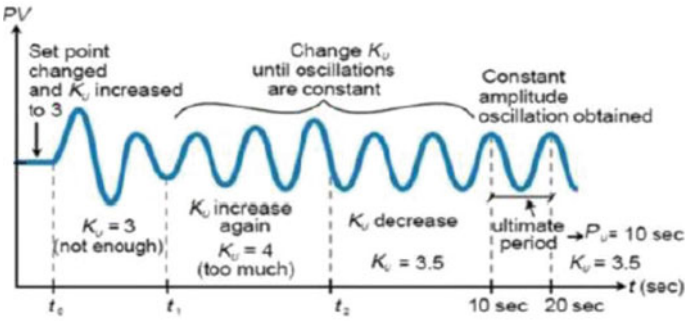

Fig. 8 Parameters values calculation from (Z–N) controller

3.3 Ziegler-Nichols Controller (Z-N Controller)

The Ziegler-Nichols rule is a trial and error PID tuning procedure, which aims to produce decent values for parameters of gain of PID controller. Figure 9 depicts block diagram of Ziegler-Nichols controller of DC servomotor.

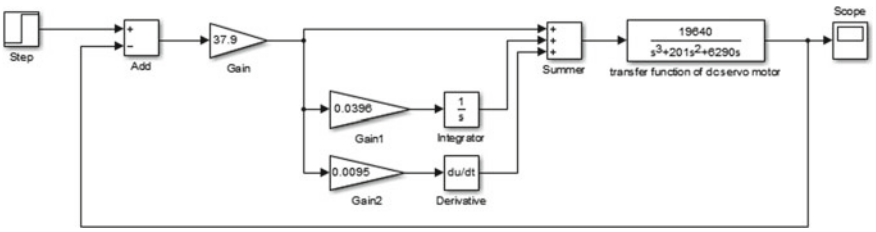

Fig. 9 Block diagram of Ziegler-Nicholas controller of DC servomotor

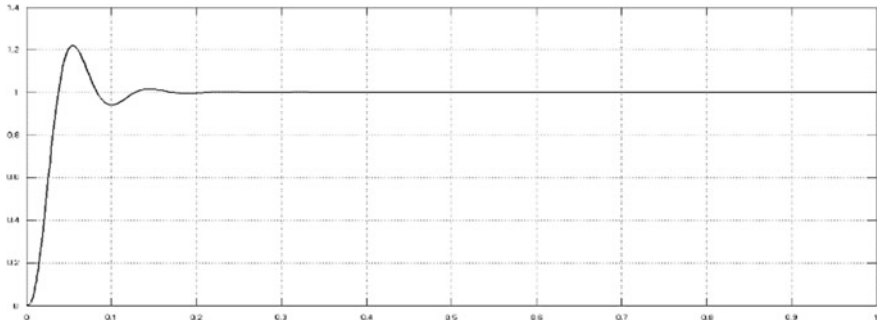

Fig. 10 Ziegler-Nichols controller-speed response of DC servomotor

The reasoning comes from the heuristic theory of neutrality. Initially, whether the optimal proportional gain is positive or negative is tested. For this function, step input is increased a bit manually; otherwise, if the steady-state output rises, it is positive; otherwise, it is negative.

Figure 8 depicts the parameters values calculation from Ziegler-Nichols controller. Then, K_i and K_d are set to zero and K_p value is raised until a periodic oscillation is generated at the output response. This critical K_p value succeeds in being the ultimate gain (K_c), and the duration in which the constant oscillation process occurs is considered as the ultimate time (P_c). As a consequence, the whole cycle depends on two variables and the other systematize parameters discussed. Figure 10 depicts speed response of DC servomotor using Ziegler-Nichols method.

Type of controller	K_p	T_i	T_d
P	0.5 Kcr	00	0
PI	0.45 Kcr	11.2 Pcr	0
PID	0.6 Kcr	0.5 Pcr	0.125 Pcr

Where K_p implies controller path gain

T_i implies controller's integrator time constant

T_d implies controller's derivative time constant.

3.4 Fuzzy Logic Controller

Fuzzy logic controller is a control logic which is based on the functions of the member ship. In fuzzy logic controller, human knowledge is converted to automatic control logic. Fuzzy logic controller does not need critical mathematical calculations like the others control strategies. On the other hand, other control methods need mathematic

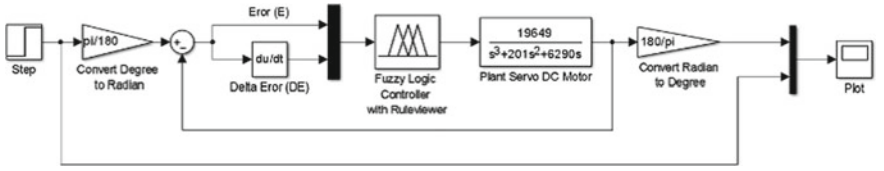

Fig. 11 Simulink model for simulating FLC

parameters and algebraic expressions, but fuzzy logic controller only need expert knowledge to convert into membership functions. Figure 11 depicts block diagram of FLC.

Fuzzification: In this controller, the measured inputs are called the crisp values. The transformation of these crisp values to the linguistic fuzzificated values is called a fuzzification.

Knowledge Base: Gathering the principles of expert knowledge required to achieve the stated goal.

Fuzzy Reasoning Mechanism: Using this method, fuzzy logic operations are performed and control action is taken about the inputs of the fuzzy logic controller.

Defuzzification Unit: It transforms the output of the fuzzy reasoning system into the requisite crisp value within this unit

Fuzzy Controller Design: In fuzzy logic controller, the very crucial thing is to establish the membership functions for both input and output.

There are 7 rules that used at the controllers which are based on human experience and information are:

1. If E is PL, then CONTROL is PL
2. If E is NL, then CONTROL is NL
3. If E is Z and DE is N, then CONTROL is NM
4. If E is Z and DE is P, then CONTROL is PM
5. If E is Z, then CONTROL is Z
6. If E is NM, then CONTROL is NM
7. If E is PM then CONTROL is PM.

After anticipating the rule from the observation, we can get the surface viewer in figure that depicts the rule of FLC.

Figure 12 depicts the surface of fuzzy logic controller. Figures 13, 14, and 15 depict membership functions of error, change in error, and control signals. Fuzzy infernce system features two-sourced inputs and an expected output regarding inputs. Two sources here are error (E) and change in error (DE). One output which is utilized as a control signal input to the plant. The fuzzy membership functions are depicting in figure for correction, error, and control signal. NL implies Negative High, NM implies Negative Small, Z implies Zero, PL implies positive large, and PM implies Positive

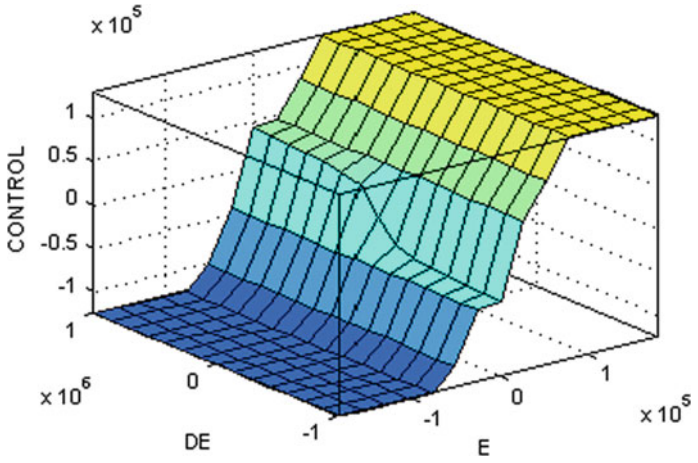

Fig. 12 FLC surface

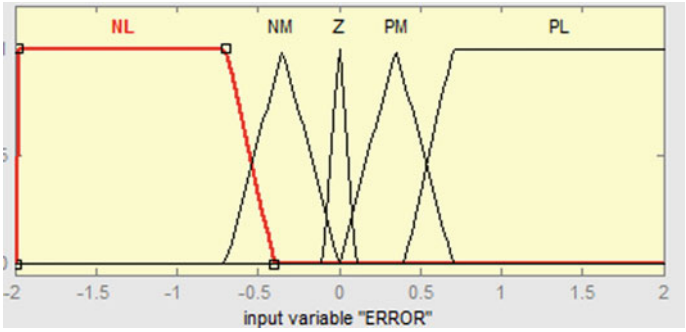

Fig. 13 Chosen membership function of error (E) as input

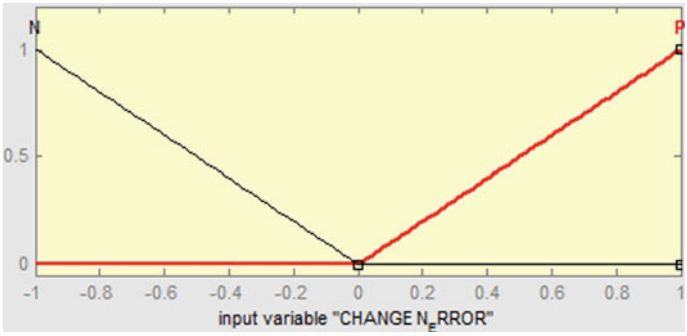

Fig. 14 Chosen membership function of delta error (DE) as input

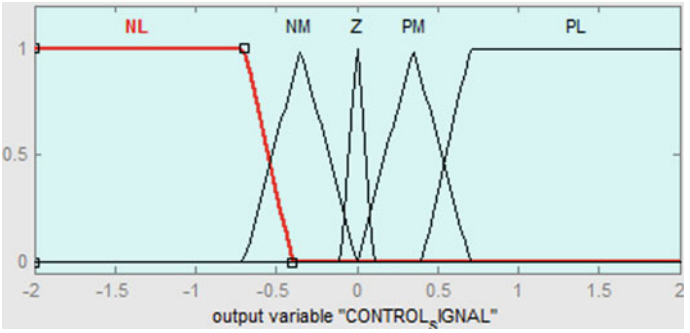

Fig. 15 Chosen membership function of control as output

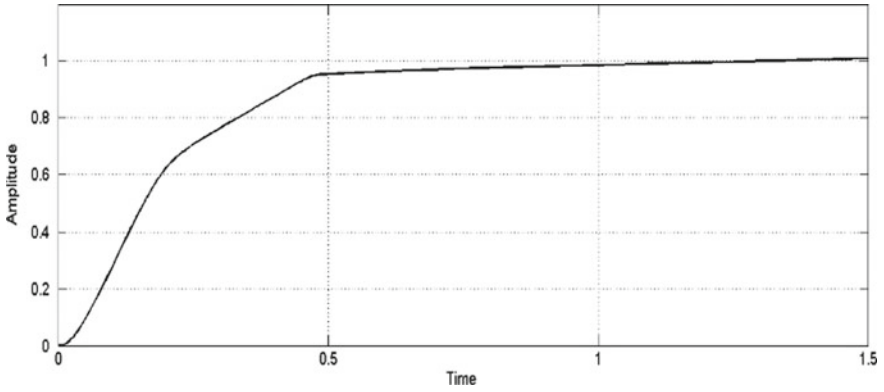

Fig. 16 FLC-speed response of C servomotor

Medium. Figure 16 depicts the speed response of DC servomotor using fuzzy logic controller [4].

4 Proposed Chopper Based Controller

In this proposed controller technique, DC servomotor is controlled by chopper-based controller. Figure 17 depicts chopper-based PI controller of DC Servomotor.

In this controller, transfer function of DC servomotor is taken as in terms of functional blocks in way to get the signals of input current and speed of DC servomotor.

Speed of the DC servomotor is compared with reference speed. The compared signal is in terms of error speed signal which is converted to current signal using PI controller. PI controller is used to convert error signal to respected current signal. This current signal which is derived from PI controller again compared with input current

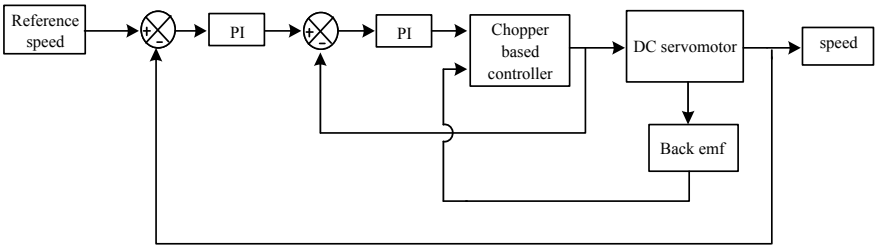

Fig. 17 Block diagram of chopper-based PI controller of DC servomotor

signal of the DC servomotor. This error current signal is converted to amplified current signal using PI controller.

This amplified current signal is used to control the chopper operation. Switching of switches can be done by two relays whose are fed by amplified current signal. The EMF signal developed in the DC servomotor is fed to the chopper load to get the desired load current. This load current is the controlled current signal which is fed to DC servomotor as input current.

This technique is completely based on closed-loop operation which is used to get the desired speed of DC servomotor with controlled time-domain parameters. Figure 18 represents speed response of DC servomotor using chopper-based PI controller.

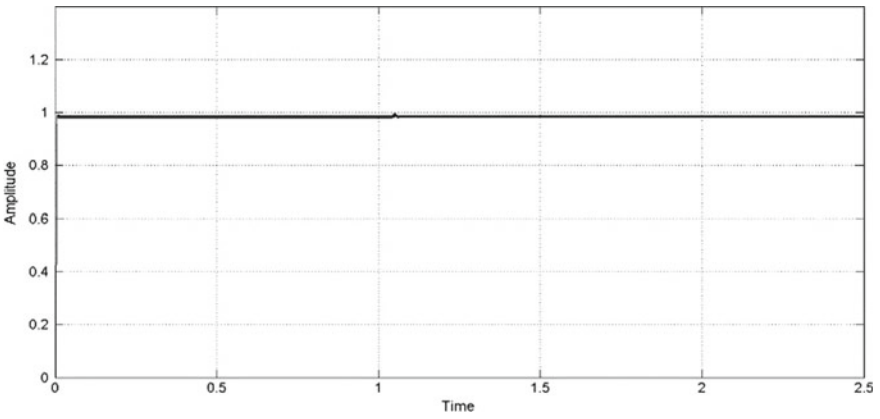

Fig. 18 Speed response of DC servomotor using chopper-based PI controller

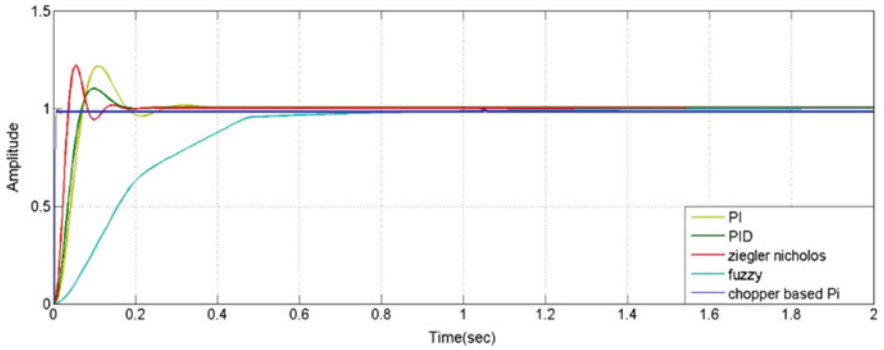

Fig. 19 Comparison among speed control of DC servomotor using different controllers

Table 2 Comparison of time-domain parameters

Controller	Rise time (s)	Settling time (s)	Overshoot (%)	Peak amplitude	Oscillations
PI	0.056	0.24	21.5	1.22	Moderate
PID	0.049	0.18	10.1	1.1	No
Ziegier-Nicholas	0.044	0.15	21	1.21	Moderate
FLC	1.0	0.9	0	1	No
Chopper-based PI controller	0.01	0.01	0	1	No

5 Results

Figure 19 depicts the comparison among speed control of DC servomotor using different controllers. On comparing DC servomotor with different controllers, the time-domain specifications are as graph and table follows. Table 2 depicts the counterparts of tim-domain parameters of above discussed controllers.

References

1. Mahir Dursun T, Engin S (2018) Deadbeat control of a DC servo motor at low speed. In: 4th international conference on control, automation and robotics
2. Usoro IH, Itaketo UT, Umoren MA (2017) Control of a DC motor using fuzzy logic control algorithm. Nigerian J Technol (NIJOTECH)
3. Ekpoudoml II, Archibong IE, Itaketo UT (2017) Speed control of dc motor on load using fuzzy logic controller (a case study of emergency lube oil pump motor of h25 hitachi turbine generator). Nigerian J Technol (NIJOTECH)

4. Munadi B, Amirullah Akbar M (2014) Simulation of fuzzy logic control for DC servomotor using Arduino based on Matlab/Simulink. In: International Conference on Intelligent Autonomous Agents, Networks and Systems

Chapter 3
Application of PID Controller-Based Automatic Generation Control for Interconnected Power System with Governor Dead-Band Non-linearity Using MOL Algorithm

M. D. Pabitra, Sangram Keshori Mohapatra, Asini Baliarsingh, and Radhakrishna Das

Abstract In this paper, MOL algorithm is used in two-area non-reheat thermal power system in the presence of governor dead-band with PID controller is considered. For design and analysis of the purposed system, at first ISE and ISTE two objective functions are considered than 3rd type of objective function which is the modified form by using ISE, ISTE, IAE, ITAE and summation of power deviation and the settling times of frequency. For obtaining the dynamic performance of AGC, PID controller parameters are tuning by applying MOL technique. Then, superiority of MOL techniques is verified by comparing the published result in CPSO-based design of the purposed system. The transient analysis performance of MOL-based PI controller is superior than CPSO-based PI Controller.

Keywords PID controller · MOL algorithm · Governor dead-band · AGC

1 Introduction

When two or more power systems are interconnected, then its main function is generated, transmitted and distributed power in nominal range of system frequency [1–5]. The change of nominal frequency generally occurs due to mismatch of generation

M. D. Pabitra
Department of Electrical Engineering, BEC, Bhubaneswar, Odisha, India

S. K. Mohapatra
Department of Electrical Engineering, G.C.E., Keonjhar, Odisha, India

A. Baliarsingh
Department of Electrical Engineering, G.C.E., Kalahandi, Odisha, India

R. Das (✉)
Department of Electrical Engineering, GIET, Bhubaneswar, Odisha, India
e-mail: radhakrishna@gietbbsr.com

S. Mahapatra et al. (eds.), *Advances in Energy Technology*, Advances in Sustainability Science and Technology, https://doi.org/10.1007/978-981-15-8700-9_3

of power and load demand. In order to maintain the balance of net power generation by synchronous machine which is sense for variation of frequency takes place in the power system to use the concept of AGC. As some researcher attempts the LFC of single- and multi-area system by applying different optimization techniques and controllers [6–8], the conventional PI type controller attempts in different LFC of single- and two-area system [9]. It shows that in convention PI type of controller, the dynamic performance is very poor in term of settling time of variation of frequency and variation of tie-line power and its overshoot. As in the literature survey, the AGC of fuzzy-based PI with tabu search algorithm applied in two-area system for LFC [10]. The LFC of generalized neural network with different controllers in AGC system is proposed in [11], the fuzzy logic-based controller in multi-area system [12], and fuzzy-neuro in hybrid approach [13]. In this paper, the Many Optimizing Liaisons (MOL) algorithm is used for optimization for controller parameters [14]. In the propose analysis the optimal design of MOL algorithm-based two areas with governor dead-band by considering PI and PID controllers. The purpose analyses of modified fitness or objective function are considered, and dynamic performance of modified fitness function is compared with conventional type of objective function. It is also compared that both PI and PID controllers using MOL algorithm better than PI-based CPSO algorithm in two-area system in the presence of governor dead-band [16].

2 System Model

2.1 Two-Area System

Figure 1 is the simulation model of interconnected system in the presence of governor dead-band with two non-reheat thermal power plant. The purposed model can be designed by using relevant parameters taken as per appendix. In the purpose system by considering a governor dead-band which affect the simulation performance of oscillation of purposed system and the transfer function taken in the above system as per the per the reference [16].

$$G_g = \frac{0.8 - \frac{0.2}{\pi} s}{1 + sT_g}$$

The PI and PID controllers are taken for the given two-area interconnected power system for stability performance analysis. The structures of the PI and PID controllers having gain (K_P, K_I and K_D) are considered as

$$K(S) = K_P + \frac{K_I}{S}$$

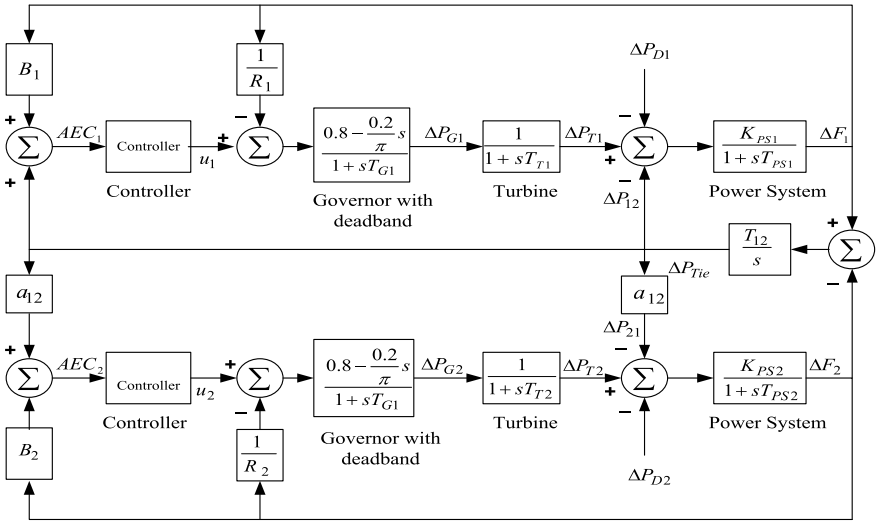

Fig. 1 Interconnected two-area system in the presence of governor dead-band

$$K(S) = K_P + \frac{K_I}{S} + SK_D \tag{1}$$

The PI/PID controller (K_P, K_D and K_P, K_I, K_D) in the purposed system is same (both area-1 and -2), so that it can be taken as in the controllers $K_{P1} = K_{P2} = K_P$, $K_{I1} = K_{I2} = K_I$ and $K_{D1} = K_{D2} = K_D$. The area-1 having AEC1 (error control in area-1) is the input of controller taken as Eq. (2)

$$e_1(t) = \text{AEC}_1 = B_1 \Delta f_1 + \Delta P_{\text{Tie}} \tag{2}$$

The area-2 having area controller error (AEC2) is taken as in Eq. (3)

$$e_2(t) = \text{AEC}_2 = B_2 \Delta f_2 - \Delta P_{\text{Tie}} \tag{3}$$

The u_1 and u_2 are the output of controller (area-1 and -2). In PI controller ($K_{D1} = K_{D2} = 0$), the control inputs are attained as:

$$u_1 = K_{P1}\text{AEC}_1 + K_{I1} \int \text{AEC}_1 \tag{4}$$

$$u_2 = K_{P2}\text{AEC}_2 + K_{21} \int \text{AEC}_2 \tag{5}$$

2.2 Objective Function

The ISE (*J1*), ISTE (*J2*) and modified objective function (*J3*) are considered for the purpose analysis of frequency variation of two-area power system and variation of tie-line power. The above fitness function (J_1, J_2, J_3) is used to minimized the fitness value as

$$J_1 = \text{ISE} = \int_0^{t_{\text{sim}}} (\Delta f_1)^2 + (\Delta f_2)^2 + (\Delta P_{\text{Tie}})^2 \cdot \text{d}t \tag{6}$$

$$J_2 = \text{ITSE} = \int_0^{t_{\text{sim}}} \left[(\Delta f_1)^2 + (\Delta f_2)^2 + (\Delta P_{\text{Tie}})^2\right] \cdot t \cdot \text{d}t \tag{7}$$

$$J_3 = \omega_1 \cdot \text{ISE} + \omega_2 \cdot \text{ITSE} + \omega_3 \cdot \text{ITAE} + \omega_4 \cdot \text{IAE} + \omega_5 \cdot T_S \tag{8}$$

T_S is the summation of power deviation and the settling times of frequency; ω_1 to ω_5 are weighting factors. The weighting factor in the process of optimization is taken as $\omega_1 = 10{,}000$, $\omega_2 = 1000$, $\omega_3 = 50$, $\omega_4 = 70$ and $\omega_5 = 0.1$.

The purpose of fitness function (J_1, J_2, J_3) minimized the value subjected to minimum to maximum value of controller parameters. The purpose system with controllers of PI/PID taken the same value of both areas. So that $K_{P1} = K_{P2} = K_{P,}$ $K_{I1} = K_{I2} = K_{I\text{ and}}$ $K_{DF1} = K_{D2} = K_D$, where $\Delta f1$, $\Delta f2$ and $\Delta P_{\text{tie,}}$ are the variation in frequency in area-1 and -2 and variation of tie-line power.

3 Many Optimizing Liasisons (MOL) Algorithm

The purpose algorithm is the shorten form of PSO algorithm. In PSO algorithm, all the positions of particles are move randomly in the search space direction [14]. The best position can be obtained by each particles changing the direction in the search space locality to move the next best position in the reference of fitness measures $f : \Re^n \rightarrow \Re$. The initial velocity of the particle and position of particle is updated iteratively randomly in the search space. The updating velocity of particle is taken as per reference article [15]. The position $\vec{X} \in R^n$ and velocity $\vec{V}$ be the velocity of a particle.

$$\vec{V} \leftarrow w\vec{V} + \Phi_P R_P\left(\vec{P} - \vec{X}\right) + \Phi_G R_G\left(\vec{G} - \vec{X}\right) \tag{9}$$

In Eq.(9), w be the inertia weight that can control the velocity of particle. $\vec{P}$ and $\vec{G}$ are the global better positions of particle and swarm having weighted by the random variables R_P, $R_G \sim U(0, 1)$. $\Phi_P \Phi_G$ are the parameters which depend on

behavioural parameters. In the search space, the new position is obtained by the merger of current position and velocity of the particles

$$\vec{X} \leftarrow \vec{X} + \vec{V} \tag{10}$$

The particle is transferred in one step from one search space to another after updating the position of particles. The purpose algorithm velocity of particle updated randomly but in case of CPSO algorithm abrupt change of velocity and a craziness factor changes the direction. In the MOL algorithm, the best position of swarms $\vec{P}$ is removed by setting $\Phi_P = 0$ and the update velocity as follows:

$$\vec{V} \leftarrow w\vec{V} + \Phi_G R_G\left(\vec{G} - \vec{X}\right) \tag{11}$$

where w is inertia weight and $R_G \sim U(0, 1)$ is stochastic nature algorithm and Φ_G is behavioural parameters. The $\vec{X}$ is the current position of particle and updated using Eq. (10) as before. The best known position of overall swarms is $\vec{G}$.

4 Results and Discussion

The dynamic performances analysis is comparing in the three cases of objective function with disturbance which is considering in the area-1 and area-2 of the purpose system. Case-1: ISE objective function by considering disturbances is taken separately (area-1, area-2). Case-2: ISTE objective function by considering disturbance is taken separately (both area-1 and -2). Case-3: Modified objective function by considering disturbances is taken separately (area-1, area-2). The minimum of 15–20 time to run optimization till to get global value of parameters. Table 1 shows the best value of controller parameters obtained in the process, and Table 2 shows the ISE objective function with settling times. Table 3 is ISE, ITSE, ITAE, IAE and settling times with proposed objective function

Table 1 Optimization controller parameters

Controller	Gain parameters	J1 (ISE)	J2 (ISTE)	J3 (Modified)
PID	K_P	0.5610	0.3610	0.2299
	K_I	0.9579	0.9348	0.9692
	K_D	0.6712	0.6299	0.4892
PI	K_P	−0.5190	−0.5549	−0.5401
	K_I	0.2199	0.2150	0.2199

Table 2 Settling times and ISE objective function values

Parameters		MOL optimized PI controller	MOL optimized PID controller	CPSO optimized PI controller [16]
ISE		18.765×10^{-4}	4.875×10^{-4}	21.2158×10^{-4}
Ts Sec	$\Delta f1$	19.89	7.12	23.66
	$\Delta f2$	15.57	5.12	16.82
	ΔP_{tie}	21.92	6.89	23.66
Parameters		MOL optimized PI controller	MOL optimized PID controller	CPSO optimized PI controller [16]
ISTE		32.654×10^{-4}	3.987×10^{-4}	35.6968×10^{-4}
Ts Sec	$\Delta f1$	16.51	6.94	18.83
	$\Delta f2$	12.17	5.89	13.42
	ΔP_{tie}	16.78	7.12	18.83

Table 3 ISE, ITSE, ITAE, IAE and Ts with proposed modified objective function

Parameters		MOL optimized PI controller	MOL optimized PID controller	CPSO optimized PI controller [16]
ISE		35.542×10^{-4}	5.120×10^{-4}	43.8016×10^{-4}
ITSE		68.651×10^{-4}	4.673×10^{-4}	83.1849×10^{-4}
ITAE		46.897×10^{-4}	8.509×10^{-2}	58.2969×10^{-2}
IAE		18.923×10^{-4}	5.473×10^{-2}	21.875×10^{-2}
Ts Sec	$\Delta f1$	16.51	6.94	18.83
	$\Delta f2$	12.17	5.89	13.42
	ΔP_{tie}	16.78	7.12	18.83

Case-1: ISE objective function

Case-2: ISTE objective function

Case-3: Proposed objective function.

The 1% of step greater in demand given at time = 0 s in the area-1 and area-2 separately for the above cases in different types of objective function is considered. For the case-1 ISE fitness function variation of frequency and variation of tie-line power for the area-1 and area-2 in Figs. 2a, b, 3, 4a, b, the simulation result performance of purpose PI controller is superior than PI base craziness PSO design controller of the same system. However, the settling time of PID controller is superior than PI of MOL- and CPSO-based algorithm of the power system. Similarly for the case-2, ISTE objective function simulation result performance of MOL-based PI is superior of CPSO-based PI controller in the result as shown in Figs. 5a, b, 6a, b, 7. In the case-3 modified objective function of purposed area of interconnected system, the settling time of PID controller is better than PI-based MOL and CPSO algorithm of the same

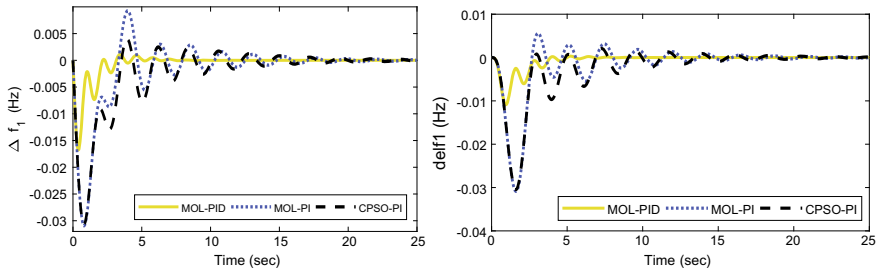

Fig. 2 **a**, **b** Frequency changes of the area-1 due to disturbance in area-1 and change in frequency of the area-1 by virtue of perturbation in area-2, respectively

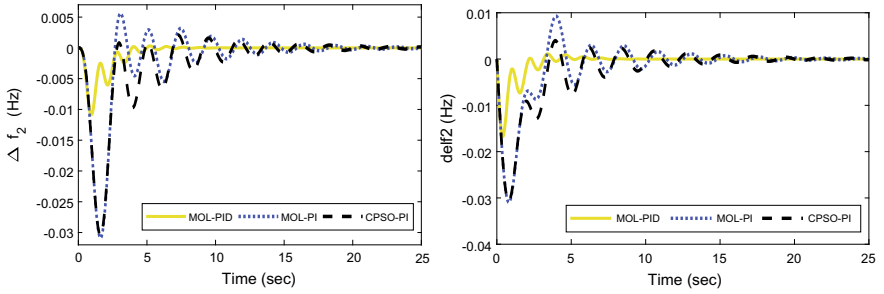

Fig. 3 **a**, **b** Frequency changes of the area-2 due to disturbance in area-1 and frequency changes of the area-2 by virtue of perturbation in area-2, respectively

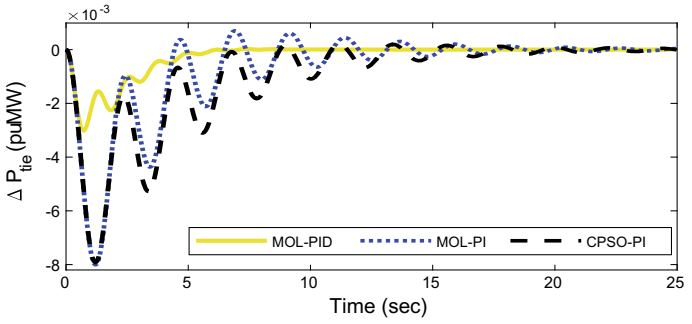

Fig. 4 Tie-line power changes of the area-1 by virtue of perturbation in area-1

system. It is also discussed that the simulation result of PI-based purposed system of frequency variation and tie-line power deviation is superior than PI controller with CPSO based on the same system as shown in Figs. 8a, b, 9a, b, 10.

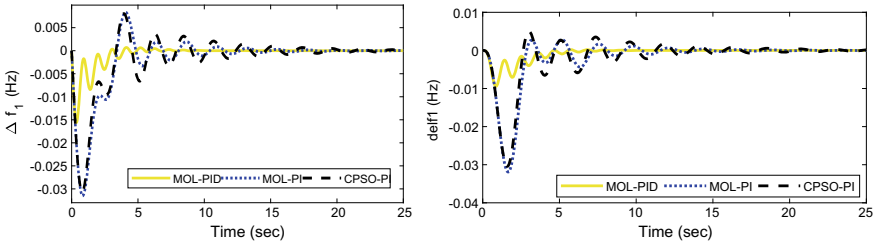

(a) (b)

Fig. 5 **a**, **b** Frequency changes of the area-1 due to disturbances in area-1 and Frequency changes of the area-1 by virtue of perturbation in area-2, respectively

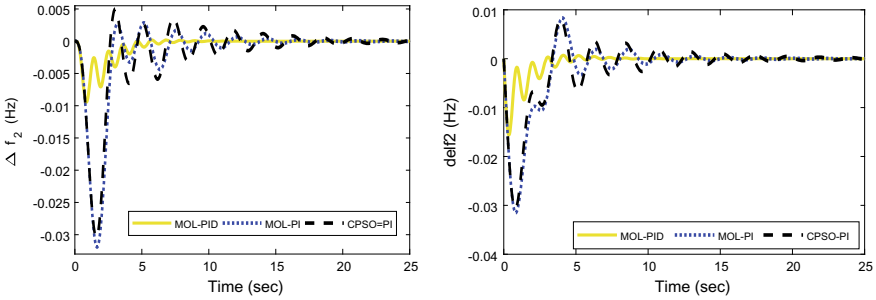

(a) (b)

Fig. 6 **a**, **b** Frequency changes of the area-2 by virtue of disturbance in area-1 and Frequency changes of the area-2 due to disturbance in area-2, respectively

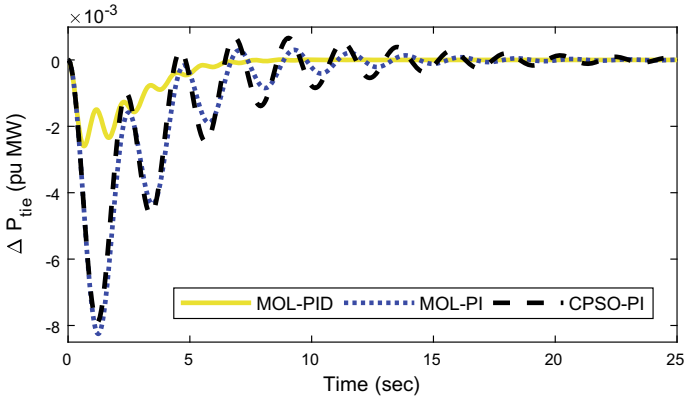

Fig. 7 Tie-line power changes of area-1 by virtue of perturbation in area-2

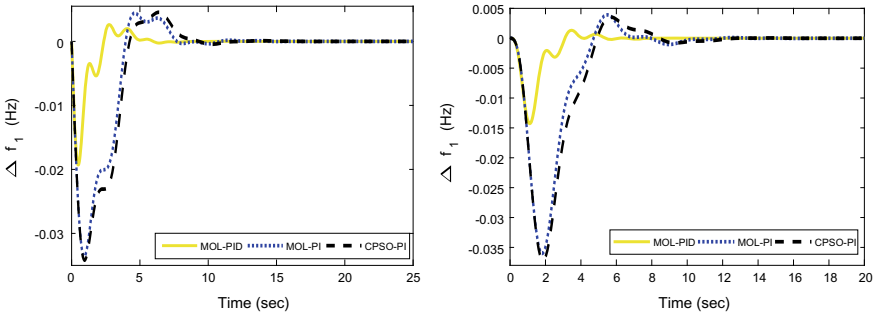

Fig. 8 **a**, **b** Frequency changes of the area-1 due to perturbation in area-1 and Frequency changes of the area-1 by virtue of disturbance in area-2, respectively

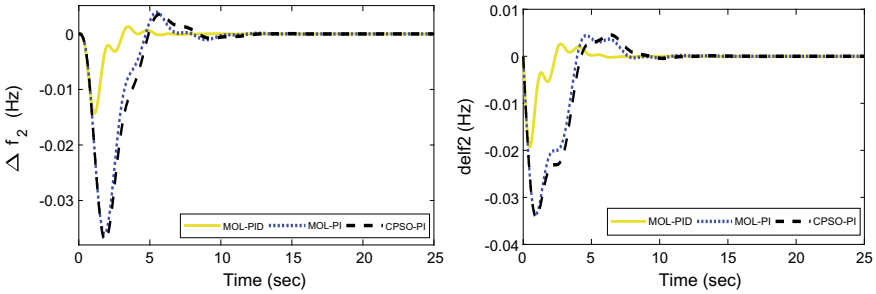

Fig. 9 **a**, **b** Frequency changes of the area-2 by virtue of perturbation in area-1 and frequency changes of the area-2 by virtue of disturbances in area-2, respectively

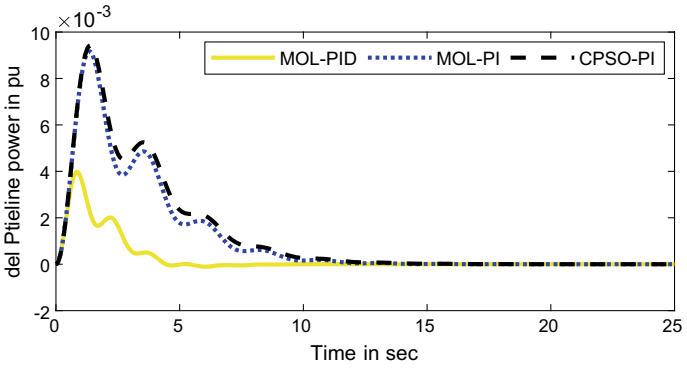

Fig. 10 Tie-line power changes of area-1 by virtue of disturbance in area-2

5 Conclusion

This analysis shows that MOL-based design and performance of PI and PID controllers of interconnected two areas of AGC in the presence of governor dead-band. The selection of objective function is important for finding out of optimization controller parameters. The ISE and ISTE two types conventional objective function is considered in the purposed analysis than modified objective function considered by using ISE, ISTE, IAE, IATE and sum of frequency variation of settling time and tie-line power (Ts) with appropriate weights. The dynamic performance of modified objective function is better than ISE and ISTE objective function of the same system. It is also observed that PI controller of purpose system is better than PI based CPSO based PI controller.

Appendix

The parameter is taken of purposed two areas with governer dead-band as: TPS1 = TPS2 = 20 s, B1 = 0.045 p.u., MW/Hz, B2 = 0.045 p.u., MW/Hz, R1 = 2 Hz/p.u., R2 = 2.4 Hz/p.u., KPS1 = KPS2 = 120 Hz/p.u., MW, T12 = 0.545 p.u., a12 = −1, TG1 = 0.08 s, TG2 = 0.08 s, TT1 = 0 .3 s, TT2 = 0.3 s.

References

1. Elgerd OL (2001) Electric energy systems theory—an introduction. McGraw Hill Co., New York
2. Elgerd OI, Fosha CE (1970) Optimum megawatt-frequency control of multi-area electric energy systems. IEEE Trans PAS PAS-89(4):556–563
3. Rerkpreedapong D, Hasanovic A, Feliachi A (2003) Robust load frequency control using genetic algorithms and linear matrix inequalities. IEEE Trans Power Syst 18(2):855–861
4. Yang TC, Cimen H, Zhu QM (1998) Decentralized load frequency controller design based on structured singular values. IEE Proc-Generat Trans Distrib 145(1):7–14
5. Kundur P (1994) Power system stability and control. Mc-Grall Hill, New York
6. Ghosal SP (2003) Multi-area frequency and tie-line power flow control with fuzzy logic based integral gain scheduling. J Inst Electr Eng 84:135–141
7. Ghosal SP (2004) Application of GA/GA-SA based fuzzy automatic generation control of a multi-area thermal generating system. Electr Power Syst Res 70(2):115–127
8. Kothari ML, Nanda J, Kothari DP, Das D (1989) Discrete-mode automatic generation control of a two-area reheat thermal system with new area control error. IEEE Trans Power Syst 4(2):730–738
9. Venkateswarlu K, Mahalanabis AK (1978) Load frequency control using output feedback. J Inst Eng (Ind), pt. El-4 58:200–203
10. Pothiya S, Ngamroo I, Runggeratigul S, Tantaswadi P (2006) Design of optimal fuzzy logic based PI controller using multiple Tabu Search algorithms for load frequency control. Int J Contr Autom Syst 4(2):155–164
11. Chaturvedi DK, Satsangi PS, Kalra PK (1999) Load frequency control: a generalized neural network approach. Intl J Electr Power Energy Syst 21:405–415

12. Çam E, Kocaarslan I (2005) Fuzzy logic controller in interconnected electrical power systems for load-frequency control. Int J Electr Power Energy Syst 27(8):542–549
13. Panda G, Panda S Ardil C (2012) Automatic generation control of interconnected power system with generation rate constraints by hybrid neuro fuzzy approach. Int J Electr Comput Electr Commun Eng 6(4)
14. Kennedy J, Eberhart RC (1995) Particles swarm optimization. In: Proceedings of the IEEE international conference on neural networks, Perth Australia, pp 1942–1948
15. Shi Y, Eberhat R (1998) A modified swarm optimizer. In: Proceedings of the IEEE international conference on evolutionary computation, Anchorange
16. Gozde H, Taplamacioglu MC (2011) Automatic generation control application with craziness based particle swarm optimization in a thermal power system. Int J Electr Power Energy Syst 33:8–16

Chapter 4
Power Quality Enhancement in Smart Grid Power Systems Using Buck Converter

Akash K. Pati, Arunjyoti Priyadarshini, Atma P. Sethy, Prativa Muduli, Prateek Kr. Sahoo, and P. K. Satpathy

Abstract Smart grids are the most efficient selection for the distribution of electrical energy in a bidirectional way. The buck converter is one of the most essential parts of the smart grid system as it regulates the power from the renewable sources and because of its fast dynamic response, compactness, and high efficiency. But the open-loop controlling technique of buck converter causes instability in the system. The use of output voltage for the feedback purpose and proportional integral (PI) controller for enhancement of stability increases the demand of single loop buck converter. However, such techniques do not perform satisfactorily under load disruption and fault conditions; thereby, causing transients in the output. Here, we are proposing a technique in which the current loop is cascaded with the voltage loop to minimize the transients in the output, to improve the power quality. The mathematical model for the proposed technique is tested on MATLAB–Simulink platform and the simulation results so obtained justify that the output of the proposed cascaded loop control of the buck converter results in lesser transients along with lesser settling period and peak overshoot in the output waveform as compared to the conventional single loop control of buck converter.

Keywords Single loop control system · Cascade loop control system · Smart grid · Power quality

1 Introduction

In the present scenario, electricity is a major need for everyone. But, even in this fast-moving world, there are still many isolated areas which are not yet electrified as they are not connected to the national grid. However, in those remote areas, green

A. K. Pati · A. Priyadarshini · A. P. Sethy · P. Muduli · P. K. Satpathy (✉)
CET, Bhubaneswar, India
e-mail: satpathy.pks@gmail.com

P. Kr. Sahoo
ITER, Siksha 'O' Anusandhan (Deemed to be University), Bhubaneswar, Odisha, India

S. Mahapatra et al. (eds.), *Advances in Energy Technology*, Advances in Sustainability Science and Technology, https://doi.org/10.1007/978-981-15-8700-9_4

energy can be a major source of energy which can be obtained from the renewable sources like solar energy, wind energy, etc., and can be backed up by different energy storage elements. Buck converters are used as DC-DC link to regulate the power from all the sources as well as it provides constant output voltage that ensures uniform supply of electricity. But it is observed that the performance of buck converters suffers from disadvantages like instability and poor performance in the absence of suitable feedback. Further, in view of increasing the reliability and efficiency of the system, the controlling techniques of buck converter may also be modified. We need to meet various challenges like changes in load and contingencies in the form of occurrence of various faults, which demands further improvement in the controlling techniques of various devices.

To minimize the transients in the output waveform, cascade loop control technique is implemented here. In cascade loop control technique, the current loop and voltage loop are cascaded with each other along with the proportional integral controllers that provide the gate pulse to the switch of buck converter. By this technique, the overall transients are considerably reduced which is tested and justified in this work by using the MATLAB–Simulink platform.

2 Mathematical Analysis of Single Loop Controller

Applying KCL and KVL in standard buck converter system as shown in Fig. 1, we find (Fig. 2)

$$CV_0(t) = i_L(t) - \frac{V_0(t)}{R} \tag{1}$$

$$Li_L(t) + V_0(t) = V_1(t) \tag{2}$$

Applying Laplace transfer function, we get

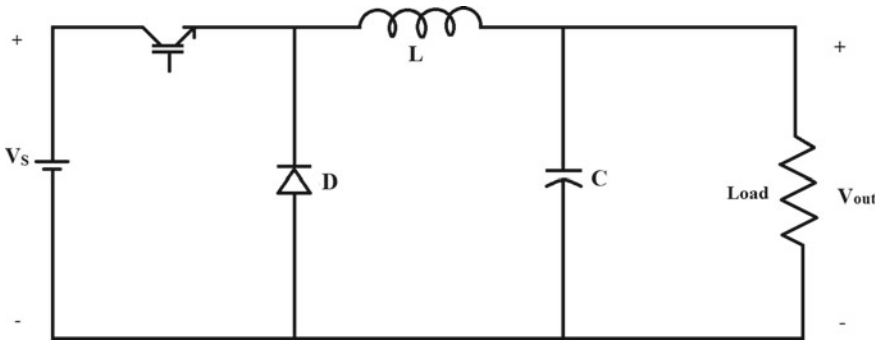

Fig. 1 Buck converter circuit diagram

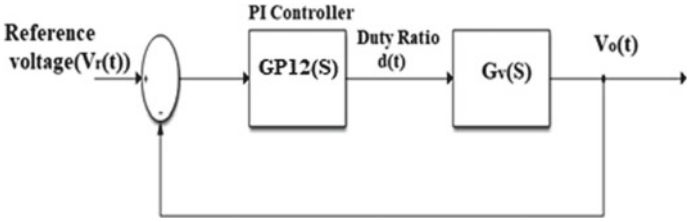

Fig. 2 Block diagram of single loop control system

$$\mathrm{G}_v(s) = \frac{V_0(t)}{i_L(s)} = \frac{R}{RCs + 1} \tag{3}$$

$$G_{PI_1}(s) = \frac{K_1(sT + 1)}{s} \tag{4}$$

Applying closed loop concepts, the transfer function may be found as indicated below.

$$\frac{V_0(s)}{V_r(s)} = \frac{\left(s + \frac{1}{T}\right)\frac{K_1 T}{C}}{s^2 + \left(\frac{1}{RC} + \frac{K_1 T}{C}\right)s + \frac{K_1}{C}} \tag{5}$$

$$\omega_n = \sqrt{\frac{K_1}{C}} \tag{6}$$

Comparing with standard second-order system, we find

$$2\delta\omega_n = \frac{1}{RC} + \frac{K_1 T}{C} \tag{7}$$

where 'δ' is the damping ratio, and 'ω_n' is the un-damped natural frequency of the system. Assuming critical damping condition, which takes $\delta = 1$ and $K_1 T = \frac{1}{R}$ that gives

$$\omega_n = \frac{1}{RC} \tag{8}$$

If the loading resistor approaches zero, then putting($R = 0$), we get

$$2\delta\omega_n = \infty \tag{9}$$

If the loading resistor approaches infinity, i.e., ($R = \infty$), then, we get

$$2\delta\omega_n = \frac{K_1 T}{C}, \text{ which gives } \delta = 0.5$$

From the above expressions, it is observed that the damping ratio varies with the change in the load resistance; thereby, causing transients in the output of the system. In order to reduce transients and improve the system performance, the cascade loop controller is used in this work.

3 Mathematical Modelling of Cascaded Loop Controller

The block diagram of a cascaded loop controller based on current loop control is shown in Fig. 3, where current dynamics are considered for the controlling purpose. In this model, $i_L(t)$ is the current through the inductor and $i_r(t)$ is the reference value of current. The closed loop transfer function for this controller is given in Eq. (13).

When $V_0(t) = 0$

$$\frac{i_L(t)}{i_r(t)} = \frac{\frac{K_2(Ts+1)}{s} \times \frac{V_i}{Ls}}{1 + \frac{K_2(Ts+1)}{s} \times \frac{V_i}{Ls}} \tag{10}$$

$$\frac{i_L(t)}{i_r(t)} = \frac{K_2(Ts+1) \times V_i}{Ls^2 + K_2 T s V_i + K_2 V_i} \tag{11}$$

$$\frac{i_L(s)}{V_0(s)} = \frac{-\frac{1}{Ls}}{1 + \frac{1}{Ls} \times \frac{K_2(Ts+1)}{s} \times V_i} \tag{12}$$

$$\frac{i_L(s)}{V_0(s)} = \frac{-s}{Ls^2 + K_2 T V_i s + K_2 V_i} V_0(s) + \frac{K_2(Ts+1) \times V_i}{Ls^2 + K_2 T V_i s + K_2 V_i} I_r(s) \tag{13}$$

where $\omega_{n_2} = \sqrt{\frac{K_2 V_i}{L}}$

The inner loop and outer loop have different frequency, which can be related using a gain factor 'N'. Therefore,

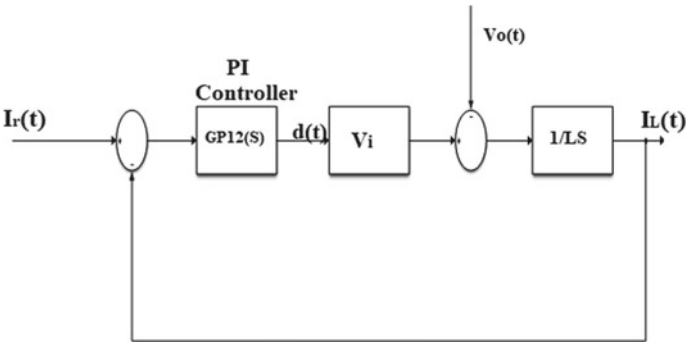

Fig. 3 Block diagram of cascade loop controller

$$\omega_{n_2} = N\omega_{n_1} = \sqrt{\frac{K_2 V_i}{L}} \tag{14}$$

When, $\delta = 1$, $2\omega_{n_2} = \frac{K_2 T s V_i}{L}$, So, we get,

$$2N\omega_{n_1} = \frac{N^2\omega_{n_1}^2 \times T s V_i}{V_i L}, \text{ and } T = \frac{2}{N\omega_{n_1}}$$

4 Mathematical Modelling of Buck Converter

A step-down switching mode DC power converter as shown in Fig. 4 is commonly known as a buck converter and it has a higher value of efficiency and very robust design. Diode becomes reverse biased when the switch is in conducting state. The inductor current $I_L(t)$, capacitor voltage $V_c(t)$, and the output voltage $V_0(t)$.

Applying KVL, we get

$$V_{in} - V_L - V_{RL} - V_0 = 0$$

Taking Laplace transformation, we get

$$i_L(s) = \left[\frac{V_{in}(s) - V_0(s) - i_L(s)R_L}{Ls}\right] \tag{15}$$

$$V_0 = (i_L(s) - i_0(s))R_c + \frac{1}{Cs}(i_L(s) - i_0(s)) \tag{16}$$

The simulation of the buck converter is based on the above two equations, Eqs. (15) and (16), as indicated below.

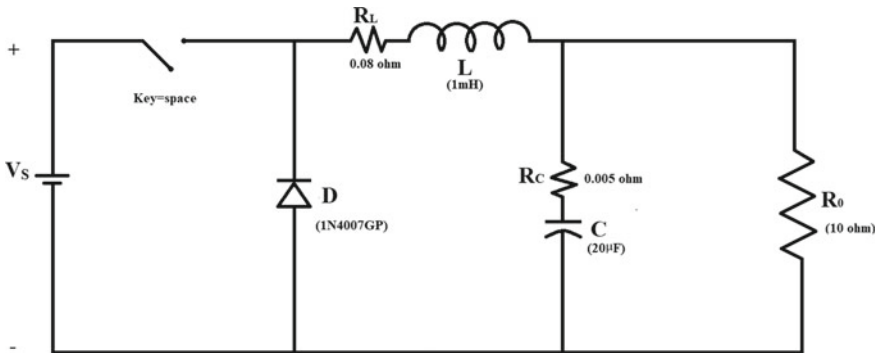

Fig. 4 Block diagram of buck converter

In this part, we discuss the simulation performance in MATLAB according to the proposed model and further the dynamic of buck converter input and load variation is also discussed. The peak overshoot, settling time, and steady state error are noted and compared between single loop and cascaded loop outputs and thus, we justify that cascade loop controller is a better technique than single loop controller. In order to proceed with the simulation of buck converter model, we first present the open loop control aspects and based on this, we consider the single loop and cascaded loop controllers.

The Simulink model for open loop controller is shown in Fig. 5, where we are using multiplier, summing block, gain block, and fed into to integrator. This system is obtained from the calculation of output voltage and inductor current from the transfer function modeling of buck converter.

In this model, we are supplying an input of 12 V with a gate pulse 0.413; we are using a load resistance of 10 Ω. We have changed the step input from 12 to 30 V at time 0.005 s. The simulation result for open loop control is shown in Fig. 6.

From Fig. 6, we observe that the output voltage is 5 V at steady state with a supply voltage of 12 V and a duty ratio of 0.413. But, we have seen a transient which has an overshoot of 6.408 V and settling time of 2.3 ms which depicts the poor performance of buck converter. At 0.005 s, when the input voltage is changed from 12 to 30 V, the output voltage also changes from 5 to 12.4 V.

As there is no control of output voltage, we see here a rise in load voltage with a change in input voltage which may damage the load connected. Hence, the limitations of open loop controller are justified.

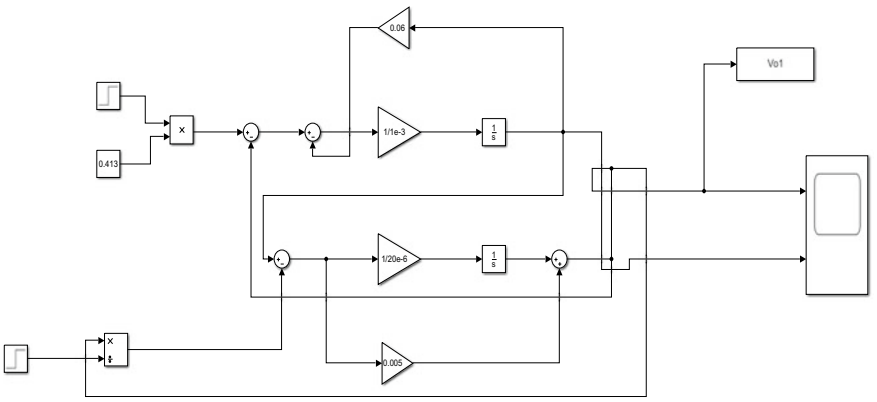

Fig. 5 Open loop control model

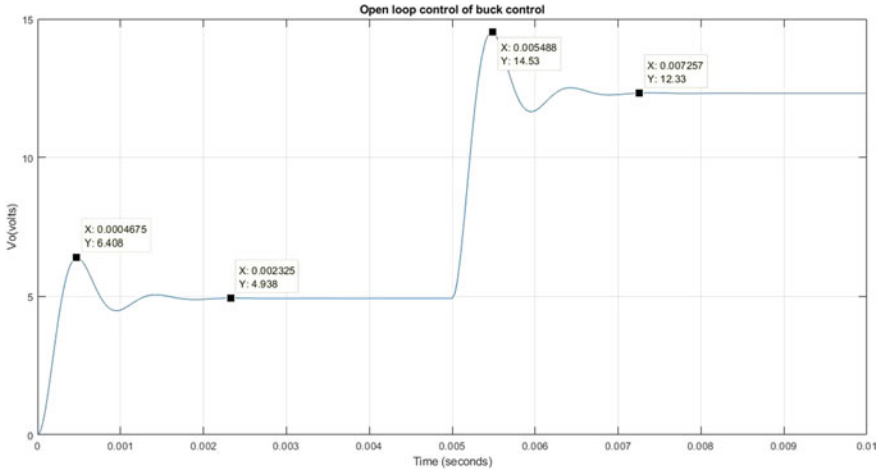

Fig. 6 Simulation result of open loop control model

5 Single Loop Voltage Control

In this Simulink model (Fig. 7), we have used the above buck converter transfer function model of as a subsystem. Input voltage, duty cycle, and output current are given as input to the subsystem, whereas the output voltage and inductor current are the subsystem output.

The input voltage is set at 12 V and the load at 10 Ω. Here, the output voltage is taken as feedback and compared with the reference voltage of 5 V and the error signal is fed to the PI controller which evaluates the error signal and creates the gate pulse which is given as a duty cycle to the buck converter. The simulation results are presented in Fig. 8, which indicates that the output voltage is 5 V. But a transient exists there, which has an overshoot of 4.12V and settling time of 3.1 ms. This shows

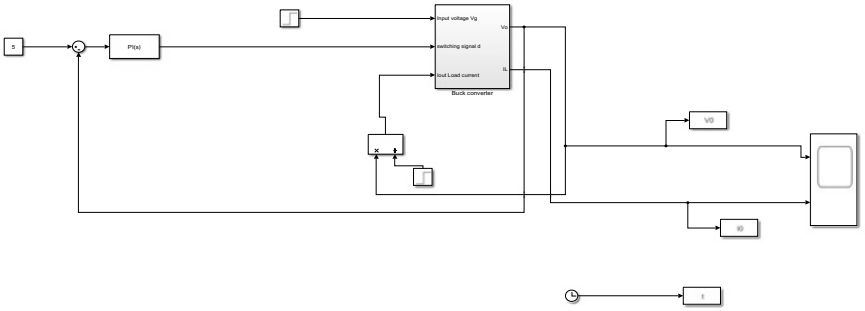

Fig. 7 Simulink model of single loop voltage control

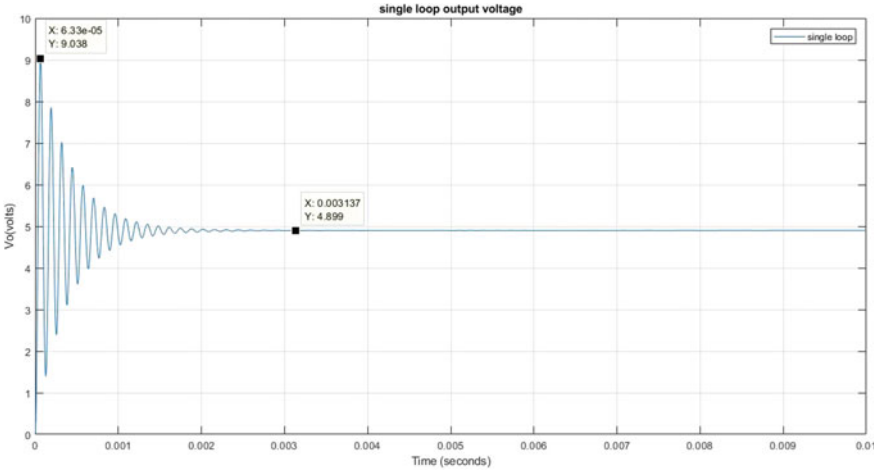

Fig. 8 Simulation result of single loop voltage control

the poor operation of buck converter. Thus, we can say that it has high transient but it can control the output voltage.

6 Cascaded Loop Control

The Simulink model for cascaded loop control is shown in Fig. 9. In this Simulink model, we have used the above transfer function model of buck converter as a subsystem.

Input voltage, duty cycle, and output current are given as input to the subsystem, whereas the output voltage and inductor current are the subsystem outputs. The input voltage is 12 V and the load is 10 Ω. Here, the output voltage is taken as feedback and compared with the reference voltage of 5 V and the error signal is fed to the PI controller and again that is taken as a reference and compared with the feedback from inductor current, the error signal is again fed to a PI controller that will evaluate the

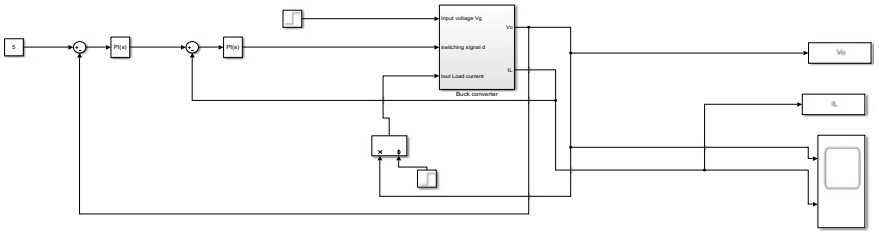

Fig. 9 Simulink model of cascaded loop control

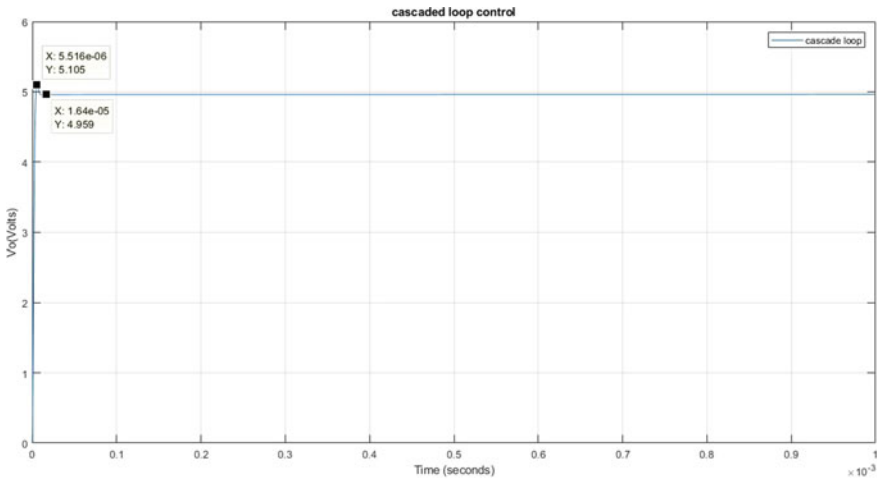

Fig. 10 Simulation result of cascaded loop control

error signal and create the gate pulse which is given as a duty cycle to buck converter. We will simulate this and observe the result.

From Fig. 10, we observe that the output voltage is 5 V. But the transient here is very less, which has an overshoot of 0.0105 V and settling time of 0.016 ms. This shows a desirably better operation of buck converter.

7 Comparison Between Single Loop and Cascaded Loop

In the above figure below (Fig. 11), the single loop and the cascade loop output voltage transient analysis are presented.

The red wave form indicates the response of cascaded loop, which has a very improved performance and the blue wave form shows the response of single loop, which has a very poor performance. Further, cascade loop has less settling time and less peak overshoot than the single loop.

Figure 12 shows the single loop and the cascade loop output current transient analysis. The red wave form shows the response of cascaded loop which has a very improved performance and the blue wave form shows the response of single loop which has a very poor performance. The single loop has 0.4034 A peak overshoot and cascade has an overshoot of 0.0102 A. Thus, the cascade loop has less settling time and less peak overshoot and no steady-state error as compared to the single loop.

In Fig. 13, we present the change in output voltage subject to changes in input voltage from 12 to 20 V at 0.005 s, which indicates that the cascade loop control has no transient, whereas single loop shows some transient. Thus, we can successfully

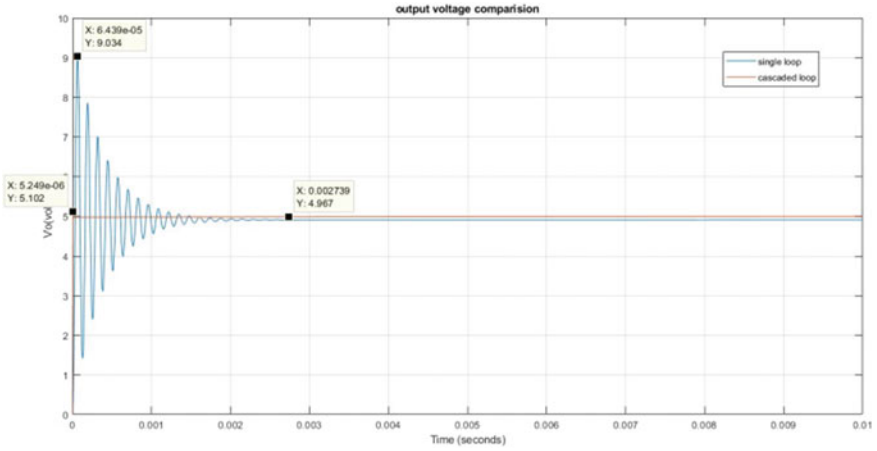

Fig. 11 Simulation result of output voltage comparison between single loop and cascaded loop control

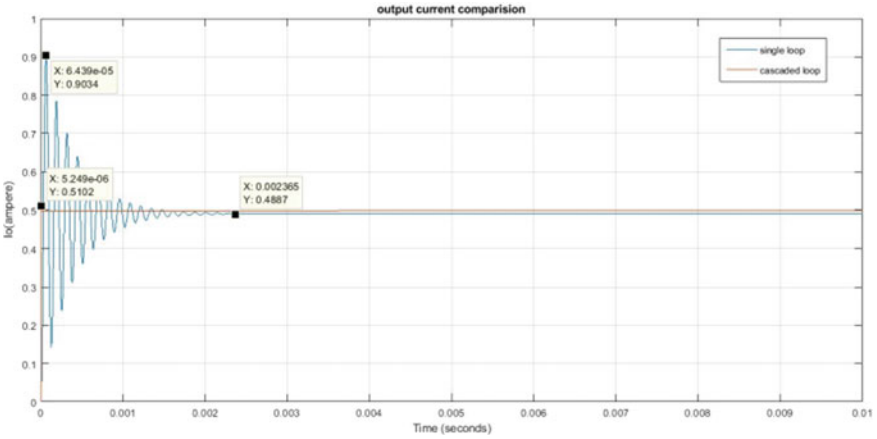

Fig. 12 Simulation result of output current comparison between single loop and cascaded loop

control the output voltage even if there is change in input voltage. Hence, justifying the robustness of cascade loop converter.

In Fig. 14, we present the change in output voltage subject to changes in load from 10 to 20 Ω at 0.007 s. In this case, it is found that the cascade loop control has no transient, whereas single loop shows transient. Thus, we can successfully control the output voltage even if there is change in load.

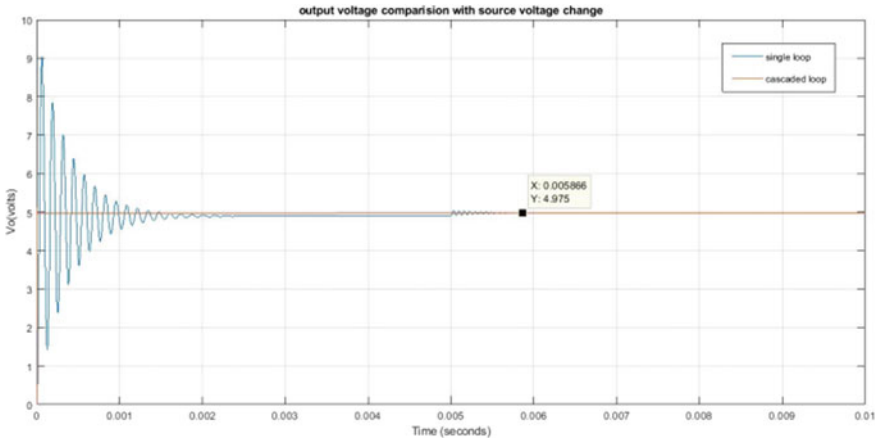

Fig. 13 Effect due to change in input voltage

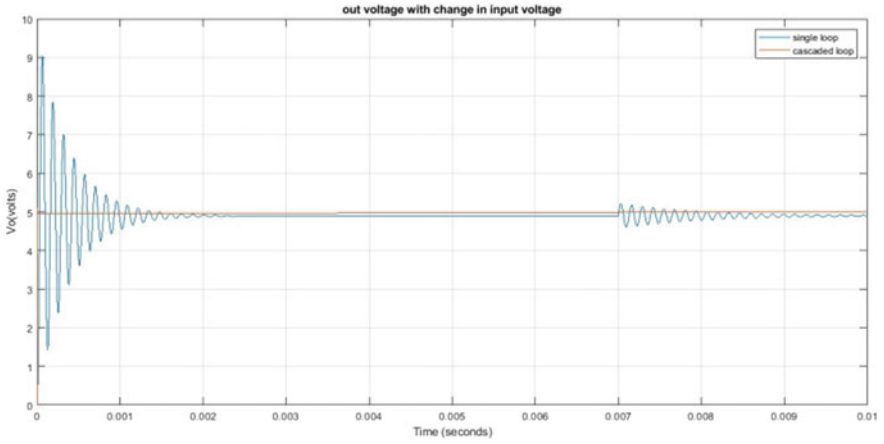

Fig. 14 Effect due to change in load

8 Conclusion

By comparing transient responses of both single and cascaded loop controllers, we conclude that the former has more transients as compared to cascade controller. From the results, it is observed that there is no steady-state error, very less peak over shoot, rise time, and settling time in the output voltage of buck converter in cascade loop controller. During line voltage variation of a buck converter under cascaded technology, controller has largely reduced transients than a single loop. During load variation of buck converter with cascade, the controller has lesser transients than single loop controller. The cascade controller has overall good performance, better

disturbance rejection and faster speed of response. The controller has been shown to be robust against load changes and supply changes. The simulation model of a buck converter with a single loop as well as cascade loop is successfully developed in MATLAB–Simulink software.

References

1. Gowda NM, Kiran and Parthasarthy SS (2014) Modeling of buck DC/D converter using simulink. Int J Innov Res Sci Eng Technol 3:16–17
2. Sahito AA et al (2014) Nonlinear controller design for buck converter to minimize transient disturbances. Sci Int 26(3):1033–1037
3. Verma SSK, Rao AG (2013) Overview of control techniques for DC/DC convertor. Natl Inst Electr Inf Technol V2
4. Kumar N, Sadasivam N, Sukriya HM (2008) Comparative study of PI, Fuzzy and ANN controller for chopper fed DC drive with embedded system. Approach Electr Power Component Syst 36(7):680–695
5. Mamatha S, Rao K, Laxmideshpande (2014) A Novel digital current mode control technique for buck converter. Int Conf Sci 2:3
6. Suryanarayana K, Parbhu LV, Vishwas K (2012) Analysis and modeling of digital peak current mode control. Power electronics, drives & energy system (PEDES) IEEE international conference, pp 1–6
7. Grote T, Schafmeister F, Figge H (2009) Adaptive digital slope compensation for peak current mode control. University of Paderborn
8. Kularatna (2008) Electronic circuit design: from concept to implementation
9. Kazi MA, Ahmed M (2017) Department of Electrical Engineering, Isra University, Hyderabad, Pakistan. Department of Electrical Engineering, MUET, Jamshoro, Pakistan

Chapter 5
Challenges Toward Blockchain and Renewable Energy Linked to IoT: A Survey

Suman Sourav Prasad, Jyoti Prakash Mishra, Sambit Kumar Mishra, and Samarjeet Borah

Abstract The Internet of things in general linked and focused with artificial intelligence, real-time analytics, machine learning, and sensors along with cloud storage. It may be associated with creating new thoughts and prospects along with its merits for businesses in current and new market. In the networked structure of IoT, the blockchain may be associated to monitor the relevant records linked with smart devices. As a matter of fact, the blockchain may be defined as the technology to chain as well as link scalability, privacy, and reliability concerns associated with things in virtual platforms. In practical situation, the applications linked to Internet of things in blockchain being decentralized may be more useful and may eradicate the associated complexities. Also, it may be more faithful toward centralized, brokered communication models with the challenges to secure IoT deployments. Being associated with the cloud architecture, sometimes, it may be very sensitive during storage of large amount of data in the cloud. Considering the blockchain applications in IoT, it may be observed that the automobile industries mostly may be associated with blockchain as it may be considered as a part-intensive industry. The centralized supply chain and trust-based distribution may be the recent innovation to achieve new technologies and may be automatically updated to maintain the records. In this context, it may also be associated with multi-layered and may involve toward device authentication and verification of transactions. As being observed, the storage associated with blockchain may be quite expensive and the amounts of IoT data sometimes may be increased continuously. As it is seen the incremental changes of energy systems to accumulate renewability, the flexibilities in such case must be maintained toward regeneration as well as storage allocation in energy systems. In many situations, the transformational changes are being observed linked to distributed energy

S. Sourav Prasad (✉)
Ajay Binay Institute of Technology, Cuttack, India
e-mail: prasadsuman800@rediffmail.com

J. P. Mishra · S. K. Mishra
Gandhi Institute for Education and Technology, Baniatangi, India

S. Borah
Sikkim Manipal Institute of Technology, East Sikkim, Majitar, India

S. Mahapatra et al. (eds.), *Advances in Energy Technology*, Advances in Sustainability Science and Technology, https://doi.org/10.1007/978-981-15-8700-9_5

sources with smart applications. Therefore, in this work, it has been thought of to include inter-serviced managed system to generalize the solution which is also treated as distributed peer-to-peer file system employed to manage file systems with heterogeneity.

Keywords Big data · Blockchain · Public key · Actuator · Throughput · ISMS · IoT deployment

1 Introduction

The technology linked to blockchain technologies sometimes plays the major role as necessitated in IOT industry. It can be used to link as well as track numerous connected devices, to enable the process of transactions, and co-ordination between the devices. Blockchains use the cryptographic algorithms which would help the consumers to keep data more private. In such case, the approaches meant for decentralization can eliminate single points of failure. The benefits of decentralizing IOT are numerous and better than centralized systems. As observed, the technology associated with blockchain can be viewed as a recent invention and quite similar to Internet of things. The present applications sometimes focus toward scalability and integration. In many situations, gathering all unstructured information may not have most optimal solutions toward implementation of data. There may be many challenges to integrate the voluminous data along with IoT data and to process simultaneously. Also considering the security of IoT data, it may be required to provide security as well as sensitive information to obtain secure solution for IoT data management. In such case, sometimes, IoT blockchains may be linked toward scalability. To minimize the high multi-agent collaboration from being attacked, it may be required to implement secure and trustful data transactions. Considering the application of IoT, it may be required to obtain the blockchain linked to heterogeneous network. In all respect, sharing of data as well as provision of service may be responsible toward the blockchain platform and to coordinate problem of many sub-networks. Therefore, it may be required focus on latest technologies and to make improvement on the blockchain technologies where in each block in the block chain may be associated with relevant transactions. Each device in this case can have unique keys associated with public and private domains to encrypt the sensor data to the required nodes. In this technology, crypto-currency applications are also experienced where the distributed database expands huge transactions methodically. The main intention in this case is to eradicate the requirement of linked intermediaries and replacement of distributed network and maintain the integrity. Accordingly, the digital transactions can be stored securely without intervention of central point of authority.

As the energy system tends toward transformational changes of resources linked with computational mechanisms, it is essential to resolve the challenges of decentralization as well as to provide solution to control and manage complex energy systems.

2 Literature Survey

Perera et al. [1] during their research have discussed the methodologies linked to IoT solutions. In that scenario, they have considered some decentralized consensus systems to be shared among resources. The system may be adopted toward blockchain with provision to trace the data with proper authentication and security.

Yeow et al. [2] in their work have pointed out the significance blockchain applications in IoT and observed that as being observed that the storage associated with blockchain may be quite expensive and the amounts of IoT data sometimes may be increased continuously.

Dorri et al. [3] in their research have conceptualized the methodology of framing smart home applying a blockchain technology analyzed its security. They have introduced some mechanisms linked to security and privacy.

Sun et al., [4] during their studies, have focused about the real-time applications of blockchain technology and the services.

Sagirlar et al. [5] during their research work have thought of hybrid blockchain architecture for IoT. Basically, in this case, the devices linked to Internet of things form subgroups to analyze and work with consensus algorithms.

Alphand et al. [6] during their study have focused on IoT chain as application with a provision to develop mechanism to obtain end-to-end solution for securely authorized access to IoT resources. In such situation, the data may be stored by the server, and may be implemented through IPFS to store the data.

Novo et al. [7] focused on the system with control mechanisms during their research toward IoT as well as blockchain technology. It has been observed that, the system sometimes links to latency with high transaction along with underlying blockchain.

Al-Fuqaha et al. [8] during their research have focused about Internet architecture along with the standardization and mechanisms linked to IoT. They also tried to make modifications focusing on standardization on IoT and layers of device network.

Jin Y et al. [9] in their work tried to aggregate different sensor data. Accordingly, the process to aggregate the data may minimize the number of transmission on the wireless links though they may have good impact on consumption of energy. Also the major task in data aggregation in this case may be to determine an optimal flow of information to correlated data into the processing nodes.

Yan Z et al. [10] have concentrated on generation huge volume of data linked to IoT devices in their research domain. In this regard, it may be essential to prioritize the role of IoT along with data fusion and information security considering the reliability as well as security features of entities.

Gubbi J et al. [11] during their research have focused on the development and application of Internet of things. Also they made research on connected physical devices along with their virtual display. They also cited the examples of new potential services linked to necessary linked logistics, green technologies, smart homes, e-health, automation as well as intelligent transportation systems.

Lee J et al. [12] in their research domain have tried to implement the strategies to control the devices with heterogeneity along with access along with their applications to network resources. They have also focused on the techniques toward encrypting the tokens to grant permission to these devices.

Li J et al. [13] considered the group-based AKA protocol during their research to enhance security level linked to machine-to-machine communications. During their studies, they focused on authentication and Key agreement process to channelize security policies for nodes.

Antoni A et al. [14] during their studies have concentrated on cloud-based middleware linked toward mobile crowd sensing. They observed the capabilities of acquisition and adaptability of sensors data. These data can be aggregated further and after filtering process may be resent to cloud for efficient processing.

3 Problem Formulation and Conceptualization

The basic characteristics toward implementation of technologies associated with blockchain application may be to differentiate it from other similar technologies. Also it may provide the stability along with data security with solution. In such cases, the decentralization may also provide proper solution toward all processes. Citing example of implementation of IoT in many sectors especially in security system in home monitoring, banking, pharmaceuticals, it may be observed that applying and implementing decentralization features and blockchain methods, many problems may be automatically solved. It may also provide the security and privacy for the transactions and processes by the banks and protect from vulnerable to cyber attacks. It may be presumed that any e-transaction done on IoT devices may be more secure with the integration of decentralized technology. Considering the pharmaceutical industries, now, it may be big challenges toward counterfeiting of medicines. In this context, the solution mechanism may have to be developed implementing the blockchain as well as IoT toward sharing the important information securely with access only to authorized individuals. Practically, it has been observed that the storage on the blockchain may be quite expensive as per continuous increment of IoT data and also may be facng challenges implement storage system for IoT data. In this regard, it may be very essential to include inter-serviced managed system intended toward distributed peer-to-peer file system.

4 Algorithm

Step 1: Generalization and creation of instance of request

Step 2: Defining the request considering the requestor, key values, data time access, completion time, and required cluster

Step 3: Achieve the authorized list and key linked to requestor

Step 4: if(publickey(requestor)! = publickey) { check if the public key may be twisted in the mass Step 5: else initiate separate access to request linked to publickey (requestor)

Step 6: Move the request to access state setting request.setaccess()

Step 7: Return with processed request and cluster initiating return cir.ISMSlist.getISMS(ClusterID) to storage buffer

Step 8: Reformation of actuator assigning asset registry and device_id

Step 9: Update the asset linked to the transaction returning performassetregistry (org.mc,iot.actuator) and return assetregistry.get(id)

Step 10. Update the asset in the asset registry

Step 11. Implement the actuator enabling the current state with authenticate ID Step 12. Link the device owner-ID with actuator-ID

Step 13. Update the database by initiating the database triggers and querying for IoT linkage in network

Step 14. Match the device-owner-Id with the actuator-event-ID and accumulate the data

5 Experimental Results

As per Fig. 1 and, the results obtained, and it may be noted that the throughput may increase as per the increase in send data rate. It is being observed that the enhancement of memory with the resources including processing elements consolidates the data rates during the application. In such case, the frequency of transaction processing

Fig. 1 Data sending rate versus latency (ms)

Table 1 Accumulation of data sending rate with latency

Serial and test no	Data sending rate (bps)	Maximum latency (ms)	Throughput (bps)
1	100	0.37	100
2	200	0.79	160
3	300	1.6	190
4	400	0.9	193

is also gradually being dependent toward the situation. Especially the increase of processing elements may have the proper significance with the throughput obtained as well as the data rates (Table 1).

6 Discussion and Future Direction

It is obvious that the blockchain along with the Internet of things along with IoT-centric consensus protocol may achieve the requirements in terms of transaction delay and scalability. In such scenario, it may be required to include the hybrid blockchain architecture for IoT to focus on specific interconnection framework. By implementing such technique, definitely the IoT devices may be customized toward their access control along with acquiring autonomy. Also the throughput may be permissible by considering the overhead of cross-chain interaction. Application toward blockchain technologies is facilitated toward point-to-point transaction enabling the machine-to-machine communication toward exchange of data among smart devices. Mostly, in energy sectors, smart devices with smart applications must be adopted toward power systems, toward transformation of chain values in energy sector to minimize the cost of application.

7 Conclusion

Blockchain technology is somewhat secure, reliable, and when integrated with IoT can give rise to some effective and efficient real-life solutions. As further studies, it may also be highly essential to focus on current privacy access control schemes to enhance privacy as well as security. Application of smart devices implementing the block chain technologies definitely enhances the security as well as privacy of different transactions. To maintain the same, it is required to preserve the technology to a great extent.

References

1. Perera C, Liu C, Jayawardena H, Chen S (2014) A survey on internet of things from industrial market perspective. IEEE Access 2:1660–1679
2. Yeow K, Gani A, Ahmad RW, Rodrigues JJ, Ko K (2018) Decentralized consensus for edge-centric internet of things: a review, taxonomy, and research issues. IEEE Access 6:1513–1524
3. Dorri A, Kanhere SS, Jurdak R, Gauravaram P (2017) Blockchain for IoT security and privacy: The case study of a smart home. In: Proceedings of the 2017 IEEE international conference on pervasive computing and communications workshops (PerCom Workshops), Kona, HI, USA, 13–17 March 2017, pp 618–623
4. Sun J, Yan J, Zhang KZ (2016) Blockchain-based sharing services: What blockchain technology can contribute to smart cities. Financ Innov 2:26
5. Sagirlar G, Carminati B, Ferrari E, Sheehan JD, Ragnoli E (2018) Hybrid-iot: hybrid blockchain architecture for internet of things-pow sub-blockchains. arXiv:1804.03903
6. Alphand O, Amoretti M, Claeys T, Dall'Asta S, Duda A, Ferrari G, Rousseau F, Tourancheau B, Veltri L, Zanichelli F (2018) IoT chain: a block chain security architecture for the internet of things. In: Proceedings of the 2018 IEEE Wireless Communications and Networking Conference (WCNC), Barcelona, Spain, 15–18 April 2018, pp 1–6
7. Novo O (2018) Block chain meets IoT: an architecture for scalable access management in IoT. IEEE Internet Things J 5:1184–1195
8. Al Fuqaha A, Guizani M, Mohammadi M, Aledhari M, Ayyash M (2015) Internet of things: a survey on enabling technologies, protocols, and applications. IEEE communications surveys & tutorials, 17(4):2347–2376
9. Jin Y, Gormus S, Kulkarni P, Sooriyabandar M (2016) Content centric routing in IoT networks and its integration in RPL. Comput Commun 89–90:87–104
10. Yan Z, Zhang P, Vasilakos A (2014) VA survey on trust management for internet of things. J Netw Comput Appl 42:120–134
11. Gubbi J, Buyya R, Marusi S, Palaniswami M (2013) Internet of Things (IoT): a vision, architectural elements, and future directions. Future Generation
12. Lee J, Seo JW, Ko H, Kim H (2017) TARD temporary access rights delegation for guest network devices. J Comput Syst Sci 86:59–69
13. Li J, Wen M, Zhang T (2016) Group-based authentication and key agreement with dynamic policy updating for MTC in LTE-A Networks. IEEE Internet of Things J 3(3):408–417
14. Antoni A, Marjanovi M, Pripuzic K, Zarko IP (2016) A mobile crowd sensing ecosystem enabled by CUPUS-Cloud-based publish-subscribe middleware for the Internet of Things. Fut Gener Comput Syst 56:607–622

Chapter 6
Concept of Virtualization Linked to Energy Storage and Green Computing: A Case Study

Zdzislaw Polkowski and Sambit Kumar Mishra

Abstract In broad sense, the concept of virtualization is termed as platform consisting of numerous of virtualized and interconnected systems. In such case, the system hardware in large scale with strong Internet connectivity is linked to virtual machine-based servers with adequate operating systems and deployment of relevant software. In many cases, the platform as a service is having a provision to execute the application in the environment with suitable programming-level platforms. Accordingly, the database in virtual platform is interlinked with the communication network initiating the nodal activities. In this case, each node is termed as single database with individual local database management system. The database management system in this case controls the creation, maintenance, and use of a database. Also it gives permission to conveniently develop databases for other numerous applications. Citing the concept of virtual databases, it may be noted that Windows Azure, Amazon EC2, etc., typically run in virtual platform. Manytimes, it has been observed that the organizations become data-centric and continuously produce large amounts of data along with other commercial information. In such case, the mechanism data stored in the database requires to be managed in proper way. In many cases, the diversities are observed linked to energy systems. So, during accumulation, it is essential to maintain the sequence of storage allocation in energy systems. The concept of green computing links to utilization of resources including computer peripherals in the eco-friendly environment and proper disposal of computing devices. Also implementation of green data centers gives positive support toward designing, coding, and yielding proper utilization of power with minimal consumption of energy. In this work, it is aimed to analyze the mechanisms as well as efficiency of cloud databases in virtual machines and examining feasible solutions. Also it is aimed to exploit

Z. Polkowski (✉)
Wroclaw University of Economics and Business, Wrocław, Poland
e-mail: zdzislaw.polkowski@ue.wroc.pl

S. K. Mishra
Gandhi Institute for Education and Technology, Bhubaneswar, India

Biju Patnaik University of Technology, Rourkela, Odisha, India

S. Mahapatra et al. (eds.), *Advances in Energy Technology*, Advances in Sustainability Science and Technology, https://doi.org/10.1007/978-981-15-8700-9_6

the knowledge of database management systems along with mechanisms of virtual storage system to enhance the deployment of databases in the cloud.

Keywords Virtual machine · Virtual machine monitor · Cloud storage · Hypervisor · Virtualization

1 Introduction

Many times, the execution time of processes is minimized during optimization and also the duration to transact the queries is minimized by indexing the database and improving the performance. Accordingly, while indexing the database, the database management system can be linked with other heterogeneous databases toward storing the metadata. Considering the triggers of the databases, the operations may be processed only after updating all the corresponding indexes associated with the CPU cycles while synchronizing the databases. It is clearly meant that the virtualization provides dramatic benefits for a computing system, to improve speed deployment, maintenance capability along with encapsulation. There can be a number of reasons toward effectiveness of virtualization. First of all, while running multiple applications at the same time in the same server, the resource utilization is high. Similarly, the dynamic configuration and link among resources give permission to acquire different resources at different levels. Also the check points are linked toward recovery from different linked sources. In broad sense, the methods of virtualization can be categorized as full virtualization as well as semi-virtualization. It has been observed that the various support linked to virtualization starting from code translation to implementation of operating system may be emulated while associated with the mechanisms of full virtualization. But sometimes, it may be too tedious to maintain the source codes. On the other hand, the semi-virtualization may seek the presence of hypervisor to achieve better performance as compared to full virtualization. Also it permits the operating system to work on the virtual system. Each operating system is protected from the others and is thus unaffected by any instability or configuration issues of the others. In such scenario, the virtual machine monitor implements on physical resources after mapping through virtual resources. Also the execution of instructions can be managed efficiently by virtual machine monitor. Sometimes, the unique keys linked with domain of server encrypt the data toward required destination. In such case, the distributed network maintains the integrity and the energy system secures the transformational changes during processing and storage of digital transactions.

2 Review of Literature

Saha et al. [1] during their presentation have discussed toward similarity of green computing with green chemistry as it minimizes implementation of hazardous

materials and enhan ce the efficiency. It basically focuses toward sustainability of computing linked to data center facilities.

Joan et al. [2] in their research have discussed the basic practices linked to green computing. Implementing the computing resources, maximum productivity can be achieved. In this regard, the key objectives of green computing link to utilization of green energy sources and minimization of unnecessary requirements.

Debnath et al. [3] during their study focused on recycle of e-waste and proper utilization of green computing. They observed that proper management of electronic waste is a better potential route toward implementation of green computation.

Pandey et al. [4] in their research domain have cited on the trends associated with green computing and differentiated from cloud computing. As per their observation, cloud computing can be treated as fundamental mechanism toward determining the energy efficiency linked to information and communication and can provide better resource utilization toward sustainability movement for green technology.

Paul et al. [5] in their work have suggested the improvements toward implementation of green computing platform.

Lakhani et al. [6] have prioritized Green I.T 1.0 toward greening of information technology by focusing on the emerging technologies linked with information technology. In fact it is intended to improve the energy efficiency linked to information technology.

Sharma et al. [7] during their research have focused on benefits and utilization of green computing and resulting in faster execution as compared to any single-core implementation of the program. They observed that as number of computation is more, the multi-core approach shows better performance else the performance would be inferior as compared to the single-core computation.

Pahlevan et al. [8] in their work have discussed about the optimization framework for managing green data centers implementing multilevel energy reduction techniques. As being observed, the results obtained focused to better results as there is considerable, up to 96% savings in electricity bill.

Also during their study, they also focused to cloud computing and green information technology to discover the important factors that influence adoption of software as a service linked to green information technology.

Asad et al. [9] during their experiment have considered the large-scale data with heterogeneity with different aspects as well as influencing on the energy consumption of data centers. A survey is also made by them about these aspects to obtain optimal results implementing the green computation.

Sofia et al. [10] in their study have proposed a scheduling algorithm known as Green Task Scheduling. A decrease in cost of hardware is also an advantage of this algorithm. In order to manage the efficiency of the processor without impairing the performance and adopting dynamic voltage frequency scaling technique can be implemented.

Rivoire et al. [11] during their studies have focused on the mechanisms linked to green technologies toward implementation in the environment. It has been observed that the information and communication technology industries usually generate about

two percentages of the total global carbon dioxide emissions, which is equal to the aviation industry.

As per Academiaonline et al. [12], the mechanisms of computing sometimes becomes tiny, cheap as well as more accessible to users which may affect to the computing power. The main reason for the evolution of the cloud computing is that evolution of pc-based software's to Internet-based applications.

Vinh et al. [13] during their research have focused on the techniques associated with green computation based on predictor to save energy in cloud computing. It makes prediction to turn servers depending on the pre-collected data. Accordingly, depending on the prediction of load demand, it minimizes the number of servers running.

Satoh et al. [14] during their study have focused on energy management system for future energy management implementing the supervised virtual machine allocation tool. It will help in minimizing the consumption of energy up to thirty percentages in multiple data centers and reduction of energy in carbon emissions.

Beik et al. [15] during their study have evaluated the performance of data centers and observed that the efficiency in energy to common users in all respect.

Lucio et al. [16] in their research domain have considered hybrid optimization model for green cloud computing. It produces somehow non-dominated solutions which sometimes have provision to interact with cloud to choose the better bargain in terms of energy consumption and Network Quality of Service.

Garg et al. [17] during their study have focused on green computation as well as green cloud architecture to enhance the efficiency of cloud computing. It consists of Green Offer for available green cloud services and carbon emission, for energy efficiency of those services.

Kliazovich et al. [18] during their experiment tried to identify the requirement of optimum distribution of workload among the available servers and data centers to develop an energy consumption metric in terms of packet level. It will be available toward packet-level communication and convenient synchronization of operations.

Sindhu et al. [19] during their research have focused on the techniques associated with green computation as well as virtualization and to some extent grid computing. The benefits of usage of these technologies definitely reduce the energy consumption of the computing resources.

3 Comparing Virtual Machine with Physical Machine

Considering the full virtualization, it possesses the method of full trap as well as implement technique and completely linked to virtual machine. It also requires complete virtualized architecture. However, sometimes, it modifies the guest operating system toward virtualization. Its performance can be measured by replacing through non-virtualized instructions. The virtual machine monitor implements the machine architecture allocating the virtual machines in similar platforms. The software associated with virtual machine monitor permits different process schedulers

to categorize allocation in processors along with assigned weights. After that, the processors implement the virtual machines and share with physical machines in the similar platforms. Sometimes, it is observed that deployment of databases in the linked systems is challengeable. The capability of dynamically allocation linked to virtual machine monitor provides high availability and elastic scalability for database systems. Also the services deployed in the virtual environment will store the data efficiently. The systems with elasticity characteristics maintain the infrastructures with adequate processing capabilities. After segregation, the records linked to virtual machines are unified to process the data in the databases. Then, the weight may be computed to evaluate the data redundancies linked to databases in the servers. Also the threshold values along with optimality are evaluated. In such case, the algorithm is written the process the data linked to virtual machines. The services linked to database or database as a service usually fills the gap between traditional database systems and cloud storage systems. But, sometimes, the system may not be acquainted with elastic scalability. In this regard, it may be too essential to design and implement new technologies with a provision of high availability, consistency as well as elastic scalability linked with virtual storage system.

4 Adoption of Green Computation Linked to Data Centers

Usually, for the data centers, backup facility is very essential along with cooling mechanism. Specifically, the green data center has the capabilities of consumption of less power while accessing requests online linked to physical nodes or virtual machines. In specific term, virtualization symbolizes abstraction of operating system and applications where the physical resources can be split into numerous logical segments or virtual machines.

Every virtual machine may be associated with specific operating system and performance may be observed defining path from virtual machine to physical machine. In many cases, mechanisms linked to dynamic resource management are adopted to scale the dynamism as well as utilization of processors in virtual environment. In such cases, the data centers may be heavily loaded and the host systems will be responsible to link these to virtual machines with minimal power usage. Therefore, it is very essential to evaluate the optimal operating frequency of each virtual machine along with the highest ratio of instructions or data in the virtual machines.

5 Algorithm: Processing Linked to Virtual Machines

Step 1: Accumulate the requisite records from physical systems

Step 2: Transfer the records to signified databases linked to virtual servers

Step 3: Retrieve the attributes from servers

Step 4: Calculate the amount of data linked to individual databases

Step 5: Segregate the databases linked to virtual servers, vs (size: n)

ds = d1,d2,……vs;

Step 6: Update vs1 = t & vs2 = q, where, vs1 and vs2 are virtual servers

```
for (i = 1; i < = n; i++)
    {
for (j = 1;j < = n; j++)
    {
di = data linked to databases;
if (di==vs1)
    {
vs = d;
    }
else if (di==vs2)
    {
vs = d;
    }
```

Step 7: Obtain the position of attributes and link to databases

Step 8: Evaluate the weight of individual databases

Step 9: Obtain the optimality of attributes linked to databases

Step 10: Minimize the redundancies of data linked to virtual platforms

5.1 Implementation of Firefly Algorithm Toward Databases Linked to Virtual Servers

Step 1: Specify the initial databases linked to the servers, ds

Step 2: Generate the populations, maxp, and formulate the light intensity, LI

Step 3: Obtain the absorption coefficient

Step 4: Generate the possible solutions by linking databases

While(q <= maxp)

for i = 1:k (databases linked to virtual servers)

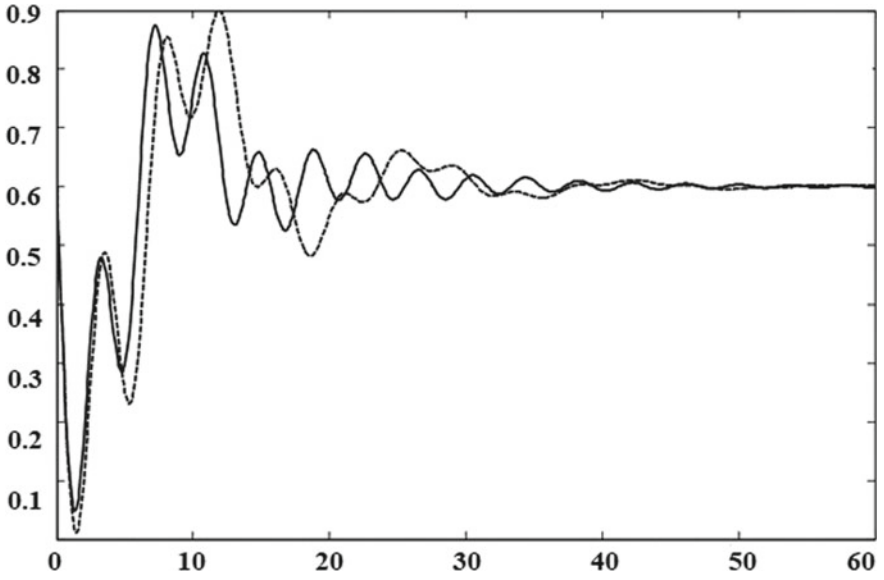

Fig. 1 Data centers linked to virtual platform versus elapsed time

Table 1 Estimation of elapsed time of data centers linked to virtual platform

S. No.	Number of data centers	Elapsed time (ms)
1	19	0.58
2	37	0.61
3	46	0.63
4	55	0.64

for j = 1:i (databases linked to individual server)

measure the differential gap between the databases

Step 5: obtain the possible solutions and update the light intensity, LI

Step 6: Sequence the databases and obtain the optimal solution (Fig. 1 and Table 1).

6 Impact of Green Computing to Society

The adoption of green computing can be diversified into several service sectors as well as industries to prove quite adequate tool for attaining better energy efficiency. In many cases, the data centers can be standardized to obtain the characteristics and better optimization. Optimized performance through data centers is quite linked with green computing to maintain balance among the data centers.

7 Conclusion

In this paper, many techniques have been discussed linked to power management as well as computing sources. The concept of virtualization has been well adopted to maintain the energy efficiency. It indicates the importance of the green computing applications. The techniques linked to green computing require managing power consumption in data centers. The strategies toward adopting green computing also have strong impact over global warming. Accordingly, green computing is very much useful toward protecting environment and accumulates the power toward creating a more sustainable environment.

References

1. Saha B (2014) Green computing. Int J Comput Trends Technol 14(2)
2. Joan DRR (2014) Introduction to green computing model for clouds. i-manager's J Cloud Comput 1(3):1–7
3. Debnath B, Roychoudhuri R, Ghosh SK (2016) E-waste management—a potential route to green computing. Procedia Environ Sci 35:669–675
4. Pandey R et al (2017) The rising era of green computing. Int J Comput Sci Mob Comput 6(2):127–130
5. Paul PK et al (2014) Green and environmental friendly domain and discipline: emerging trends and future possibilities. Int J Appl Sci Eng 2(1):55–62
6. Lakhani L (2016) Green computing—a new trend in It. Int J Sci Res Comput Sci Eng 4(3):11–13
7. Sharma MK (2017) Software level green computing with multi-core processors using fork-and-join framework (2017)
8. Pahlevan A et al (2017) Joint computing and electric systems optimization for green datacenters. Handbook of Hardware/Software Codesign, pp 1163–1183
9. Asad Z, Chaudhry MAR (2017) A two way street: green big data processing for a greener smart grid. IEEE Syst J 11(2):784–795
10. Sofia AS, Ganesh Kumar P (2017) Energy efficient task scheduling to implement green cloud. Asian J Res Soc Sci Hum 7(2):443–458
11. Rivoire S, Shah MA, Ranganathan P, Kozyrakis J (2007) A balanced energy-efficiency benchmark. In: Proceedings of ACM SIGMOD international conference on management of data, NY, USA, pp 365–376
12. Academiaonline (2015) available: https://www.acad emia.edu/7166874/
13. Vinh T, Duy T, Sato Y, Inoguchi Y (2010) Performance evaluation of a green scheduling algorithm for energy savings in cloud computing. In: IEEE international symposium of the parallel & distributed processing, Workshops and PhD Forum (IPDPSW), pp 1–8
14. Satoh F, Yanagisawa H, Takahashi H, Kushida T (2013) Total energy management system for cloud computing. IEEE international conference of the cloud engineering (IC2E), pp 233–240
15. Beik R (ed) Green cloud computing: an energy-aware layer in software architecture. In: Proceedings of the Spring Congress of the Engineering and Technology (S-CET)
16. Rocha LA, Cardozo E (2014) A hybrid optimization model for green cloud computing. IEEE/ACM 7th international conference on utility and cloud computing, pp 11–20
17. Garg SK, Yeo CS, Buyya R (2011) Green cloud framework for improving carbon efficiency of clouds. 17th International European Conference on Parallel and Distributed Computing

18. Kliazovich D, Bouvry P (eds) (2010) Green cloud: a packet-level simulator of energy-aware cloud computing data centers. In: Proceeding of the IEEE Global Telecommunications Conference (GLOBECOM), pp 1–8
19. Sindhu S, Pandya C (2014) Green cloud computing. Int J Inf Comput Technol 4(4):431–436. ISSN 0974-2239

Chapter 7
Detection and Classification of Fault in Distributed Generation System Using Neuro-Fuzzy Technique

Saurabh Singh, Kishora Sasamal, and Santi Behera

Abstract The inclusion of distributed generation in usual distribution system has several advantages and technical harms. This inclusion has been done for fulfillment of several challenges such as fast growing population, world's growing economy, improvement of life's quality, and sustainability of resources. However, with this, several harms have also been seen which are yet to be solved and one such harm is fault detection in distributed generation (DG) system. The existing protecting equipment and fault detecting techniques cannot perform the same as in usual distribution system. This paper deals with a DG system consisting of two wind farms connected to a regular distribution network which is simulated using MATLAB for data collection and on the basis of the data of current and voltage samples various features are extracted. The features are trained and tested using the Neuro-Fuzzy classifier which identifies the type of fault during testing with a error very close to zero having RMSE of 0.031.

Keywords Distributed generation (DG) · Neuro-Fuzzy (NF) · Neuro-Fuzzy classifier (NFC) · Neural network (NN) · Root mean square error (RMSE) · Doubly fed induction generator (DFIG)

1 Introduction

With regular improvement in the quality of lives of people, fast increase in population, fast growing economy, and sustainability of resources, various technological advancements are happening and this has led to the encroachment in the complexity of power system. Nowadays, much emphasis is taken on green technology for making the world sustainable and for resources to last long and also it is very important for us human creature as well as for nature to survive. Electricity is in much demand and has become one of the most important obsession without which life cannot be imagined. The conservative way of generating electricity is based on the usage of

S. Singh (✉) · K. Sasamal · S. Behera
Department of Electrical Engineering, VSSUT, Burla, Odisha, India
e-mail: saurabh1697singh@gmail.com

S. Mahapatra et al. (eds.), *Advances in Energy Technology*, Advances in Sustainability Science and Technology, https://doi.org/10.1007/978-981-15-8700-9_7

usual fossil fuel like coal, natural gas, etc. However, the use of these has led to degradation of nature, scarcity of resources, and affecting the health of humans. One such step in solving this setback is being done in power system by using non-conventional sources like solar, wind, geothermal, etc., the development in this field is called Green Technology Development. The use of non-conservative sources such as wind, solar in form of wind farm, photovoltaic arrays in the distribution side is called Distributed Generation System [1, 2]. Despite of several advantages such as no greenhouse gas emission, sustainable, no use of fossil fuel, reduction in Tx, and distribution cost, can be installed in remote places where there is scarcity of electricity and installation capability is easy there are several harms to it as well.

Mostly, the power system has a unidirectional flow of power, however, with the inclusion of DG this concept converts to bidirectional flow. Thus, most of the protective equipment connected and various protection schemes applied for detection purpose will not be able to deliver the same results as earlier when power flow was unidirectional. The several negative forces of connecting a DG [1] to the usual distribution side are:

- Fault detection becomes a main concern after the connection of DG as due to its presence short circuit level of current increases and can cause mal-operation of breaker.
- There is a reduction in the reach of impedance relay and this happens due to extra supply of voltage by DG thus causing to increase the actual measured impedance by the relay.
- Islanding is another critical fact which occurs when grid is disconnected due to some abnormal condition however DG is still supplying and can huge voltage and frequency instability.
- Distribution system generally uses radial feeder due to unidirectional flow of power however with DG connection power flow direction is bidirectional and also sets up a reverse gradient of voltage which must be taken care of.

From the various problems faced due to the DG in distribution network, fault plays a significant role in bringing a normal power system network to abnormal condition. The effect of faults leads to imbalance in the system, equipment failures, and hampers the insulation of equipment. The part of the power system which is most frequently affected by the faults is the overhead transmission lines. Thus, it is very incumbent to distinguish the fault as fast as feasible and hence classify its type so to reduce the down time of the power failure. Classification of fault is a vital process in distance relaying depending upon which the distance estimation is attained and overall assessment is acquired. This work deals with a hybrid intelligence technique called Neuro-Fuzzy implementation for "Fault detection and classification" in a system consisting of two DFIG. The layout of this paper is as follows. In Sect. II, problem formulation has been done; in Sect. III Neuro-Fuzzy is described separately as well as in combination. The simulation and results are discussed in Sect. IV and finally, Sect. V concludes this paper with conclusion.

2 Problem Formulation

The problem is formulated by considering a system consisting of two numbers of WIND energy systems (9 MW each), conventional system (100 MVA), Neuro-Fuzzy controller, Faults (11 nos.), transformers (three), feeders (20 km), loads (two numbers each of 500 KW rated value) as shown in Fig. 1.

Wind energy system [3] which is a DFIG [4, 5] based 9 MW wind farm connected to a 11 kV distribution system transmits power to a 220 kV grid through a 20 km, 11 kV feeder. Wind farm using DFIG consists of wound rotor induction generator and Ac/Dc/Ac-IGBT-based PWM converter. The DFIG equipment allows extracting maximum energy from wind for low wind speeds by optimizing the turbine speed, while minimizing mechanical stresses on the turbine during gusts of wind. The conventional system consists of a 100 MVA, 220 kV grid, a 20 km length feeder which is again steeped down to 400 V for supplying load. The Neuro-Fuzzy controller used is a hybrid fault classifier which is based on two types, namely Mamdani approach and Takagi-Sugeno approach. However, in this paper, Takagi-Sugeno approach has been used which is called ANFIS [6, 7] (Adaptive Neuro-Fuzzy Inference System). Fault plays a significant role in the power system. Short circuiting of conductors due to branches falling on transmission line, wind, and storm comprises the natural happenings. The effects of faults lead to unbalance in the system, equipment failures, and hampers the insulation of equipment. Faults are segregated into two category: series and shunt faults. Series faults mainly represent the broken conductors or if any one or two phases are opened and the other remains in the circuit. These are signalized by increase in voltage and frequency but decrease in current. The shunt faults are commonly known as short-circuit fault and are signalized by increase in current. These are further categorized into symmetrical and unsymmetrical faults. The triple line faults are known as balance or symmetrical faults and all other remaining faults come under asymmetrical faults. 11 cases of short-circuit faults [8, 9] (LG, LL,

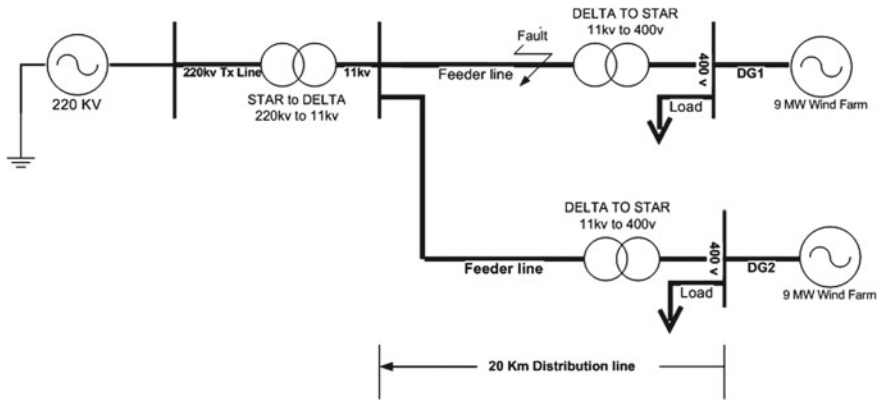

Fig. 1 Single-line diagram of the system

LLG, LLL, and LLG) are applied to the simulated system and results are observed. Three transformers are used which can be seen from Fig. 1 one is star-to-delta-type transformer which has been used to step down the grid voltage of 220 to 11 kV feeding the feeder. Other two are delta-to-star-type transformer which is used to step down the 11 kV feeder voltage to 400 V. The feeder is a 20 km long pi network consisting of inductance (L) and capacitance (C) where C is divided into two parts that is C/2 and C/2 forming the Pi network. Two loads are connected to each branch which can be seen from the single-line diagram in Fig. 1. Each load is 500 KW rated value. Each load is a series-type load consisting of only resistive part.

3 Neuro-Fuzzy Technique

Fault classification technique is generally done using three methods and these are prominent method, hybrid method and modern method.

From Fig. 2, it is clear that prominent technique has three sub-methods, namely wavelet method, ANN method, and fuzzy logic method for classification of fault. The prominent techniques nowadays are not in much use because each one has its own advantages and disadvantages and also results obtained are not highly accurate. Hence, in order to overcome each other's disadvantages, hybrid methods were introduced which comprises of Neuro-Fuzzy, Wavelet and ANN, Wavelet and fuzzy logic and wavelet and Neuro-Fuzzy. Modern techniques comprise of nature inspired algorithm such as genetic algorithm (GA), particle swarm, and space vector machine (SVM).

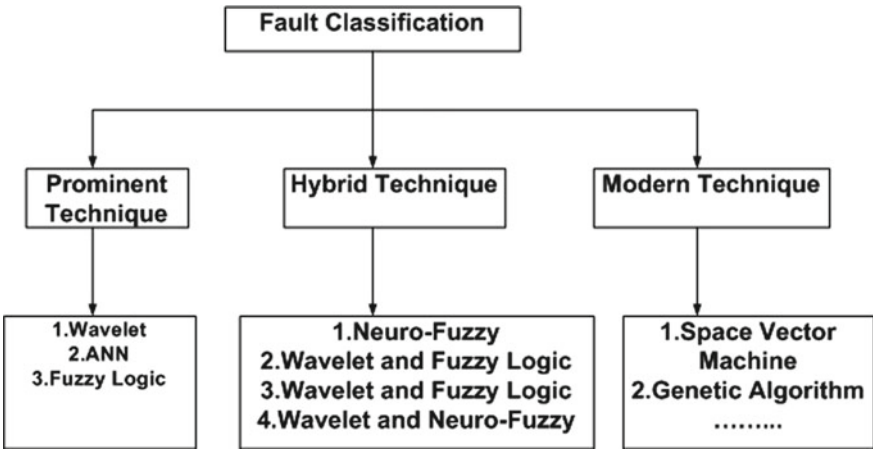

Fig. 2 Tree diagram of fault classification techniques [8]

A. Artificial Neural Network

Neural network can be defined in the specific group of neurons which are connected in bio-inspired structures and assembled in different layers. ANN [10–12] serves many problems, out of which the pattern recognition is of our interest. It is one of the ingenious algorithms which are used for identification and control. The neural networks can assimilate the system behavior. These networks can be used to recognize the relevant system behavior in nonlinear system. In ANN, the data gathered from the faulted set of current and voltage is applied and neural network then tries to follow the hidden pattern in the data and then according to it learns the pattern. After learning, during testing, it applies whatever it has learned and produces the output. ANN uses various algorithms like back propagation, feed forward propagation, etc., and a large number of neurons can be used by it upon which the accuracy of results depends. The main drawback with ANN is that it is good at recognizing pattern but not good at explaining how to reach their decision (Fig. 3).

B. Fuzzy Logic

Fuzzy logic system is inflected in three basic elements that are fuzzification, fuzzy inference, and defuzzifiction. Here, several inputs in form of crisp value are given to it and then membership function is defined in terms of linguistic variables such as low as L, medium as M, and high as H. The membership function can be a triangle, sigmoid, Gaussian, etc., depending upon output desired. The degree of membership is calculated in the fuzzifier layer. The output of this layer is sent to fuzzy inference system which is actually an intelligence layer which receives membership values as input and depending upon the fuzzy rule base produces an output. The output of this layer is sent to defuzzification layer which produces the crisp output.

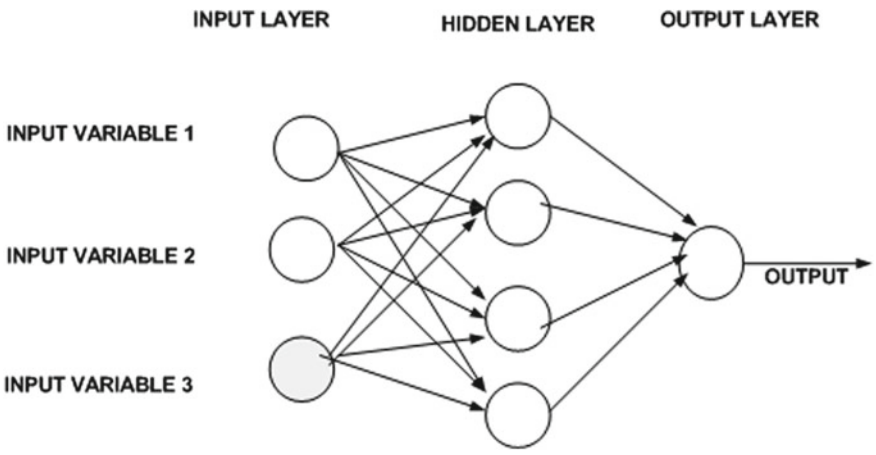

Fig. 3 Artificial neural network

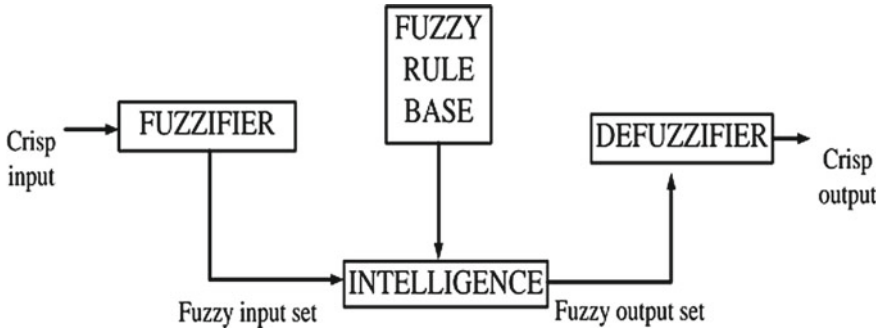

Fig. 4 Fuzzy logic model

The negative aspect of this approach is that number of fuzzy rules increases exponentially with respect to input. Also the Fuzzy logic [13–15] has the capability to take decision but is not capable of adapting to the changes (Fig. 4).

C. Neuro-Fuzzy

Incorporation of fuzzy logic in artificial neural network leads to fruitful and valuable output. Artificial neural network can be trained but no such training is possible in fuzzy logic. By integrating these two techniques, creates a new hybrid technique known as Neuro-Fuzzy [16–20] inference system which helps in memorizing the data set by providing a learning procedure. This technique is based upon data processing. It produces a felicitous input/output mapping with membership function which is based upon "fuzzy IF-THEN rules to procreate the input/output match up." The back propagation technique can be used to adjust these control parameters. Therefore, the input/output data must be operated on a wide range so that the control performance of this method will be guaranteed; otherwise, the previous designed controller will not yield the accurate output or result. In Fig. 5, P to Q are the inputs; in this paper, these are extracted features, the 1st and 4th layers nodes are adaptive and other nodes are fixed. It can use the feed forward back propagation network which has a very simple procedure for the learning process that comprises of providing the data having patterns of inputs and the target outputs, accessing the network performance, adaption of connection strength to produce better output. In neural network, the input/output behavior of the system can be determined by the use of weights between the input and output layers. The parameters obtained in the fuzzification and defuzzification process of the fuzzy logic system can thus be trained using the updated weights of neural network. This hybrid approach has been considered in many applications successfully and also few works have been done on fault classification purpose of the power system in transmission and distribution lines but not in distributed generation system. Looking to the extensive use and higher performance, in this work, the Neuro-Fuzzy (NF) classifier also considered as one of the approach. The neural network has the edge over other techniques in terms of robustness, work efficiently

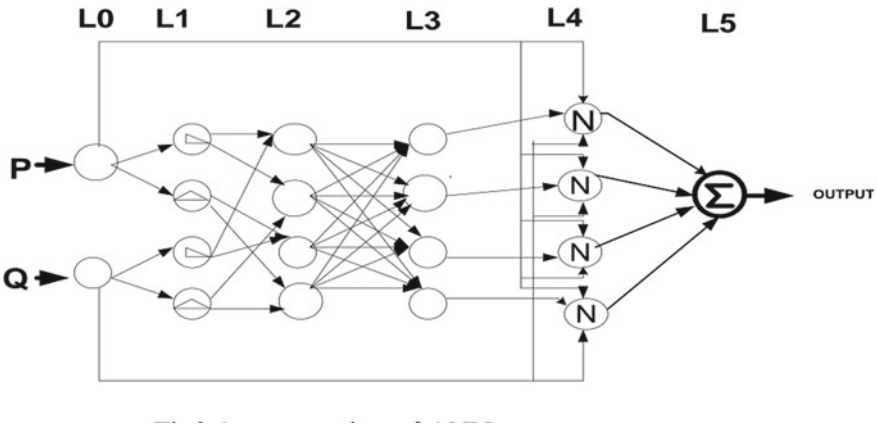

Fig. 5 Neuro-Fuzzy system

with both quantitative and qualitative data, computational burden and do not need exact mathematical modeling of the system.

4 Simulation and Results

A distribution network is being considered and modeled in MATLAB Simulink, the wind farm considered here is of DFIG type that is doubly fed induction generator because of increased power quality, energy efficiency, and controllability. Several Go-to are used to detect the current and voltage of the entire system under normal and faulty condition. A monitor is also being modeled so that each output voltage and current can be observed at once which is shown in Fig. 6.

Different short circuit faults were created at different locations of feeder that is at a distance of 4 km from 11 kV feeder end. Similarly, other faults were created at a distance of 8, 12, and 16 km from feeder end, respectively. With variation in fault distance, fault resistances were also changed varying from 0.001 to 10 Ω. Thus, in this way, a total of (5 × 4) 20 cases were observed for each short circuit fault.

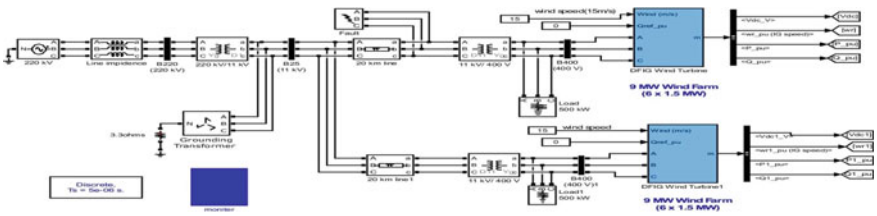

Fig. 6 Distributed generation system on Simulink

Thus, a total of (20 × 9) 180 cases for whole nine short circuit faults was taken into consideration. The results of faulted current and voltage for a fault distance of 4 km and fault resistance of 0.01 Ω are shown as in Figs. 7, 8 and 9.

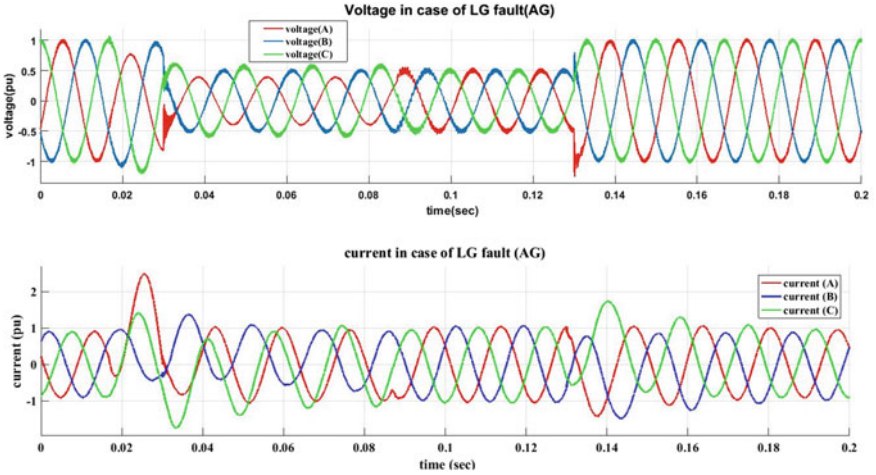

Fig. 7 Voltage and current sample in case of L-G fault

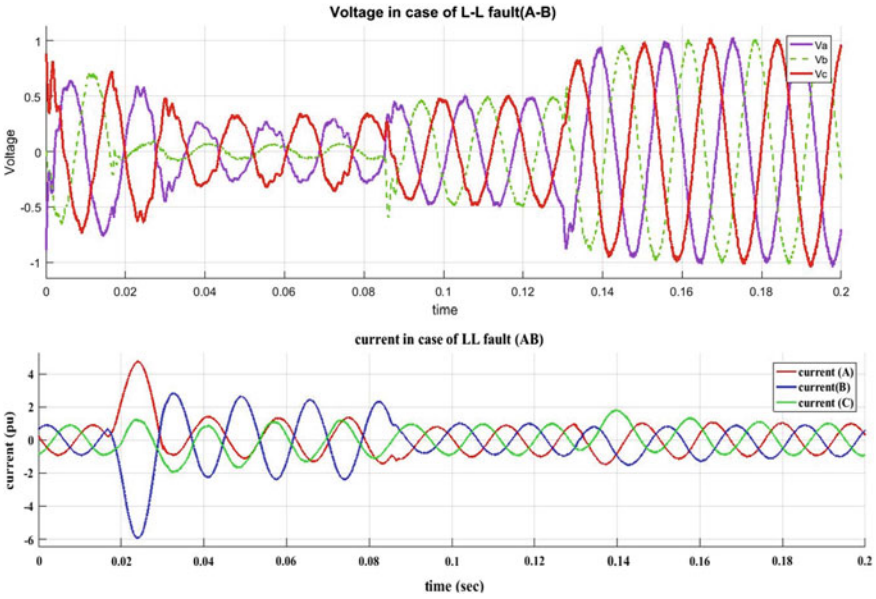

Fig. 8 Voltage and current sample in case of L-L fault

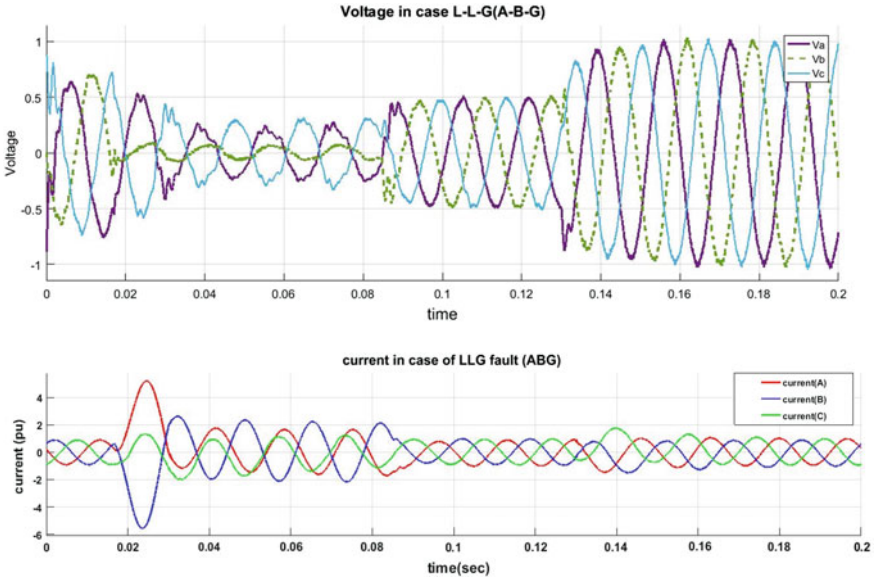

Fig. 9 Voltage and current sample in case of L-L-G fault

From above faulted current and voltage signals, we can calculate several features [21] such as total harmonic distortion (THD), signal-to-noise ratio (SNR), kurtosis, entropy, standard deviation, skewness, and mean. These features were selected on the basis of accuracy of results for classification and also provide improved results in case of noise factor. Thus, for 180 cases as discussed, seven features are calculated for each forming an input data matrix of 180 × 7. A sample data set has been in Table 1. The output (target) matrix consists of values from 1 to 11 representing each

Table 1 Sample data

Faults	Features						
	STD.	Skewness	Entropy	Mean	Kurtosis	THD	SNR
AG	0.6943	−8.935e−05	4.8491	−4.385e−04	1.5424	−42.2042	27.4420
BG	0.6945	−0.001189	4.8442	0.0011	1.5344	−41.9154	28.1674
CG	0.6925	1.6781e−4	4.8453	−7.126e−04	1.5464	−41.4045	28.6244
AB	0.6852	0.0030	4.8613	−4.598e−04	1.5386	−44.5682	27.6362
BC	0.6855	−0.0024	4.8603	0.0012	1.5339	−44.8153	27.6435
AC	0.6946	−15.910e−4	4.8400	6.6820e−04	1.5620	−41.6923	28.2300
ABG	0.6731	−0.0010	4.8530	0.0012	1.6017	−45.5898	27.5616
BCG	0.6737	0.0010	4.8575	−7.453e−04	1.6125	−39.2755	27.4535
ACG	0.6708	0.0018	4.8572	−7.1984e−04	1.6448	−42.0662	27.2386

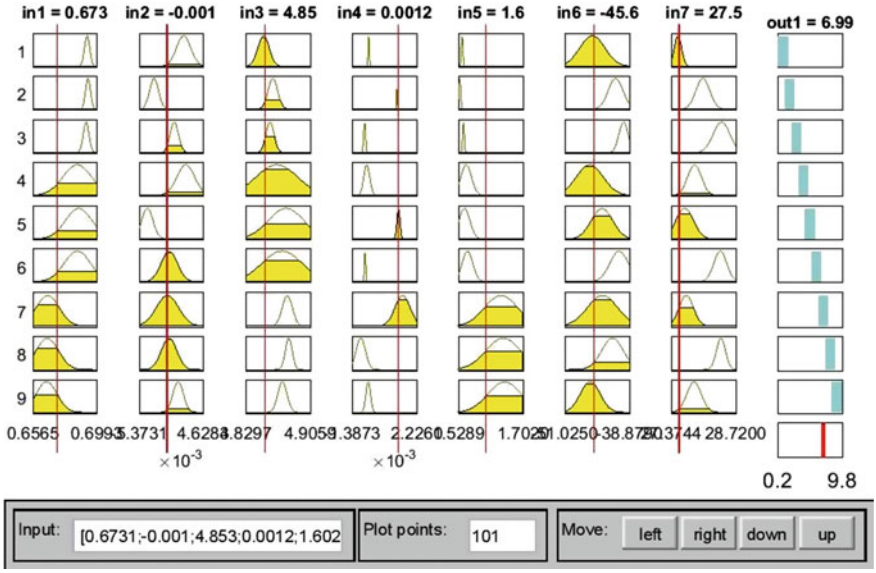

Fig. 11 Neuro-Fuzzy viewer

short circuit fault (AG-1, BG-2, CG-3, AB-4, BC-5, AC-6, ABG-7, BCG-8, and ACG-9).

The dataset so prepared is given as input to Neuro-Fuzzy classifier for training and half of the prepared data set is used for testing purpose. The Neuro-Fuzzy classifier output is a crisp output varying from 1 to 9 and performance evaluation is done by plotting RMSE VS EPOACH plot which is shown below.

From Fig. 11, we can see that there are seven inputs which are actually the seven features which were extracted from the faulted current and voltage. We can vary the input and depending upon this, the classifier output changes. Here, as in Fig. 11, for a particular set of input, the output which is crisp value is seen to be seven that means ABG fault has occurred in this way the different short circuit faults are classified.

Also in Fig. 12, we can see this classification is done with a higher accuracy having RMSE of only 0.031 which almost close to zero.

5 Conclusion

The problem was formulated to detect and classify the different types of faults. Nine cases of different fault types were simulated over a range of fault resistances from 0.001 to 10 Ω and fault distance of 4 to 16 km. The current and voltage samples were recorded. Through this process, different faulted data samples were collected. By using the voltage and current samplesm the different features of power system

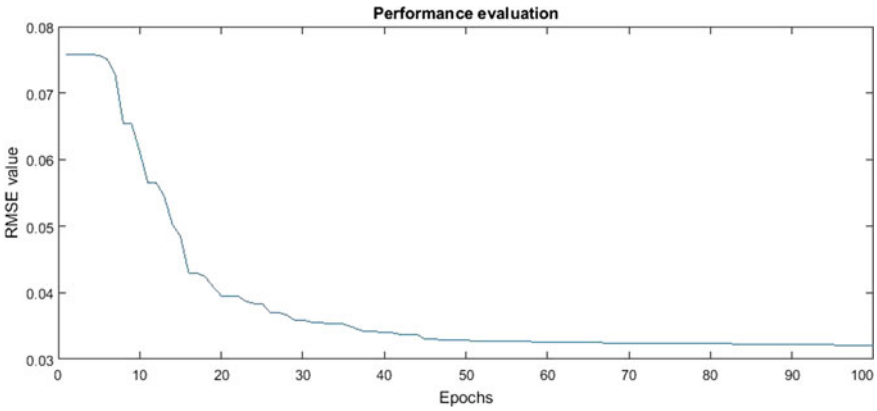

Fig. 12 Performance plot

were extracted. A data set was prepared from the extracted features. The prepared data set is then acts as the input to the Neuro-Fuzzy classifier.

The complete data set is again split into two halves for the training and testing purposes. The training data set is given as input to the fuzzy neural network and the fuzzy neural network attempts to learn from these training data and provides the fuzzy if then rules in output. With the help of this, fault classification was performed and output performance was evaluated.

References

1. Kumar R, Saxena D (2016) Fault location in distribution network with distributed generation: an overview and key issues. IEEE
2. Singh SN, Ostergaard J, Jain N (2014) Distributed generation in power system: an overview and key issues. In: Proceedings of IEC, May 2014
3. Baroudi JA, Dinavahi V, Knight AM (2007) A review of power converter topologies for wind generators. Renewable Energy 32:2369–2385
4. Lei Y, Mullane A, Lightbody G, Yacamini R (2006) Modeling of the wind turbine with a doubly fed induction generator for grid integration studies. IEEE Trans Energy Convers 21(1):257–264
5. Musab Bayat M, Torun Y (2017) Modeling and linearization of DFIG based wind turbine. Euro Sci J 158–168
6. Kamel TS, Moustafa Hassan MA. Adaptive neuro fuzzy inference system (ANFIS) for fault classification in the transmission lines. Online J Electron Electr Eng (OJEEE) 2(1):164–169
7. Elbaset AA, Hiyama T (2009) Fault detection and classification in transmission lines using ANFIS. Institute of Electrical Engineers of Japan, pp 705–713
8. Prasad A, Belwin Edward J, Ravi K (2017) A review on fault classification methodologies part II
9. Prasad A, Belwin Edward J, Ravi K (2016) A review on fault classification methodologies part I
10. Padhy SK, Panigrahy BK, Ray PK, Satpathy AK, Nanda RP, Nayak A (2018) Classification of faults in a transmission line using artificial neural network. In: 2018 International conference on information technology (ICIT), pp 239–243. IEEE

11. Perera WPDR, Danawardana UATI, Thamel WAL, Ireshika MAST (2017) Fault detection in distribution lines using artificial neural network. Research gate on 27 October 2017
12. Awasthi Saurabh, Singh Ranjay (2016) Identification of type and location of fault in a distributed generation system using neural network. Int J Sci Res (IJSR) 5:2059–2065
13. Joseph Lekie A, Idoniboyeobu DC, Braide SL (2018) Fault detection on distributed line using Fuzzy logic. Int J Sci Eng Res (IJSER) 9:490–503
14. Vimal M, Vaghamshi AL, Matang D (2017) Simulation and analysis of transmission line fault detection and location using Fuzzy Logic. Int J Technol Res Eng 4:1463–1470
15. Prasad A, Belwin Edward J, Shashank Roy C, Divyansh G, Kumar A (2015) Classification of falts in power transmission lines using Fuzzy Logic Technique. Ind J Sci Technol (IJST) 8
16. Wang H, Keerthipala WWL (1998) Fuzzy-Neuro approach to fault classification for transmission line protection. IEEE Trans Power Del 13(4)
17. Babayomi O, Keku G, Ofodile NA (2017) Neuro-Fuzzy based fault detection identification and location in a distribution network, 2017 IEEE PES-IAS Power Africa
18. Keerthipala WWL, Wang H, Wai CT (2000) On-line testing of a fuzzy-neuro based protective relay using a real-time digital simulator. IEEE Conf Publ 3:1917–1922
19. Rashidi F (2004) Sensorless speed control of induction motor derives using a robust and adaptive neuro-fuzzy based intelligent controller. IEEE international conference an industrial technology (ICIT), pp 617–627
20. Dash PK, Pradhan AK, Panda G (2000) A novel fuzzy neural network based distance relaying scheme. IEEE Trans Power Deliv 15(3):902–907
21. Mahmud MN, Ibrahim MN, Osman MK, Hussain Z (2015) Selection of suitable features for fault classification in transmission line. 2015 IEEE international conference on control system, computing and engineering, pp 591–596, 27–29 Nov 2015

Chapter 8
Comparison of Neural Network Models for Weather Forecasting

Reeva Mishra and Debani Prasad Mishra

Abstract Weather forecasting has a big impact on people's lives from event planning to cultivation. Conventionally, it has been performed by simulating physical conditions of the atmosphere. Due to nonlinear and irregular kind of weather data, machine learning methodologies can be seen as an alternative of the physical model for forecasting weather. This paper traverses the potential of deep neural networks in the field of weather prediction. It compares the performance of two different neural network models. First model uses the feed- forward network while other uses recurrent neural network to feed the weather data. The models illustrate that neural network models are emulative with the conventional methods and can be perused as a better alternative to predict general meteorological conditions.

Keywords Forecast · Machine learning · Deep learning · Weather

1 Introduction

Weather forecasting is an application of applied science to anticipate the atmospheric condition for forthcoming time and at a specified location. Earlier, it was based on observing periodic astronomical and climatological events. Currently, forecasting is done by gathering data about the present climatic conditions and applying knowledge of atmospheric processes to understand how the weather will transform in the future. But these models are unstable to perturbations due to which the prediction become less precise and more expensive for long duration of time [1].

Recently, the demand for more precise weather prediction is increased. There are various types of needs for weather forecast from factories to business and agriculture. Even there is need of more accurate weather predictions during the time of floods

R. Mishra
Research and Development Engineer, Mahindra Comviva, Bhubaneswar, Odisha, India

D. P. Mishra (✉)
Department of Electrical Engineering, IIIT Bhubaneswar, Khurda 751003, Odisha, India
e-mail: debani@iiit-bh.ac.in

S. Mahapatra et al. (eds.), *Advances in Energy Technology*, Advances in Sustainability Science and Technology, https://doi.org/10.1007/978-981-15-8700-9_8

and droughts. Since, artificial neural networks comparatively show more robustness to perturbations and also there is no need of comprehensive knowledge of physical factors that affect the atmosphere. It can act as a better alternative than the traditional existing statistical methods.

In this paper, two neural network models are analyzed: feed forward neural network (FFNN) model with back propagation algorithm and a LSTM-based RNN model. FFNN model is trained with 10 yrs of data of the weather condition of particular day. Weather data includes max and min temperature, humidity and wind speed. The output was the max temperature of the next day. Whereas, LSTM-based RNN model is trained with 15 years of hourly data of weather conditions which includes hourly temperature, moisture content, and wind speed. The output was the prediction of weather data for the upcoming 24 h.

2 Related Work

Related works comprised different techniques for weather forecasts. While prevailing forecast technology associate models subjected to physics and differential equations, but, nowadays, numerous strategies of ML techniques are employed, predominantly neural networks and few produced results by using probabilistic models.

In reference to the few papers on weather forecast with the by applying machine learning techniques that we have examined, nearly all applied neural networks and one [2] applied "Support Vector Machines" (SVM) technique. Neural networks which is the most prominent model of machine learning, are preferred for weather conditions estimation since it has the capability to acquire both nonlinear and linear dependencies of former weather characteristics and forthcoming aspects of climate, in contrast with the functional and linear regression models. It acts as a boon for the models as it does not require the consideration of simple linear dependencies of all features. In addition, the application also enforced the classifier for weather prediction but inhabited very little scope than neural network applications. Out of all the neural network applications, one [3] of them utilized a composite model that aided neural networks to model the weather forecasting by applying the physics, another [4] applied learning directly to predict weather aspects. One model [5] predicted weather by applying a specified ML algorithm, Bayesian networks and their criteria. It was immensely overpriced but performed very well. Another approach [6] concentrated on a specific case of predicting weather for a definite geographical location which limited in the requisite for one harmonize Bayesian network dependencies but limited in scope. One [7] concentrated on "developing ANN models with scaled down average forecast error in which the idea of broadening measure of discrete observations was utilized in training by adding extra input terms that described the moment of a single observation, expanding the time period of preceding weather data of each and every observation, and re-examining the measure of intermediate (hidden) layers used in the network." Weather forecast models were developed on by taking periods from 1 to 12 h ahead and it was done on an hourly basis. Another

[8] studied about ANN subjected to multi-layer-perceptron (MLP) that was trained as well as tested using ten years of weather data. The outcomes demonstrated that MLP network contains the min calculation flaws and can be treated as a favorable method to predict the weather for a short period.

3 Neural Networks

Neural networks are simplified model of nervous system and have derived motivation from the sort of processing performed by the human brain. They can be trained by examples and can be utilized to tackle untrained or unknown instances of problems.

Feed forward neural network and back propagation
An essential property of FFNN with back propagation is that it should at least abide three types of layers—first an input layer, an intermediate (also called hidden layer), and an output layer. Often neurons are associated in a feed forward manner with input units completely linked with their adjacent neurons prevailing in the intermediate or hidden layer. The neurons present in the intermediate layer are completely linked to neurons present in the final output layer. Back propagation is a training algorithm for FFNN using method of chain rule in which the neurons adjust their weights to attain new knowledge. In this, after every forward pass over a network. Further, the back-propagation complies a backward pass during adjusting the model's weights and biases [9, 10] (Fig. 1).

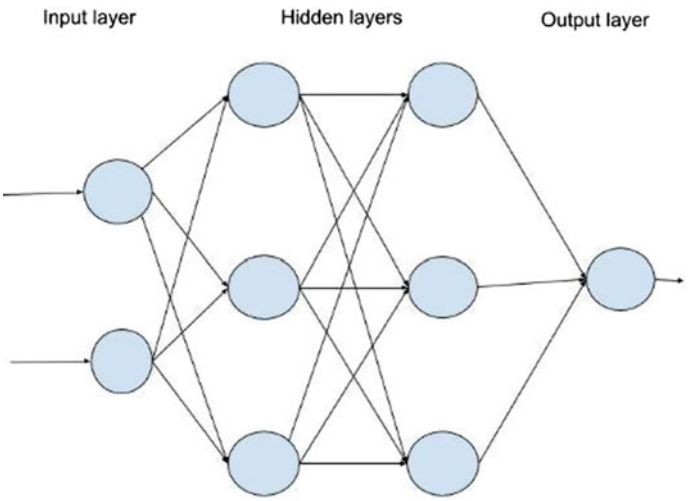

Fig. 1 A FFNN with two fully connected hidden layers

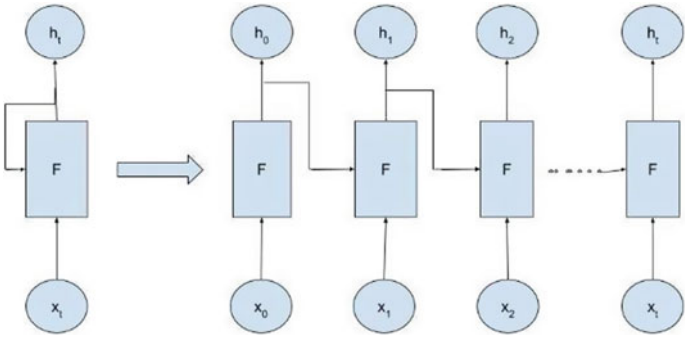

Fig. 2 Rolled and unrolled RNN

Recurrent Neural Network

RNN is a sub-class of ANN in which output(s) are affected by weights applied on inputs as well as by hidden layer vector representing the preceding output(s). RNN can recollect essential information from the input they receive, which permits them to predict the climate precisely. This is why is a preferred technique for serial data such as machine translation, weather series and many more since they develop a sequence and its context, contrasted with different strategies. In RNN, the data passes from a feedback loop. At that point, the present input and the data it received formerly are taken into consideration. Therefore, RNNs keep up a memory of what they had experienced previously, which makes it perfect. Still, RNNs usually fail to keep up memory for long dependencies (Fig. 2).

Long short-term memory RNN

The most popular class of RNN is LSTM, which has the ability to widen its memory. The units of LSTM networks are the supporting units to the surface of RNN. It allows RNN to recall the given data for a prolonged period. Since, RNN contains data in memory, LSTM is able to write, read and also eliminate some of the stored data present in the memory, like re-writing it. LSTM contains memory blocks in hidden layer, which is the biggest advantage. The memory blocks comprise of memory cells with interconnections including self-connections storing the temporary outlook of network along with special units called gates to regulate the flow of data (Fig. 3).

Three different types of gates of each memory block are:

- Input gate (it): It regulates the flow of input activations inside memory cells
- Output gate (ot): It regulates the flow of output activations to remaining part of the network
- Forget gate (ft): It draws the inner state of a cell prior adding as input to cell using self recurrent association of the cell; hence, blanking out or modifying the memory of the cell.

The equation for the gates is as follows:

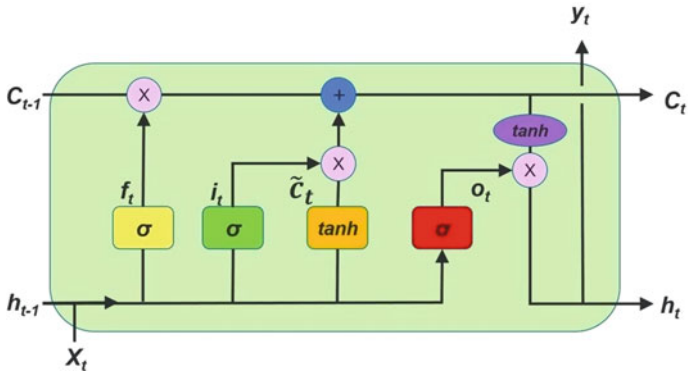

Fig. 3 LSTM network

$$f_t = \left(W_f \cdot \left[h_{t-1}, x_t\right] + b_f\right) \tag{1}$$

$$i_t = \left(W_i \cdot \left[h_{t-1}, x_t\right] + b_i\right) \tag{2}$$

$$o_t = \left(W_o \cdot \left[h_{t-1}, x_t\right] + b_o\right) \tag{3}$$

$$C^{\sim} = \tan h\left(W_c \cdot \left[h_{t-1}, x_t\right] + b_c\right) \tag{4}$$

$$C_t = f_t * C_{t-1} + i_t * C_t^{\sim} \tag{5}$$

$$h_t = o_t * \tan h(C_t) \tag{6}$$

LSTM was used as basis for forecasting since it has an ability to resolve long lag associations in time series data and it also has the capacity to deal with vanishing gradient issues that arise during the training of the model. It can also sort error back-flow issues so that the model uses error feedback only for more accurate predictions. Modern LSTM model consists of peephole connections from its inner cells to the gates present in the corresponding cell to memorize the accurate time of the output [11, 12].

4 Methods

Two different types of model are discussed in this section. One model uses FFNN model [13] while other uses LSTM networks [14].

Feed forward neural network with back propagation
In this model, the FFNN is trained by employing a standard training algorithm called Levenberg-Marquardt algorithm. The training function returns forecast results using mean square error (MSE) deprecation criteria. For an epoch of the training, the maximum temperature of ten years is provided in a series at the input node. This model comprises of five hidden layers. The synonymous objective output gives the max temp for the preceding day and it helps to examine how the network is performing and its behavior. After getting the output from output node, the comparison of the obtained output and the target output is made and if there is some error then that error is calculated. With the help of generated error, the altering of bias and weights of the neuron are controlled, so that the model can become able to generate the output with maximum accuracy. The restorative changes proceed up till the adjustments of weight accomplishes the ideal mapping to get the most accurate output. After various emphasis, the neural system with its final weights is prepared. The test dataset is provided to the prepared neural system to check its effectiveness. The outcome is taken into consideration to perceive the model performance after altering weights.

The dataset provided in input, comprises of weather samples of a year i.e., 365 samples organized in MS Excel. Each sample is consisting of the max temperature recorded on that particular day in the previous ten years and arranged row-wise. From the overall dataset, 60% of the data are selected randomly for training purpose. 20% of the data act as validation set for the network, this data is unknown for the network and the remaining samples act as test data. The performance of model is measured in terms of MSE, i.e., by calculating the squaring of difference of the output and the target, hence always positive. It is acknowledged that training is better with bigger dataset. So, the dataset has been augmented two times of its size, i.e., 730 samples by basically appending it with itself. Even though it does not offer the variability desired for preferable generalization, it enhances the rate of learning (Fig. 4).

Long-short term memory (LSTM)-based recurrent neural network (RNN)
This model comprising of two LSTM layers and a completely associated hidden layer with hundred neurons was implemented to form the basis for the model; the standard layers are shown in the consequent figure (Fig. 5):

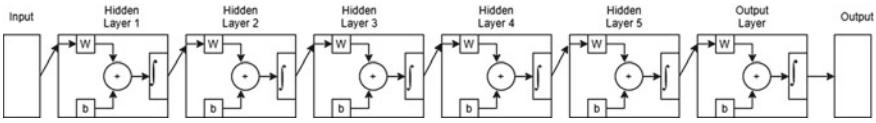

Fig. 4 FFNN model

Fig. 5 LSTM-based model

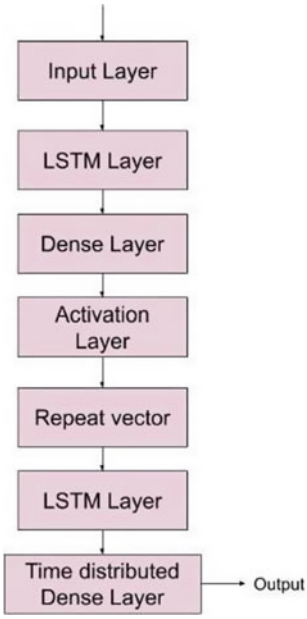

- Dense: A layer of 100 fully connected hidden neurons is preferred to train the model on various samples.
- Activation: The rectifier function is preferred as activation function.
- Repeat Vector: This layer iterates the final output of activation layer as a fixed data to every single time step.
- Time Distributed Dense: Applies dense (completely connected) operation to each time-step of a 3D tensor.

In order to adjust the model in response to the loss, RMSprop optimizer is used and "Mean Square Error (MSE)" is selected for loss estimation.

Relatively, climatological data on hourly basis consisting of temperature, moisture content, and wind speed value of the previous 15 years was used for training purposes. There was presence of many missing values in dataset; however, any continuous lost data (like for days) was not present. For cleaning the data, the missing or noisy values were replaced by filling those using previous data. After cleaning all the values present in dataset, they were normalized to avoid problems like local optima. All the input sequences are provided to the network, each input containing 24 triplets' values [T, M, WS]. 80% data of total input sequence was used as training data, 10% data was used for testing while the rest 10% data as validation set. All the parameters of LSTM were initialized with the even distribution in the range [-0.05, 0.05]. For mini-batch gradient descent, learning rate was 0.001. For model training, batches of 512 input sequences were used and 100 epochs were performed.

5 Result

In feed forward neural network, five hidden layers are used and 80 neurons were distributed among these layers such that 16 neurons per layer. Here, tan-sigmoid is used as transfer function. Since, the validation vectors remain unaffected or fail to improve for any epoch, the training of the network stops early. After training the model, MSE of 2.75 was found as result which denotes that model is not facing over fitting problem and also achieves accuracy (Table 1).

The following graph shows the performance of model for training, validation and testing set. The validation MSE plot appears to pursue the plot for test MSE closely validating better generalization (Fig. 6).

In LSTM-based neural network model, the MSE is applied to examine the characters of the predictions. The scores for a city of Morocco (North Africa) are evaluated using the test data which is untrained with the following results as an example (Table 2).

The graphical representation of results on test dataset is shown (Figs. 7, 8 and 9).

Table 1 MSE score based on the performance of FFNN model

Sample	Intermediate layer	Transfer function	MSE
730	16	TAN-SIGMOID	2.75

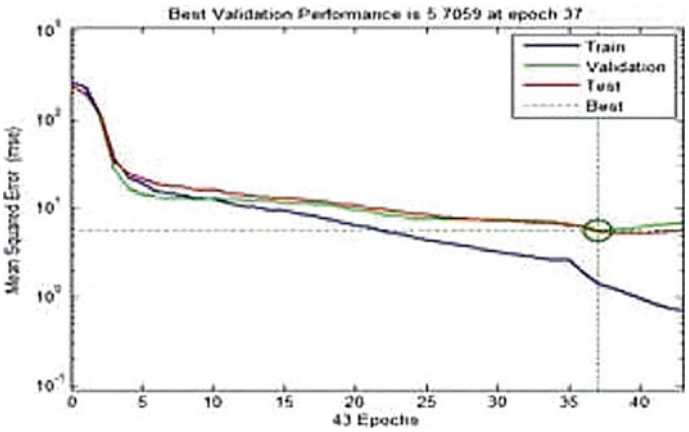

Fig. 6 Proximity of the validation data with test data (good generalization)

Table 2 MSE score for test data of Morocco city

City of Morocco	24 h MSE
Nouasseur	0.00516

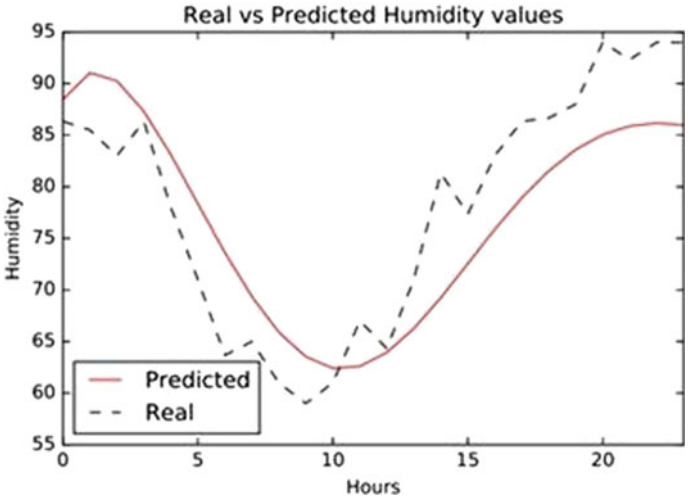

Fig. 7 Study of temperature [T] values for 24 h

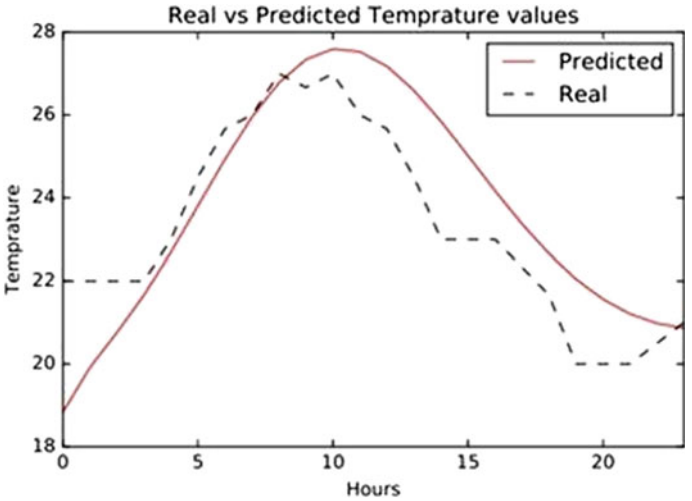

Fig. 8 Study of humidity [H] for 24 h

6 Conclusion

From experimental results, it is observed that both networks provide considerable results with good accuracy. It shows that FFNN model was outperformed by deep LSTM model. Usually, a low MSE value is treated as good accuracy, but we have to acknowledge that the reason behind very low MSE value can be over fitting. Other

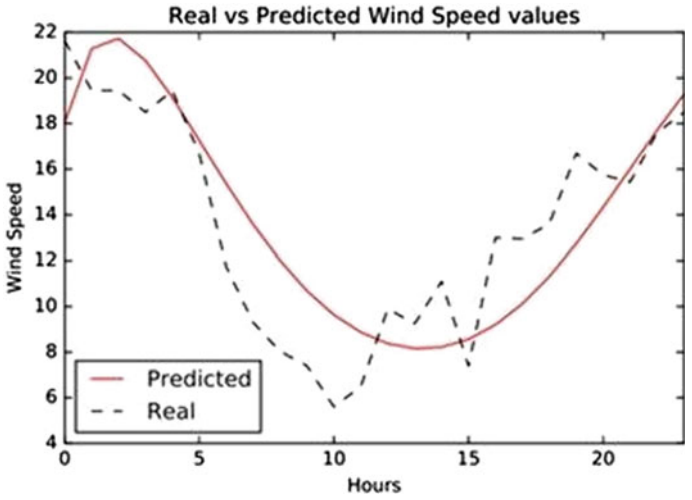

Fig. 9 Study of wind speed [WS] for 24 h

reasons behind low MSE can be poor generalization. However, the most significant deduction from our study was that neural network models can be perused as a better alternative to predict general meteorological conditions. By doing some more improvements in these models, they can also outclass and overcome the traditional way of forecasting and turn out to be the new standard in weather prediction.

References

1. The Weather Company (2016) "Stanford, CA" in Weather Underground
2. Ray P, Mishra DP (2016) Support vector machine based fault classification and location of a long transmission line. Eng Sci Technol Int J 19:1368–1380
3. Krasnopolsky VM, Fox Rabinovitz MS (2006) Complex hybrid models combining deterministic and machine learning components for numerical climate modeling and weather prediction. Neural Netw 19(2):122–134
4. Lai LL et al (2004) Intelligent weather forecast. In: Proceedings of the 2004 international conference on, vol 7. IEEE
5. Ray P, Mishra DP (2014) Artificial intelligence based fault location in a distribution system. In: 13th international conference on information technology, 22nd–24th December, ICIT 2014, Bhubaneswar, India pp 18–23
6. Ray P, Mishra DP, Lenka RK (2016) Short term load forecasting by artificial neural network. International conference on next generation intelligent systems, (ICNGIS-2016), 1st–3rd Sep 2016
7. Ray P, Mishra DP, Dey K, Mishra P (2017) Fault detection and classification of a transmission line using discrete wavelet transform & artificial neural network. In: 16th international conference on Information Technology, India, December
8. Ray P, Panda SK, Mishra DP (2017) Short term load forecasting using genetic algorithm. In: 4th international conference on computational intelligence in data mining, 11–12 Nov 2017

9. Panda SK, Ray P, Mishra DP (2019) A review on ANN in short term load forecasting using artificial intelligence techniques. In: International conference on intelligent and cloud computing, Dec 2019
10. Panda SK, Ray P, Mishra DP (2019) Short term load forecasting using empirical mode decomposition (EMD). In: Particle swarm optimization (PSO) and adaptive network-based fuzzy interference systems (ANFIS). In: 10th international conference on innovations in bio-inspired computing and applications, 16–18 Dec 2019
11. Panda SK, Ray P, Mishra DP (2019) Effectiveness of PSO on short term load forecasting. In: 1st international conference on application of robotics in industry using advanced mechanisms, August, 16–17, 2019
12. Panda SK, Ray P, Mishra DP (2019) Effectiveness of GA on short term load forecasting. In: 18th international conference on information technology, (ICIT-2019), IIIT Bhubaneswar, 19–21 December 2019
13. Mishra DP, Ray P (2018) Fault detection, location and classification of a transmission line. Neural Comput Appl 30(5):1377–1424
14. Zaytar MA, Amrani CE (2016) Sequence to sequence weather forecasting with long short-term memory recurrent neural networks. Int J Comput Appl 143(11):7–11

Chapter 9
Differentiating Storage Essentiality in Thermoelectric and Non-thermoelectric Integrated Conventional Microgrid

Sasmita Jena, Shalini Patro, Subham Subhrajeet Barik, and Sanjeeb Kumar Kar

Abstract The inflation of clean, efficient, sustainable, effective, secure, and reliable electricity demand has been triggered much interest for Microgrid (MG) at a miraculous and quickened pace. The necessity of reliability enhancement, diversity of fuel, cutback of greenhouse gases, severe weather fluctuation, etc. has stimulated the inclusion of MG concept not only in utility level but also in customer and community level. Incorporation of solar photovoltaic (SPV) and thermoelectric (TE), termed as Solar photovoltaic-thermoelectric (SPV-TE) hybrid system is found to be a very promising technique to broadening the utilization of solar spectrum and enhancing the power output effectively-cum-efficiently. This hybrid architecture caters electrical energy with additional thermal energy that signifies upon harnessing of solar insolation in an exceptional way. But in order to retain the voltage profile in the permissible level, MG needs storage mechanism for smoothening of renewable-based power inconstancy, catering significantly high active power and dodging the long-term reactive power rising. This paper illustrates the comparative analysis of two systems such as Conventional MG; TE coupled Conventional MG defining the necessity of employment of energy storage system (ESS). The superiority of proposed system has been outlined in terms of lesser complexity in source integration, mitigating the detriment of WES and FCT integration in real-life application, delivery of higher active power and lesser reactive power absorbance over the other system. The studied system is modeled in MATLAB/Simulink environment and the results are presented to support, verify, and validate the analysis.

Keywords Solar PV system · TEG · Nonconventional distribution generation · Wind energy system · Reactive power · Active power

S. Jena (✉) · S. Patro · S. S. Barik · S. K. Kar
Department of Electrical Engineering, ITER, Siksha 'O' Anusandhan (Deemed to be University), Bhubaneswar, Odisha, India
e-mail: sasmita.jena500@gmail.com

S. Mahapatra et al. (eds.), *Advances in Energy Technology*, Advances in Sustainability Science and Technology, https://doi.org/10.1007/978-981-15-8700-9_9

1 Introduction

Supplementary energy resources are becoming mandatory upon the enduring energy reserves to cope with the energy demand of surging population and technological advancement in the world [1]. Though the Sun is a boundless energy resource which also clean as well as unreservedly available energy resource from nature, it suffers from the curse of having lower efficiency upon the most used renewable energy resources. Concentrated solar photovoltaic modules (CPV) are also sunlight based energy generator that converts a portion of solar irradiance into electrical energy having much more efficient than traditional solar PV system. Several portions of the solar irradiation has wasted as heat while converting sunlight into electricity. SPV system suffers from having lower quantum efficiency as it dissipates greatly (around more than half) of the solar irradiation as heat. Hence, by utilizing the dissipated heat into conversion of electricity the power generation and ultimately efficiency can be increased. Many researchers have been working on the hybridization of solar PV-Wind energy system (WES)-FCT, its control aspect, storage. In source side design of MPPTs for SPV and WES such as optimization-based MPPT, Modified MPPT that raises the system cost as well as mathematical complexity [2]. As per our knowledge, Implementation of SPV-TEG based system has not been employed in non-conventional distribution generation yet. Most of the researchers have been working upon the hybridization of solar PV, WES, and FCT based power generating sources in Microgrid resulting substantial generation of active power and reactive power [3–5]. These papers lag the complete use of the solar irradiation for extracting significant amount of power from the solar PV array resulting in higher electrical efficiency. But as far as our concern, implementation of solar PV-TEG based hybrid system in conventional Microgrid has not been studied yet. The novelty of the paper lies in employment of aforementioned technique (SPV-TEG hybrid system) for availing higher active power and lesser reactive power from the traditional Microgrid. Finally, system performance has been studied in this paper for employment of SPV-TEG-based system in non-conventional distribution generation system under zero fault and numerous faulty conditions.

2 System Modeling and Description

The modeling of thermoelectric generator (TEG) and solar PV modules (SPV) has been performed by insertion of corresponding number of modules in parallel and series as per the requirement. After being designed individually, both the systems have been combined in order to perform the study upon the hybrid system. The model is described in individual subsection namely:

- Modeling of Solar PV array
- Modeling of TEG
- Modeling of WES

- Modeling of DC-DC Converter
- Modeling of VSC (Voltage Source Converter)
- Modeling of Control Algorithm
- Modeling of Filter
- Modeling of Electrolyzer and its bidirectional converter.

2.1 Modeling of Solar PV Array

Solar irradiation and temperature on the solar PV module surface are solely responsible for *the* characteristics of SPV array. As the solar irradiance upon the SPV array is increased, the power generated from SPV array is also increased. In order to construct an SPV array, number of SPV modules need to combine in a particular fashion either in series or parallel to obtain the requisite power. The equivalent circuit of the solar cell is shown in Fig. 1 where I_{ph} Defines the function as current source, R_{sh} defines the internal shunt resistance, R_{se} is the series resistance and a diode connected in parallel with the current source [6]. The output current of the solar PV module

$$\text{i.e. } I_{pv} = N_p I_{ph} - N_p I_0 \left[\exp\left\{ \frac{q\left(V_{pv} + I_{pv} R_s\right)}{N_S A k T} \right\} - 1 \right] - I_{sh} \tag{1}$$

where k = Boltzmann's constant = 1.3805×10^{-5} J/K, A = ideality factor of the solar PV cell depend on PV manufacturing technology, some of them are presented in Table 1. T = operating temperature of the module, $q = 1.6 \times 10^{-19}$ C.

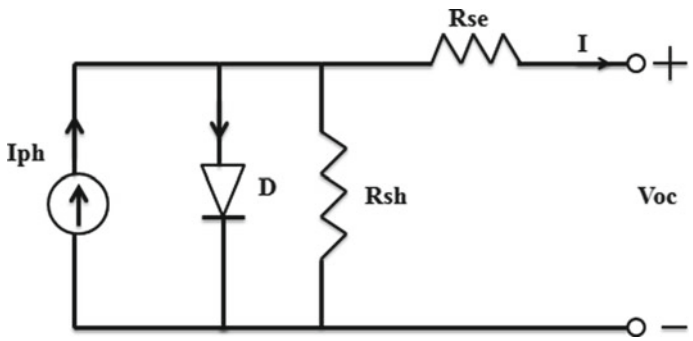

Fig. 1 Equivalent circuit of solar PV module

Table 1 Parameters of the solar panel used

Parameters	Values
Open circuit voltage (V)	8.8
Cold junction temperature (°C)	30
Hot junction temperature (°C)	300
Load resistance (Ω)	1.25
Load output voltage (V)	4.27
Load output power (W)	15
Load output current (A)	3.52
Heat flow density (W/cm^2)	~12
Heat flow across the module (W)	~370

2.2 Modeling of Thermoelectric Generator

The working of TEG constitutes of three elementary thermoelectric effects with two accessorial effects. The three elementary effects are named as Seebeck effect, Peltier effect, and Thomson effect while the accessorial effect can be named as: Joule effect and Fourier effect. Seebeck effect is responsible for electromotive force (EMF) and Peltier heat, Thomson heat and Joule heat are caused by the effect of Peltier, Thomson, and Joule, respectively. As a matter of fact Peltier effect is not an interface effect; it produces heat only at the end sides of the semiconductors. Volumetric effects like Thomson and Joule heat production are pretended to be uniformly transferred to the cold and hot junctions of the semiconductor elements [7]. Though Thomson effect is very small it is often neglected in many cases.

For steady-state analysis at cold and hot junction of TEG an energy balance equation is used which can be expressed as follows:

Mathematically'

$$\begin{aligned} Q_{\mathrm{h}} &= \propto * T_{\mathrm{h}} * I - k_{\mathrm{tc}}\, \Delta T - 0.5 I^2 R \\ Q_{\mathrm{c}} &= \propto * T_{\mathrm{c}} * I - k_{\mathrm{tc}}\, \Delta T + 0.5 I^2 R \end{aligned} \tag{2}$$

The electrical current can be expressed as follows:

$$I = \frac{\propto \Delta T}{(1+n)R} \tag{3}$$

The short circuit current is the maximum current at a load voltage of zero i.e. $V_{\mathrm{L}} = 0$. Hence can be written as follows:

$$I_{\mathrm{SC}} = 2I_{\mathrm{m}} = \frac{2W_{\mathrm{m}}}{V_{\mathrm{m}}} \tag{4}$$

Table 2 Parameters of the thermoelectric generator

Parameters	Symbols	Corresponding values
Seebeck coefficient	$\propto$	0.035 V/K
Resistance	Ω	1.22
Thermal conductivity	k_{tc}	20.91 W/K
Figure of merit	Z	$0.387 \times 10^{-6}\ K^{-1}$

Finally, the voltage of TEG can be expressed by using Ohm's Law, and the corresponding equation obtaining short circuit current and current through TEG, i.e.,

$$V = -R(I - I_{SC}) \tag{5}$$

A model of TEM specified by TEPI-12656-0.6 has been used over here to model the hybrid system and the behavioral analysis has been conducted. The parameter specifications of the thermoelectric Module (TEM) have been listed in Table 1. The constraints that have been considered for modeling are presented in Table 2.

2.3 Modeling of Wind Turbine

About 350–400 W power is generated from a permanent magnet based self-regulated variable speed wind turbine at a wind speed of 12 m/s. Stall control or self-control can be achieved by adjustment of wind turbine blades in a particular direction. At a wind speed of 17 m/s, this wind turbine can be able to extract power from the wind.

The aerodynamics of the rotor can be stated as

$$P_w = \frac{C_p \rho A v_w^3}{2} \tag{6}$$

where P_w = wind power,

C_p = power coefficient.

2.4 Modeling of Electrolyzer

A resistor (contact resistance) connected in series with the controlled voltage source (CVS) is considered for modeling of an Electrolyzer. A shepherd's model has been used for representation of nonlinear voltage which varies with amplitude of current and amplitude of the actual voltage. The CVS can be represented mathematically as:

$$E = E_0 - K\frac{Q}{Q - \int i\,\mathrm{d}t} + A\exp(-B\int i\,\mathrm{d}t) \tag{7}$$

where E is No Load Voltage, E_o is Constant Electrolyzer Voltage, K is the Polarization Voltage.

Q is the Capacity of Electrolyzer, A is the Exponential Voltage, B is the Exponential Capacity, i is the Current of the Electrolyzer. Bidirectional converter is an integral part of connecting an Electrolyzer with a system. As the name suggests the flow of power is in both the directions. Generally, system integrated with Fuel Cell, Supercapacitors use bidirectional converter for power flow in both directions.

2.5 Modeling of DC-DC Converter

In order to stepping up the voltage at the output of the terminal, dc-dc converter is used which is also termed as boost converter.

It can be stated as

$$V_0 = \frac{V_s}{1 - D} \tag{8}$$

where V_o denotes Output Voltage of the System

V_s denotes Input/Source Voltage of the System

D denotes Duty Cycle (it varies from 0 to 1).

2.6 Modeling of Voltage Source Converter (VSC)

For mitigation of power quality issues, converting dc side voltage into ac voltage for feeding it to the grid; VSC is connected to the system. This can also be acted as an active shunt filter. Natural a-b-c reference frame has been considered for modeling of the VSC. The following equations have been used in order to model the VSC.

Mathematically,

$$S_a = 2S_1 - 1 \tag{9}$$

$$S_b = 2S_3 - 1 \tag{10}$$

$$S_c = 2S_5 - 1 \tag{11}$$

$$V_{ia} = \left(\frac{2}{3}\right) * \frac{V_{\mathrm{dc}}}{2} * S_a - \frac{1}{3}S_b - \frac{1}{3}S_c \tag{12}$$

$$V_{ib} = \left(\frac{2}{3}\right) * \frac{V_{\mathrm{dc}}}{2} * S_b - \frac{1}{3}S_a - \frac{1}{3}S_c \tag{13}$$

$$V_{ic} = \left(\frac{2}{3}\right) * \frac{V_{\mathrm{dc}}}{2} * S_c - \frac{1}{3}S_a - \frac{1}{3}S_b \tag{14}$$

where, S_a, S_b, S_c define Three-phase Switches;
S_1, S_3, S_5 define switching state of switches;
V_{ia}, V_{ib}, V_{ic} define voltage output of inverter;
V_{dc} define DC link voltage.

2.7 *Modeling of Control Strategy of VSC*

There is a self-uniqueness of this control strategy for operation during healthy as well as faulty conditions. The control strategy thus used is found to be efficient as after the clearance of fault, it brings the system back to the steady-state. No controller will be going to work during fault; hence the control strategy is designed in such a way that as soon as the fault is cleared the system comes back to the initial position as soon as possible. Whatever non-conventional sources are proposed to integrate this strategy holds well every time. A multiplication factor of 0.0045 is considered for phase voltages. The control strategy thus used can be shown in block diagram in Fig. 2.

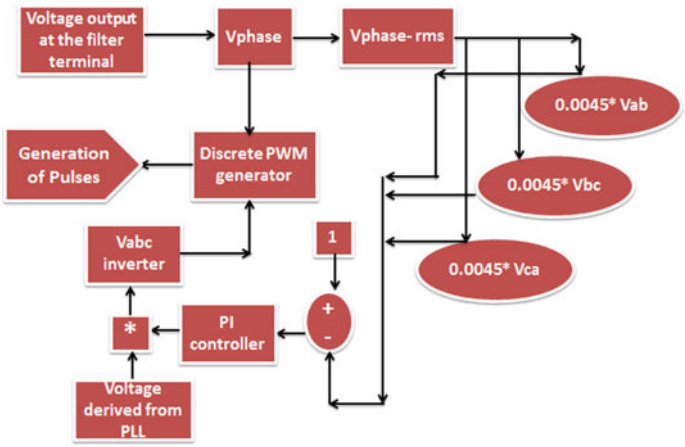

Fig. 2 Control strategy of VSC generating gate signal

2.8 Filter Modeling

Though the system uses many power electronics based switches there is the chance of generation of harmonics in the system. In order to lessen the harmonics filter circuits have been implemented. The Synchronous reference frame (SRF) has been used in order to model the filter circuit that can be explained below.

$$V_{id} = R_f i_d + L_f \frac{\mathrm{d}i_d}{\mathrm{d}t} - \omega_e L_f i_q \tag{15}$$

$$V_{iq} = R_f i_q + L_f \frac{\mathrm{d}i_q}{\mathrm{d}t} + \omega_e L_f i_d \tag{16}$$

where, R_f denotes Resistance of Filter;

L_f denotes Inductance of Filter;

ω_e Denotes Angular Frequency;

i_d, i_q denotes d and q-axis inverter currents;

V_{id}, V_{iq} denotes d and q-axis inverter voltages.

3 Proposed System Configuration

Figure 3 represents the proposed system of employing thermoelectric generator (TEG) in NDG. The newness of this work lies in integrating TEGs with solar PV array so that the power generation from the RE sources could be maximized in a significant manner. As per our knowledge, implementation of TEGs has not yet been considered for Microgrid. Hence the proposed system is compared with conventional NDG to infer the superiority of employing TEGs to NDG.

4 Results and Discussion

The system is subjected to healthy conditions as well as several variations (fault conditions). The reliability of the whole NDG system is studied for several parameters such as active power delivered to the system by the RE sources (P) and Reactive power supplied to the system (Q). The control strategy applied to the system has been studied precisely during variations. Because the main aim of control strategy will be defined best when the fault is cleared means as soon as the fault is cleared the control strategy starts its action in order to retain the system back to the initial condition. Thus the applicability of the proposed system is verified for healthy conditions (during zero faults), and faulty conditions such as Line-to-Ground (L-G) fault (Figs. 4).

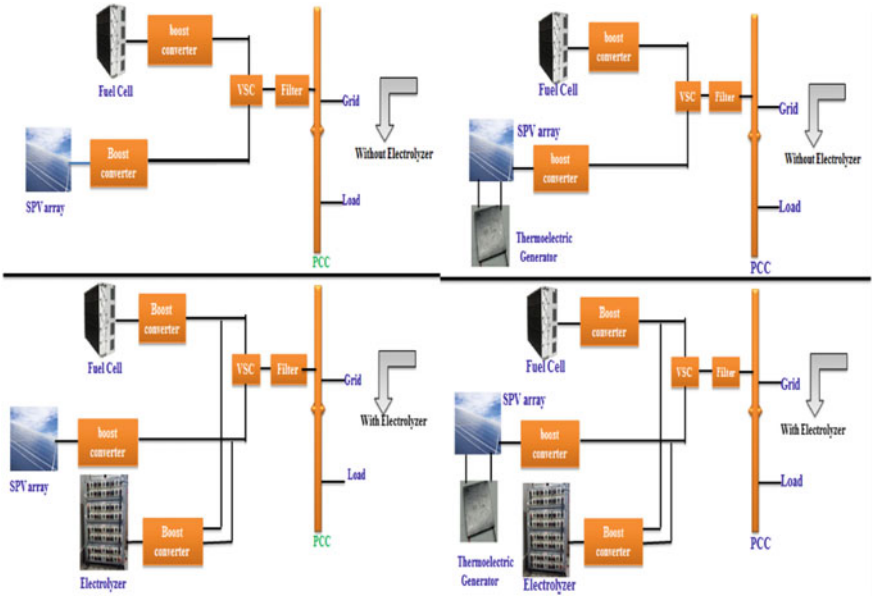

Fig. 3 Proposed system configuration

4.1 During Healthy Condition (Zero Fault Condition)

The electrolyzer integration plays a vital role in mitigating higher reactive power absorbance and lower active power delivery for the system. The higher active power delivery is due to the presence of an additional DC source i.e. an Electrolyzer that provides power in both directions. It supplies power to the load and grid and charged through grid during off sunshine hours in order to retain the system operation and without interrupting the power supply to the load. The solar PV receives sunlight for electricity generation during these sunshine hours and also charges the Electrolyzer to mitigate the power demand during peak hours as well as off sunshine hours.

4.2 During Line to Ground Fault Condition

The proposed system is studied under fault conditions in order to check the reliability of the controller during disturbances. The system fault is created in virtual scenario. In the above studied single L-G fault active power, reactive power (Fig. 5).

About 1.297 times higher active power has been delivered to the system when the EESS has integrated whereas about 1.281 times lower reactive power has been absorbed without integration of EESS in case of SPV-FCT system, 1.213 times

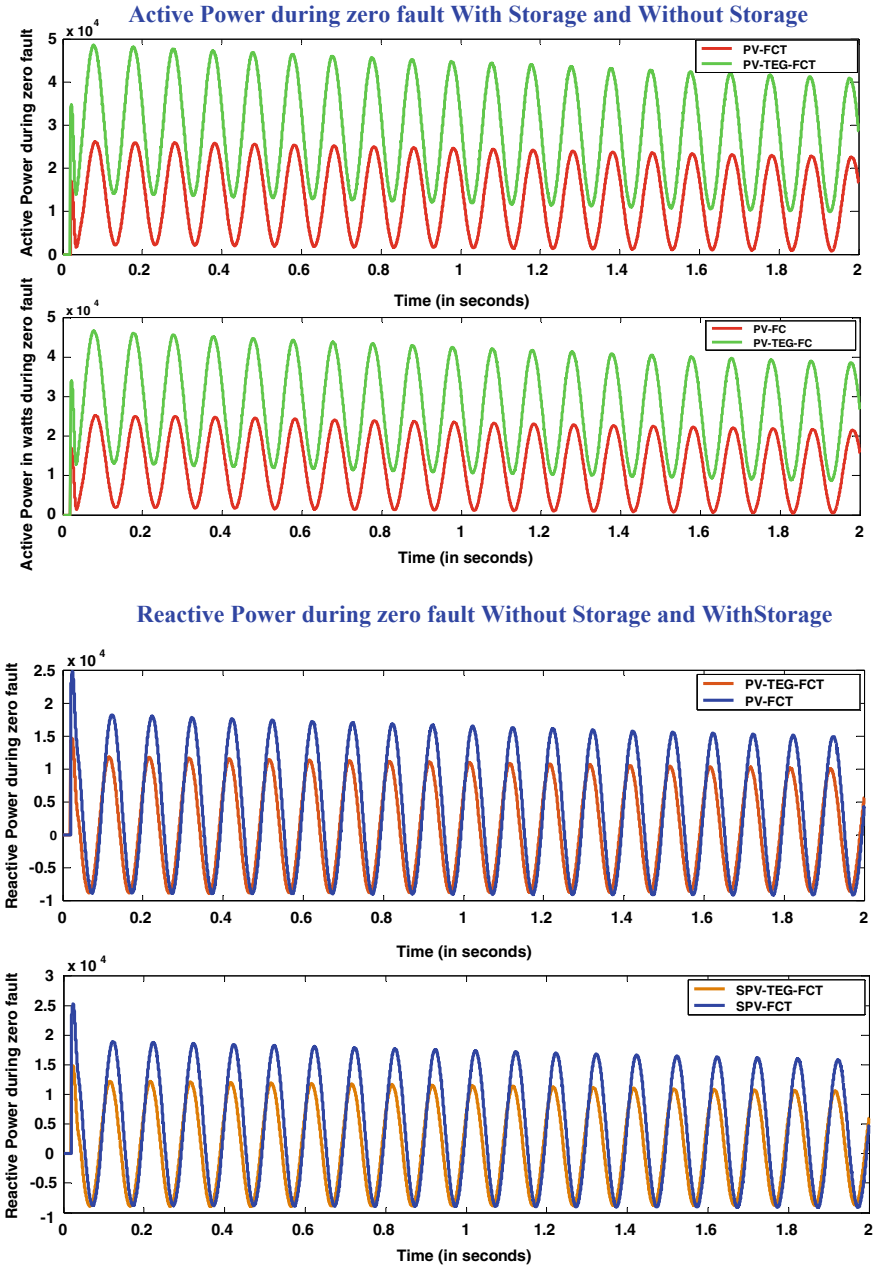

Fig. 4 **a** Active power delivered for PV-TEG-WIND and PV-WIND system. **b** Reactive power supplied for PV-TEG-WIND and PV-WIND system

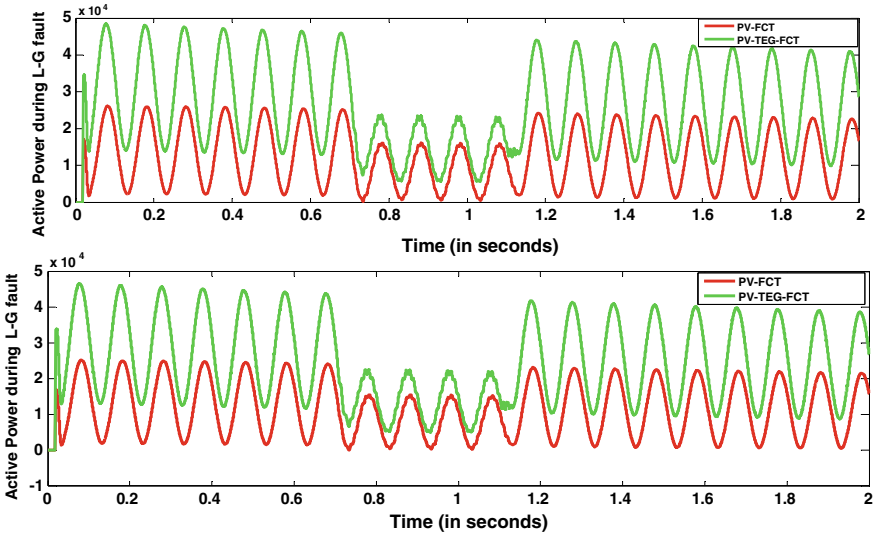

Fig. 5 Active power during L-G fault for PV-TEG-WIND and PV-WIND system

higher active power delivery whereas 1.24 times lower reactive power absorbed in SPV-TEG-FCT system (Fig. 6).

5 Observational Analysis

See Table 3.

6 Conclusion

Thermoelectric Generators (TEG) are integrated with solar PV system in order to process the lost heat by thermoelectric effect. The conversion of light energy into electricity by photoelectric effect and converting heat into electricity by thermoelectric effect combinedly generate a significant amount of power from solar PV array. Also, it can be observed that presence of EESS affects less to the system during disturbances to its compensating nature. The system is less affected in case of EESS integration as during power fluctuations the EESS itself serves as an auxiliary power source at the time of dynamic variation.

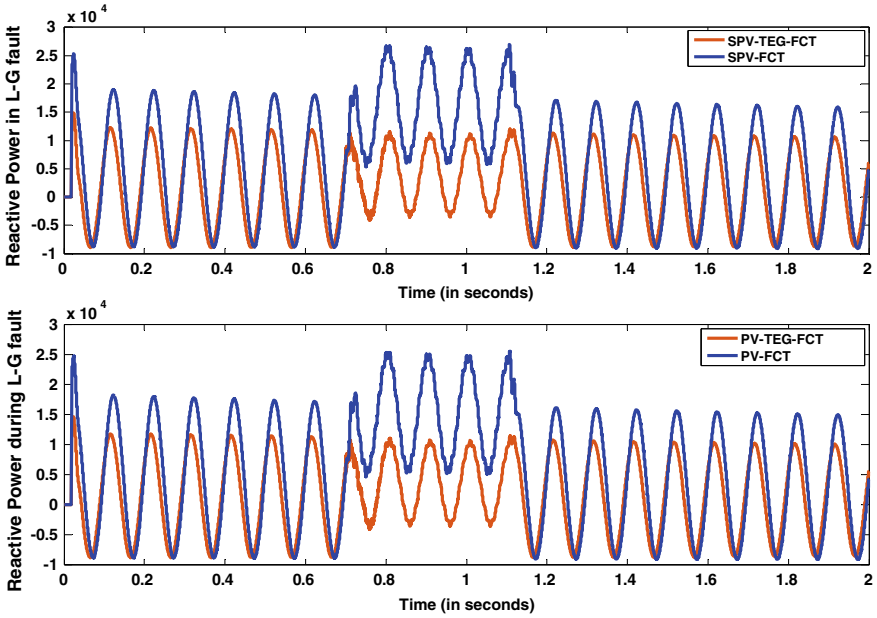

Fig. 6 Reactive power during L-G fault for PV-TEG-WIND and PV-WIND system

Table 3 Observation analysis of the system in terms of active and reactive power

Reliability checking condition	Active power (P)	Reactive power (Q)
Healthy condition	Without storage 1. SPV-FCT $P_{WS} = 1.3 \times 10^4$ W 2. SPV-TEG-FCT $P_{WS} = 2.14 \times 10^4$ W	Without storage 1. SPV-FCT $Q_{WS} = 7687$ W 2. SPV-TEG-FCT $Q_{WS} = 5990$ W
	With storage 1. SPV-FCT $P_S = 1.67 \times 10^4$ W 2. SPV-TEG-FCT $P_S = 2.859 \times 10^4$ W 3. SPV-TEG $P_S = 3.332 \times 10^4$ W	With storage 1. SPV-FCT $Q_S = 5996$ W 2. SPV-TEG-FCT $Q_S = 4803$ W 3. SPV-TEG $Q_S = 6265$ W
Single L-G fault	Without storage 1. SPV-FCT $P_{WS} = 1.289 \times 10^4$ W 2. SPV-TEG-FCT $P_{WS} = 2.345 \times 10^4$ W With storage 1. SPV-FCT $P_S = 1.672 \times 10^4$ W 2. SPV-TEG-FCT $P_S = 2.846 \times 10^4$ W	Without storage 1. SPV-FCT $Q_{WS} = 7690$ W 2. SPV-TEG-FCT $Q_{WS} = 5992$ W With storage 1. SPV-FCT $Q_S = 6002$ W 2. SPV-TEG-FCT $Q_S = 4826$ W

References

1. Jena S, Kar SK (2019) Setting a fostered energy network by decarbonizing the grid: Hybridization, control, and future solutions upon storage. Int J Energy Res 43(1):455–474
2. Jena S, Kar SK. Demonstrating the benefits of thermoelectric-coupled solar PV system in microgrid challenging conventional integration issues of renewable resources. Int J Energy Res
3. Jena S, Kar SK (2019) Employment of solar photovoltaic-thermoelectric generator-based hybrid system for efficient operation of hybrid nonconventional distribution generator. Int J Energy Res
4. Jena S, Kar S, Satpathy PR. Encapsulating the challenges of storage in solar PV based microgrid. ISBN:97-3-659-35285-0
5. Senthilkumar J, Charles Raja S, Srinivasan D, Venkatesh P (2018) Hybrid renewable energy-based distribution system for seasonal load variations. Int J Energy Res 42(3):1066–1087
6. Wu YY, Wu SY, Xiao L (2015) Performance analysis of photovoltaic–thermoelectric hybrid system with and without glass cover. Energy Convers Manag 93:151–159

7. Beeri O, Rotem O, Hazan E, Katz EA, Braun A, Gelbstein Y (2015) Hybrid photovoltaic-thermoelectric system for concentrated solar energy conversion: Experimental realization and modeling. J Appl Phys 118(11):115104

Chapter 10
A Concept Note on Aqueous Type Graphite Dual-ion Battery: A Promising Low-Cost Electrical Energy Storage Technology

Sunny Nandi, Arnab Dutta, and Shyamal K. Das

Abstract Electrical energy storage technologies are an integral part of renewable energy generation infrastructure. The rechargeable battery is a unique example of portable storage technologies. Among various rechargeable batteries, dual-ion batteries are catching the attention recently. Herein, we present a proof-of-concept of a novel and eco-friendly dual-ion battery with electrochemically processed graphite electrodes in aqueous electrolyte. We also take the advantage of the three electrons transfer process of Al^{3+} ion while operating the battery. The battery shows excellent cycling stability over 100 cycles with specific capacity of 10 $mAhg^{-1}$. The notable part of the work is that it proposes to use exceptionally low-cost and easily available raw materials.

Keywords Energy storage · Dual-ion battery · Graphite

1 Introduction

The global carbon-dioxide emission due to fossil fuel burning for energy generation is estimated to be 33 gigatonnes in 2019 [1]. This massive quantity of carbon footprint is a major cause in bringing certain degree of uncertainty and instability to our environment. In a bid to circumvent this problem, harnessing energy from small- and large-scale renewable sources is gaining unprecedented popularity worldwide. The United Nations also acknowledged this very idea of eco-friendly electricity generation and consumption by pinning 'Affordable and Clean Energy' as one of Sustainable Development Goals. However, the unpredictable and intermittent nature of renewable energy sources demand its integration with electrical energy storage devices for a more viable and consumer friendly on-demand consumption. It has unambiguously propelled the research interest in the area of energy storage technologies. In order to tap the vastness of renewables, a wide variety of storage technologies is available. For

S. Nandi · A. Dutta · S. K. Das (✉)
Department of Physics, Tezpur University, Tezpur, Assam 784028, India
e-mail: skdas@tezu.ernet.in

S. Mahapatra et al. (eds.), *Advances in Energy Technology*, Advances in Sustainability Science and Technology, https://doi.org/10.1007/978-981-15-8700-9_10

instance, a pumped hydroelectric system is an excellent storage technology capable of storing electricity in gigawatts [2]. These kinds of large-scale systems are permanently installed in desired geographical territories for the delivery of electricity in the grid. However, this option has limited opportunity for portable consumption of electricity. The revolution that has undergone in the last decade in the electronics industry relentlessly demands for more-efficient, long-lasting, lightweight, and small-scale energy storage devices. Hence, rechargeable batteries emerged as the powerhouse for storing and on-demand delivery of portable mode of electricity. The most notable among rechargeable batteries which made remarkable contributions to our modern way of living is lithium-ion battery. These types of batteries possess exceptionally high energy density, long life time, and require low maintenance. In recent times, however, the depleting condition of the essential ingredients for the manufacturing of lithium-ion batteries and a rapid surge in their cost have set off alarm bells both in academia and industry. Consequently, it has a triggering effect to find alternative rechargeable batteries base on inexpensive and naturally abundant resources.

There are several propositions on analogues of lithium-ion batteries based on elements such as Na, K, Zn, and Mg [3]. However, an old concept of dual-ion batteries is resurfaced and gaining immense popularity recently. There is a clear distinction in the operation of dual-ion and lithium-ion batteries as shown in Fig. 1. In lithium-ion

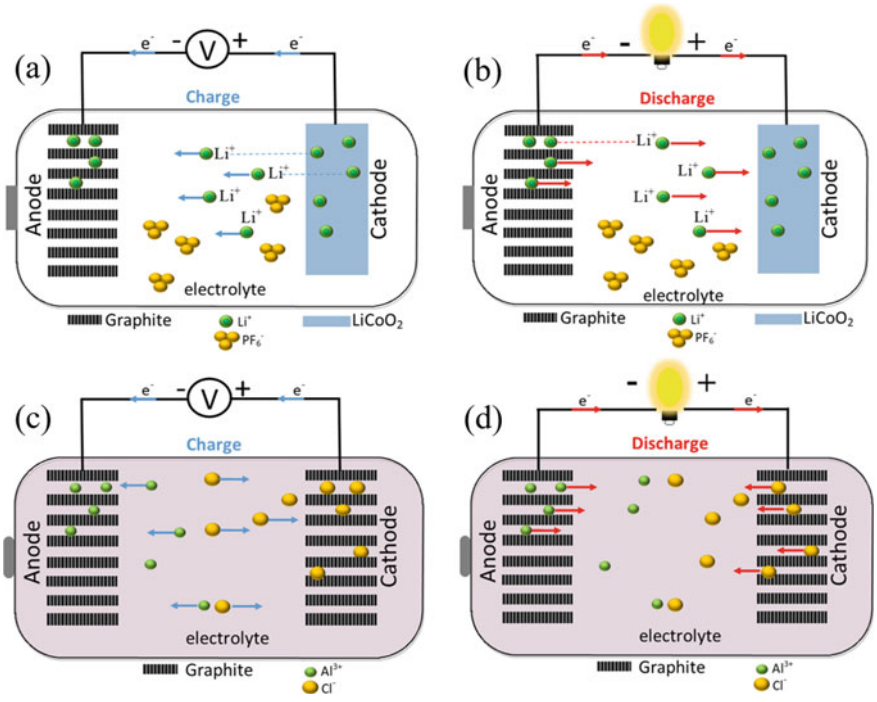

Fig. 1 Schematic of **a**, **b** Lithium-ion battery and **c**, **d** Dual-ion battery in charge and discharge conditions

batteries, the cation (i.e., Li^+ ion) shuttles between the cathode and anode through the electrolytic medium (Fig. 1a, b). The direction of Li^+ ion migration depends on the discharge and charge cycles. The source of Li^+ ions is an inorganic lithium salt such as $LiPF_6$ dissolved in non-aqueous solvent or solvent mixtures. This electrolyte also contains PF_6^- anion, which remains inactive during the operation of the battery. The typical cathode and anode in lithium-ion batteries are lithium cobalt oxide and graphite, respectively. On contrary, in dual-ion battery, both the cation and anion available in the electrolytic medium simultaneously shuttle between the cathode and anode. In the charging process, the cation (e.g., Al^{3+} ion) and anion (e.g., Cl^- ion) intercalate in the anode and cathode, respectively (Fig. 1c). The reverse process occurs during the discharge cycle. The opposite charge transport processes in two opposite directions result in enhanced electron transport in the external circuit and, hence, it boosts the energy and power density of the system. The challenge in dual-ion battery is to find an electrode material which could host anions. The cations such as Li^+, Na^+, Mg^{2+} could, in general, be easily diffused in an electrode due to their small ionic radii. However, the large-sized anions encounter steric barrier during the diffusion process in an electrode. Hence, there are very few known electrode materials as anion host [4]. One such promising candidate is graphite. Rüdorff and Hofmann, in 1938, first demonstrated the electrochemical intercalation of HSO_4^- anion from concentrated sulfuric acid electrolyte in graphitic electrode [5]. It is well-known that graphene sheets are stacked in ABAB configuration in graphite. The interplanar spacing in graphite is 0.335 nm and the graphene sheets are held together by weak van der Waals forces. Under suitable electrochemical conditions, certain cations and anions can intercalate in between the graphene sheets overcoming the van-der-Waals force. Some of the examples of anions that intercalate in graphite are PF_6^-, BF_4^-, $AlCl_4^-$, ClO_4^-, $TFSI^-$, etc. [6]. Based on the intercalation of these types of anions, there are demonstrations of the operation of dual-ion batteries in recent times [4]. However, these studies make use of non-aqueous carbonate or ionic liquid-based electrolytes. The demerits of such type of electrolyte are high cost, harmful to environment, and difficulty in handling them in ambient atmosphere. Hence, despite graphite being a low-cost and eco-friendly material, the choice of electrolytes may not make dual-ion batteries a green and sustainable system.

In an effort to build an exceptionally low-cost and sustainable dual-ion battery system, we embark on to investigate the operation feasibility of such system in water based (or aqueous) electrolyte. This type of electrolyte has the merits of being low-cost, ease in processing, and environment friendly. We demonstrate here the proof-of-concept of a dual-ion battery utilizing graphite as electrodes and aqueous electrolyte. The demonstrated battery could be easily assembled in ambient atmosphere unlike lithium-ion battery or non-aqueous dual-ion battery. We note that further studies are essential for improving the performance of the system. It is also noted here that this work draws inspiration from the outcome of our previous work on aqueous aluminum–graphite battery [7].

2 Experimental Section

2.1 Materials

Commercially available graphite foil of thickness 0.5 mm is used in the work. The aqueous electrolyte is prepared by dissolving aluminum chloride hexahydrate ($AlCl_3.6H_2O$) in 1 M concentration in ambient atmosphere. It is worth to mention here that one should be extremely careful while preparing the electrolyte since $AlCl_3$ exothermically reacts with water. The electrolyte can be stored for several months without any degradation.

2.2 Processing of Graphite Electrode

An electrochemical process was applied to obtain the functional graphite electrodes for the dual-ion battery. Two pieces of graphite foil of dimension 1 cm × 1.5 cm (breadth x length) were submerged in a glass cell containing 1 M $AlCl_3$ aqueous electrolyte. The separation between the two was maintained at 1 cm. The immersion length of both the electrodes in the electrolyte was 1 cm. A DC potential (or bias) of 3 V was applied between the electrodes using a DC power source for 5 min. The experimental setup is shown in Fig. 2. After the application of the bias, the graphite electrodes were washed with deionized water for several times and dried at 110 °C for 12 h. These dried electrodes were further used for assembling the dual-ion battery.

2.3 Characterization of the Processed Graphite Electrode

The crystallographic phase identification was performed by using powder X-ray diffraction (BRUKER AXS D8 FOCUS; Cu-K_α radiation, $\lambda = 1.5406$ Å). The surface morphology of the electrodes was observed by scanning electron microscopy (SEM, JEOL JSM 6390LV) and transmission electron microscopy (TEM, JOEL JEM 2100).

2.4 Electrochemical Analysis

The dual-ion battery was assembled with two processed graphite electrodes. These two electrodes were dipped in 1M $AlCl_3$ aqueous electrolyte. Galvanostatic discharge/charge experiments at different current rates were performed to test the feasibility of operation of the battery. All experiments were performed at room temperature and in ambient conditions.

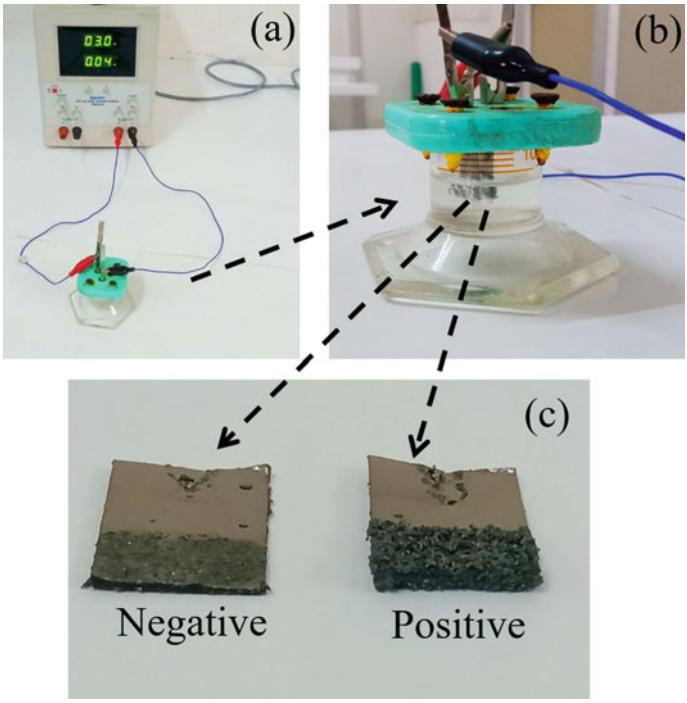

Fig. 2 **a** Experimental setup for performing the electrochemical processing of the graphite electrode, **b** enlarged view of the electrochemical cell, and **c** digital photograph of the graphite electrodes connected to the positive and negative terminals of the electrochemical cell

3 Results and Discussion

As discussed earlier, one of the fundamental criteria for the functioning of a dual-ion battery is the availability of sufficient cation and anion in the electrolyte. It is noted here that the utilized electrolyte contains hydrated Al^{3+} cations and Cl^{-} anions as charge carriers [7]. Hence, the selection of the electrolyte for the present work is well justified. Another prime reason for using Al^{3+} ion electrolyte is that each Al^{3+} cation pushes three electrons across the load unlike one electron per Li^{+} ion. In addition, $AlCl_3$ electrolyte is extremely cheap and easily available.

Our previous reported work on aqueous Al-graphite battery evidenced that pristine graphite electrode is not suitable for Al^{3+} ion storage in aqueous electrolyte. It is because the intercalation process of Al^{3+} ions between the graphene layers in pristine graphite electrode is extremely slow due to the large dimension of the electrode. Hence, it is important to process the pristine graphite electrode to obtain graphene like nanostructures so that the diffusion process could be reasonably enhanced. This is the reason for the electrochemical processing of the graphite electrode prior to the assembly of a dual-ion battery. It is worth to note here that only the graphite electrode

connected to the positive terminal of the DC power source shows expansion (Fig. 2c) and, hence, only this processed electrode is used in the dual-ion battery.

Figure 3 compares the surface morphology of pristine graphite and the processed graphite electrode. It is clearly evident that the surface of the processed graphite electrode is covered with nanoflakes (Fig. 3b), whereas the pristine graphite surface is smooth (Fig. 3a). The digital photograph, as shown in Fig. 2c, shows an expansion of the processed electrode. Thickness measurement by Vernier calipers indicates 200–250% expansion of the graphite electrode after processing. TEM images (Fig. 3c, d) show few layers of graphene nanoflakes.

The phenomenon of Cl^- anion intercalation in graphene like electrode is evidenced from the ex situ XRD investigations conducted on the charged and discharged state graphene electrodes derived from an aqueous Al-graphite cell. Figure 4 shows the normalized ex situ patterns. The charged state electrode shows the disappearance of (002) graphitic peak usually observed at $2\theta = 26.33°$. In fact, this peak is prominently observed for the pristine electrode. Now, there is emergence of two new peaks at 25.03° and 27.52°. This splitting of the (002) peak during charging cycle indicates an additional intercalation process with Al^{3+} ion intercalation in the graphene electrode. Since the only other available charged species is Cl^- anion, it gives an indirect evidence of Cl^- anion intercalation in the graphene electrode during the electrochemical process and this process is reversible. Hence, both Al^{3+} cation and Cl^- anion can participate in the redox process when a graphitic electrode is used

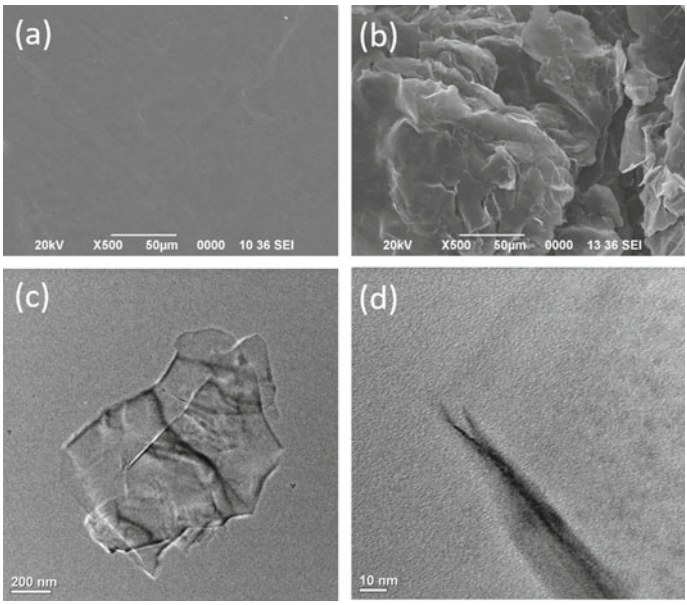

Fig. 3 SEM images of **a** pristine graphite electrode and **b** processed graphite electrode. **c**, **d** TEM images of the processed graphite electrode

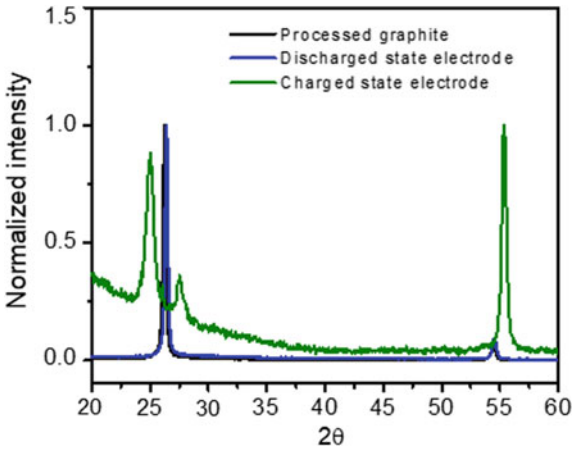

Fig. 4 Ex-situ XRD patterns of discharged and charged state electrodes to verify Cl^- anion intercalation in graphene like electrode. Adapted with permission from Ref. [7], Copyright (2019) American Chemical Society

in a battery. Based on this outcome, we explore the feasibility of a dual-ion battery with the processed graphite as both cathode and anode in $AlCl_3$ aqueous electrolyte.

Galvanostatic charge–discharge experiments were performed to test the viability of a graphite–graphite dual-ion battery in the $AlCl_3$ aqueous electrolyte. Figure 5a shows the charge–discharge curves obtained at a current rate of 3 Ag^{-1} in the voltage range of 0.01-2 V. The discharge capacity is observed to be 10 $mAhg^{-1}$. The battery shows excellent durability test. It could show sustainability over 100 cycles without loss of any specific capacity as shown in Fig. 5b. The energy density of the investigated dual-ion battery is lower in comparison to commercially available lead-acid battery. The low energy density is attributed to the higher weight of the graphite electrodes. There exists tremendous opportunity to improve it by utilizing low-mass and thin processed graphite electrodes. The operating reactions in the battery could be summarized as follows: (a) graphite anode: $C_x + Al^{3+} + 3e^- \leftrightarrow [Al]C_x$, (b) graphite cathode: $C_y + Cl^- \leftrightarrow [Cl]C_y + e^-$ (x and y are, respectively, the molar ratios of carbon atoms to intercalated Al^{3+} and Cl^- ions in the graphite electrode).

4 Conclusions

In summary, a concept note on rechargeable aqueous dual-ion battery is proposed with processed graphite electrode. The battery utilizes raw materials which are locally available in high abundance, low-priced, and eco-friendly. It is noted here that the energy density is quite low in comparison to lithium-ion or lead-acid battery. However, this kind of concept is an important basis for future studies and further improvements in energy storage technologies.

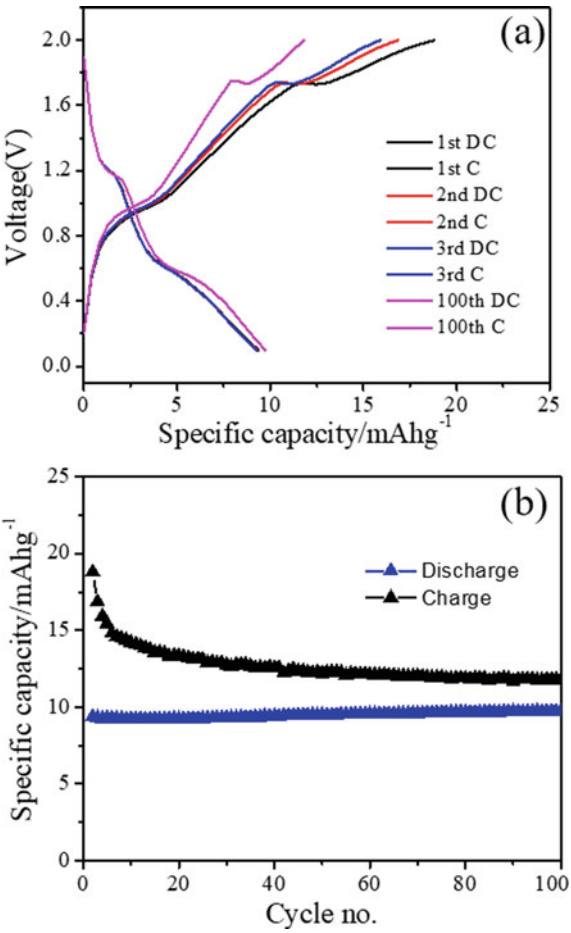

Fig. 5 **a** Galvanostatic charge–discharge curves of graphite–graphite dual-ion battery, **b** variation of charge–discharge capacities with cycle number

Acknowledgements This work is supported by Science and Engineering Research Board, Department of Science and Technology, Government of India (Grant No.: CRG/2018/000263). The authors acknowledge the TEM facility available at SAIF, NEHU Shillong.

References

1. https://www.iea.org/articles/global-co2-emissions-in-2019
2. Dunn B, Kamath H, Tarascon JM (2011) Electrical energy storage for the grid: a battery of choices. Science 334:928–9353
3. Das SK, Mahapatra S, Lahan H (2017) Aluminium-ion batteries: developments and challenges. J Mater Chem A 5:634–6367
4. Sui Y, Liu C, Masse C, Neale Z, Atif M, AlSalhi M, Cao G (2020) Dual-ion batteries: the emerging alternative rechargeable batteries. Energy Storage Mater 25:1–32

5. Rüdor W, Hofmann U (1938) Über Graphitsalze. Zeitshrift Fur Anorg. Und Allg. Chemie 238:1–50
6. Li Y, Lu Y, Adelhelm P, Titirici M-M, Hu Y-S (2019) Intercalation chemistry of graphite: alkali metal ions and beyond. Chem Soc Rev 48:4655–4687
7. Nandi S, Das SK (2019) Realizing a low-cost and sustainable rechargeable aqueous aluminum-metal battery with exfoliated graphite cathode. ACS Sustain Chem Eng 7:19839–19847

Chapter 11
Tar Generation in Open-Top and Closed-Top Downdraft Gasifiers

Adity Bora and Sadhan Mahapatra

Abstract Biomass gasification converts solid fuel to combustible gases along with tar. Tar removal is the major practical challenge for use of gaseous fuel produced in the gasification process in any applications. Gasifier types, operating conditions, and fuel properties have an important role for tar generation. Tar generation is estimated for two types of downdraft gasifiers. The tar concentration decreases with the increase of air mass fluxes in case of an open-top downdraft gasifier. In the case of closed-top gasifiers, tar concentration decreases with the increase of biomass consumption rate. The study observed that higher bed temperature increases the thermal cracking of the pyrolysis products and resulted in lower tar concentration in the output gas. Two-stage air supplies in case of open-top downdraft gasifier resulted in lower tar generation.

Keywords Tar generation · Open-top downdraft · Closed-top downdraft

1 Introduction

Biomass gasification converts solid fuels (biomass, coal, municipal solid wastes, refinery byproducts) to combustible gases called producer gas or synthesis gas (syngas) in presence of gasification medium (air, steam, oxygen, etc.). The gasification technology consists of four simultaneous processes viz., drying, pyrolysis, oxidation, and reduction. Physical moisture present in the biomass evaporates in the drying zone and the rate depends on the prevailing temperature in this zone. In the pyrolysis zone, biomass breaks down in absence of oxygen to condensable volatiles, char, tar, and gaseous products. The products of pyrolysis depend upon temperature, heating rate, residence time, and heat losses. Pyrolysis process takes place in the temperature range of 280–500 °C. The products are complex H, C, and O molecules bonding identified as volatiles. The volatiles are reactive and less strongly bonded in the biomass than the fixed carbon, which is the direct C–C bond. The outputs from

A. Bora · S. Mahapatra (✉)
Department of Energy, Tezpur University, Tezpur 784028, Assam, India
e-mail: sadhan.mahapatra@gmail.com

S. Mahapatra et al. (eds.), *Advances in Energy Technology*, Advances in Sustainability Science and Technology, https://doi.org/10.1007/978-981-15-8700-9_11

this process are tar (liquid, sticky substances) and char. The pyrolysis reaction of the biomass is represented by the following equation.

$$C_nH_mO_p(\text{Biomass}) \xrightarrow{\text{Heat}} \sum_{\text{Liquid}} C_aH_bO_c + \sum_{\text{Gas}} C_xH_yO_z + H_2O + \text{Char} \quad (1)$$

Heat released during oxidation processes breaks down the large complex molecules such as tar into lighter gases due to thermal cracking. Oxidation process takes place in the temperature range of 800–1400 °C. The products of the oxidation process (water, carbon dioxide and un-combusted partially cracked pyrolysis products) pass through a red hot charcoal bed in the reduction zone. The temperature in the reduction zone is normally 800–1000 °C. Lower the reduction zone temperature lower is the calorific value of the gas and higher is the tar generation. Here, one CO_2 molecule is reduced by carbon (red hot char bed) to produce two CO molecules, and H_2O is reduced by carbon to produce H_2 and CO. Producer gas is the key product of biomass gasification which comprises combustible (H_2, CO, CH_4), and non-combustible gases (N_2, CO_2), water vapor, higher hydrocarbon traces, and various contaminants. The producer gas after cleaning and cooling can be utilized in IC engines, gas turbines, or fuel cells for generation of heat and electricity [1].

There are various advantages associated with biomass gasification like abundant and widespread availability of biomass, carbon-neutral, etc. However, during biomass gasification, the feedstock is not completely converted to producer gas but remains as carbonaceous solid residues (char, particulates) and condensable products (tars) [2]. The major challenge toward the commercialization of gasification is the removal of tar from the output gas [1]. This can be optimized by controlling the operating conditions during the gasification process. The biomass properties (particle size, moisture content, ash content, etc.) and gasifier operating condition (temperature, pressure, air mass flux, etc.) have the influence on the quality of producer gas and the gasification performance [3]. Air mass flux and reactor temperature are the most critical parameters that influence the tar generation and output gas composition. Increase in the gasification temperature promotes better thermal cracking in the oxidation zone, which effectively reduces the tar generation in the gasifier. The permissible level of tar depends on the downstream applications such as the requirement is about 50, 5, 1 mg/Nm^3 for gas engines, gas turbines, and fuel cells, respectively [1]. Again, the tar cracking and the consequent tar production depend on the design of the gasifier. It is observed that updraft gasifier produces more tars than fluidized bed and fluidized bed produces more tars than downdrafts [4]. There are two types of downdraft gasification system viz., open-top and closed-top systems. Air comes from the top of the reactor and through the air nozzle in case of open-top gasifier, whereas in case of closed-top gasifier, air inlet is only through the air nozzle. The open-top downdraft reactor with dual stage of air supply from the top and the air nozzles creates an extended combustion zone as compared to the case of closed top, where air enters only through air nozzle. Kinoshita et al. have done experimental studies on tar generation at various temperatures, equivalence ratio, and residence time in a fluidized bed gasifier [5].

The study observed that major species of tar are benzene and naphthalene in all these experiments. Abatzoglou et al. have reported gravimetric and chromatographic methods for tar sampling [6]. The method consists of iso-kinetic probe for sample extraction, filter for particulate collection, water condenser, and cooled solvent to collect the tar present in the output gas. Devi et al. observed that the gasifier operating conditions like reactor temperature, equivalence ratio, and residence time play an important role for tar generation [3]. The study also found that two-stage gasification or secondary air input in the gasifier can reduce tar concentration in the output gas. Nunes et al. observed that with the increase in bed temperature, tar concentration in output gas reduces [7]. The study reported that optimal design and reactor parameters can decrease the tar concentration, but cannot eliminate it completely. Hernández et al. reported that the fuel conversion increases with the smaller fuel particles due to particle external surface area/volume is higher [2]. Phuphuakrat et al. observed that as the equivalence ratio increases, tar generation decreases [8]. The oxidation zone temperature increases with the increase in equivalence ratio, which resulted in reduction in tar generation. Yin et al. reported that the gas yield increases and tar concentration decreases with the increase in particle size [9]. The study also observed that smaller particle size is better for gasification in downdraft gasifier, as smaller particles show better combustion performance than larger size particles. Mahapatra and Dasappa concluded that higher surface area particles had lower pyrolysis time and resulted in higher tar fraction in output gas [10]. It is also observed that double-stage air flow increases the residence time and reduces the tar concentration in output gas. Prando et al. compared different approaches for tar sampling and analysis for an open-top downdraft gasifier [11]. The study concluded that dual fuel entry in the open-top downdraft gasifier exhibits low tar content in the output gas. Tar generation in the gasification process is a matter of great concern in the downstream applications. Tar concentration in output gas is a function of the reactor design, reactor temperature. The present study aims to investigate the tar generation in an open-top and closed-top downdraft gasifiers.

2 Methodology

Bamboo (*Pseudopallida bambusa*) is used as fuel samples for the present experiments. The selection of the biomass is made on the basis of its availability in the nearby location. An open-top downdraft gasifier is used for the experiments. Both the biomass and the gas move in the downward direction in case of downdraft gasifier. Figure 1a presents the open-top downdraft reactor that is used for the experiments. The rated capacity of the gasifier is 4 kg/h. The inner diameter of the reactor is 130 mm and height from the ignition nozzle is 650 mm. Experiments are carried out in the open-top reactor keeping the air nozzle is open. The reactor has a provision of two-stage air supply. The air required for gasification is drawn partially from top of the reactor (first level of air supply) and the remaining through the air nozzle, which is located at the combustion zone (second level of air supply). Air mass flux

Fig. 1 **a** Open-top downdraft gasifier. **b** Closed-top downdraft gasifier

or input air in the gasification process is the most critical parameter for regulating the temperature attained inside the reactor and tar generation. K-type thermocouples are used to measure the reactor temperatures along the reactor length. Charcoal and ash are removed by a manually operated screw provided at the bottom of the gasifier. Bamboo fuel samples of specific size are sun dried for the experimental study. Charcoal bed is maintained above the ignition port of height 150 mm and the rest of the reactor is fed with the bamboo fuel samples. The experiment is conducted for different air flow rate and the reactor temperatures are recorded with the help of Personal Data Acquisition (PDAQ) system.

Figure 1b presents the closed-top downdraft reactor, where air inlet is only through the air nozzles. The rated capacity of the gasifier is 10 kg/h. Experiments are carried out in this closed-top reactor. The experiments are carried out for different biomass consumption rates. The air flow rate and reactor temperatures are not measured due to non-availability of air flow measurement devices or thermocouples arrangement inside the reactor. The air enters through the ignition port located at the oxidation level. In case of a closed-top downdraft gasifier, as air enters only through the air nozzle, flame does not move upward. Temperature profile of this type of reactor lies in narrow band of combustion zone, unlike in case of open-top gasifier, where flame front moves toward top of the reactor.

2.1 Tar Sampling

The tar sampling methodology is followed in accordance with the guidelines and protocols for sampling and analysis of tars and particles in producer gas [10, 11]. It is desired that the temperature profile inside the reactor has nearly become steady before initiating the tar sampling. Tar sampling system consists of a sampling probe, gas bubblers (impinger bottles filled with solvent), vacuum pump followed by a gas flow meter and a burner in the isokinetic setup [10]. The output gas from the reactor exit passed through seven impinges bottles. First, the gas passes through two impinger bottles containing 30 ml water to remove the dust and ash particles carried by the gas. After that, the gas passes through an empty bottle to trap carried over moisture and finally through three impinger bottles which contain 30 ml of solvent. The solvent used in this study is anisole (methoxy benzene). Anisole is selected as a solvent since the evaporation loss during sampling is acceptably low (boiling point of anisole is 153.8 °C). The gas then passes through another empty bottle to collect the droplets of solvent which may have escaped, after which the gas is burned in the swirl burner. The gas is pumped through the system with the help of the vacuum pump and the volumetric flow rate is monitored by a flow meter. The tar sampling is carried out for 1 h duration in each set of experiments. The gravimetric tar mass is estimated by evaporating the solvent at its boiling point. The evaporation process required in these experiments nearly 3 h to completely evaporate the solvent. Gravimetric tar residue is estimated by determining the weight difference of with and without tar content beaker. The particulate matter content is calculated by measuring the weight differences of the paper filter with and without tar content. The gasification parameters used in the present study is the air mass flux for open-top downdraft gasifier and biomass consumption rate for closed-top downdraft gasifier. Air mass flux is the flow rate of air through the unit cross-sectional area of the reactor. The air mass flux is calculated by the equation.

$$\text{Air mass flux} = \frac{A/F}{\frac{A}{F}+1} \times \frac{k\sqrt{H}}{1000 \times A_r} \tag{2}$$

where A/F is the air to fuel ratio, ranging from 1.5 to 1.8, k is the orifice constant with a value of 0.38 in the present experimental setup, H is the difference in water column height (mm), and Ar is the area of the reactor (m^2). However, we were not able to measure the air mass flux in case of closed-top gasifier due to non-availability of the flow measurement devices. Biomass consumption rate at different air flow rate by changing the opening of the valve is considered in case of closed-top gasifier.

3 Results and Discussion

The physical properties of the fuel sample bamboo are measured and presented in Table 1. The proximate and ultimate analysis of the biomass sample is performed at BioTech park, IIT, Guwahati (Instrument: *EuroEA Elemental Analyzer*). Reactor temperature along the length of the reactor is measured in case of the open-top gasifier. Temperature profiles of the reactors are analyzed for various air mass fluxes. Figure 2 presents the temperature profile at an air mass flux of 0.082 kg/m^2-s. The analysis of the temperature profiles attained at various air mass fluxes concludes that with the increase in air mass flux, the temperature inside the reactor increases. The present study considered five different air mass fluxes for tar concentration estimation. Air nozzle is kept open during all the experiments. It is also observed that gas temperature also increases with the increase in air mass flux. This is due to the higher bed temperature at higher air mass flux, enhanced the combustion of volatiles, and accompanied by the oxidation of char. It is observed that the maximum bed temperature of 883 °C occurs at an air mass flux of 0.202 kg/m^{2}s. The influence of higher-level air supply is not only an increase in bed temperature, but also improves the residence time.

Table 2 presents the tar concentration and particulates at various air mass fluxes. It is observed that the tar concentration decreases with the increase in air mass flux. The tar concentration is 343.2 mg/m^3 at an air mass flux of 0.082 kg/m^2-s, which deceases to 92.35 mg/m^3 as the air mass increases to 0.202 kg/m^2-s. Tar content at the reactor outlet is a function of the air mass flux or the bed temperature. The variation of gravimetric tar content with the varying air mass flux is presented in Fig. 3. Figure 3 shows that tar concentration decreases with the increase in air mass flux. This is due to the increase in temperature with the increase in air mass flux that leads to more tar cracking inside the reactor and lesser tar generation at higher air mass flux. A higher temperature can lead to an increase in the degradation of the tars by transforming them to the combustible gases. The Boudouard reaction and thermal cracking effectively degraded the residual char and tar at higher temperature. During the gasification

Table 1 Ultimate and proximate analysis of biomass samples

Proximate analysis, %	
Moisture	12.32 ± 0.6
Fixed carbon	16.85 ± 1.2
Volatiles	68.42 ± 2.3
Ash content	2.41 ± 0.8
Ultimate analysis, %	
Carbon	45.13 ± 2.1
Hydrogen	2.23 ± 0.8
Nitrogen	1.24 ± 0.6
Oxygen	51.4 ± 1.3
Calorific value (MJ/kg)	17.85 ± 1.7

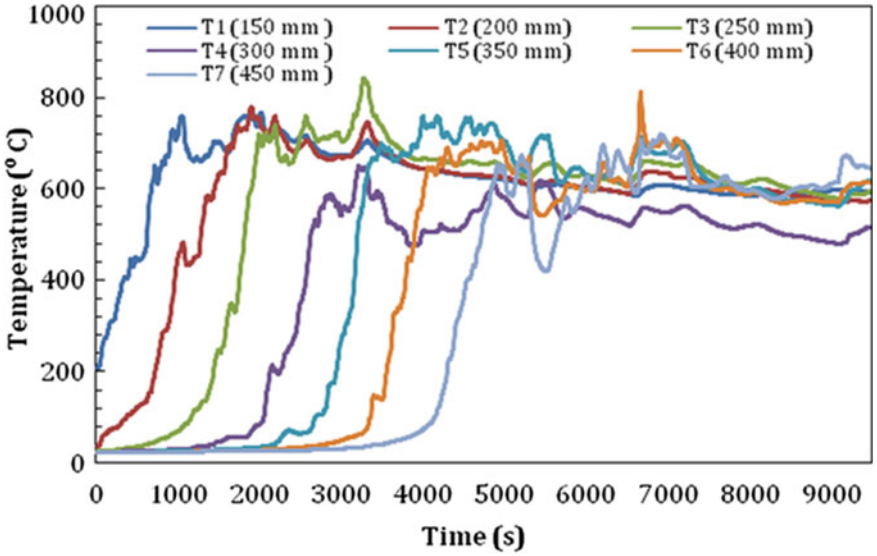

Fig. 2 Temperature profile at 0.0823 kg/m^{2}s air mass flux

Table 2 Tar concentration and particulates for open-top gasifier

Air mass flux (kg/m^{2}s)	Tar (mg/m^3)	Particulates (mg/m^3)
0.082	343.2 ± 21.2	415.9 ± 19.5
0.130	286.5 ± 18.1	291.4 ± 12.3
0.154	226.3 ± 15.6	213.8 ± 21.3
0.184	159.8 ± 14.2	165.6 ± 12.1
0.202	92.4 ± 8.3	101.7 ± 10.4

process of biomass other than tar, particulate matter accompanies the producer gas which is also affected by the air mass flux. As the air nozzle is kept open, secondary air gets injected through the ignition port inside the reactor and a thick oxidation zone is formed inside the reactor. The injection of secondary air helps in improving the temperature profile inside the reactor and resulted in lower tar production. This suggests that the injection of secondary air has considerable effect on reducing the tar content. The elevation of residence time along with higher air mass flux, promotes effective tar decomposition/cracking resulting in lower tar concentration in the output gas. Dual air entry (through the top and the air nozzles) enables the upward movement of the flame front leading to the establishment of a larger heating zone, greatly improving the gas residence time and lower tar concentration.

The tar concentration in a closed-top downdraft gasifier is estimated for different biomass consumption rate. Table 3 presents the tar and particulates for different biomass consumption rate in case of closed-top downdraft gasifier. It is observed

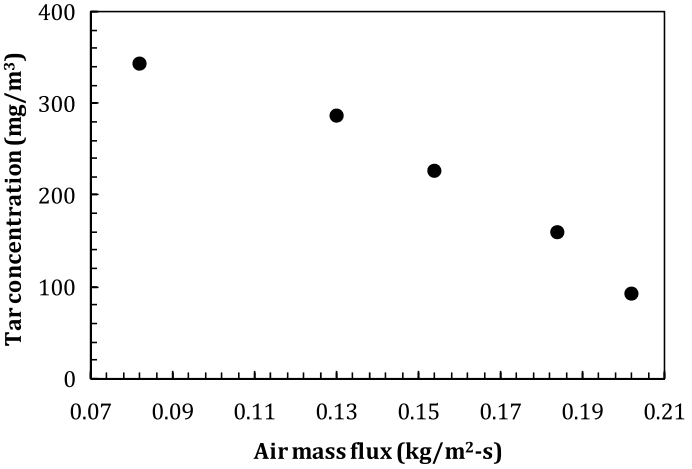

Fig. 3 Tar concentration at different air mass flux

Table 3 Tar concentration and particulates for closed-top gasifier

Biomass consumption (kg/h)	Tar (mg/m^3)	Particulates (mg/m^3)
8	502.3 ± 17.6	635.0 ± 24.5
10	395.0 ± 15.4	436.4 ± 20.9
14	279.5 ± 12.7	219.8 ± 14.6

that with the increase in biomass consumption, tar, and particulate concentration decreases. Biomass consumption increases due to increase in air flow rate in the reactor. Air enters only through the ignition ports present on the reactor in a closed-top downdraft gasifier. Figure 4 presents the tar concentration for different biomass consumption. It is observed that the tar concentration decreases from 502.3 to 279 mg/m^3 as the biomass consumption rate increases from 8 to 14 kg/h. The tar concentration decreases with the increase in biomass consumption rate because biomass consumption rate increases with the increase in air mass flow.

Higher air mass flow increases the biomass consumption, resulting in higher bed temperature. Higher bed temperature leads to an increase in tar degradation and results in lower tar concentration at higher biomass consumption rate. In case of closed-top downdraft gasifier, flame does not move upward unlike open-top downdraft gasifier, as air is available only through air nozzle. In case of closed-top downdraft gasifier, cool zones are created near the air nozzles, where the temperature is not sufficiently higher or thermal cracking of the available tar does not take place. The bed diameter is large and the larger bed diameter causes non-uniform combustion of fuel particles throughout the bed, which is another possible reason for higher tar concentration in this type of gasifier. Tar concentration is higher in closed-top downdraft gasifier compared to open-top gasifier due to the above reasons.

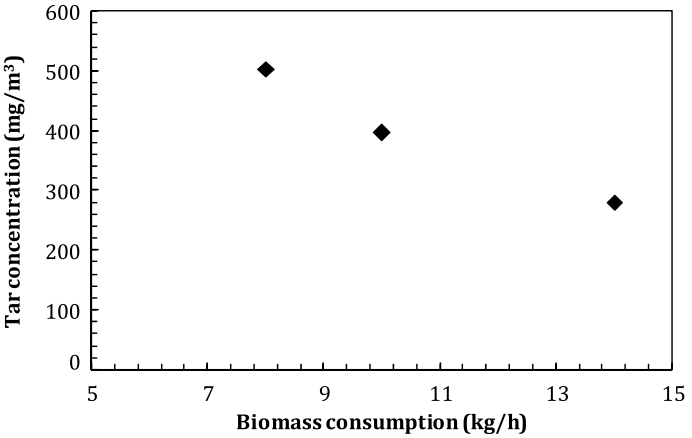

Fig. 4 Tar concentration at different biomass consumption

4 Conclusions

The present study estimates tar generation in an open-top and closed-top downdraft gasifier. The study observed that the gasification temperature and air flow rate has an immense effect on the tar generation. The two-stage air supply in case of open-top downdraft gasifier contributed toward the increase in combustion zone, and resulted in lower tar concentration. Higher bed temperature increases thermal cracking of the pyrolysis products and results in lower tar concentration in the output gas. It is found that air flow is the most important parameter, as it regulates the tar generation in the downdraft gasifiers. The comparison of tar generation between these two types of downdraft gasifier could not be done due to the limitation in measurements of air flow rate or reactor temperatures in case of closed-top downdraft gasifier.

Acknowledgements The authors duly acknowledged the financial support from DST (Grant No. 100/IFD/R/GIA/2686/2013-14), Government of India for the RHEES Project.

References

1. Dasappa S, Paul PJ, Mukunda HS, Rajan NKS, Sridhar G, Sridhar HV (2004) Biomass gasification technology—a route to meet energy needs. Curr Sci 87:908–916
2. Hernández JJ, Ballesteros R, Aranda G (2013) Characterisation of tars from biomass gasification: effect of the operating conditions. Energy 50:333–342
3. Devi L, Ptasinski KJ, Janssen FJJG (2003) A review of the primary measures for tar elimination in biomass gasification processes. Biomass Bioenerg 24(2):125–140
4. Sikarwar VS, Zhao M, Clough P, Yao J, Zhong X, Memon MZ, Shah N, Anthony EJ, Fennell PS (2016) An overview of advances in biomass gasification. Energ Environ Sci 9(10):2939–2977

5. Kinoshita CM, Wang Y, Zhou J (1994) Tar formation under different biomass gasification conditions. J Anal Appl Pyrol 29(2):169–181
6. Abatzoglou N, Barker N, Hasler P, Konef H (2000) The development of a draft protocol for the sampling and analysis of particulate and organic contaminants in the gas from small biomass gasifiers. Biomass Bioenerg 18(1):5–17
7. Nunes SM, Paterson N, Herod AA, Dugwell DR, Kandiyoti R (2008) Tar formation and destruction in a fixed bed reactor simulating downdraft gasification: Optimization of conditions. Energ Fuel 22(3):1955–1964
8. Phuphuakrat T, Nipattummakul N, Namioka T, Kerdsuwan S, Yoshikawa K (2010) Characterization of tar content in the syngas produced in a downdraft type fixed bed gasification system from dried sewage sludge. Fuel 89(9):2278–2284
9. Yin R, Liu R, Wu J, Wu X, Sun C, Wu C (2012) Influence of particle size on performance of a pilot-scale fixed-bed gasification system. Biores Technol 119:15–21
10. Mahapatra S, Dasappa S (2014) Influence of surface area to volume ratio of fuel particles on gasification process in a fixed bed. Energy Sustain Dev 19:122–129
11. Prando D, Ail SS, Chiaramonti D, Baratieri M, Dasappa S (2016) Characterisation of the producer gas from an open top gasifier: assessment of different tar analysis approaches. Fuel 181:566–572

Chapter 12
Morphology of the Alumina Nanoparticles for the Arrangement of the KF Stacked Nano–γ–Al_2O_3 as Catalyst for Conversion of Biomass to Fuel

Nabnit Panigrahi, Ayusman Nayak, and Sruti Ranjan Mishra

Abstract A feasibility investigation, transformation of industrial use micro-alumina (Al_2O_3) of 70 μm size to nano-alumina of 23 nm size was carried out by ball milling for 120 h. Top-down approach for ball milling is adopted for the conversion to nano from micro. Result shows that the average size of one micron is found for every sample. This is may be expected to be agglomeration or coating layer of some foreign material. To eradicate the coating, the process of leaching was adopted, and observed that it is reduced to nm size. Also, during the transesterification process, Mahua biodiesel production from Mahua vegetable oil using heterogeneous catalyst was adopted. The biodiesel obtained by using heterogeneous base catalyst was compared with homogeneous KOH catalyst and the result is about equivalent.

Keywords Nanoparticles · Mahua biodiesel · Heterogeneous catalyst

1 Introduction

Nowadays as biodiesel does not lead to global warming or climate change, so, it becomes popular as eco-friendly fuel. Biodiesel developed from vegetable or animal fats is found functionally identical to fossil fuel. In India, from non-edible vegetable oils are the best option for production of biodiesel source as it does not compete with food. Researchers reported that the biodiesel pollutes much less than regular diesel [1–3]. Generally, biodiesel blends with diesel in different volumetric composition in internal combustion engines [4, 5]. Worldwide, the research demonstrated that biodiesel can run in any diesel engine without any modification with any blend and reduce net CO_2 emission by 77% than common diesel fuel. Biodiesel can be an

N. Panigrahi · A. Nayak
Gandhi Institute for Technology, Gangapada, Bhubaneswar 752054, India

S. R. Mishra (✉)
Gandhi Institute for Education and Technology, Baniatangi, Khordha, Odisha 752060, India
e-mail: sruti76@gmail.com

S. Mahapatra et al. (eds.), *Advances in Energy Technology*, Advances in Sustainability Science and Technology, https://doi.org/10.1007/978-981-15-8700-9_12

effective substitute fuel for diesel engine which will be an influential technology for the upcoming. Many researchers favored 20% blend of biodiesel with diesel fuel in diesel engine without any modifications [4, 6–8].

The composition of biodiesel is monoglyceride derived from non-edible oil like mahua, karanja, neem, Jatropha, Simarouba, etc. The process adopted was the conversion of triglyceride to diglyceride, followed by the conversion of diglyceride tomonoglyceride and glycerol, yielding one methyl ester molecule from each glycerideat every step. Usually, a strong base such as NaOH or KOH acts as catalyst, required to carry out the reaction to convert triglyceride to mono-alkyl ester. The biodiesel is produced through the process known as transesterification. In the conventional method, to distinct and clean the catalyst and the products, a large amount of water was wasted. Our objective is to reduce the cost of production and for the development of an environmentally process, the heterogeneous catalyst is adopted.

A lot of research had also been experimented on preparation of methyl esters using heterogeneous catalyst. Xie et al. reported that for preparing soybean biofuel NaX zeolites encumbered with KOH used as heterogeneous catalyst. The catalytic activity of NaX zeolites toward the transesterification reaction was increased [9]. Xie and Li used alumina-supported iodide as a heterogeneous catalyst for biodiesel production from soybean oil and the result showed that the alumina was loaded with potassium iodide, which prepared the alumina powder by mixing it with an aqueous KI solution and then calculating it at high temperatures in the air to show a high catalytic activity for the reaction of transesterification [10]. Xie et al. used heavy-weight potassium in alumina as a potent additive and concluded that potassium-loaded alumina is a slide-based additive for the transfer of soybean esterified oil with methanol. 35-h infrared with KNO_3 weight, the weight of L2A3, and then 5 h at 773 K was proved to be the highest base and the best infrared for response [11]. Kim et al. were found that the heterogeneous base Na/NaOH/γ–Al_2O_3 catalyst can have approximate same role in the reaction as the NaOH catalyst [12]. Boz et al. researched with 298–338 kg of canola oil and methanol, atm under pressure, and nano-gamma Al_2O_3 treated with FFA. The best load was found at 15 wt. And the maximum alkalinity and uppermost biodiesel conversion were detected at a calcination temperature of 773 K. The conversion was high at 97.7% [13]. The present research has focused on the conversion of 70 μm aluminum to 100 nm in size using a top-down approach and a wet grinding process in ball milling. For the alteration of mahogany vegetable oil to mahogany oil methyl ester, heterogeneous catalysts were prepared with aluminum-filled fluorine catalysts.

Table 12.1 Specification of alumina

Alumina parameter	Specifications
Surface area	7 m^2/gm
Alpha content	90%
Specific gravity	3.935 g/cc
LOI (at 1100 °C)	0.34%
SSA	0.501 m^2/gm
Median dia (D50)	68.308 μm
Al_2O_3	99.58%
Na_2O	0.398%
SiO_2	0.0076%
Fe_2O_3	0.0096%

1.1 Materials and Methods

1.1.1 Nanoparticle Preparation

The alumina was collected from NALCO. The properties of alumina were having high rigidity, exceptional dielectric properties, and virtuous thermal properties which make it for a wide range of applications.

The specification of alumina is stated in Table 12.1.

The report from particle size analyzer showed that the average particle size is 68.03 shown in Fig. 12.1.

Alumina nano-powder was prepared from the available alumina grains of micrometer size. The alumina grains were put in a ball mill grinder and after grinding, the micro-alumina was converted to nano-alumina. The result of the ground sample of 120 h has reached and coming satisfactory. The ball mill used for grinding is shown in Fig. 12.2 and the specification of the ball mill was given in Table 12.2.

The result of 120 h ground materials is given in Fig. 12.3.

The material was ground for 120 h, the jar and ball used were alumina, and the particle size is 1.301 μm. It was observed that about 1 micron was the usual size o fevery particle (sample). This was due to particle accumulation or coating layer of some other substance. For the removal of coating, leaching process was carried out. Removal of aluminum to the highest concentration (20 and 30%) of HCl dust has been completed in Fig. 12.4. After leaching, the average size of sample was 23.1 nm which shown in Fig. 12.5.

1.1.2 Preparation of Heterogeneous Catalyst

Dry alumina of 1.2 g was weighted and placed in a centrifuge tube and 1 mm of distilled water was placed into the centrifuge tube. The mixture was centrifuged for 2 min by balancing the centrifuge cylinder at 1000 rpm and by incorporating a same

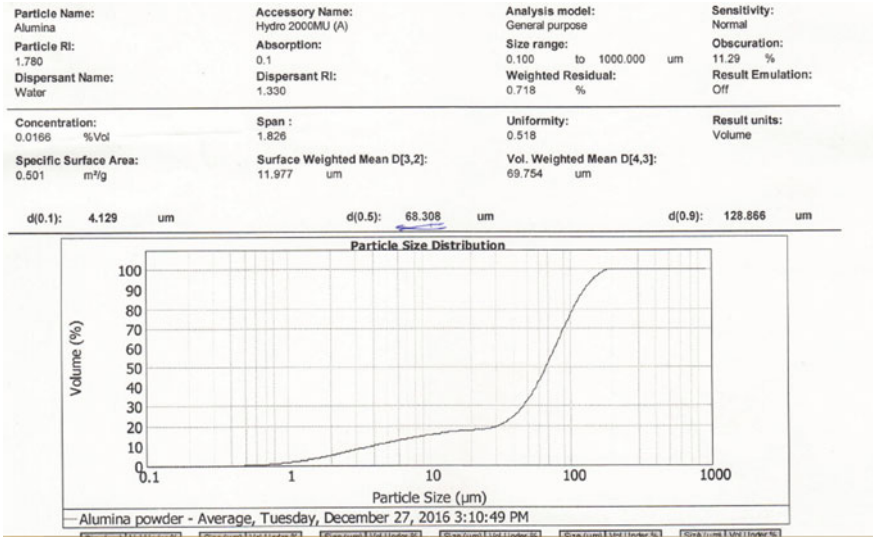

Fig. 12.1 Average particle size of the sample: alpha alumina

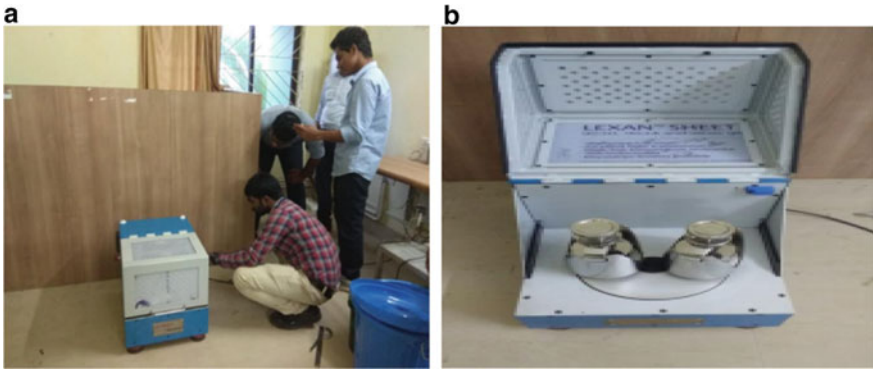

Fig. 12.2 **a** Ball mill grinder setup **b** ball mill grinder jar

mass at the opposite end. After removing the excess water at top of the mixture, the wet alumina was weighted.

An aqueous solution containing 15% concentration of KF was prepared. 4.25 g of nano–γ–Al_2O_3 was placed in a 250 ml flask in an ultrasonic water bath. The prepared KF solution was propelled droplet wise on to nano–γ–Al_2O_3 based on alumina water absorbance capacity.

The nano-size particle permeated with KF was dehydrated in an oven at 373 K for 16 h. Hence, the nanoparticle was calcinated at 773 K at 3 h resulting in KF loaded nano–γ–Al_2O_3.

Table 12.2 Specification of ball mill grinder

Ball mill parameter	Specifications
Make	Insmart system, Hyderabad
Size of the bowl	80 ml each (2 pcs.)
Size of the balls	10, 5, 3, and 1 mm
Material of bowl and ball	Alumina
Rotation speed	450
Run time	1 min
Number of cycle	2
Input size of alumina	60–100 microns
Output size of alumina	Nano-alumina

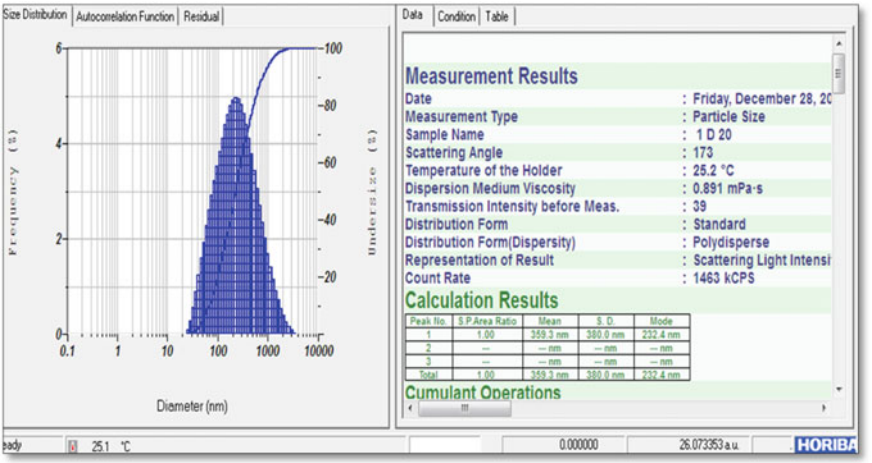

Fig. 12.3 120 h ground materials result

Fig. 12.4 Sample with 30% leaching

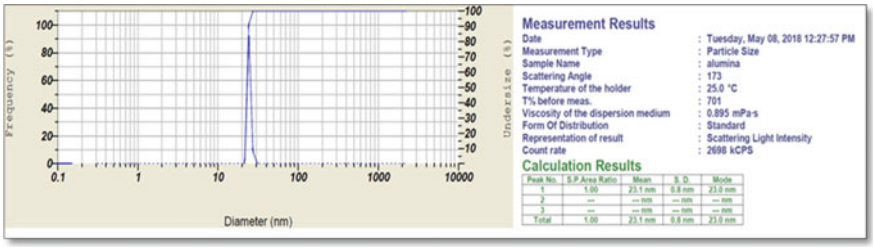

Fig. 12.5 Average size of alumina after leaching

1.1.3 Conversion of Mahua Oil to Mahua Oil Methyl Ester

The transesterification of the pre-treated oil was done using the conventional method. The oil is pre-heated to 65 °C in a magnetic stirrer shown in Fig. 12.6 and a blend of CH_3OH and nano–γ–Al_2O_3 was mixed to the oil. The molar ratio of MeOH to oil was 6:1 and catalyst/oil wt. ratio (1:7% wt.) and response time on the adaptation of the triglyceride to methyl ester was inspected. To separate the liquid and glycerol layer, the transestrified product was permitted to stand 24 h. The upper-layer biodiesel was separated and washed with hot water and hot methanol to eliminate the catalyst, alcohol, and traces of glycerol.

All experiments were performed under atmospheric condition. To remove the moisture and methanol, the washed methyl ester layer is dehydrated at 70 °C under vacuum, and again it is passed over anhydrous Na_2SO_4. The biodiesel obtained from

Fig. 12.6 Magnetic stirrer

Table 12.3 Comparison of biodiesel yield

Catalyst	Calcination temp (K)	Biodiesel yield (%)
KF(15%)/nano–γ–Al_2O_3	773	96
Homogeneous KOH	773	85

Table 12.4 Properties of Mahua biodiesel by using homogeneous catalyst and heterogeneous catalyst

Properties of Mahua biodiesel	Using homogenous catalyst (KOH)	Using heterogeneous catalyst KF(15%)/nano–γ–Al_2O_3
Calorific value (Mj/kg)	39.10	39.00
Density (gm/cc)	0.88	0.88
Free fatty acid	0.23	0.21
Kinematic viscosity (cSt)	4.98	1.87
Flash point (°C)	168	165

the above-mentioned non-edible oil seeds is designated as Mahua oil methyl ester (MOME).

2 Results and Discussion

Biodiesel yield of synthesized catalysts is shown in Table 12.3.

The biodiesel yield increase with heterogeneous catalyst is observed. The various properties of Mahua biodiesel by using homogeneous catalyst and heterogeneous catalyst are shown in Table 12.4.

The above result shows that the biodiesel obtained by heterogeneous catalyst resembles with biodiesel obtained by using homogeneous catalyst.

3 Conclusion

A method to prepare alumina nanoparticle has been established. The biodiesel yield is more in case of heterogeneous catalyst. Esterification method can be eliminated by using heterogeneous catalyst. The properties of Mahua biodiesel by using homogeneous catalyst resembles with using heterogeneous catalyst.

References

1. Raheman H, Gadge SV (2007) Performance of compression ignition engine with mahua (Maducaindica) biodiesel. Fuel 86:2568–2573
2. Panigrahi N, Mohanty MK (2012) Experimental investigation on the performance of NOME fuelled CI engines. Int Rev Mech Eng 6:1586–1592
3. Puhan S, Vedaraman N, Boppana GS et al (2005) Performance and emission studey of Mahua oil (Maducaindica oil) ethyl ester in a 4-stroke natural aspirated direct injection diesel engine. Renew Energy 30:1269–1278
4. Navindgi MC, Dutta M, Kumar BSP (2012) Performance evaluation, emission characteristics and economic analysis of four nonedible straight vegetable oils on a single cylinder CI engine. ARPN J Eng Appl Sci 7(2):173–179
5. Saravanan N, Nagarajan G, Puhan S (2010) Experimental investigation on a DI diesel engine fuelled with Madhuca Indica ester and diesel blend. Biomass Bioenergy 34(6):838–843
6. Agarwal AK (2007) Biofuels (alcohols and biodiesel) applications as fuel for internal combustion engines. Prog Energy Combust Sci 33:233–271
7. Demirbas (2009) Progress and recent trends in biodiesel fuels. Energy Convers Manag 50:14–34
8. Sahoo PK, Das LM, Babu KG, Arora P, Singh VP, Kumar NR, Varyani TS (2009) Comparative evaluation of performance and emission characteristics of Jatropha, Karanja and Polanga based biodiesel as fuel in a tractor engine. Fuel 88:1698–1707
9. Xie W, Huang X, Li H (2007) Soybean oil methy esters preparation using NaX zeolites loaded with KOH as a heterogeneous catalyst. Biores Technol 98:936–939
10. Xie W, Li H (2006) Alumina supported potassium iodide as a heterogeneous catalyst for biodiesel production from soybean oil. J Mol Catal A: Chem 255:1–9
11. Xie W, Peng H, Chen L (2006) Transesterification of soybean oil catalyzed by potassium loaded on alumina as a solid–base catalyst. Appl Catal A 300:67–74
12. Kim HJ, Kang B, Kim M, Park Y, Kim D, Lee J, Lee K (2004) Transesterification of vegetable oil to biodiesel using heterogeneous base catalyst. Catal Today 93–95:315–320
13. Boz N, Degirmenbasi N, Kalyon DM (2009) Conversion of biomass to fuel: transesterification of vegetable oil to biodiesel using KF loaded nano–γ–Al_2O_3 as catalyst. Appl Catal B 89:590–596

Chapter 13
Effect of Fuel Properties on Reaction Front in an Open-Top Downdraft Gasifier

Chandan Kumar and Sadhan Mahapatra

Abstract The effect of biomass physical properties, i.e., particle size, particle density, and moisture content on propagation rate at various air mass fluxes is studied. The biomass fuel samples used in the study are Bamboo (*Bambusoideae*) and Krishnachura (*Delonix regia*). The increase in moisture content decreases the reaction front propagation because the endothermicity of bed increases and peak bed temperature decreases. The peak front propagation rate for Bamboo and Krishnachura is 0.14 mm/s and 0.24 mm/s, respectively. The front propagation rate decreases as the particle size increases for the same operating conditions. The larger particle size leads to incomplete pyrolysis and thus, affects the front propagation and gasification performance. Particle density has an inverse relationship with flame propagation. The result of this study provides an understanding on the effect of biomass physical properties on the front propagation rate.

Keywords Biomass gasification · Propagation rate · Downdraft gasifier

1 Introduction

Gasification is an efficient technology used for the conversion of lignocellulosic biomass into gaseous fuels. The gasification is a heterogeneous reaction process in which solid fuel reacts with sub-stoichiometric amount of oxidizer present inside the gasifier and generates producer gas along with some amount of tar. Different types of gasifier viz., updraft, downdraft, fluidized bed, etc., have been developed over a period of time and classified on the basis of fuel feeding, gas extraction direction, and behavior of oxidizer. The downdraft gasifier is the simplest type of gasifier, widely used because of low tar generation, ease of operation, and lower maintenance cost. The performance of gasifier, i.e., composition of the output gas and amount of tar generation is influenced by the physical properties of the fuel and the amount of oxidizer [1].

C. Kumar · S. Mahapatra (✉)
Department of Energy, Tezpur University, Tezpur, Assam 784028, India
e-mail: sadhan.mahapatra@gmail.com

S. Mahapatra et al. (eds.), *Advances in Energy Technology*, Advances in Sustainability Science and Technology, https://doi.org/10.1007/978-981-15-8700-9_13

Mahapatra and Dasappa investigated the effects of air mass flux and moisture content of the biomass on reaction front propagation in a packed bed gasifier [2]. The result shows that with the increase in air mass flux, propagation rate increases, attains a peak and with further increase in air mass flux, the propagation rate decreases. It is also reported that with the increase in the moisture content of biomass, propagation rate decreases. This decrease in propagation rate with the increase in moisture content is because of the increase in endothermicity of the gasifer, i.e., reduces the heat transfer rate between the fuel particles [2]. Porteiro et al. measured the ignition front propagation for different biomasses [3]. The result shows that with the increase in air flow rate, ignition mass flux increases and after attaining a peak, it reduces. The effect of excess air shows a quenched flame, whereas with the increase in moisture content the ignition front decreases [4]. Tinaut et al. reported that biomass particle size has no effect on the bed temperature, but the bed temperature increases with the increase in airflow [4]. The increase in airflow means increasing the turbulence and it increases the diffusion rate and due to this, the bed temperature increases. The flame propagation characteristic inside the gasifier is an important parameter which needs to consider in designing the gasifier [5]. In the present study, experimental investigations have been carried out to study the effect of particle size, moisture content, and particle density for two different types of biomass on the reaction front in an open-top downdraft gasifier. The present study will be helpful for designing a downdraft gasifier based on multi-fuel and to enhance the gasifier performance.

2 Experimental Procedure

An open-top downdraft gasifier is used for the experiment and the schematic diagram of the experimental setup is shown in Fig. 13.1. The inside reactor diameter is 130 mm and the height of the reactor above the ignition nozzle is 600 mm. The flame propagation rate is measured for various air mass fluxes. The temperatures along the length of the reactors are measured using K-type thermocouples at different heights of the reactor for a set of experiment. The flame front propagation rate is estimated by using the following relation.

$$R_{\mathrm{FP}} = \frac{\Delta x}{\Delta t}$$

where R_{FP} is the flame front propagation rate, Δx is the distance between two adjacent thermocouples, and Δt is the time required to reach the reference temperature between two consecutive thermocouples attached at different heights of the reactor. The reference temperature used for the calculation of the reaction front propagation rate is 500 °C [2].The bed movement is measured through topping up method at a regular time interval of 10 min. The output gas from the gasifier is cleaned through a two-stage water spray system and after that, cooled in a chiller. The gas flow rate is measured through a calibrated orifice plate.

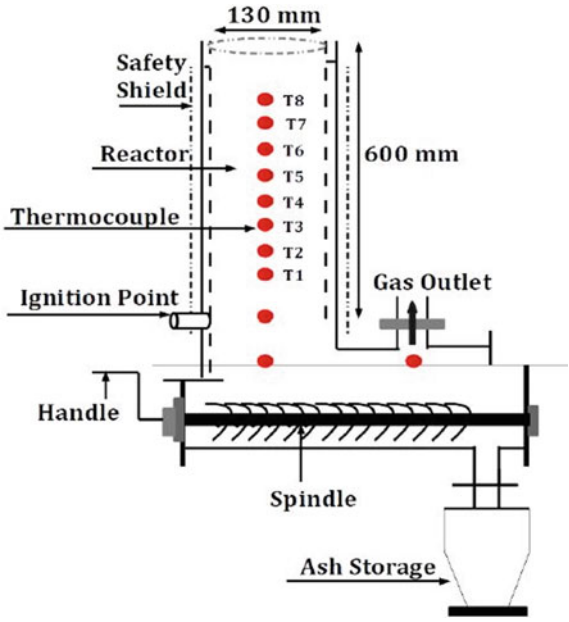

Fig. 13.1 Reactor configuration of the open-top downdraft gasifier

Charcoal is filled into the reactor up to 100 mm above the height of the ignition nozzle and rest of the reactor is filled with biomass fuel samples of specific sizes. Ignition is done through ignition nozzle and once the charcoal started burning, ignition nozzle is closed during the experiment. The complete amount of required air for the gasification process comes from the reactor top. The ignition front tends to move upward opposite to the bed movement as the air is coming only from top of the reactor. Bamboo and Krishnachura are used as biomass fuel samples. Two different moisture content biomass fuel samples (bone-dry and 10% moisture) are used in the experiments. The fuel sample shape is cuboid and having dimensions 12 × 8 × 6, 18 × 8 × 6, and 24 × 8 × 6 mm. The ultimate and proximate analysis of the biomass fuel samples are shown in Table 13.1. The bed density for different sizes of bamboo samples at bone-dry condition is presented in Table 13.2.

3 Results and Discussion

A typical temperature profile inside the reactor at a particular air mass flux is presented in Fig. 13.2. The reactor front propagation rate is estimated from the temperature profiles at various air mass fluxes. The bed movement is movement of bed per unit time in the downward direction due to fuel consumption. Biomass consumption is the fuel consumption per unit time during the gasification process. The effective propagation is the summation of flame front movement which is in the upward

Table 13.1 Ultimate and proximate analysis of biomass samples

Parameters	Bamboo (%)	Krishnachura (%)
Proximate analysis		
Moisture	12.32	9.20
Fixed carbon	16.85	12.77
Volatiles	68.42	72.82
Ash content	2.41	5.21
Ultimate analysis		
Carbon	45.13	47.63
Hydrogen	2.23	6.16
Nitrogen	1.24	1.89
Oxygen	51.40	44.32

Table 13.2 Bed density for different bamboo particles

Particle size (mm)	Equivalent diameter (mm)	Surface area/volume (mm^{-1})	Bed density (kg/m^3)
$12 \times 8 \times 6$	10.32	0.75	410 ± 12
$18 \times 8 \times 6$	11.80	0.69	355 ± 16
$24 \times 8 \times 6$	13.00	0.67	315 ± 11

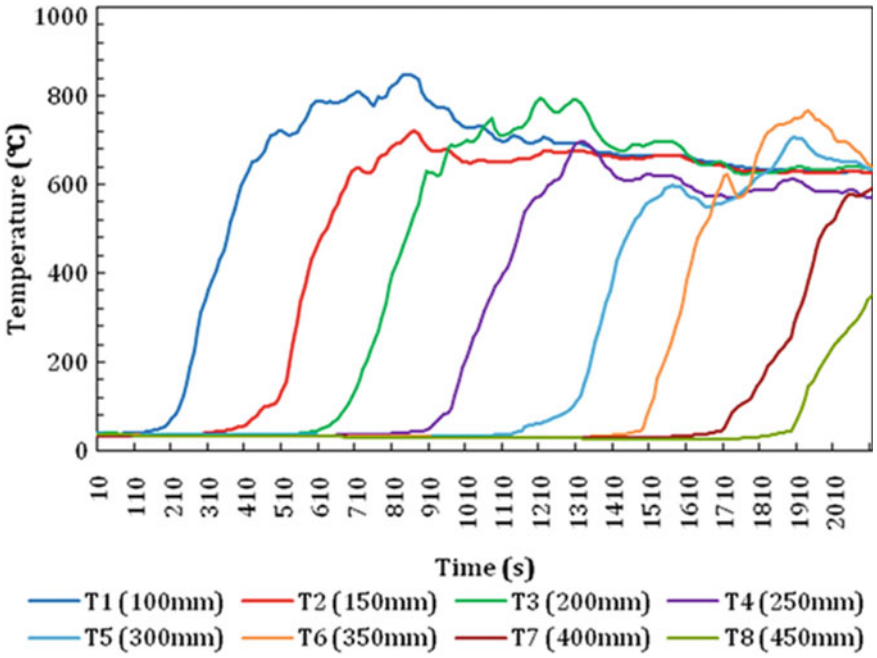

Fig. 13.2 Temperature profile along the reactor length

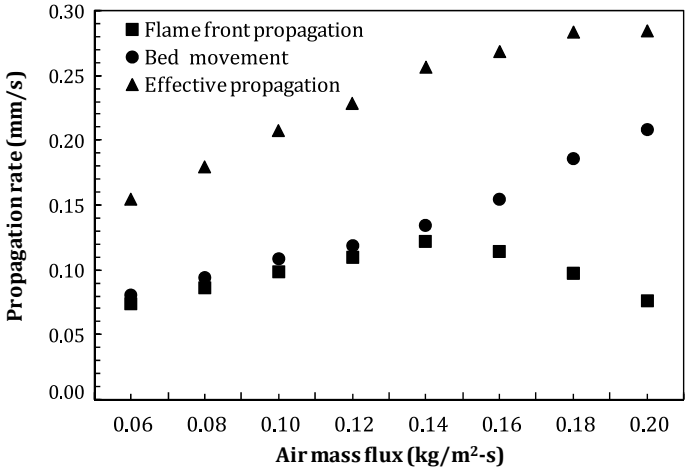

Fig. 13.3 Flame front, bed movement, and effective propagation for bone-dry bamboo

direction and bed movement which is in the downward direction in a downdraft gasifier.

Figure 13.3 presents the flame front propagation, bed movement, and effective propagation for bone-dry fuel sample at various air mass fluxes. The flame front propagation initially increases with the increase in air mass flux, attains a peak and then with further increase in air mass flux, front propagation decreases. This result is very similar to that found by different studies related to propagation rate [2–4]. As the air supply increases in the reactor, it carries away more heat from the bed compared to the heat generation, and thus, at higher air mass flux, the reaction front decreases. The bed movement depends on the biomass consumption. The biomass consumption increases with the increase of air mass flux. Hence, the bed movement linearly increases with the increase in air mass flux. The effective propagation rate also increases with the increase of air mass flux. The effective propagation rate is found very similar to the result presented by Horttanainen et al. [6].

3.1 Effects of Moisture

Figure 13.4 presents the front propagation for bone-dry and 10% moisture content bamboo fuel sample with particle size of 12 × 8 × 6 mm. The flame front propagation rate is found to be higher for bone-dry fuel samples. The peak propagation rate obtained is 0.14 and 0.10 mm/s for bone-dry and 10% moisture content bamboo samples. This is due to the particles containing higher moisture content need more energy in drying and that leads to decrease in the propagation rate. The bed contains higher moisture content absorbs more heat and this decrease in flame propagation and also the bed temperature. The combustion depends on the surrounding environment

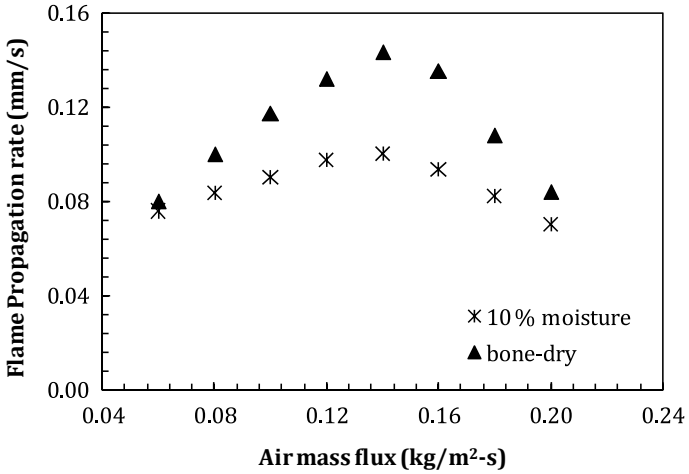

Fig. 13.4 Flame front propagation for various moisture contents in bamboo samples

and change in moisture content in bed increases the endothermicity of bed and thus lower the propagation rate. The effective propagation increases with the increase in air mass flux. The effective propagation for bone-dry and 10% moisture content fuel samples are 0.34 mm/s and 0.26 mm/s, respectively, at an air mass flux of 0.20 kg/m^2 s. There is a decrease in effective propagation by 23% and peak reaction front decrease by 29.5% due to increase in 10% moisture content.

3.2 Effects of Particle Size

Figure 13.5 shows the effect of particle size on the flame front propagation rate. It is observed that flame front propagation rate decreases with the increase in particle size of the fuel samples. The decrease in flame front propagation rate is due to a decrease in available surface area of the fuel samples for combustion and increase in bed density which restricts the air flow through the bed. Bed porosity also affect the propagation rate, higher porosity means lower heat transfer coefficient. It can be concluded that packing factor of the bed also effects the front propagation. The maximum propagation rate for 12 × 8 × 6 mm and 24 × 8 × 6 mm particle sizes are 0.14 mm/s and 0.12 mm/s, respectively. The peak reaction front decreases by 15% with the increase in 26% in equivalent diameter of the fuel particle. The effective propagation also decreases for the higher size particles. It is due to the exposed surface area per unit volume for is higher for 12 × 8 × 6 mm particle size compare to 24 × 8 × 6 mm particle size. The heat diffusion time is higher for the larger particle size and thus, reaction front propagation rate reduces. The inter-particle heat transfer rate is also lower in larger size particles than smaller particles. It is found

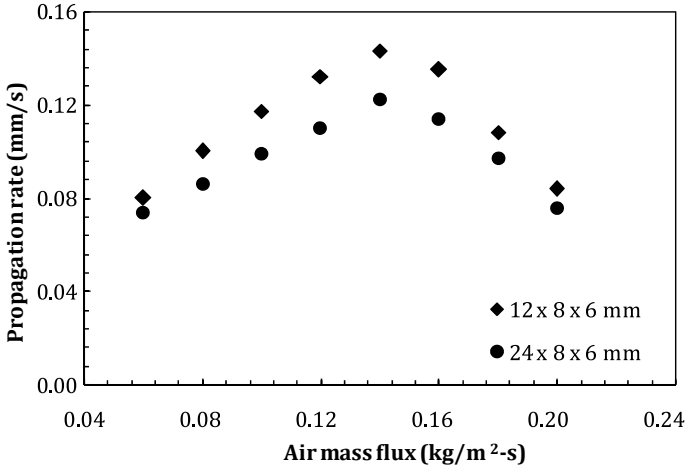

Fig. 13.5 Propagation rate for various particle size

that for larger particle, there is a chance of incomplete pyrolysis and this leads to an increase in the concentration of tar in output gas.

3.3 Effects of Particle Density

Figure 13.6 represents the effect of fuel particle density on propagation rate. It is found that the front propagation is higher for lower density biomass sample. The

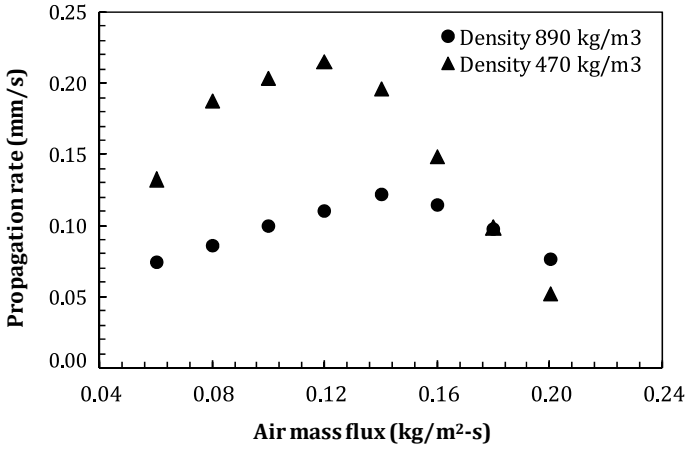

Fig. 13.6 Propagation rate for various biomass density

rate of devolatilization depends on the particle density of solid fuel. The particle density directly relates to the porosity, less dense particles are more porous in nature. The heat diffusion into the core of the fuel depends on the porosity of fuel particle. Higher heat diffusion with oxidiser to the core of the particle resulted in a reduction in burning time. Moreover, the higher density fuel particles have lower heat diffusion rate and hence the propagation rate decreases. Again, higher density particle has more thermal inertia, so it requires more energy for thermal decomposition of the particle. The peak propagation rate for krishnachura with density 470 kg/m^3 is 0.22 mm/s at air mass flux of 0.12 kg/m^2 s. In case of bamboo with particle density of 890 kg/m^3, it is 0.12 mm/s at an air mass flux 0.14 kg/m^2 s. The peak reaction front propagation for Krishnachura occurs at lower air mass flux compare to bamboo. This might happened due to higher devolatilization rate, lower thermal inertia for krishnachura compared to bamboo.

4 Conclusions

The present study shows that the reaction front increases with the increase in air mass flux attain a peak and with further increase in air mass flux reaction front decreases. The reaction front propagation is higher for bone-dry than 10% moisture content biomass. Smaller particle size fuel samples have higher propagation rate compared with the larger size fuel particles. The reaction front is higher for lower density biomass than the higher density biomass fuel samples. The peak propagation rate obtained for lower density biomass at lower air mass flux than the higher particle density fuel samples. The peak bed temperature difference is higher between bone-dry and 10% moisture content at lower air mass flux. However, this difference in peak temperature decreases at higher air mass flux. This experimental investigation provides a clear understanding on the effect of fuel samples physical properties on the reaction front propagation.

Acknowledgements The authors duly acknowledged the financial support from DST (Grant No. 100/IFD/R/GIA/2686/2013-14), Government of India for the RHEES Project.

References

1. Buragohain B, Mahanta P, Moholkar VS (2010) Biomass gasification for decentralized power generation: the Indian perspective. Renew Sust Energ Rev 14(1):73–92
2. Mahapatra S, Dasappa S (2014) Experiments and analysis of propagation front under gasification regimes in a packed bed. Fuel Process Technol 121:83–90
3. Porteiro J, Patino D, Collazo J, Granada E, Moran J, Miguez JL (2010) Experimental analysis of the ignition front propagation of several biomass fuels in a fixed-bed combustor. Fuel 89(1):26–35

4. Tinaut FV, Melgar A, Perez JF, Horrillo A (2008) Effect of biomass particle size and air superficial velocity on the gasification process in a downdraft fixed bed gasifier: an experimental and modeling study. Fuel Process Technol 89(11):1076–1089
5. Yin R, Liu R, Wu J, Wu X, Sun C, Wu C (2012) Influence of particle size on performance of a pilot-scale fixed-bed gasification system. Bioresour Technol 119:15–21
6. Horttanainen M, Saastamoinen J, Sarkomaa P (2000) Ignition front propagation in packed beds of wood particles. IFRF Combust J (Article number 200003).

Chapter 14
Power Extraction from Several Interconnecting Solar PV Networks for an Electrically Integrated TEG System Under Weather Fluctuation

Sasmita Jena, Sambit Tripathy, Keshav Krishna, and Sanjeeb Kumar Kar

Abstract With the extensive demand for energy harvesting systems from various renewable resources, researches have been carried out in several areas among which thermoelectric generator (TEG)-based system is an emerging one. In this paper, eight solar PV modules are interconnected in numerous fashions in order to investigate the behavior of the hybrid system. The transiency of the solar PV modules inside the network has been examined under healthy irradiance and sectional irradiance. Rise in solar concentration tends to decrease the solar PV module efficiency, and this curse to solar PV becomes the boon to the TEG giving rise to higher power output at the terminals. Incorporation of solar photovoltaic (SPV) and thermoelectric (TE), termed as Solar photovoltaic-thermoelectric (SPV-TE) hybrid system is found be a very promising technique to broadening the utilization of solar spectrum and enhancing the power output effectively-cum-efficiently. This hybrid architecture caters electrical energy with additional thermal energy that signifies upon harnessing of solar insolation in an exceptional way.

Keywords Hybrid system (SPV+TEG) · Thermoelectric generator · Operating temperature · PV networking · Power generation

1 Introduction

Lower quantum efficiency is found to be a major demerit of solar photovoltaic cells in these days. Though only a smaller portion of incident radiation is converted into electricity directly, efficiency is found to be a crucial factor to be improved, so that the popularity will be gained for solar photovoltaic cells [1, 2]. Further the non-convertible radiations will heat the panels that reduce the efficiency. Hence, at present, cooling systems have been integrated, so that the temperature could be decreased to a greater extent and enhancing efficiency of the solar panels. Therefore, realization

S. Jena (✉) · S. Tripathy · K. Krishna · S. K. Kar
Department of Electrical Engineering ITER, Siksha O Anusandhan Deemed To Be University, Bhubaneswar, Odisha, India
e-mail: sasmita.jena500@gmail.com

S. Mahapatra et al. (eds.), *Advances in Energy Technology*, Advances in Sustainability Science and Technology, https://doi.org/10.1007/978-981-15-8700-9_14

of photovoltaic-thermoelectric systems comes into picture [3]. Direct conversion of sun light into electrical energy is an effective-cum-efficient way in this renewable era. Furthermore, some significant part has been absorbed as heat; to get rid of this some of the heat recovery system has been proposed in combination of conventional solar photovoltaic cells. Thus, TEG has come into picture, so that the non-convertible radiation which is dissipated as heat can be further converted to electrical energy. Researches have been going on such hybrid system for gaining popularity upon the renewable-based generation system [4]. The concept of solar energy spectrum energy utilization by a solar PV-thermoelectric module and finding of an optimized geometry for SPV-TE based hybrid systems has been outlined. Current SPV-TE module-based hybrid systems are mostly based upon dye-sensitized solar cells(DSSC), a Si-based solar cells for the solar PV part while Bi–Te modules for the thermoelectric part. Also maximum power point tracking plays a vital role in all solar PV based systems. Such combination-based systems are generally relying upon absorption of light spectrum by solar cells and secondly on the optimum operating temperature of the TE modules [5]. Many researchers are also working upon Perovskite solar cells which are found to be reasonable choice for SPV-TEG based hybrid system. It has been found that the temperature coefficient of the Perovskite solar cells is lower than 2%, and this is found to be advantageous for Perovskite solar cells-TE based systems. There is nearly about 1% difference in Perovskite solar cell-TE based system (18.8%) and only Perovskite solar cells (17.9%). Also by altering the thermal concentration, the volume of thermoelectric material can be lowered, and at the same time, cost will be cut off remarkably. For analyzing such influence of thermal concentration upon the desired hybrid system, a 3D numerical model has been also developed [6].

In this paper, the solar PV modules are connected in parallel in order to form an array which is helpful in system requiring higher amount of power. In this paper, eight modules are connected in several manners in order to analyze and predict the system performance. The array thus formed by the SPV modules is connected with TEG in order to produce power. Solar panels receive solar irradiance to generate power which can be termed as conversion of light energy into electrical energy. But the demerit lies upon the heat lost at the panel surface which causes rise in surface temperature. This in turn declines the solar PV performance at a greater rate, and panel suffers from lower quantum efficiency. Thus, the TEGs use this lost heat and converts this heat energy into electricity. Hence, the power generated using solar irradiance and power generated by using the excess heat of panel gives a significant output at the solar panel terminals. This system also aims to provide another perspective of understanding the volatility of SPV-TEG hybrid module under partly cloudy conditions. The system is tested for single SPV module integrated with TEG and then tested upon five different types of SPV networking structure with integrated TEG. The entire study has been carried out using eight solar PV modules with networking namely:

- Network-I
- Network-II

The entire study is subjected to be tested under two types of irradiance namely:

- Healthy irradiance (HI)
- Sectional irradiance (SI).

Though daily solar insolation which is an inevitable part of solar energy to generate power is very reliant to time, factually it has impact upon the temperature of SPV-TEG hybrid system, consequently the power generation and hence the efficiency of the system. Therefore, light has been put upon the implication of changing weather condition on the system performance and power generation. This sectional irradiance (SI) is further subdivided into two parts such as:

- 3/4th (75% shaded)
- Fully shaded (100% shaded).

The paper organization is as follows. In Sect. 2, the hybrid PV-TEG system is modeled, and hence, the theoretical approach is outlined. Sect. 3 is followed with the interconnection of solar PV panels with TEG integration. Section 4 consists of power generation from the hybrid interconnection.

2 System Modeling and Description

The modeling of thermoelectric generator (TEG) and solar PV modules (SPV) have been performed by insertion of corresponding number of modules in parallel and series as per the requirement. After being designed individually, both the systems have been combined in order to perform the study upon the hybrid system. The power generated from SPV array, i.e., conversion of light energy into electrical energy, and power generated from TEG, i.e., conversion of lost heat into electrical energy, is added in order to obtain the required power from the hybridized SPV-TEG system. Generally, inconstancy nature of weather specifically partly cloudy condition plays a vital role on the system's cohesion and hence marking critical issues like power generation, efficiency, etc. The model is described in individual subsection namely:

- Modeling of solar PV array
- Modeling of TEG

2.1 Modeling of Solar PV Array

Solar irradiation and temperature on the solar PV module surface are solely responsible for the characteristics of SPV array. As the solar irradiance upon the SPV array is increased, the power generated from SPV array is also increased. In order to construct an SPV array, number of SPV modules need to combine in particular fashion either in series or parallel to obtain the requisite power. The equivalent circuit of the solar cell is shown in Fig. 1.

The output current of the solar PV module, i.e., I_{pv}

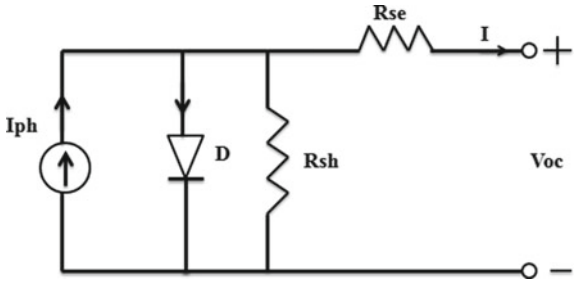

Fig. 1 Equivalent circuit of solar PV module

Table 1 Specification of solar PV module used (WAREE solar PV modules)

Parameters	Values
Maximum power voltage	17.47 V
Maximum power current	2.86 A
Maximum power	50 W
Short-circuit current (I_{sc})	3.1 A
Open circuit voltage (V_{oc})	21.57 V

$$I_{pv} = N_p * I_{ph} - N_p * I_o \left[\exp\left\{ \frac{q * \left(V_{pv} + I_{pv} Rs\right)}{N_s A_{kt}} \right\} - 1 \right] - I_{sh} \qquad (1)$$

where k = Boltzmann's constant = $1.3805 * 10^{-5}$ J/K, A = ideality factor of the solar PV cell depend on PV manufacturing technology, and some of them are presented in Table 1, T = operating temperature of the module, $q = 1.6 * 10^{-19}$ C.

2.2 Modeling of Thermoelectric Generator

The working of TEG constitutes of three elementary thermoelectric effects with two accessorial effects. The three elementary effects are named as: Seebeck effect, Peltier effect, and Thomson effect, while the accessorial effect can be named as: Joule effect and Fourier effect. Seebeck effect is responsible for electromotive force (EMF); and Peltier heat, Thomson heat, and Joule heat are caused by the effect of Peltier, Thomson, and Joule, respectively. As a matter of fact, Peltier effect is not an interface effect; it produces heat only at the end sides of the semiconductors. Volumetric effects like Thomson and Joule heat production are pretended to be uniformly transferred to the cold and hot junctions of the semiconductor elements. Though Thomson effect is very small, it is often neglected in many cases.

For steady-state analysis at cold and hot junction of TEG, an energy balance equation is used which can be expressed as follows:

Mathematically'

$$Q_h = \propto * T_h * I - k_{tc}\Delta T - 0.51^2 R \tag{2}$$

$$Q_c = \propto * T_c * I - k_{tc}\Delta T + 0.5 I^2 R$$

The electrical current can be expressed as follows:

$$I = \frac{\propto \Delta T}{(1+n)R} \tag{3}$$

The short-circuit current is the maximum current at a load voltage of zero, i.e., $V_L = 0$, and hence, can be written as follows:

$$I_{SC} = 2I_m = \frac{2W_m}{V_m} \tag{4}$$

Finally, the voltage of TEG can be expressed by using Ohm's Law, and the corresponding equation obtaining short-circuit current and current through TEG, i.e.,

$$V = -R(I - I_{SC}) \tag{5}$$

A model of TEM specified by TEPI-12656–0.6 has been used over here to model the hybrid system, and the behavioral analysis has been conducted. The parameter specifications of the thermoelectric module (TEM) have been listed in Table 2. The constraints that have been considered for modeling are presented in Table 3.

Table 2 Parameters for thermoelectric generator

Parameters	Values
Open circuit voltage (V)	8.8
Cold junction temperature (°C)	30
Hot junction temperature (°C)	300
Load resistance (Ω)	1.25
Load output voltage (V)	4.27
Load output power (W)	15
Load output current (A)	3.52
Heat flow density (W/cm^2)	~ 12
Heat flow across the module (W)	~ 370

Table 3 Thermal parameters specification

Parameters	Symbols	Corresponding values
Seebeck coefficient	$\propto$	0.035 V/K
Resistance	Ω	1.22
Thermal conductivity	k_{tc}	20.91 W/K
Figure of merit	Z	$0.387 * 10^{-6} K^{-1}$

3 Results and Discussion

The solar PV panel receives solar irradiation and generates electricity directly through the photovoltaic effect. Though solar panel is considered as less quantum efficient due to excess heat absorption at the surface, the heat recovered from the module surface is considered to be reused and generate power. Thence, thermoelectric generator comes into picture that effectively as well as efficiently use this lost heat and produce electricity. The solar PV modules and the TEG combined deliver substantial amount of power. This makes the solar PV modules much more efficient-cum-effective. The system is tested under two types of irradiance namely:

- Healthy irradiance (HI)
- Sectional irradiance (SI)

The HI shows the system receiving sunlight at standard testing condition (STC), i.e., at 1000 W/m^2, and the modules receiving solar irradiance generate power, and subsequently the heat absorbed by the modules is further reused by the TEG that are connected in parallel. The system is tested for only solar PV based, only TEG based, and both SPV-TEG based sources in order to verify the results. All the connections have been subjected to be tested under sectional irradiance (partly cloudy condition). The following types of sectional irradiance (SI) are considered over here. (Figs. 2 and 3).

- 3/4th (50% shaded) and
- Fully shaded (100% shaded).

3.1 Type-I Network: Table 4

Healthy irradiance (HI) means system performance during non-shading condition. During the experiment, the irradiance varies from 900–1000 W/m^2; that is why the theoretical analysis is also done at 1000 W/m^2 in MATLAB/Simulink. The power obtained from hybrid SPV and TEG system is much significant than that of only SPV based or only TEG based system which can be seen in Fig. 4. The result for every subconditions of SI is shown in Figs. 5, 6, 7, 8. It can be interpreted from the graph that every time shading occurs, power is decreasing gradually. It can also be seen that the power obtained from SPV and TEG based hybrid system is always

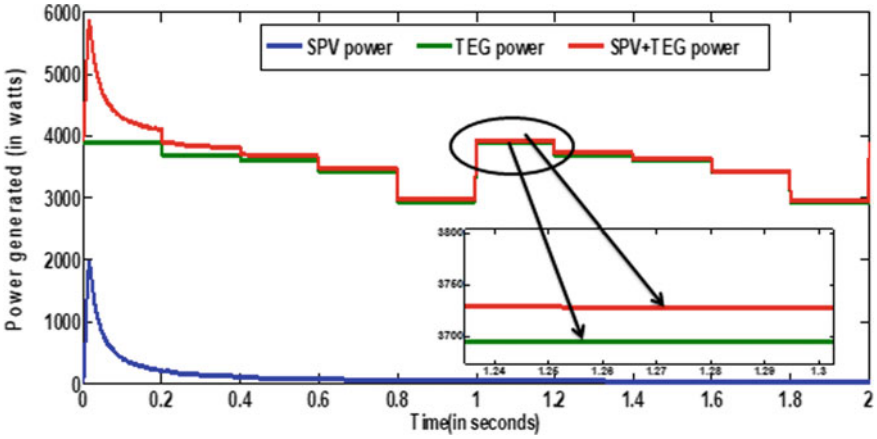

Fig. 2 Power obtained using Type-I network at healthy irradiance (HI)

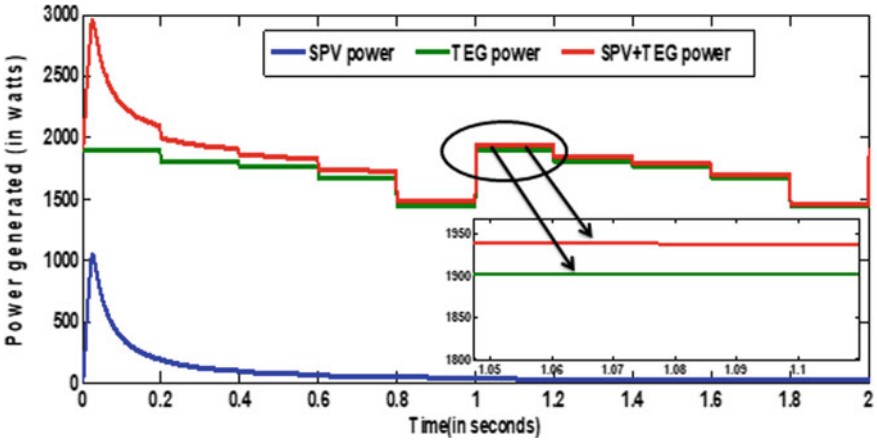

Fig. 3 Power obtained due to sectional irradiance (SI)-3/4th of shading

very significant than that of only SPV based system and only TEG based system, no matter what type of shading occurs.

3.2 Type-II Network: Table 5

The connection diagrams have been shown with values that are obtained experimentally and theoretically that can be seen in Table 5. The modeling has done by using MATLAB/Simulink, and the experiment has been carried out at the rooftop of ITER, Siksha O Anusandhan (Deemed to be university).

Table 4 Type 1 network

Type of connection	Connection diagram	Output values obtained	
At healthy irradiance (non-shading condition)	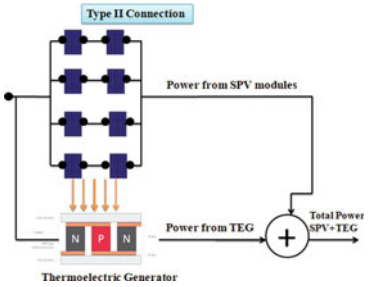	Experimental 1. Only SPV 20.54 W 2. Only TEG 3881 W 3. SPV + TEG 3901.4 W	Theoretical 1. Only SPV 20.72 W 2. OnlyTEG 3886 W 3. SPV + TEG 3907 W
At sectional irradiance 3/4th section (75% shading)	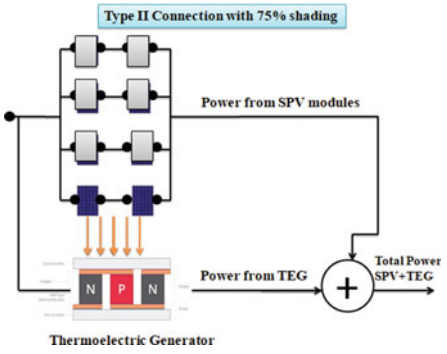	Experimental 1.Only SPV 18.85 W 2. Only TEG 1897.57 W 3.SPV + TEG 1916.42 W	Theoretical 1. Only SPV 19.15 W 2. OnlyTEG 1902 W 3. SPV + TEG 21921W
At sectional irradiance Whole section (100% shaded)	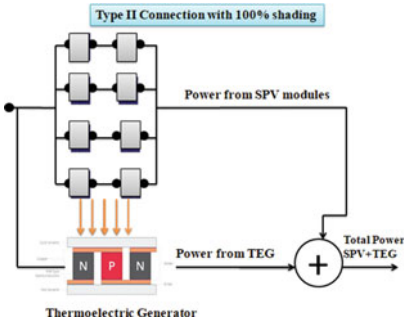	Experimental 1. Only SPV 17.77 W 2. Only TEG 1556.77 W 3. SPV + TEG 1574.54 W	Theoretical 1. Only SPV 18.32 W 2. Only TEG 1571 W 3. SPV + TEG 1590 W

It can be interpreted from the graph that every time shading occurs, power is decreasing gradually. It can also be seen that the power obtained from SPV and TEG based hybrid system is always very significant than that of only SPV based system and only TEG based system, no matter what type of shading occurs. It can also be outlined that the TEGs work according to the sun light incident on the SPV modules. During HI, the solar irradiance has incident on panel that in turn raising the temperature of the SPV module surface, and hence, yields a significant amount

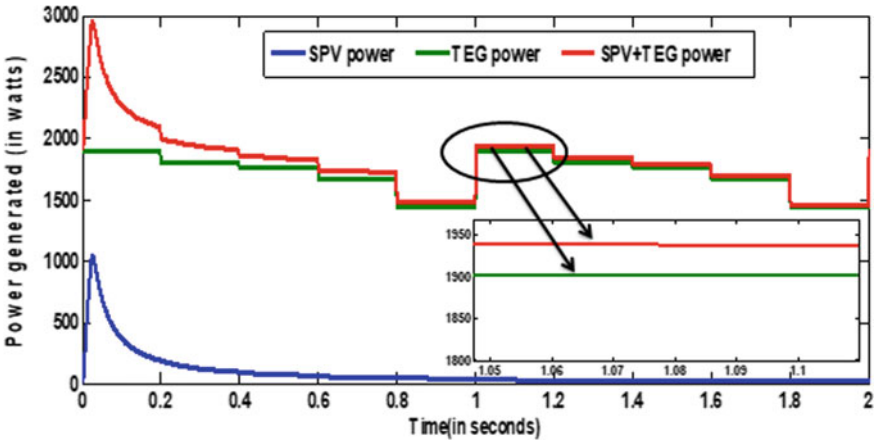

Fig. 4 Power obtained due to sectional irradiance (SI) 100% of shading

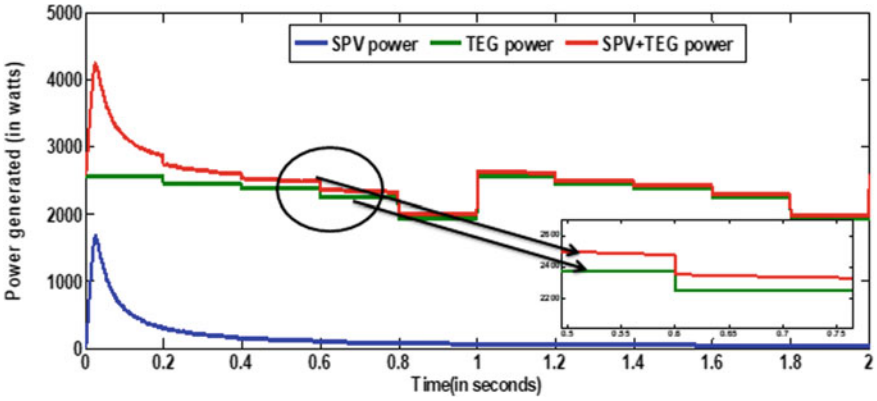

Fig. 5 Power obtained using Type-II network at healthy irradiance (HI)

of power from the hybrid system such as for Network = 4212 W (4.212 Kw) and Network-IV = 4010 W (4.010 Kw), respectively. However, during SI, the solar irradiation became lesser than that of HI; this leads to lesser power generation from TEG and consequently from hybrid SPV + TEG. Because lesser is the irradiance, lesser heat will be absorbed and lesser will be the power generation.

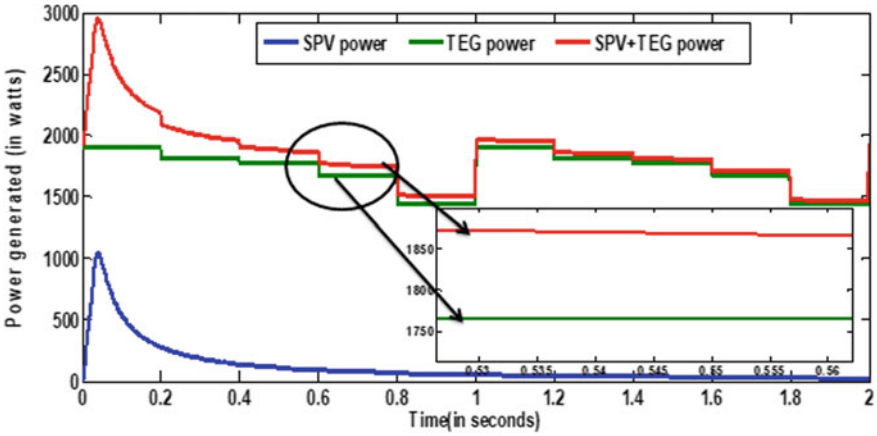

Fig. 6 Power obtained due to sectional irradiance (SI)-3/4th of shading

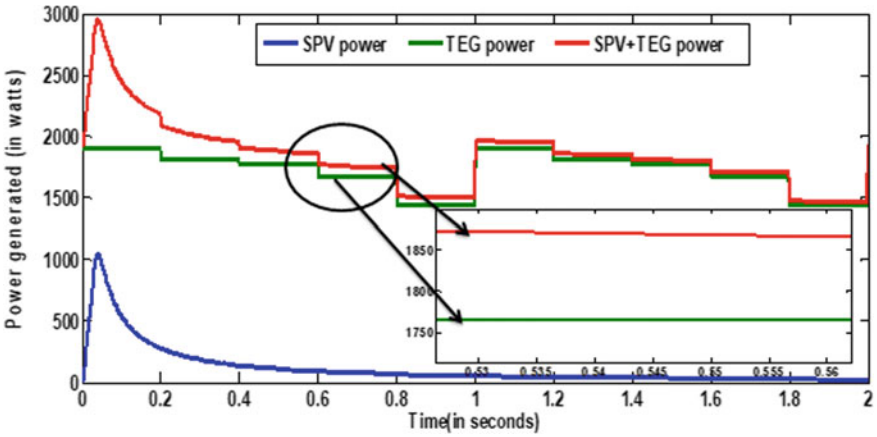

Fig. 7 Power obtained due to sectional irradiance (SI) 100% of shading

4 Experimental Setup for the Proposed Solar PV Networks

The experimental was carried out at the rooftop of ITER, Siksha O Anusandhan (Deemed to be University), Bhubaneswar, India. Eight PV modules are interconnected under earlier mentioned networking structures namely Network-I and Network-II. All the modules are interconnected as per the connection diagram given in Tables 4 and 5. The experiment was carried out under HI and SI. Under HI, the irradiance was found to be varied in between 850–950 W/m^2. The experiment has been conducted in April though in summer, the irradiance received by the solar PV module is higher consequently rising the surface temperature. This in turn lowers the module efficiency. To overcome this lowering of quantum efficiency, the TEG

Fig. 8 Field setup for proposed solar PV network at the rooftop

is connected in order to use the higher temperature and generate power. The power obtained at the output terminals will be the combination of power generated from solar PV module using photovoltaic effect and power generated from TEG using thermoelectric effect.

5 Conclusion

Thermoelectric generator is integrated with solar PV system in order to process the lost heat by thermoelectric effect. The conversion of light energy into electricity by photoelectric effect and converting heat into electricity by thermoelectric effect combined generate significant amount of power from solar PV array**.** During HI, the power generated is much higher than that of SI conditions. Because the irradiance thud incident on the modules during HI is higher that tends to excessive heat absorption at the junction of TEG. The experimental and theoretical evaluation has been conducted in order to verify the output power for only SPV based system, only TEG based system, and hybrid SPV-TEG based system. This study clearly states that the power during hybridization is much significant as compared to other two. The augmentation of the solar concentration decreases the SPV module efficiency and this in turn helpful for TEG for increasing its efficiency. This concept has been validated in this study. Employment of hybrid SPV-TEG based system delivers steady power for varying weather condition than only SPV/only TEG. Elementary understanding of overall output performance of the studied system has been made by consideration of thermoelectric effect and can be implemented in the places where rapid fluctuation of solar insolation and partly cloudy conditions degrades the solar PV array output with procurement of stability.

Table 5 Type 2 network

Type of connection	Connection diagram	Output values obtained	
At healthy irradiance (Non-shading condition)	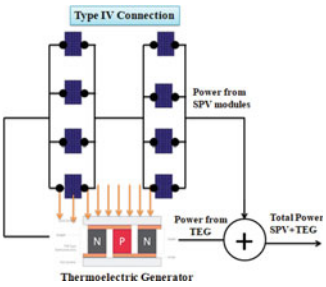	Experimental 1. Only SPV 29.98 W 2. Only TEG 3881 W 3. SPV + TEG 3911.98 W	Theoretical 1. Only SPV 31.06 W 2.OnlyTEG 3886 W 3. SPV + TEG 3917 W
At sectional irradiance 3/4th section (75% shading)	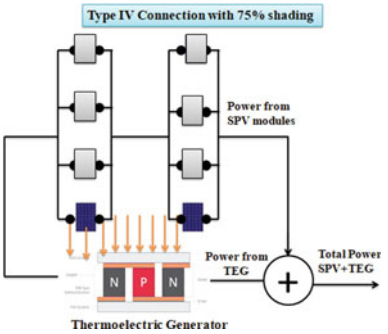	Experimental 1. Only SPV 26.89 W 2. Only TEG 1897.57 W 3. SPV + TEG 1924.46 W	Theoretical 1. Only SPV 28.67 W 2. Only TEG 1902 W 3. SPV + TEG 21931 W
At sectional irradiance Whole section (100% shaded)	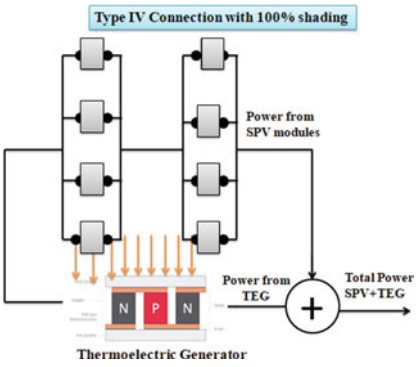	Experimental 1. Only SPV 25.45 W 2. Only TEG 1556.77 W 3. SPV + TEG 1582.22 W	Theoretical 1. Only SPV 27.46 W 2. OnlyTEG 1571 W 3. SPV + TEG 1599 W

References

1. Jena S, Kar SK (2019) Setting a fostered energy network by decarbonizing the grid: hybridization, control, and future solutions upon storage. Int J Energy Res 43(1):455–474
2. Jena S, Kar SK Demonstrating the benefits of thermoelectric-coupled solar PV system in microgrid challenging conventional integration issues of renewable resources. Int J Energy Res
3. Jena S, Kar SK (2019) Employment of solar photovoltaic-thermoelectric generator-based hybrid system for efficient operation of hybrid nonconventional distribution generator. Int J Energy Res

4. Jena S, Kar SK, Satpathy PR Encapsulating the challenges of storage in solar PV based microgrid. ISBN: 978–3–659–35285–0
5. Senthilkumar J, Charles Raja S, Srinivasan D, Venkatesh P (2018) Hybrid renewable energy-based distribution system for seasonal load variations. Int J Energy Res 42(3):1066–1087
6. Wu YY, Wu SY, Xiao L (2015) Performance analysis of photovoltaic–thermoelectric hybrid system with and without glass cover. Energy Convers Manage 93:151–159

Chapter 15
Economic Evaluation of a Solar Photovoltaic-Generator System-A Case Study

Sonali Goel and Renu Sharma

Abstract Renewable energy is the best alternative to supply electricity in off-grid remote areas and in areas with frequent power cut. A study was conducted to find the feasibility of a solar photovoltaic-generator system for meeting the electrical need of the ground floor of E-block in ITER, SOA (Deemed to be University), Bhubaneswar, India (20° 29′ N Latitude, 85° 82′ E Longitude). The economics of this solar photovoltaic-generator system was analysed by a software tool HOMER. It was found that 100 kW solar photovoltaic system in combination with a 20 kW generator is the optimum one for the load demand. The levelized cost of energy (LCOE) of the system was seen as $ 0.471/kWh with a net present cost (NPC) of $664,685 with 20% capacity shortage.

Keywords Hybrid energy system · Solar · Economic evaluation

1 Introduction

Accessibility of electricity is a significant parameter for economic and social development of a nation. Today, on a worldwide basis, the fuels used to produce electricity are: natural gas, nuclear, coal, hydroelectric power, and modern renewable like solar, wind, hydro and biomass. Source-wise world electricity generation indicates 24.50% global electricity is generated by renewables [1]. But, a single renewable energy source cannot be relied due to seasonal variations and weather conditions [2]. Many countries are now promoting renewable energy projects to generate electricity to solve their energy crisis. In 2016, total global renewable power generating capacity was 921 GW (excluding hydro power). The top six countries generating renewable energy are China, the USA, Germany, Japan, India, and Italy [1].

Reliability of a system can be increased by means of hybridisation. However, for improved operational performance, sizing of the component and selection of

S. Goel (✉) · R. Sharma
Department of Electrical Engineering, ITER, Siksha 'O' Anusandhan (Deemed To Be University), Bhubaneswar, India
e-mail: sonali19881@gmail.com

S. Mahapatra et al. (eds.), *Advances in Energy Technology*, Advances in Sustainability Science and Technology, https://doi.org/10.1007/978-981-15-8700-9_15

proper technology are very much essential for designing of such systems [3–7].Many researches have been carried out worldwide on the use of renewable energy sources for rural electrification. Numerous hybrid energy configurations such as PV-Wind, diesel-PV, diesel-wind, diesel-hydel are reported in [8–20]. Twelve isolated off-grid HRES for rural electrification have been studied by Diaz et al. [21] in Jujuy province of Argentina. Seven of these hybrid system contained solar and DG and five of solely solar photovoltaic system. An investigation has been led by Gupta et al. [22] in a group of nine remote un-electrified villages in Uttarakhand in India for supplying electricity by means of renewable energy. They found that hybrid energy system consisting of SHP-biomass-biogas-solar photovoltaic-DGare cost effective but when a single energy source was considered, highest cost of energy of INR 15.68/kWh found in case of SPV system while lowest of INR 1.45/kWh for micro hydro-photovoltaic system. One such hybrid renewable energy system has been studied by Bajpai and Dash [23] and found that the hybrid renewable energy system has a huge potential for supplying electricity to remote and inaccessible location across the globe. Another study conducted by Yamegueu et al. [24] in France to generate electricity from photovoltaic-diesel hybrid energy system and concluded that DG size should be equal to the peak load for finding the reliability of a PV-diesel system. A performance study was conducted by Shenaz et al. [25] in off-grid rural area by considering solar-wind-diesel-battery hybrid system in Malaysia for 33 kW/day load. Analysis of the system was done by using HOMER software tool and concluded that the net present cost can be reduced by 29.65% as compared to conventional power plants. Another study was conducted by Karakoulidis et al. [26] to meet the electrical load of an electrical machinery laboratory located in Kavala town in Greece by PV-DG-battery system. They analysed by considering various combination of PV-generator-battery by HOMER to get the optimum combination on the basis of lowest NPC. One micro-grid having DG-renewable mixed energy system was studied by Hafez and Bhattacharya [27] in Canada and found that emission of CO_2 decreases with increase in diesel price.

2 Methodology

The load requirement of the ground floor of E-block, ITER, SOA (Deemed to be University) was calculated by considering all electrical equipment and gadgets and their usable hours per day. The components of solar-generator-battery hybrid energy system were analysed by Hybrid Optimization of Multiple Energy Resources (HOMER) software tools which was developed by National Renewable Energy Laboratory (NREL), Colorado, USA.

Our aim is to find a cost effective and feasible solution to meet the electrical demand of the ground floor of the E-block, ITER of SOA University. Taking into consideration of the load profile of the floor, a cost-effective solar photovoltaic-generator-battery system was optimised by HOMER.

Table 1 Details of the study location

Location	Bhubaneswar, India
Geographical coordinates	20.29° N, 85.82° E
Typology	New construction
Climate type	Tropical climate
Study area	Ground floor of E block, ITER
Grid connectivity	Not connected

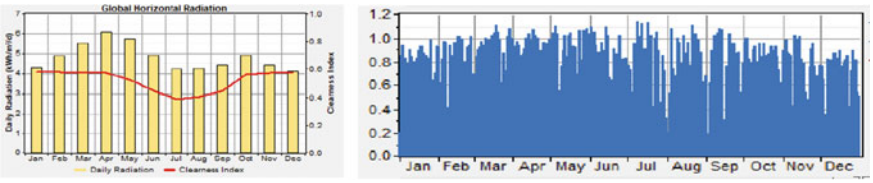

Fig. 1 Yearly global solar radiation and clearness index of the site

2.1 Renewable Energy Resources at the Site

Geographical area and accessibility of renewable energy power sources are most essential factor for developing an energy system. This study area of Bhubaneswar has a huge potential of solar energy sources for generating power for electrifying the ground floor of ITER, SOA Bhubaneswar. The meteorological monthly solar irradiance data for this system are imported from NASA meteorological site for Bhubaneswar location (Longitude 85°59′ E and Latitude 20°24′ N) (Table 1). The daily average solar radiation was seen to be 4.81 kWh/m^2/day (Fig. 1 and Table 2).The highest solar irradiance was seen in the month of April (6.06 kWh/m^2/day).

2.2 Study Location

The details of the study location and solar resources are shown in Tables 1 and 2.

The yearly global solar radiation of the site is shown in Fig. 1.

2.3 Load Assessment of the Site

The details of the load of the ground floor of ITER are divided into two seasonal variations, i.e. summer and winter load.

Table 2 Solar irradiance data of the site

Month	Clearness index	Daily radiation (kWh/m^2/d)
January	0.580	4.306
February	0.580	4.886
March	0.576	5.535
April	0.577	6.066
May	0.524	5.728
June	0.445	4.901
July	0.386	4.221
August	0.402	4.265
September	0.446	4.407
October	0.563	4.922
November	0.577	4.404
December	0.577	4.090
Avg	0.511	4.809

1. Primary load—The load of the building (Ground floor) was assessed by the actual number of electrical equipment and machinery in position and their daily hours of use. This load demand with 125 kW peak comes to 351 kWh/day.

The seasonal variation of loads for the whole year which show that the load for the month of April to October (summer) and November to March (winter) is almost equal as shown in Table 3 and Fig. 2.

3 System Architecture

The system architecture includes solar/battery/converter/generator which is shown in Fig. 3. It consists of a 30 kW diesel generator, 60 number of impact batteries, a 45 kW inverter, and a 100 kW of solar panel. Different system configurations are optimised by HOMER but it displays the most cost-effective configuration.

3.1 Equipment and System Size

Homer uses different configurations of equipment sizes that can be used for generating electric energy. Solar radiation, diesel etc., are some of the recourses taken and is shown in Table 4 and their component unit cost is shown in Table 5.

Simulation variables (Equipment sizes): $3 \times 5 \times 3$.

Sensitivity variables (Resource sizes): 3

Table 3 Load requirement of the site

			Summer (Apr to Oct)		Winter (Nov to Mar)	
			hrs/day	Wh./day	hrs/day	Wh./day
A. Domestic houses (Load in ground floor)	Nos.	Watt				
CFL light (2 × 11 W)	25	20	8	4000	8	4000
Tube light	100	40	8	32,000	8	32,000
Concealed LED	130	9	7	8190	7	8190
	30	9	16	4320	16	4320
Ceiling fan	60	70	8	33,600	0	0
Exhaust fan	10	180	4	7200	4	7200
Computer	100	130	7	91,000	7	91,000
Laboratory load	4	4000	2	32,000	2	32,000
AC	50	1350	3.5	236,250	0	0
Fridge	2	250	12	6000	12	6000
Pump (5 hp)	1	3750	3	11,250	3	11,250
Total (A)				465,810		195,960

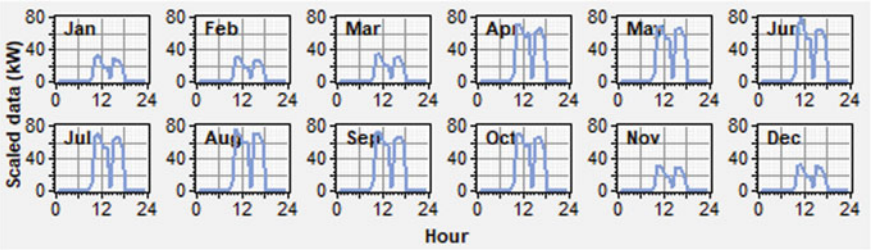

Fig. 2 Seasonal variation of loads

Various combinations of the above factors were considered and analysed by HOMER tool. The most ideal arrangement is presented in results.

4 Results and Discussion

The results obtained by considering three capacity shortage, i.e. 10, 15, and 20% are presented in Fig. 4. It is found that the minimum net present cost (NPC) of $664,685 with lowest cost of energy (COE) of $0.471/kWh obtained with 20% capacity shortage while with 10% capacity shortage, the same were $774,300 and

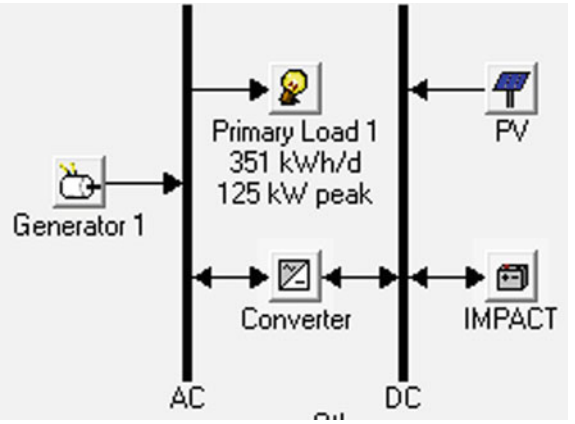

Fig. 3 System architecture

Table 4 Analysis of **r**esource size and equipment considered

Equipment	Sizes considered
Solar photovoltaic	90, 95, 100 kW
Generator	20, 25, 30, 35, 40 kW
Converter	40, 45, 50 kW
Battery of 150 Ah, 12 V (4 batteries per string)	10, 15, 20
Resources	
Capacity shortage	10, 15, 20

Table 5 Components and their unit cost

Equipment	Cost ($/kW)	Replacement cost, ($/kW)	Operation and maintenance cost
PV array	2500	2500	$0/kW
Biogas generator	1000	900	$0.240/kW per hour
Battery of 150 Ah,12 V	$114/battery	$114/battery	$5/battery/year
Inverter	700	700	$70/kW/year
Rectifier	700	700	$70/kW/year

Max. Cap. Shortage (%)	PV (kW)	Gen (kW)	IMPACT	Conv. (kW)	Initial Capital	Operating Cost ($/yr)	Total NPC	COE ($/kWh)	Ren. Frac.	Capacity Shortage	opy of Dies (L)	Gen (hrs)
10.0	100	30	60	45	$ 152,040	48,677	$ 774,300	0.502	0.73	0.10	18,676	2,083
15.0	100	20	80	50	$ 149,320	44,213	$ 714,510	0.481	0.76	0.14	15,938	2,535
20.0	100	20	60	40	$ 137,040	41,276	$ 664,685	0.471	0.77	0.20	15,390	2,477

Fig. 4 Optimization results

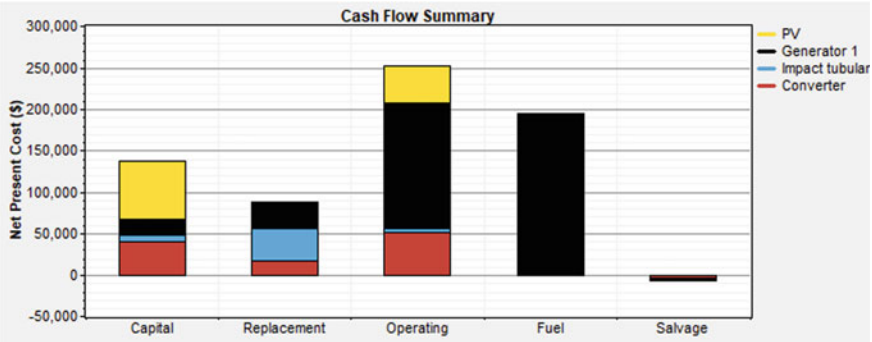

Component	Capital ($)	Replacement ($)	O&M ($)	Fuel ($)	Salvage ($)	Total ($)
PV	70,200	0	44,742	0	0	114,942
Generator 1	20,000	32,169	151,989	194,773	-3,656	395,275
Impact tubular	6,840	39,065	3,835	0	10	49,750
Converter	40,000	16,691	51,133	0	-3,107	104,717
System	137,040	87,925	251,699	194,773	-6,753	664,684

Fig. 5 Cash flow summary of the optimised hybrid system

$0.502/kWh, respectively. The 100 kW solar PV system, 30 kW generator with 45 kW converter, and 60 batteries were found to be the optimum combination for meeting the load demand with 10% capacity shortage while 100 kW PV, 20 kW generator with 40 kW converter and 60 batteries are the optimised combination for 20% capacity shortage. As the lower size of generator and converter is employed with 20% capacity shortage that will result the lowest NPC and lowest COE, this combination is preferred for the site.

4.1 Cash Flow Summary

The cash flow summary of the optimised hybrid system (with 20% capacity shortage) is shown in Fig. 5. The total system cost is $6,64,684 and total replacement cost is $87,925.

4.2 System Economics with Variation of Capacity Shortage

Capacity shortage is the deficiency that takes place between required operating capacity and the actual operating capacity of the system. HOMER monitors this shortage and calculates the total shortage throughout the year.

Table 6 shows the techno economic details of three different capacitive shortages which show that 20% capacity shortage is preferable due to lowest NPC ($664,685) and lowest COE ($0.471/kWh).

Table 6 Techno economics aspect of the hybrid energy system

Configuration	Unit	10% capacity shortage	15% capacity shortage	20% capacity shortage
Solar photovoltaic	kW	100	100	100
Generator	kW	30	20	20
Battery, 12 V, 150 Ah	Nos	60	80	60
Converter	kW	45	50	40
Initial capital cost	$	152,040	149,320	137,040
Total net present cost	$	774,300	714,510	664,685
Operating cost	$/yr	48,677	44,213	41,276
Fuel cost	$/yr	236,354	201,706	194,773
Cost of energy	$/kWh	0.502	0.481	0.471
PV production	kWh/yr	148,983	148,983	148,983
Generator production	kWh/yr	54,706	47,530	45,710
Total electricity production	kWh/yr	203,688	196,513	194,693
AC primary load served	kWh/yr	120,633	116,158	110,280
Capacity shortage	kWh/yr	12,461	18,118	25,572
Unmet load	kWh/yr	7482	11,957	17,835
Excess electricity	kWh/yr	65,547	59,921	67,105

4.3 Share of Electricity

The total share of electricity production by the solar photovoltaic system and the generator is shown in Table 7. It is seen that 73% electrical load is generated by PV system while only 27% is met by generator.

Table 7 Share of electricity production

Components	Production in (kWh/yr)	Fraction in %
PV array	148,983	73
Generator 1	54,706	27
Total	203,688	100

Table 8 Emissions of each pollutant

Pollutant	Emissions (kg/year)		
	10% capacity shortage	15% capacity shortage	20% capacity shortage
Carbon dioxide	49,180	41,970	40,528
Carbon monoxide	121	104	100
Unburned hydrocarbons	13.4	11.5	11.1
Particulate matter	9.15	7.81	7.54
Sulphur dioxide	98.8	84.3	81.4
Nitrogen oxides	1083	924	893

4.4 Emission of Pollutants

The total emissions of different pollutant created every year by the hybrid system are shown in Table 8.

The minimum CO_2 of 40,528 kg with 100 kg CO, 7.54 kg particulate matter, 81.4 kg SO_2 and 893 kg nitrogen oxides is discharged by the optimised system with 20% capacity shortage.

5 Conclusion

The renewable hybrid energy model recommended in this study will certainly meet the electrical need of the ground floor of E-block in ITER, SOA (Deemed to be University), Bhubaneswar. The combination of different sizes of component were analysed by considering three capacity shortage, i.e. 10, 15, and 20% by using HOMER. The most economic and feasible hybrid model was found with 20% capacity shortage with minimum NPC of $664,685 and lowest COE of $0.471/kWh. The highest NPC of $774,300 was found with 10% capacity shortage having highest COE of $0.502/kWh.

References

1. REN 21 (2017) Renewables: global status report. REN 21 Secretariat. Paris, France
2. Sharma R, Goel S (2016) Stand-alone hybrid energy system for sustainable development in rural India. Environ Dev Sustain 18(6):1601–1614

3. Kellogg WD, Nehrir MH, Venkataramanan G, Gerez V (1998) Generation unit sizing and cost analysis for stand-alone wind, photovoltaic, and hybrid wind/PV systems. IEEE Trans Energy Convers 13(1):70–75
4. Chedid R, Akiki H, Rahman S (1998) A decision support technique for the design of hybrid solar-wind power systems. IEEE Trans Energy Convers 13(1):76–83
5. Borowy BS, Salameh ZM (1996) Methodology for optimally sizing the combination of a battery bank and PV array in a wind/PV hybrid system. IEEE Trans Energy Convers 11(2):367–375
6. Giraud F, Salameh ZM (2001) Steady-state performance of a grid-connected rooftop hybrid wind-photovoltaic power system with battery storage. IEEE Trans Energy Convers 16(1):1–7
7. Marnay C, Venkataramanan G, Stadler M, Siddiqui AS, Firestone R, Chandran B (2008) Optimal technology selection and operation of commercial-building microgrids. IEEE Trans Power Syst 23(3):975–982
8. Kinoshita CM, Turn SQ, Overend RP, Bain RL (1997) Power generation potential of biomass gasification systems. J Energy Eng 128:88–89
9. Liu S, Dougal RA, Solodovnik EE (2006) VTB-based design of a standalone photovoltaic power system. Int J Green Energy 1(3):297–300
10. Muselli M, Notton G, Louche A (1999) A design of hybrid photovoltaic power generator, with optimization of energy management. Sol Energy 65:143–150
11. Nafeh AES (2011) Optimal economical sizing of a PV-Wind hybrid energy system using genetic algorithm. Int J Green Energy 8(1):25–43
12. Eke R, Kara O, Ulgen K (2005) Optimization of a wind/PV hybrid power generation system. Int J Green Energy 2(1):57–66
13. Elhadidy MA, Shaahid SM (1999) Feasibility of hybrid (wind + solar) power systems for Dhahran Saudi Arabia. Renewable Energy 16:970–976
14. Good JT, Ugursal VI, Fung AS (2007) Modeling and technical feasibility analysis of a low emission residential energy system. Int J Green Energy 4(1):27–43
15. Shaahid SM, Elhadidy MA (2008) Economic analysis of hybrid photovoltaic–diesel–battery power systems for residential loads in hot regions—a step to clean future. Renew Sustain Energy 12(2):488–503
16. Toke D, Oshima K (2007) Comparing Market-Based Renewable Energy Regimes: The Cases of the UK and Japan. Int J Green Energy 4(4):409–425
17. Rehman S, El-Amin IM, Ahmad F, Shaahid SM, Al-Shehri AM, Bakhashwain JM, Shash A (2007) Feasibility study of hybrid retrofits to an isolated off-grid diesel power plant. Renew Sustain Energy Rev 11:635–653
18. Schmid AL, Hoffmann CAA (2004) Replacing diesel by solar in the Amazon: Short-term economic feasibility of PV-Diesel hybrid systems. Energy Policy 32:881–898
19. Sharma H, Islam S, Pryor T (2000) Dynamic modeling and simulation of a hybrid wind diesel remote area power system. Int J Renew Energy Eng 2:123–128
20. Celik AN (2002) Optimization and techno-economic analysis of autonomous photovoltaic–wind hybrid energy systems in comparison to single photovoltaic and wind systems. Energy Convers Manage 43:2453–2468
21. Díaz P, Peña R, Muñoz J, Arias CA, Sandoval D (2011) Field analysis of solar PV-based collective systems for rural electrification. Energy 36(5):2509–2516
22. Gupta A, Saini RP, Sharma MP (2010) Steady-state modelling of hybrid energy system for off grid electrification of cluster of villages. Renewable Energy 35(2):520–535
23. Bajpai P, Dash V (2012) Hybrid renewable energy systems for power generation in stand-alone applications: a review. Renew Sustain Energy Rev 16(5):2926–2939
24. Yamegueu D, Azoumah Y, Py X, Zongo N (2011) Experimental study of electricity generation by Solar PV/diesel hybrid systems without battery storage for off-grid areas. Renewable Energy 36(6):1780–1787
25. Shezan SA, Julai S, Kibria MA, Ullah KR, Saidur R, Chong WT, Akikur RK (2016) Performance analysis of an off-grid wind-PV (photovoltaic)-diesel-battery hybrid energy system feasible for remote areas. J Cleaner Prod 125:121–132

26. Karakoulidis K, Mavridis K, Bandekas DV, Adoniadis P, Potolias C, Vordos N (2011) Techno-economic analysis of a stand-alone hybrid photovoltaic-diesel–battery-fuel cell power system. Renewable Energy 36(8):2238–2244
27. Hafez O, Bhattacharya K (2012) Optimal planning and design of a renewable energy based supply system for microgrids. Renewable Energy 45:7–15

Chapter 16
Partial Shading Effect on the Performance of Electric Vehicle-Integrated Solar PV System

Priya Ranjan Satpathy, Ali Mahmoud, Suraj Kumar Panigarhi, and Renu Sharma

Abstract Solar PV system-based electric vehicles are manufactured to reduce harmful emission from the environment that uses PV as the major source of energy. In general, the PV modules are installed at the roof of vehicles that convert the energy from the sun to charge the integrated battery while running and parking modes. Also, for smooth charging of the battery, maximum power point trackers (MPPTs) are installed that maintain the required voltage to charge the battery. However, shading causes a serious problem by affecting the performance of the system by creating numerous peaks in the power curves resulting in the low power output and false tracking by the MPPT algorithms. This paper focuses on the study of shading impact on the electric vehicle roof-integrated PV module power generation. The entire study is conducted in the simulation environment using different shading conditions. It has been found that occurrence of shading results in severe power loss and voltage reduction, hence affecting the charging of the connected battery.

Keywords Photovoltaic · Maximum power point tracking · Battery · Partial shading · Electric vehicle

1 Introduction

Electric vehicles are considered as the best solution to meet the future energy crisis and reduce environmental pollution effectively [1, 2]. The automobile industry has shown a rapid growth in the last decades as compared to other industries [3]. Also, the automobile manufacturers are marching from the conventional fuel cars to energy efficient and renewable-based electric/hybrid vehicles [4].

In general, various charging stations powered by DC grid are employed at certain areas to charge the electric vehicles [5]. However, transmission of DC power in the grid results in increased losses. As a result, manufacturers come up with the idea of

P. R. Satpathy (✉) · A. Mahmoud · S. K. Panigarhi · R. Sharma
Department of Electrical Engineering, ITER, Siksha 'O' Anusandhan (Deemed To Be University), Bhubaneswar, India
e-mail: priransat3@gmail.com

S. Mahapatra et al. (eds.), *Advances in Energy Technology*, Advances in Sustainability Science and Technology, https://doi.org/10.1007/978-981-15-8700-9_16

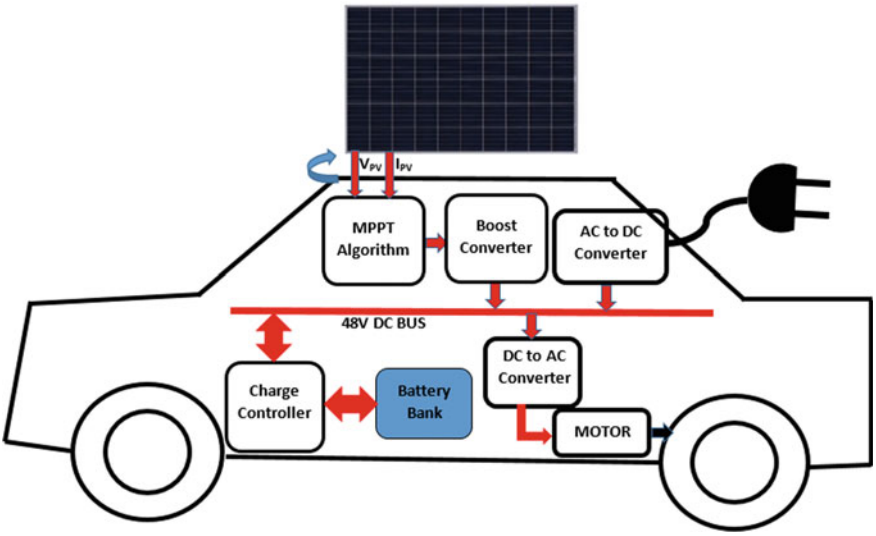

Fig. 1 Generalized block diagram of the solar PV-integrated electric vehicle

roof-integrated PV system in the vehicle in order to charge the vehicle irrespective of the availability of the charging station [6]. Also, the battery of the electric vehicle can be charged while running or parked mode provided the modules get sufficient solar irradiance level. The energy generation of the solar modules mainly relies upon the amount of received solar insolation. As a result, sometimes, the PV modules can be insufficient to charge the electric vehicle due to the intermittent nature of the sun and occurrence of shading among the roof integrated modules [7–9].

Shading is considered to be the major threat the power generation of PV modules that mainly occurs when some part of the module receives low irradiance due to presence of any obstacles like tree leaves, dust, snow, bird litter, etc.[10–13]. This results in reduction of overall power output and permanent damage of the modules by forming hotspot. Also, forming numerous peaks in the power curves of the module is the major consequence of partial shading resulting complicated operation of MPPTs while tracking the actual maximum power point (MPP) [14, 15].

This paper investigates the partial shading impact on the electric vehicle-integrated PV modules and MPPT-based boost converter power generation. The study has been done in simulation using a PV module that is divided into four sub-modules and operated under various partial shading scenarios.

2 Generalized Electric Vehicle Model

Figure 1 represents the block diagram of a generalized PV-based electric vehicle. The PV module is installed at the roof top of the vehicle that acts as a primary source

of fuel to the vehicle. The PV module converts the energy captured from the sun to useful electrical energy [16]. The system consists of a boost converter that boosts the voltage generated by solar module to 48 V. A MPPT algorithm has been equipped with the boost converter that assures the converter to generate maximum power during irradiance fluctuations. The algorithm tracks the real MPP using the present value of the maximum voltage and current generated by the vehicle-integrated module and gives the respective pulse to the switch of the boost converter.

To maintain a constant DC voltage of 48 V, a battery is connected to the system that gets charged by the PV power. A control strategy is provided to continuously monitor the power flow between solar modules and battery for smooth operation. During high irradiance hour, the solar module maintains 48 V DC voltage and provides power to the vehicle and charges the vehicle. The battery maintains the voltage during low irradiance hours and discharges to provide the power to vehicle. A bi-directional DC-DC converter is responsible for maintaining smooth power transition between the battery, module, and vehicle power unit. As, the PV power will be insufficient to charge the battery every time so, AC-DC converter is implemented to charge the vehicle from AC grid. Also, for DC power conversion, in order to drive the AC motor and run the vehicle, an inverter is provided in the system.

3 System Description and Modelling

3.1 Solar PV System Modelling

Basically, solar PV modules are the series combination of PV cells that converts solar energy from the sun to electricity on the basis of the photoelectric effect. The equivalent circuit of the PV module has been shown in Fig. 2. The circuit consists of a current generator, diode, series (R_S), and shunt (R_{Sh}) resistances. I_{Ph} is the symbolic representation of photonic current, I_O denotes the reverse saturation current, and I is the current generated from the module.

The characteristics equation of the solar module has been given in Eq. (1).

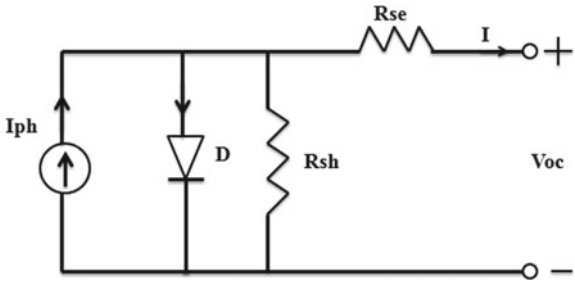

Fig. 2 Generalized circuit equivalent of the solar PV-integrated electric vehicle

Table 1 PV module and sub-module specifications at STC (1000 W/m^2 and 25 °C)

Parameters	Module specification	Sub-module specification
Power at MPP (P_M)	350 W	86 W
Voltage at MPP (V_M)	39.51 V	10.18 V
Current MPP (I_M)	8.85 A	8.85 A
Voltage during open-circuit (V_{OC})	46.4 V	11.6 V
Current during short-circuit (I_{SC})	9.2 A	9.2 A

$$I_{PV} = I_{\text{Ph}} - I_O\left[\exp\left(\frac{V_{PV} + I_{PV}R_S}{V_t}\right) - 1\right] - \left[\frac{V_{PV} + I_{PV}R_S}{R_{\text{Sh}}}\right] \tag{1}$$

and

$$Vt = \frac{aKT}{q}. \tag{2}$$

where the voltage generated by the module and thermal voltage are denoted as 'V_{PV}' and 'V_t' respectively. The ideality factor is denoted as 'a', module temperature is 'T', Boltzmann constant denoted as 'K', and 'q' is the charge of electrons.

In this, the vehicle-integrated *PV* module has been divided into four sub-modules for proper investigation of the shading impact. Table 1 portrays the specifications of the module and the sub-modules at standard testing condition (STC).

The solar module has been connected to a MPPT algorithm-based boost converter in order to maintain the voltage of 48 V in DC bus. The MPPT algorithm will track the MPP and gives duty cycle through PWM generator to the semi-conductor switch of the boost converter. The circuit representation of the system has been shown in Fig. 3 that consists of the PV sub-modules, MPPT controller, boost converter, and DC bus. The switch of the boost converter is a MOSFET that has been operated at higher frequency of 25 kHz.

3.2 Shading Scenarios

The electric vehicle-integrated PV module performance during shading has been investigated under four shading casesas shown in Fig. 4. To investigate the shading impact on power curves, distinct irradiance levels have been provided to the sub-modules. The shading scenarios may be resultant of buildings/trees shadow, cloud passage, and dust/snow coverage. The modules with no shading have been set to receive 800 W/m^2 whereas the shaded modules received various irradiance levels, i.e., 100 and 300 W/m^2.

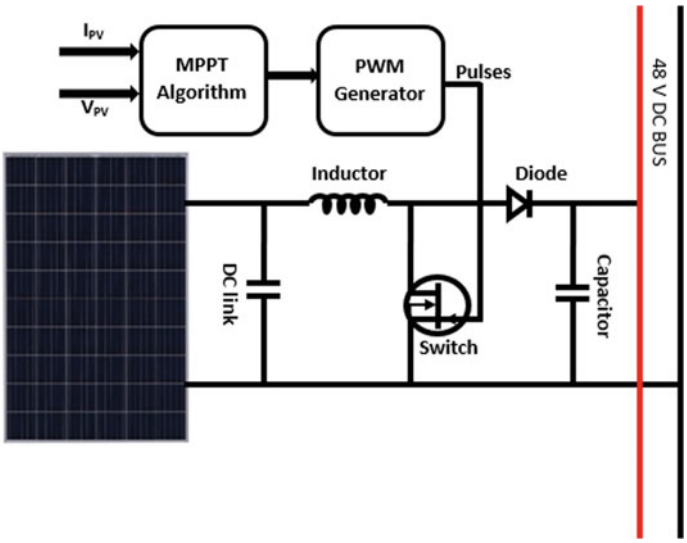

Fig. 3 Generalized block diagram of the solar PV integrated electric vehicle

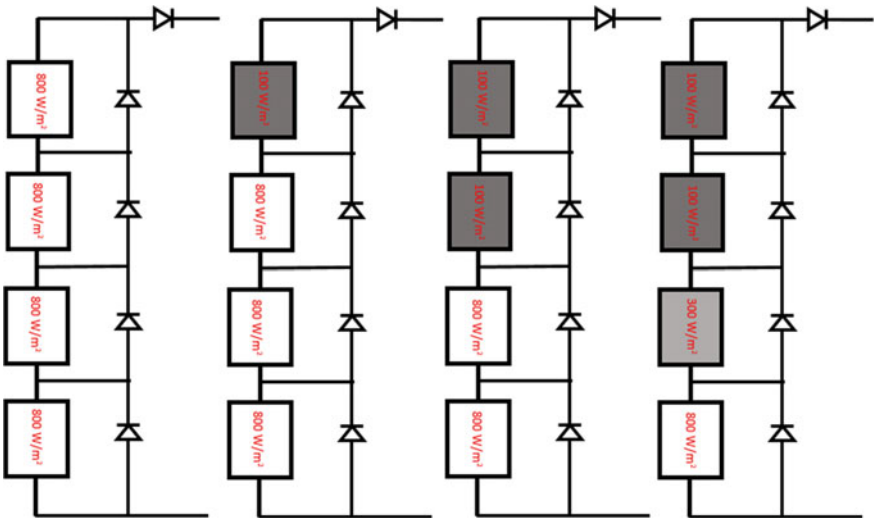

Fig. 4 Different shading cases for PV module integrated electric vehicle

4 Results and Discussions

4.1 Effect on PV Module Power Generation

The P_M, V_M, and I_M generated by the system during unshaded condition (800 W/m^2) have been found to be 277.93 W, 39.71 V, and 7.16A, respectively.

During case A, the first sub-module receives lower irradiance (100 W/m^2) indicates shading. Figure 5 illustrates the P ~ V curve of the syste munder shading case A. It has been found that the power curve of the module exhibited two MPPs where the actual MPP lies at first position. The maximum power, voltage, and current generated by the module during shading case A has been found as 202.58 W, 28.34 V, and 7.14 A, respectively.

During shading case B, the first and second sub-modules are shaded with lower irradiance of 100 W/m^2 with other sub-modules receiving 800 W/m^2. The P ~ V curve of the module has been shown in Fig. 6 which clearly represents the presence of two MPPs. The maximum power, voltage, and current generated by the module have been found to be 127.74 W, 18.10 V, and 7.05 A, respectively (Fig. 7).

The first and second sub-modules received 100 W/m^2, third sub-module received 300 W/m^2, and the fourth sub-module received 800 W/m^2 during shading case C. It has been noticed that the P ~ V characteristics curve exhibited three MPPs as the module received three irradiances. The maximum power, voltage, and current generated by the module have been found as 51.39 W, 7.10 V, and 7.23 A.

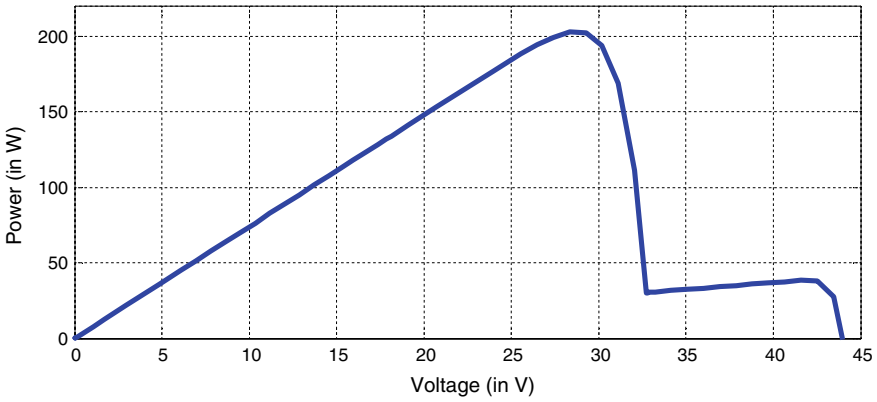

Fig. 5 Power–voltage (P ~ V) curve of the module with shading case A

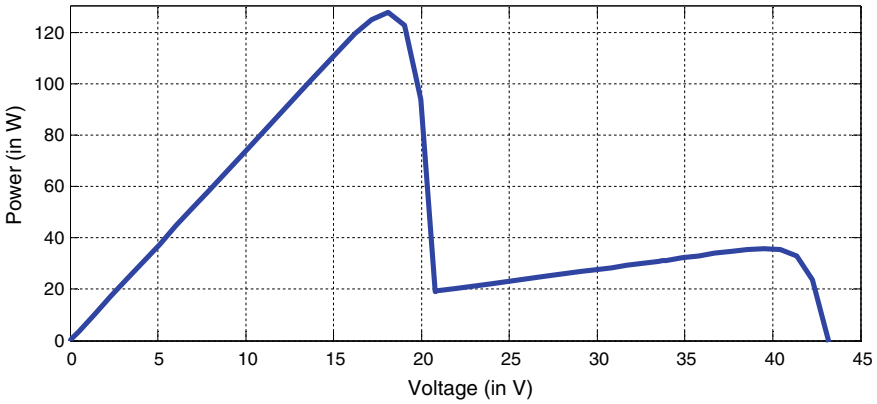

Fig. 6 Power–voltage (P ~ V) curve of the module with shading case B

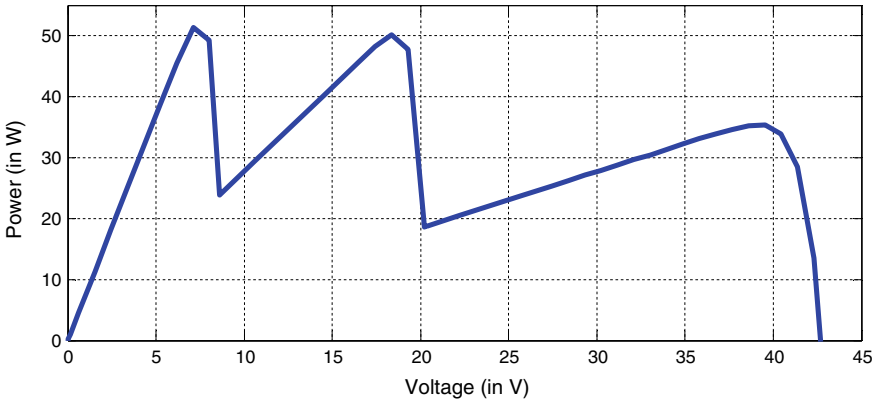

Fig. 7 Power–voltage (P ~ V) curve of the module with shading case C

4.2 Effect on Boost Converter

The shading impact on the boost converter performance has been studied using two shading cases as given in Table 2.

Figure 8a and b illustrates the power and voltage output of boost converter during both the shading cases. It has been investigated that during both the cases, the actual MPP of module lies in the second position due to which the MPPT algorithm tracked the false MPP resulting lower power generation. Also, it is noticed that the voltage output of the boost reduced to less than 48 V during shading affecting the charging of the battery connected to the vehicle.

The presented results illustrate the outcome of the shading on the PV module and boost converter power generation performance. It has been observed that the peaks count in the power curves mainly depends on the number of received irradiances by

Table 2 Shading scenarios for boost converter

Case A				
Time (s)	Irradiance received by PV sub-modules (SM) (in W/m^2)			
	Sub-module 1	Sub-module 2	Sub-module 3	Sub-module 4
0–2	800	800	800	800
2–5	400	800	800	800
Case B				
0–2	800	800	800	800
2–4	200	600	800	800
4–5	600	600	800	800

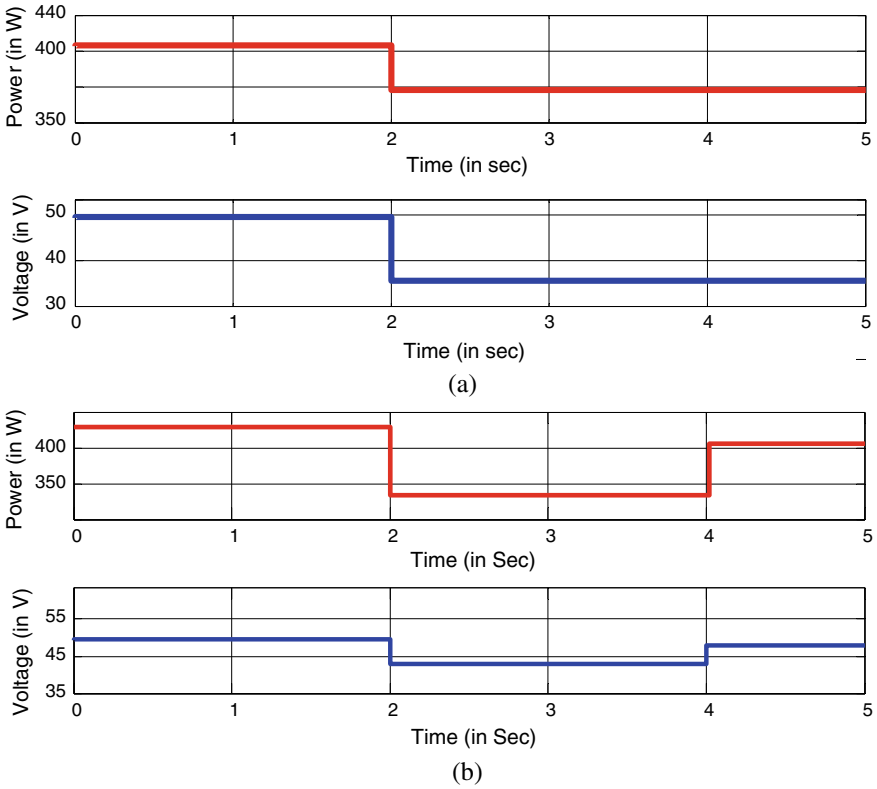

Fig. 8 Power and voltage output of the boost converter during partial shading. **a** Case A **b** Case B

the PV modules. Also, the total power generated by the series string is equivalent to the sum of power generated by the individual modules. It has been also observed that the location of actual MPP in the power curves and power generation relies on the shading nature and patterns in the modules. The boost converter delivered maximum

voltage during the unshaded condition as well as when the actual MPPT lies in the first position of the characteristics curve. However, when the actual MPP lies in other positions, the algorithm fails to determine the real MPP and falsely tracks the wrong MPP resulting low power and voltage output.

5 Conclusion

This paper investigated the impact of partial shading on the performance of the electric vehicle-integrated solar PV system. The investigation is conducted on the solar PV module and the MPPT-based boost converter. It is studied that there is a critical power loss during shade occurrence even in a small area. Also, partial shading creates numerous peaks in the power curves that complicate the MPPT algorithms operation. Also, the algorithm tracks the false MPP sometimes and hence reduces the power output of the boost converter. This scenario completely reduces the DC voltage of the system and hence charging of the vehicle and affects the charging of the battery connected to the electric vehicle.

References

1. Li Y, Lim MK, Tan Y, Lee Y, Tseng ML (2020) Sharing economy to improve routing for urban logistics distribution using electric vehicles. Resour Conserv Recycl 153:104585
2. Zheng J, Sun X, Jia L, Zhou Y (2020) Electric passenger vehicles sales and carbon dioxide emission reduction potential in China's leading markets. J Cleaner Prod 243:118607
3. Ewert A, Brost MK, Schmid SA (2020) Framework conditions and potential measures for small electric vehicles on a municipal level. World Electric Veh J 11(1):1
4. Zhou Y, Ravey A, Péra MC (2020) Multi-mode predictive energy management for fuel cell hybrid electric vehicles using Markov driving pattern recognizer. Appl Energy 258:114057
5. Gampa SR, Jasthi K, Goli P, Das D, Bansal RC (2020) Grasshopper optimization algorithm based two stage fuzzy multiobjective approach for optimum sizing and placement of distributed generations, shunt capacitors and electric vehicle charging stations. J Energy Storage 27:101117
6. Pati SS, Panigrahi TK, Behera A (2020) Performance analysis of solar and plug-in electric vehicle's integration to the power system with automatic generation control. In: Intelligent computing techniques for smart energy systems. Springer, Singapore, pp 703–711
7. Satpathy PR, Sharma R (2019a) Power and mismatch losses mitigation by a fixed electrical reconfiguration technique for partially shaded photovoltaic arrays. Energy Convers Manage 192:52–70
8. Satpathy PR, Sharma R (2019b) Diffusion charge compensation strategy for power balancing in capacitor-less photovoltaic modules during partial shading. Appl Energy 255:113826
9. Satpathy PR, Sharma R (2020) Power recovery and equalization in partially shaded photovoltaic strings by an efficient switched capacitor converter. Energy Convers Manage 203:112258
10. Nihanth MSS, Rajasekar N, Pillai DS, Ram JP (2020) A new array reconfiguration scheme for solar pv systems under partial shading conditions. In: Intelligent computing techniques for smart energy systems. Springer, Singapore, pp 387–396
11. Winston DP, Kumaravel S, Kumar BP, Devakirubakaran S (2020) Performance improvement of solar PV array topologies during various partial shading conditions. Sol Energy 196:228–242

12. Satpathy PR, Sharma R, Dash S (2019) An efficient SD-PAR technique for maximum power generation from modules of partially shaded PV arrays. Energy 175:182–194
13. Satpathy PR, Sharma R (2018) Power loss reduction in partially shaded PV arrays by a static SDP technique. Energy 156:569–585
14. Manohar M, Koley E, Ghosh S (2020) An efficient MPPT and reliable protection scheme for PV-integrated microgrid under partial shading and array faults. In: Modern maximum power point tracking techniques for photovoltaic energy systems. Springer, Cham, pp 303–329
15. Rekioua D (2020) MPPT methods in hybrid renewable energy systems. In Hybrid renewable energy systems. Springer, Cham, pp 79–138
16. Richardson DB (2013) Electric vehicles and the electric grid: A review of modeling approaches, Impacts, and renewable energy integration. Renew Sustain Energy Rev 19:247–254

Chapter 17
Site-Specific Design Optimization of Wind Turbines at Low Wind Speed Sites of North-East India

Sanzida Tasmin Ali, Pallabi Borah, and Sadhan Mahapatra

Abstract The utilization of the wind energy at a location primarily depends on the wind speed and right kind of machine installed at the site. The selection of machine for a site needs to be in such a way, so that maximum amount of energy can be effectively harnessed from the available wind spectrum. Wind speeds in the North-Eastern region of India are relatively low, highly fluctuating in directions, and localized in nature. The low wind speed creates difficulty to provide high starting torque to larger capacity machines with relatively higher rated wind speed. Thus, the region could be favorable to smaller machines having low cut-in and low rated wind speed. The present work aims to analyze the feasibility of installation of low capacity wind machines by estimating the capacity factors and annual energy generation at selected sites of the region. The low capacity machines can be used as an off-grid energy system to provide electricity access in the remote locations of the region.

Keywords Site-specific design · Capacity factor · Annual energy generation

1 Introduction

Wind power is considered as one of the fastest growing renewable energy sources, which is cleaner and cheaper alternative to the carbon-based fossil fuels. Large-scale wind farms are being established in potentially good wind sites both in onshore and offshore. Wind resource assessment is essential before installation of any wind machines, because the power output of the wind turbine depends on the site characteristics and topography. The utilization of the wind energy at a location depends primarily upon the availability of the wind spectrum. The selection of machine for the site needs to in such a way that maximum amount of energy can be effectively harnessed from the available wind spectrum. Site-specific design perfectly matches with the available wind speed and the machine characteristics for optimum energy generation or reduce the cost of energy generation.

S. T. Ali · P. Borah · S. Mahapatra (✉)
Department of Energy, Tezpur University, Tezpur, Assam 784028, India
e-mail: sadhan.mahapatra@gmail.com

S. Mahapatra et al. (eds.), *Advances in Energy Technology*, Advances in Sustainability Science and Technology, https://doi.org/10.1007/978-981-15-8700-9_17

Ohunakin et al. estimated capacity factor, annual energy generation, and cost of energy generation of two commercial wind turbines in six high-altitude locations of Nigeria [1]. Boccard reported the discrepancy in reported and actual capacity factors of wind turbines and the consequence of the miscalculation of capacity factors located in Europe [2]. Huang and Wan presented a generalized and systematic methodology for installation of wind turbine generators using capacity factor curves for maximum energy generation at a specific site [3]. Jangamshetti and Rau investigated statistical models for wind resource assessment and observed that the capacity factor calculated based on analytical method closely matches with the actual capacity factor obtained at field [4]. The study concluded that the analytical model can be used for accurate assessment toward wind turbine installation at a potential site. Fuglsang et al. reported the results of site characteristics inclusion in wind turbine design process in a European project [5]. The study observed that optimized site-specific design increase the annual energy yield and reduce the cost of energy generation. The study concluded that wind turbine should be design based on site particularly for low-wind location. Ayodele et al. estimated capacity factors of commercially available wind turbines, based on local wind characteristics in the Western Cape region of South Africa [6]. The study examined the influence of power curve of turbine on the capacity factor. It is concluded that Weibull distribution is the most suitable model to represent the wind distribution of a site. Jowder statistically analyzed and determined the most suitable locations in Kingdom of Bahrain [7]. Weibull parameters are estimated by using different methods. The study also investigated the site matching of wind turbine by estimating capacity factors of commercially available turbines. The optimum site selection has been done based on annual and monthly variation of capacity factors.

The wind resource assessment has been carried out at a few locations in the North-Eastern part of India [8]. The mean wind speed in the region is 1.8–4.9 m/s, which are relatively low in comparison with the coastal regions of India [8]. The wind in the region is also highly fluctuating in directions, turbulent in nature due to its topography, and usually localized in nature. The feasibility of installation of off-grid wind systems from available low-potential wind resource is an alternative option considering the non-availability of power in most of the remote localities of the region. This study aims at analyzing the feasibility of installation of low capacity wind machines in the region by estimating capacity factor and annual energy generation at the selected sites.

2 Methodology

Wind speed is the most important parameter to be considered in the design and operation of wind turbines since its probability density distribution greatly affects the performance of wind turbines. National Institute of Wind Energy (NIWE) has established 93 Wind Monitoring Stations in North-Eastern region of India, out of which nine stations are in operation as on 31.05.2020 [8]. Table 1 shows the number of wind monitoring stations established in the various states of the region. Wind

Table 1 Wind monitoring stations in NE states [8]

States	Installed	In operation
Arunachal Pradesh	17	7
Assam	18	–
Meghalaya	17	–
Mizoram	9	–
Manipur	15	1
Nagaland	6	–
Tripura	11	1

power density is mostly in the range of 0–100 W/m^2, and maximum wind speed occurs in the region during April–June months.

The prerequisite for the efficient planning and implementation of a wind energy project is primarily based on the wind regime characteristics. The characteristics of the wind regime of a location are defined by shape parameter (k) and scale factor (c) of Weibull distribution. Weibull parameters are helpful in estimating the probabilities of various wind speeds, such as mean wind speed and most probable wind speed, as well as their daily, monthly, or annual hours of availability for a particular site. Selection of right kind of machine or wind turbine needs to be chosen based on site characteristics in order to harness maximum wind power effectively. An important aspect in the selection of machines is the capacity factor, which is function of both the site characteristics (k and c) and machine characteristics (cut-in, rated, and cut-out wind speeds). In this study, capacity factors of five commercially available machines are estimated for the selected sites of North-East region of India. The annual energy generation is also estimated based on the capacity factor of the selected machine in these sites. The site parameters and mean wind speed data for a total number of 18 places of the North-East are obtained from C-WET [9]. Table 2 presents the mean wind speed and Weibull parameters for the selected sites of the region.

A wind turbine is designed to operate within a certain range of wind speed characterized by cut-in speed, rated speed, and cut-out speed. Five different capacity commercially available machines are selected for the analysis in this study. It is necessary to estimate the actual energy generation in a particular site from a wind machine. The energy generation is an important parameter because it affects the cost per unit electricity generation and determines the economic viability of a machine for a particular site. The energy generation depends on the site characteristics and machine characteristics. The ratio of actual energy produced at the site to the maximum energy can be generated based on its rated power of the machine which is known as capacity factor. The capacity factor (CF) is function of the site parameters (k, c) and the machine parameters (cut-in, rated, and cut-out wind speed). The capacity factor and annual energy generation can be estimated by using the following relations. Table 3 presents the commercially available wind machine characteristics data.

Table 2 Weibull parameters for various sites [9]

Location	State	Mean wind speed (m/s)	Weibull parameters	
			c (m/s)	k
Borgaon	Assam	2.4	2.7	2.3
P.Leikul	Assam	3.2	3.6	1.6
Tolpoi	Assam	2.5	2.8	2.0
Likabali	Arunachal Pradesh	2.9	3.2	2.2
Passighat	Arunachal Pradesh	2.3	2.5	1.8
Raga	Arunachal Pradesh	1.8	2.0	2.0
Phuldangsai	Tripura	3.8	4.3	2.1
Tlangsang	Tripura	3.9	4.4	2.1
Vanghmun	Tripura	3.5	3.9	2.0
Lunglei	Mizoram	3.9	4.4	2.1
Mamte	Mizoram	2.8	3.1	2.1
Reiek	Mizoram	3.8	4.3	1.7
Chawangkining	Manipur	4.5	5.0	1.8
Dolangkhnou	Manipur	4.4	4.9	2.0
Laimaton	Manipur	4.9	5.5	2.2

Table 3 Machine characteristics

Machine	Rotor diameter (m)	Rated capacity (kW)	Cut-in speed (m/s)	Rated speed (m/s)	Cut-out speed (m/s)
Machine A	29	225	3.5	14	25
Machine B	29	100	3	10	25
Machine C	29	60	3	9	25
Machine D	9	5	2.5	7.5	20
Machine E	6	1	1.9	6	15

$$CF = \frac{\exp\left(-\left(\frac{u_c}{c}\right)^k\right) - \exp\left(-\left(\frac{u_R}{c}\right)^k\right)}{\left(\frac{u_R}{c}\right)^k - \left(\frac{u_c}{c}\right)^k} - \exp\left(-\left(\frac{u_F}{c}\right)^k\right) \tag{1}$$

$$\text{Annual Energy Generation} = CF \times P_R(\text{kW}) \times 8760(\text{h}) \tag{2}$$

3 Results and Discussion

3.1 Capacity Factor

The capacity factors are estimated for five different commercially available machines for 15 different sites in various states of the region. Table 4 presents the capacity factors of all these machines in various sites. The machine A has the lowest capacity factor, and machine E has the highest capacity factor in all these sites. Capacity factor depends on the site characteristics and machine characteristics. It is observed that Chawangkining and Laimaton sites of Manipur show highest capacity factors for all the machines. The mean wind speed of these two sites is relatively higher in comparision with the other sites. It is worthy to mention that although a few more sites showed higher duration of wind availability in the desired range, i.e., in between cut-in and rated wind speed, the capacity factors are low. The maximum mean wind speed is 4.9 m/s at Laimaton, out of all these sites. However, the cut-in and rated wind speed for machine A is 3.5 and 14 m/s, respectively. Machine A has the highest cut-in and rated wind speed among the selected machine resulted lower capacity factors for all the sites. It means that machine A operates most of the time of the year near the cut-in wind speed in these sites. The maximum power coefficient (Cp) is also function of wind speed. The maximum power coefficient is lower at the lower wind speed regime. Hence, the power output or energy generation from machine A

Table 4 Capacity factors for different machines

Site	Capacity factor (%)				
	Machine A	Machine B	Machine C	Machine D	Machine E
Borgaon	0.39	1.47	1.91	4.49	10.95
P.Leikul	4.91	10.68	12.85	19.90	31.19
Tolpoi	0.89	2.73	3.45	7.05	15.03
Likabali	1.21	3.68	4.74	9.40	19.33
Passighat	0.78	2.32	2.89	5.90	12.67
Raga	0.10	0.46	0.59	1.68	5.01
Phuldangsai	4.63	11.50	14.51	23.68	38.28
Tlangsang	5.01	12.32	15.52	25.02	39.82
Vanghmun	3.70	9.23	11.59	19.42	32.63
Lunglei	5.01	12.32	15.52	25.02	39.82
Mamte	1.23	3.65	4.66	9.16	18.69
Reiek	7.33	15.49	18.58	27.36	40.17
Chawangkining	10.06	20.77	24.78	34.95	48.61
Dolangkhnou	7.84	17.73	21.78	32.40	47.23
Laimaton	9.28	21.50	26.61	38.84	54.74

which is operated near the cut-in wind speed with low power coefficient resulted lower energy generation than the energy generation at rated power.

The lower value of scale parameters also indicates lower mean wind speed of the site. It reveals that machine operates at rated power only for few hours in a year in such sites. It is also observed that as the rated wind speed reduces, capacity factor of the machines increases in all these sites. Moreover, machine E with rated capacity of 1 kW has lowest cut-in and rated wind speed among these machines exhibits higher capacity factor in all the sites. Hence, matching the machine characteristics with site characteristics is an essential assessment tool toward selection of right kind of machine for optimum power generation in a site. Low capacity machines, i.e., lower cut-in and rated wind speeds, are most suitable in low-windy sites. These kinds of machines can operate relatively longer hours in a year and generate maximum energy in a low-windy site.

Figure 1 presents the capacity factor of different machines for nine best sites. The capacity factor for machine A varies from 4.9% for P. Leikul to 10.1% for Chawangkining. The mean wind speed for P.Leikul and Chawangkining are 3.2 m/s and 4.5 m/s, respectively. However, machine A has rated wind speed of 14 m/s and rated power of 225 kW. It is important to mention that the mean wind speed of Laimaton is higher than Chawangkining. However, the capacity factor for Laimaton is lower than the Chawangkining. This happened due to the difference in Weibull scale parameter in these sites ($c = 5.5$ for Laimaton and $c = 5.0$ for Chawangkining). Higher scale parameter resulted availability of low wind speed in most of the time of the year. The capacity factor for machine *E* for Chawangkining and Laimaton is 48.6

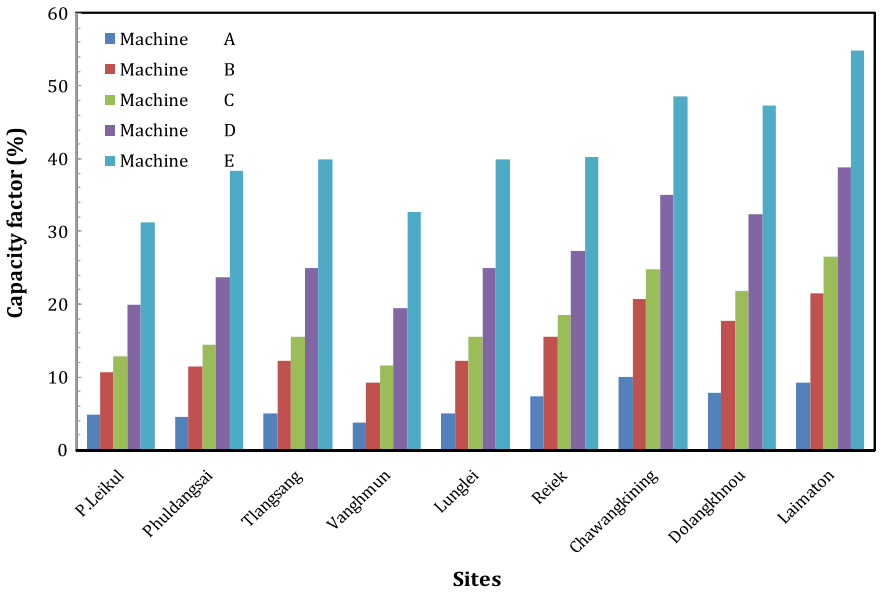

Fig. 1 Capacity factors for different machines in selected sites

and 54.7%, respectively. This is opposite to the machine A result. This is due to the cut-in and rated wind speed of machine *E* are 1.9 m/s and 6 m/s, respectively. Hence, the machine *E* is operated more number of hours in a year in Laimaton compared to Chawangkining. The capacity factor results show that low capacity machines such as machine *D* or machine *E* has higher capacity factor compare to relatively higher capacity machines like machine *A* or machine *B* or machine *C*.

3.2 Annual Energy Generation

Normalized annual energy generation is estimated for different machines in all the sites considered in this study. Normalized annual energy generation indicates the annual energy generation per unit power of the machine. This estimation is essential to compare different rated machines. Table 5 presents the normalized annual energy generation from different machines. It is observed that machine *A* is generating lowest normalized annual energy and machine *E* is generating highest normalized annual energy. Machine *A* is generating maximum energy in Chawangkining, due to maximum capacity factor of this machine at this site. Machine E has maximum generation in Laimaton due to the maximum capacity factor of this machine at this site. This analysis is significant, as annual energy generation is directly related with cost of energy generation. The cost of energy is lower for higher normalized annual

Table 5 Normalized annual energy generation of different machines

Site	Normalized annual energy generation (kWh/kW)				
	Machine A	Machine B	Machine C	Machine D	Machine E
Borgaon	34	129	167	393	959
P.Leikul	430	936	1126	1743	2732
Tolpoi	78	239	302	618	1317
Likabali	106	322	415	823	1693
Passighat	68	203	253	517	1110
Raga	9	40	52	147	439
Phuldangsai	406	1007	1271	2074	3353
Tlangsang	439	1079	1360	2192	3488
Vanghmun	324	809	1015	1701	2858
Lunglei	439	1079	1360	2192	3488
Mamte	108	320	408	802	1637
Reiek	642	1357	1628	2397	3519
Chawangkining	881	1819	2171	3062	4258
Dolangkhnou	687	1553	1908	2838	4137
Laimaton	813	1883	2331	3402	4795

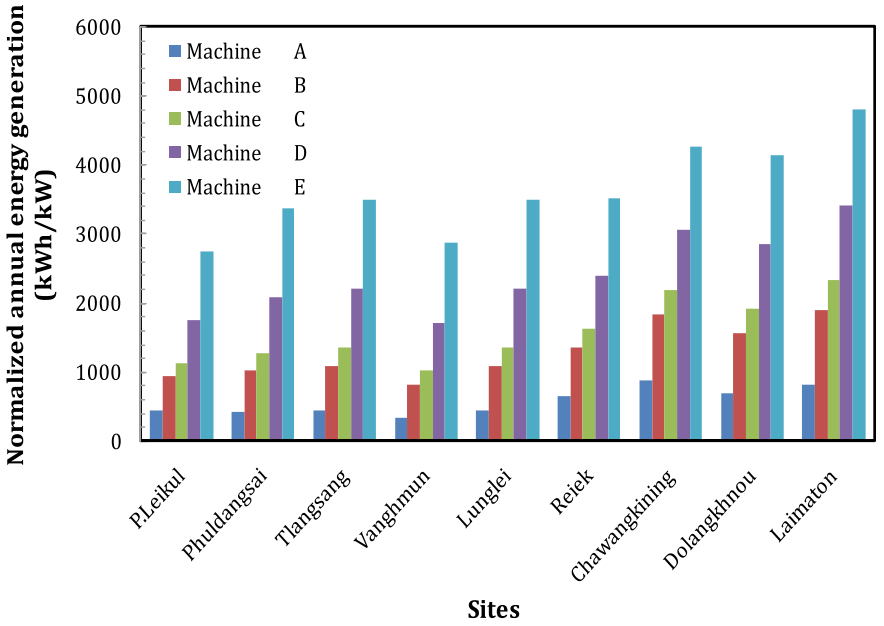

Fig. 2 Normalized energy generation from different machines in selected sites

energy generation. The cost of energy generation for machine E is the lowest among all the machines.

Figure 2 presents the normalized annual energy generation of different machines for nine selected sites. It is observed that the lowest normalized annual energy generation is in P.Leikul for machine *A* and highest normalized annual energy generation is in Laimaton for machine *E*. The normalized annual energy generation for the site Laimaton is 4795 kWh and 3402 kWh for machine *D* and machine *E*, respectively. The rated capacity of machine *D* and machine *E* is 5 kW and 1 kW, respectively. It can be concluded that Chawangkining, Dolangkhnou, and Laimaton are the best sites among all the sites selected for the analysis. The machine *D* and *E* are the most suitable machines for these low-windy sites. Off-grid wind energy systems of 1–5 kW capacity are most promising for Chawangkining, Dolangkhnou, and Laimaton sites. This off-grid system shall be able to provide power in these remote locations with lowest cost of energy.

4 Conclusions

The present study analyzed the feasibility of installation of wind machines in the North-Eastern region of India by estimating the capacity factors and normalized annual energy generation of few commercially available machines at selected sites of

the region. It is observed that few sites have potential for installation of wind turbine. However, as the mean wind speed is relatively low in these sites, smaller capacity (1–5 kW) machines are most suitable for the region. It is found that Chawangkining, Dolangkhnou, and Laimaton of Manipur are the most suitable location for installation of the low capacity wind machines. The low capacity machines can be used as an off-grid energy system to provide electricity access in these remote locations of the region with lowest cost of energy. However, performance evaluation of demonstration off-grid wind energy systems at Chawangkining, Dolangkhnou, and Laimaton of Manipur needs to be carried out. Finally, it can be concluded that smaller capacity wind turbine as decentralized off-grid system has potential for installation in the selected places of the region.

References

1. Ohunakin SO, Ojolo SJ, Ogunsina SB, Dinrifo RR (2012) Analysis of cost estimation and wind energy evaluation using wind energy conversion systems (WECS) for electricity generation in six selected high altitude locations in Nigeria. Energ Policy 48:594–600
2. Boccard N (2009) Capacity factor of wind power realized values versus estimates. Energ Policy 37:2679–2688
3. Huang S, Wan H (2009) Enhancement of matching turbine generators with wind regime using capacity factor curves strategy. IEEE T Energ Conver 24(2):551–553
4. Jangamshetti SH, Rau VG (1999) Site matching of wind turbine generators: a case study. IEEE T Energ Conver 14(4):1537–1542
5. Fuglsang P, Bak C, Schepers JG, Bulder B, Cockerill TT, Claiden P, Olesen A, Rossen R (2002) Site-specific design optimization of wind turbines. Wind Energ 5:261–279
6. Ayodele TR, Jimoh AA, Munda JL, Agee J (2012) T: Wind distribution and capacity factor estimation for wind turbines in the coastal region of South Africa. Energ Convers Manage 64:614–625
7. Jowder FAL (2009) Wind power analysis and site matching of wind turbine generators in Kingdom of Bahrain. Appl Energ 86:538–545
8. National Institute of Wind Energy (2020) https://www.niwe.res.in. Accessed on 12 Jun 2020
9. Centre for Wind Energy Technology (2012) https://www.cwet.tn.nic.in. Accessed on 12 Jan 2012

Chapter 18
Optimization of Multi-Parabolic Profile Flat-Plate Solar Collector for Space-Heating Application

Vikas Verma

Abstract In the recent decades, the demand for energy in India is growing at a very high rate such that the conventional energy sources are not sufficient to meet the demand. However, renewable energy have also been harnessed to some extent. In this work, an efficient multi-parabolic flat-plate solar collector is optimized for maximum efficiency. This collector simple is in construction and 39% more collector surface area as that of a flat-plate collector of 8 m^2. Solar collector is designed and optimized for 1.5 ton heat capacity of GSHP system during winter season for Roorkee, India, climatic condition. Theoritical analysis has been carried out for optimizing the design and performance parameters. Eight parameters at mixed levels have been considered using L_{18} ($2^1, 3^7$) orthogonal array in the Taguchi method, and the results indicate that 52.34% of maximum collector efficiency has been achieved with 6.8 m^2 of minimum collector area.

Keywords Multi-parabolic profile flat-plate solar collector · Area and efficiency · Taguchi method · S/N ratio · Space heating

Nomenclature

A_c	Area of solar collector (m^2)
C_f	Specific heat capacity (J/kg K)
CR	Concentration ratio
d	Diameter of collector pipe (mm)
FR	Heat removal factor
h	Heat transfer coefficient (W/m^2K)
I	Solar radiation (W/m^2)
L	Length (m)
m	Mass flow rate (kg/s)

V. Verma (✉)
Department of Energy, Tezpur University, Tezpur Assam, India
e-mail: vikas@tezu.ernet.in

S. Mahapatra et al. (eds.), *Advances in Energy Technology*, Advances in Sustainability Science and Technology, https://doi.org/10.1007/978-981-15-8700-9_18

r	Radius of pipe (mm)
S	Absorbed flux by MPPFPSC (W/m^2)
SAGSHPS	Solar-assisted ground-source heat pump system
GCHP	Ground-coupled heat pump
T	Temperature (°C)
U	Overall loss coefficient (W/m^{2}K)

1 Introduction

This solar collector is well understood system to convert solar energy to thermal energy. The sole aim of solar collector is to achieve higher energy conversion efficiency by using different shapes of concentrator for production of hot water, electricity, and space heating. In general, around 29% of energy spent for space-heating/cooling demand is met by conventional system. In order to overcome the uses of conventional system, solar collector plays a major role in space-heating applications such as solar-assisted ground-source heat pump system (SAGSHP). Bertram [1] simulated a SAGSHP system with ground heat exchanger using TRNSYS simulation to understand the impact of seasonal performance of solar energy on the system performance. They studied the solar energy impact by varying the flat-plate collector area from 0 to 30 m^2. Huajun Wang and Wang and Qi [2] carried out an experimental study to analyze the performance of an underground thermal storage system using a 25 m^2 area of evacuated tube solar collector and 50 m depth ground-coupled heat pump system for residential building—and they reported about 70% efficiency for the evacuated tube collector. Chen et al. [3] performed a study on 21 m depth ground-coupled heat pump with 13.6 m^2 evacuated tube solar collector for space-heating applications. Based on their experimental results, they found that the SAGSHP system is more efficient as compared to conventional system for space heating. Bakirci and Yuksel [4] investigated the thermal performance of a solar source heat pump system for residential heating through 19.68 m^2 flat-plate solar collector. Based on the experimental results, they found that the solar collector efficiency varied from 33 to 47%, while the COP of heat pump and whole system were found to be 3.8 and 2.9, respectively. Chen et al. [5] simulated long-term solar-assisted ground-coupled heat pump system with 45 m^2 area of flat-plate solar collector. They found 26.3% of improvement as compared to traditional GSHP system, also the collector efficiency varied from 55 to 58% and reported 22% energy saving of the total heating load. Wang et al. [6] showed that injection of heat into the borehole was very important to improve the overall COPsys of SAGSHPS and HSGSHPS, and he could reach 3.42 and 2.99 from 3.17 and 2.95 and proposed a hybrid ground source heat pump system which can reduce electrical energy demand by 32%. Chen and Yang et al. [7] carried out a simulation on solar-assisted ground-coupled heat pump system under specified load condition for a collector area of 40 m^2 with bore-hole length of 264 m. System performance could be reached to 3.55. Bi et al. [8]

demonstrated that the average COP of the SGSHP system is 2.78, and the vertical double-spiral coil (VDSC) GHX was also justified in decreasing the temperature interference between the interior and exterior coil pipe. Yang et al. [9] performed a short time simulation by different combination modes of solar collector and GHXs, based on 20-day simulation, and the highest COP of 3.46 and energy saving rate of 14.5% were achieved when solar collector and GHX both are connected in series mode. Yumrutas and Kaska [10] reported annual heat pump COP values between 2.5 and 3 based on experimental investigation of thermal performance of a solar-assisted heat pump system with energy storage. Trillat-Berda et al. [11] carried out an experimental study of GCHP with 180 m^2 solar collector area. After 11 month in operation, the average value of power extraction and injection into the ground were 40.3 and 39.5 W/m, respectively, and the average COP of heat pump was 3.78. Han et al. [12] designed and simulated a solar-assisted ground-source heat pump (SAGSHP) heating system with latent heat energy storage tank (LHEST) in Harbin. They also obtained an average performance around 3.28 over the whole heating period. Jilin University and Hebei Engineering University also carried out some research on the design simulation and experiments using the SAGCHP system [13, 14].

In this work a multi-parabolic profile flat-plate solar collector has been proposed with GSHP system for space-heating application for minimum solar collector area and maximum efficiency through Taguchi method for Indian climatic condition. The main objective is to understand the effect of solar collector in GSHP system for space-heating applications. Solar-assisted ground-source heat pump system is one of the best energy utilization technology for higher energy saving and environmental protection.

2 System Description

SAGSHP system consists of two different components, one is solar collector, and the second one is ground coupled heat exchanger as shown in Fig. 1. In this system, heat pump consists of a compressor, condenser, expansion valve, evaporator, and fan coil unit. In the SAGSHP system, water is considered as the working fluid for extracting heat from the solar collector and GHX unit from where it is transmitted to the heat pump through refrigerant R-22. In SAGSHP system for heating mode, the evaporation of the refrigerant takes place in the evaporator using the heat absorbed from heat sources such as ground heat exchanger and solar collector. The heat rejected in the condenser is then used for space heating by means of a fan coil unit, and then, the refrigerant is sent back to evaporator through an expansion valve, where hot water becomes cold and again sent back to solar collector and ground heat exchanger.

The performance of the MPPFFP solar collector mainly depends on factors such as collector area (m^2), solar intensity, and absorbed heat flux. As the solar insolation available during winter season is less, it is essential to optimize the solar collector to obtain maximum heat output. In the present research work, Taguchi method has been implemented to optimize the area and efficiency of the MPPFP solar collector

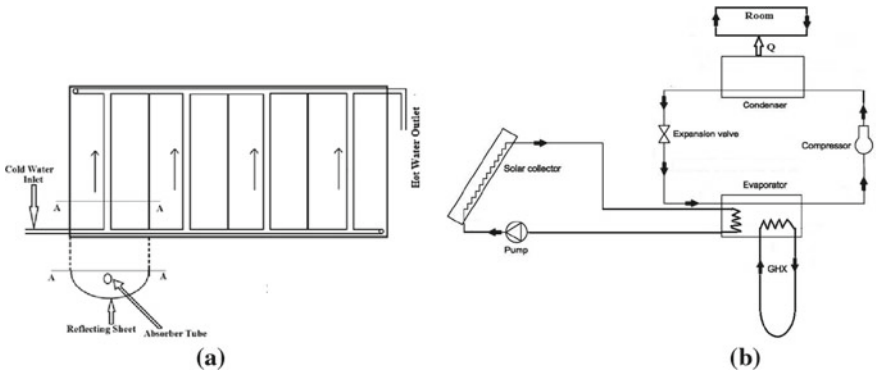

Fig. 1 Schematic diagram of **a** Multi-parabolic profile flat-plate solar collector, **b** solar-coupled heat pump system

using thermodynamic analysis. The following temperatures were measured at various points in the MPPFP solar collector during experiments in winter: water inlet temperature into the collector = 14 °C, average ambient temperature = 13.8 °C, average sky temperature = 7.8 °C.

3 Thermal Design of MPPFP Solar Collector

Multi-parabolic profile solar collector consists of four number of aluminum sheets bent in parabolic shape and are stacked in series on a support, resembling a flat-plate collector. The absorber tube is located exactly at the focal point of the parabola. All the absorber tubes are connected to inlet outlet header tubes which finally interacts with an intermediate heat exchanger. Solar collector efficiency directly depends on different factors such as outlet temperature, energy gain by collector, area of collector, and material of collector, but the important uncontrollable parameter is solar intensity. MPPFP solar collector gives high output temperature as compared to flat-plate solar collector, while solar intensity is minimum. Solar collector efficiency can be calculated by using the following relations [15]:

$$\eta_{\mathrm{i}} = \frac{Q_u}{A_{sc} I_b} \tag{1}$$

$$A_{sc} = \frac{F_R(\tau\alpha) I_b - F_R U_{\mathrm{Total}} \Delta T}{I_b\left(\frac{\tau\alpha}{1-(1-\alpha)\rho_g}\right) - \left\{\frac{1}{h_i} + \frac{r_i}{k}\mathrm{In}\left(\frac{r_o}{r_i}\right) + \left(\frac{r_i}{r_o}\right)\frac{1}{h_o}\right\}(T_{\mathrm{in}} - T_a)} \tag{2}$$

where $\tau = 0.88$ and $\alpha = 0.95$. These values correspond to the test results for thermodynamic relations [16], r_i and r_o represent the inner and outer radii of solar collector absorber tube, respectively. Total energy gain (Q_U) and total heat loss by MPPFP

solar collector system are written as

$$Q_u = F_R(W - d_0)L\left[S - \frac{U_{Total}}{CR}(T_{in} - T_a)\right], \tag{3}$$

$$U_{\text{Total}} = U_{FP} + U_{PC} \tag{4}$$

In this calculation, overall loss based on the convection and re-radiation losses is considered. Total loss of multi-parabolic profile flat-plate solar collector can be calculated as

$$U_{PC} = \frac{\frac{q_L}{L}}{\pi d_0(T_{pm} - T_a)} \tag{6}$$

$$U_{FP} = U_t + U_b + U_s \tag{7}$$

where U_t, U_b, and U_s indicate the top losses, bottom losses, and side losses, respectively.

4 Optimization of MPPFP Solar Collector

4.1 Taguchi Technique

Taguchi method is efficient and systematic approach to optimize design for performance and quality using standard orthogonal array in matrix form of experiments. Taguchi method calculates certain typical models according to the orthogonal array instead of all the possible models. The main objective of Taguchi method is to select the optimal combination of control factors. Finally, the results are analyzed from each trial runs using signal-to-noise ratio (SN), analysis of variance (ANOVA), and response table. There are three different types of performance characteristics for analysis using the S/N ratio: lower-the-better, higher-the-better, and nominal-the-best. The use of ANOVA is to find out the percentage contributions of individual parameters, and based on the above results, one will be able to find out the influential parameters and their levels that contribute for the performance parameter selected in a particular analysis.

4.2 Taguchi—Design of Experiments

In the present research, eight parameters at mixed levels are used in the Taguchi method for the experimental trial runs. Before selecting an orthogonal array, the

minimum number of experiments to be conducted can be fixed by using the following relation [15]:

$$N_{\text{Taguchi}} = 1 + NV(X - 1)$$

In the present analysis where N_{Taguchi} = number of experimental trial runs, total number of parameters ($NV = 8$) and mixed level (X) was used with L_{18} (2^1, 3^7) orthogonal array. As the main aim of the present research is to optimize the MPPFP solar collector area and efficiency, lower the better criterion is used for solar collector area, whereas higher the better criterion is selected for the collector efficiency. These ratios can be computed using the following expressions:

$$\text{Lower the better } S/N(db) = -10\log\left(\frac{1}{r}\sum_{i=1}^{r} X_i^2\right)$$

$$\text{Higher the better } S/N(db) = -10\log\left(\frac{1}{r}\sum_{i=1}^{r} X_i^2\right)$$

where X_i = performance value at a given observation and i = number of repetitions in a trial.

5 Results and Discussion

The main focus of this work is to find out the levels of parameters for optimum solar collector area and efficiency of multi-parabolic profile flat-plate solar collector system for space-heating application. Mostly the performance of collector depends on both controllable and uncontrollable parameters such as solar radiation, thermal conductivity of solar collector pipe, mass flow rate of collector fluid, diameter of collector pipe, thermal conductivity of fluid, heat transfer coefficient of fluid, reflectivity and transmissivity of glass cover, absorptivity of the material, emissivity of reflecting sheet and collector pipe, heat removal factor, concentration ratio of solar collector, overall losses by solar collector, insulation thickness, energy gain by solar collector, wind velocity, ambient temperature, sky temperature, specific heat capacity of collector fluid. However, for the purpose of optimization of the MPPFP solar collector, only eight controllable parameters have been considered. These parameters are thermal conductivity of fluid (A), diameter of pipe (B), number of glass cover (C), solar intensity (D), mass flow rate of water (E), emissivity of absorber pipe (F), height of side cover (G), reflectivity of glass cover (H), and considered an $L_{18}(2^1, 3^7)$ orthogonal array for experimental trial runs with mixed levels, considering one parameter at two levels and seven parameters at three levels are given in Table 1.

Table 1 Parameters and their levels

Label	Parameters	Level		
		1	2	3
A	Thermal conductivity of fluid (W/m K)	0.65	0.26	-
B	Diameter of pipe (inch)	1	1.5	2
C	Number of glass cover	1	2	3
D	Solar intensity	302	368	447
E	Mass flow rate of water (kg/s)	0.3	0.4	0.5
F	Emissivity of absorber pipe (−)	0.85	0.90	0.95
G	Height of side cover (mm)	300	350	400
H	Reflectivity of glass cover (−)	0.12	0.16	0.24

5.1 Taguchi Method—Signal-to-Noise Ratio

In Taguchi method, the important step after the selection of the experimental plan is to determine the signal-to-noise ratio (S/N) for all the experimental trial runs. The term signal illustrates the preferable effect for the output. In the present case, solar collector area and efficiency of MPPFPSC system and the term noise represents the undesirable effects on the outputs. In the present analysis, signal-to-noise ratios are calculated by using lower the better and higher the better concepts, respectively, for solar collector area and efficiency of MPPFPSC system. Based on the matrix of random experimental trial runs for calculating the solar collector area, efficiency, and S/N ratio of MPPFPSC system for space-heating application, the computed values are given in Table 2.

Using the values of Table 2, a response Table 3 for solar collector area and efficiency are computed to demonstrate the order of influencing parameters on the respective output on behalf of the rank of parameters defined on the basis of delta, which is the difference between the maximum and minimum values of each parameter. For example, ranks 1 and 8 indicate the most and least influencing parameter, respectively. The data given in Tables 3 are also depicted in Fig. 2 to highlight the final optimum influencing parameters. The levels of optimum parameters are A2B1C1D1E3F1G3H3 and A2B1C2D2E3F2G1H2 based on lower the better and higher the better concept, respectively, for solar collector area and efficiency.

5.2 Taguchi Method—ANOVA Analysis

ANOVA is used to formulate the relative significance of each parameter in terms of percentage contribution of overall response. The ANOVA Table 4 computed for both solar collector area and collector efficiency contain the data for Degree of Freedom

Table 2 Area and efficiency of MPPFP solar collector

Ex. no	SN ratio of MPPFPSC area	Area of MPPFPSC	SN ratio of MPPFPSC efficiency	Efficiency of MPPFPSC
1	−18.23	8.16	26.98	22.35
2	−18.04	7.98	29.46	29.73
3	−18.08	8.02	29.13	28.61
4	−17.94	7.89	28.12	25.49
5	−17.81	7.78	30.42	33.21
6	−18.65	8.57	25.95	19.84
7	−18.43	8.35	26.10	20.19
8	−18.28	8.21	26.55	21.28
9	−17.89	7.85	29.98	31.57
10	−17.21	7.26	33.86	49.36
11	−17.40	7.42	33.09	45.18
12	−17.12	7.18	33.89	49.51
13	−17.01	7.09	34.23	51.48
14	−17.75	7.72	31.94	39.56
15	−17.36	7.38	33.69	48.37
16	−17.45	7.46	33.05	44.96
17	−17.08	7.15	34.03	50.32
18	−17.60	7.59	32.50	42.17

Table 3 Response table for MPPFP solar collector area

Levels	1		2		3		Delta		Rank	
	(m^2)	(η%)	(m^2)	(η%)	(m^2)	(η%)	(m^2)	(η%)	(m^2)	(η%)
A	−18.14	28.08	−17.35	31.97	–	–	0.81	3.89	3	2
B	−17.72	31.08	−17.76	30.74	−17.79	30.54	0.07	0.54	7	6
C	−17.68	30.43	−17.73	30.93	−17.79	30.86	0.11	0.50	4	8
D	−17.09	31.00	−17.67	31.11	−17.91	30.49	0.82	0.62	2	5
E	−18.37	29.43	−17.70	30.80	−17.52	33.83	0.85	4.4	1	1
F	−17.67	30.30	−17.74	31.11	−17.76	30.92	0.09	0.0.81	6	3
G	−17.76	31.05	−17.80	30.53	−17.72	30.62	0.04	0.52	8	7
H	−17.75	30.67	−17.75	31.08	−17.65	30.8	0.10	0.70	5	4

(DF), sum of squares (SS), and mean of squares (SS); F is a ratio of the mean square error to the residual error and is traditionally used to determine the significance of a factor, and P is the ratio that indicates the percentage contribution by different control factors. The parameters with higher percentage contributions are ranked higher in terms of importance in the experiment and also have significant effects in controlling

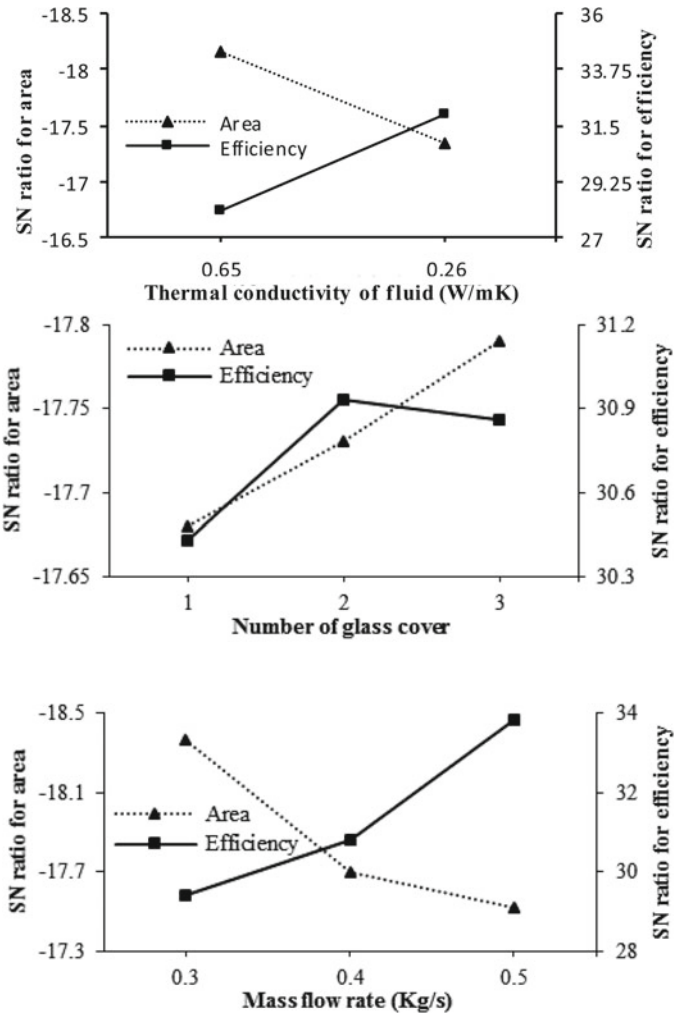

Fig. 2 Mean of S/N ratios for efficiency and area of MPPFP solar collector

the overall response. The variance and percentage contribution and sum of squares of the control factors, A, B, C, D, E, F, G, and H were computed for space-heating application with condition of maximum efficiency and minimum solar collector area of MPPFP solar collector system. The sum of squares (SS) and degree of freedom (DF) have been calculated by using the following equations:

$$SS = \frac{1}{2}\left\{(\text{sum of } S/N \text{ ratio level I})^2 + (\text{sum of } S/N \text{ ratio level I})^2 - C.F\right\},$$

$$\text{Correction factor } (C.F) = \frac{\left(\text{sum of } \frac{S}{N}\right)^2}{N}$$

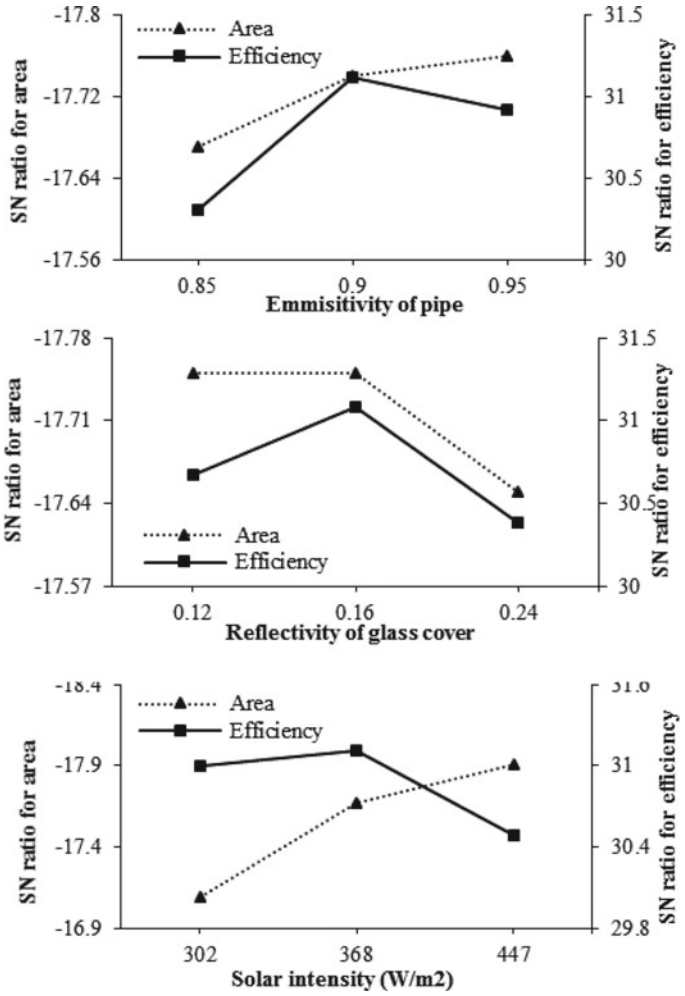

Fig. 2 (continued)

where N = total number of experiments ($N = 18$), and degree of freedom = level − 1.

5.2.1 Area of MPPFP Solar Collector

In the present analysis, the optimum levels of important parameters of solar collector have been selected to achieve the optimum area of collector. The parameters of influence considered are solar intensity and mass flow rate of fluid in collector tubes which flows inside the solar collector for extracting the heat from solar energy and

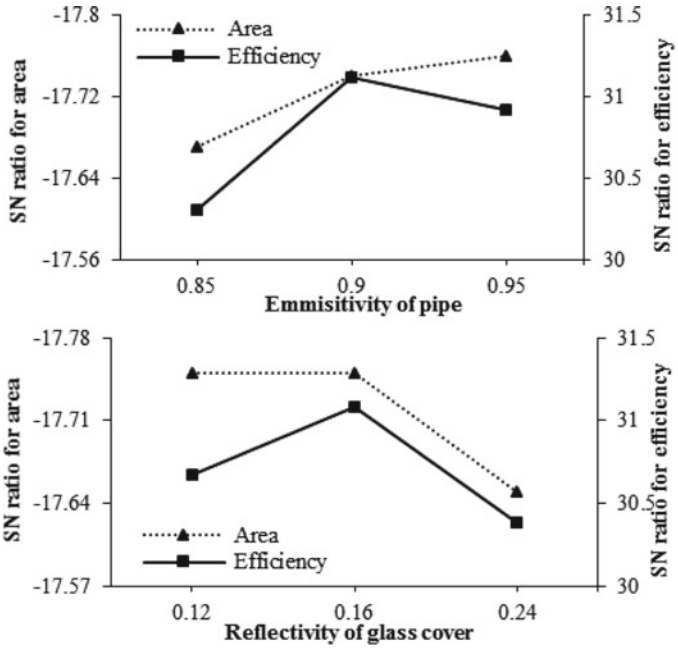

Fig. 2 (continued)

Table 4 ANOVA: Optimization of MPPFPSC area and efficiency

Source	DF	Sum of square (SS)		Mean of square (MS)		% of contribution	
		Area	Efficiency	Area	Efficiency	Area	Efficiency
A	1	6.3841	7.1532	6.3841	7.1532	13.6133	18.4083
B	2	3.4252	2.8796	1.7126	1.4398	7.8427	7.6103
C	2	5.9741	2.5486	2.98705	1.2743	12.8826	6.6577
D	2	9.2764	3.1543	4.6382	1.5771	19.4736	8.5174
E	2	12.7683	10.8275	6.4759	5.4137	26.7534	27.8487
F	2	3.8472	4.9587	1.9236	2.4793	7.9538	12.7609
G	2	1.3751	2.6759	0.68755	1.3379	2.8272	6.8853
H	2	4.2175	4.3567	2.10875	2.1783	8.6524	11.3114
Error	2	1.275	0.304	0.6375	0.152		
Total	17	48.6347	38.8585			100	100

converting in to heat energy, and the other parameters are taken as ambient temperature (Ta), transmittance of the cover (Ţ = 0.88), and absorptivity ($\alpha = 0.95$). The average ambient temperature of the given location [17] for heating period is assumed to be 13.8 °C, and also, it is assumed that the solar collector contributes heat energy around 3.5 kW, that is 50% of the total heating load. The calculated solar collector

area varies from 7.09–8.57 m^2. The main aim of ANOVA results is to predict the percentage contribution of each parameter that are used to calculate the optimum solar collector area. From Table 4, it can be noticed that the highest contribution comes from the mass flow rate of fluid (E) with 26.7% contribution followed by the solar intensity (D) with 19.47% contribution.

5.2.2 Efficiency of MPPFP Solar Collector System

In order to achieve the optimum efficiency of the MPPFPSC system, it is required to select the appropriate levels of all the contributing parameters. Table 4 shows the ANOVA results for the efficiency of MPPFPSC system. The ANOVA tabular values show that all the parameters contribute for calculating the efficiency of MPPFPSC system in the form of percentage contribution value. It can be observed that the mass flow rate of fluid (E) contributes the highest percentage (27.84%) value among all the parameters. From this table, the higher percentage contributing parameters ranking can be found as EAFHDBGC.

5.3 Taguchi Method—Confirmation Test

The solar collector area was predicted based on different parameters like heating load and average ambient temperature for Indian climatic conditions. Taguchi conformation test has been carried out from 18 experimental trial runs. Based on these calculations, the computed values of solar collector area and efficiency of MPPFP solar collector system are given in Table 2. From these results, it is observed that the solar collector area and efficiency of MPPFPSC system varies from 7.09 m^2 to 8.57 m^2 and 19.84 to 51.48, respectively. The efficiency of MPPFPSC system directly depends on the area of solar collector. Based on the best set of operating parameters among the L_{18} Taguchi array, the optimum area of solar collector and efficiency of MPPFPSC system are found to be 6.8 m^2 and 52.34%, respectively. Thus, implementation of Taguchi method has made it possible to determine the optimum values of solar collector area and efficiency of MPPFPSC system using the control factors at different levels listed in 18 experimental trial runs.

6 Conclusion

Solar-assisted ground-source heat pump is an important alternate technology for utilization of renewable energy for space-heating applications. In this study, an attempt has been made to find out the optimum area and efficiency of MPPFP solar collector for space-heating application using Taguchi method through L_{18} orthogonal array at mixed levels. Simulation results were obtained for all the 18 trial runs

for optimum solar collector area and efficiency. Based on the optimization, solar collector area is found to be 6.8 m^2 using the Taguchi method for space-heating application. Also found that mass flow rate and solar intensity are to be more influencing parameters for optimizing the solar collector area. They contributes around 26.75 and 19.47%, respectively, but for the term of efficiency, mass flow rate also contributes a more percentage around 27.84% and thermal conductivity of pipe contributes around 18.4%. Finally, it was found that with the predicted levels of parameters, the MPPFP solar collector could achieve maximum efficiency of 52.34%.

References

1. Bertram E (2014) Solar assisted heat pump systems with ground heat exchanger simulation studies. Energy Procedia 48:505–514
2. Wang H, Qi C (2008) Performance study of underground thermal storage in a solar ground coupled heat pump system for residential buildings. Energy Build 40:1278–1286
3. Chen X, Hongxing Y, Lin L, Jinggang W, Wei L (2011) Experimental studies on a ground coupled heat pump with solar thermal collectors for space heating. Energy 36:5292–5300
4. Bakirci K, Yuksel B (2011) Experimental thermal performance of a solar source heat pump system for residential heating in cold climate region. Appl Therm Eng 31:1508–1518
5. Chen X, Lin L, Hongxing Y (2011) Long term operation of a solar assisted ground coupled heat pump system for space heating and domestic hot water. Energy Build 43:1835–1844
6. Wang E, Fung A, Chengying Q, Leong W (2012) Performance prediction of a hybrid solar ground source heat pump. Energy Build 47:600–611
7. Chen X, Yang H (2012) Performance analysis of a proposed solar assisted ground coupled heat pump system. Appl Energy 97:888-896
8. Bi Y, Guo T, Zhang L, Che L (2008) Solar and ground source heat pump system. Appl Energy 78:231–245
9. Yang W, Shi C, Dong H (2006) Numerical simulation of the performance of a solar-earth source heat pump system. Appl Therm Eng 26:2367–2376
10. Yumrutas R, Kaska O (2004) Experimental investigation of thermal performance of a solar assistedvheat pump system with an energy storage. Int J Energy Res 28:163–175
11. Berdal V, Souyri B, Fraisse G (2006) Experimental study of a ground coupled heat pump combined thermal solar collectors. Energy Build 38:1477–1484
12. Han Z, Zheng M, Kong F, Wang F, Li Z, Bai T (2008) Numerical simulation of solar assisted ground source heat pump heating system with latent heat energy storage in severely cold area. Appl Therm Eng 28:1427–1436
13. Wu X (2008) Research and simulation analysis of combining solar collector and ground source heat pump heating system. PhDthesis. Department of Geology Engineering, Jilin University, PR China
14. Kanhong W (2008) Heating Experiment of solar-ground source hybrid heat pumps. HV and AC 38:665–680
15. Verma V, Murugesan K (2014) Optimization of solar assisted ground source heat pump system for space heating application by Taguchi method and utility concept. Energy Build 82:296–309
16. Sukhatme SP, Nayak JK (2008) Solar Energy, 3rd edn. Tata McGraw Hill
17. https://eosweb.larc.nasa.gov/sse/RETScreen/

Chapter 19
Energy Performance Assessment of Gas-Based Thermal Power Plants

Deepjyoti Barman, Samar Jyoti Hazarika, and Sadhan Mahapatra

Abstract Thermal power plants are energy-intensive industry, where energy auditing is required to identify the areas for energy performance improvement. The present study evaluates the energy performance assessment of a combined cycle and an open cycle gas-based thermal power plant. Assam Gas Based Power Plant, Assam, is a combined cycle power plant, and Agartala Gas Thermal Power Plant, Tripura, is an open cycle power plant which are considered for this study. The natural gas consumption, station heat rate, calorific value of fuel, energy generation, auxiliary power consumption, etc., are assessed. The energy performance of various systems and subsystems like gas turbine compressor, gas turbine, waste heat recovery boiler, steam turbine, steam condenser, cooling tower, and auxiliaries are estimated. The key finding related to various energy conservation opportunities available in the various systems are presented in this study.

Keywords Combined cycle · Open cycle · Gas-based power plant · Energy performance

1 Introduction

The installed capacity of electricity by different sources in India is 370 GW as on May 23, 2020 [1]. Thermal-based power generation dominates in the total installation in the country. Coal-based power plant shares 55.4% and diesel-based power plant shares 6.7% of total electricity installed capacity in India. Figure 1a presents the share of various source-based electricity installation capacity in India in the year 2020. The primary sources of energy for electricity are coal, gas, diesel, hydropower, and renewable energy sources like small hydropower, solar photovoltaic, and biomass

D. Barman · S. Mahapatra (✉)
Department of Energy, Tezpur University, Tezpur 784028, Assam, India
e-mail: sadhan.mahapatra@gmail.com

S. J. Hazarika
Department of Energy Engineering, North Eastern Hill University, Shillong 793022, Meghalaya, India

S. Mahapatra et al. (eds.), *Advances in Energy Technology*, Advances in Sustainability Science and Technology, https://doi.org/10.1007/978-981-15-8700-9_19

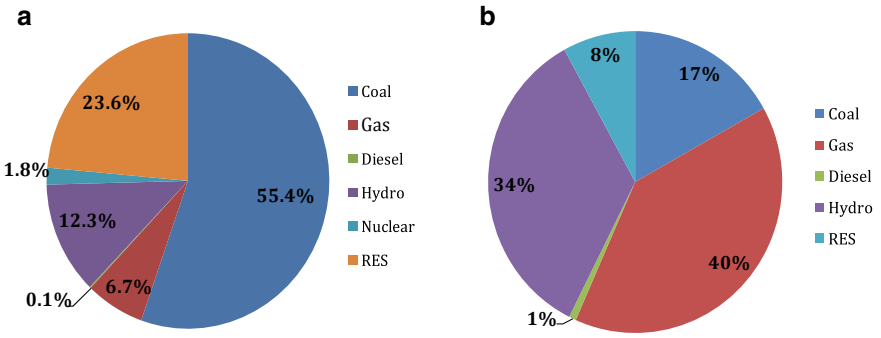

Fig. 1 **a** Share of different source-based electricity installed capacity in India, **b** share of different source-based electricity installed capacity in North-East India

in the North-Eastern region of India. The present installed capacity is 4560 MW in the North-Eastern region of India [1]. The total installed capacity of electricity is comparatively low in the North-Eastern region in comparision with other regions of India. Figure 1b presents the share of various source-based electricity installation capacity in North-Eastern region in the year 2020. It is important to note that gas-based electricity generation share is higher in the region in comparision with national share. The total installed capacity based on gas-based electricity generation is 1812 MW out of total installed capacity of 4560 MW. The Assam Gas Based Power Plant (AGBPP) with installed capacity of 291 MW (combined cycle) and Agartala Gas Turbine Power Plant (AGTPP) (open cycle) with installed capacity of 84 MW are considered for the present study. The projects were executed by North Eastern Electric Power Corporation Ltd. AGBPP plant consists of three combined cycle modules. Each module comprising of two numbers of gas turbine units, two numbers of waste heat recovery boilers, and one number of steam turbine unit. AGTPP consists of four numbers of gas turbine units operated in an open cycle mode.

Energy audit is a systematic approach to measure and analyze the use of energy to improve the energy efficiency and find out the scope for energy conservation in an industry. Various energy efficiency assessment studies for thermal power plant are carried out by various researchers. Paul et al. have done a detailed analysis of harnessing maximum energy from thermal power stations and reducing all controllable losses in all operations and system [2]. Condenser vacuum, excess airs, and all types of auxiliaries are investigated for performance improvement of the power plants. A suitable approach has been illustrated in this study to renovate, repair, or replace the components, whose performance is poor compared to modern technologies. Abdelaziz et al. present a review on energy saving in industrial sector and suggested for incorporation of modern technologies such as high efficiency motor, variable speed drives, and reducing pressure drop.[3]. Ghosh has done a detailed analysis of thermal power generation in India and compared the electricity generation and specific CO_2 emissions among the power plants [4]. The study also identified

the plants those are to be modernized. Graus et al. have compared the energy efficiency of fossil-fuel-based power generation for 14 countries including India [5]. This study concluded that, if all countries produce electricity at highest efficiencies, there is energy saving and CO_2 emission reduction potential of 45% and 860 Mtonne, respectively. Kanoglu and Dincer reported the performance assessment of various cogeneration plants through energy and exergy efficiencies [6]. The study concluded that energy and exergy analyses are useful tool for the performance assessment of cogeneration system and provide a reasonable comparison of different cogeneration systems. Aguilar et al. investigated the energy savings and CO_2 reduction potential in gas turbine/steam generator-based cogeneration plant [7]. The study predicts the performance of the plant which is operated at part load. Shrivastava et al. evaluated performance assessment of 60 coal-based thermal power plants in India [8]. The performance assessments of small, medium, and large power plants are compared. It is observed that the efficiency of small power plants is lower in comparision with medium or large capacity power plants. The study also suggested the possible measures to improve the performance of the plants. Najjar has studied 12 gas turbine systems and analyzed the applications of combined systems in industry [9]. The study reported that gas turbine engines have environmental advantages and required low capital cost in comparision with steam power plants. Rahman et al. studied thermodynamics performance and the effect of operating conditions on the performance of gas turbine power plants [10]. It is observed that the compression ratio, ambient temperature, and air-to-fuel ratio are key parameters which affect the performance of the plant.

A detail energy performance study is carried out for two thermal power plants, namely Assam Gas Based Power Plant (AGBPP), Assam, which is a combined cycle power plant, and Agartala Gas Thermal Power Plant (AGTPP), Tripura, which is operated in an open cycle mode. A gas-fired combined cycle power plant uses both gas and steam turbine generator. Gas-turbine-based combined cycle power plant consist of gas turbine cycle (compressor, combustion chamber, and gas turbine), waste heat recovery boiler, and steam turbine. Natural gas is used as fuel, which is introduced into the combustion chamber where combustion takes place with compressed air coming from the axial compressor. The hot air–fuel mixture is the working fluid which moves the gas turbine blades. The turbine drives a generator that converts a portion of the energy to electricity. The hot exhaust gases from the gas turbine are then allowed to enter into waste heat recovery steam generator for steam generation. Steam turbine rotates the generator drive shaft and converts into additional electricity from the waste heat. The objective of this study is to find out the scope for energy efficiency/performance improvement and effective utilization of energy for open cycle and combined cycle gas-based thermal power plants.

2 Performance Assessment

Assam Gas Based Power Plant (AGBPP) has the installed capacity of 291 MW. The plant consists of three combined cycle modules. Each module comprising of two numbers of gas turbine units, two numbers of waste heat recovery boilers, and one number of steam turbine unit. The ratings of each unit are presented in Table 1. Typical module overview (three modules operational) is presented in Fig. 2. The plant load factor of AGBPP varies from 67.8 to 72% against the average plant load factor of gas-based power station in India of 66.2% in the year 2010–2011. The impact of unavailability of natural gas influences the plant operations detrimentally. The effects of part load operations on overall station heat rate and overall station economy reflect the need for station to be operated at higher plant load factor.

Efficiency of thermal power plant is a function of overall station heat rate, and it is inversely proportional to station heat rate. The average operative gross station heat rate was 2372.2 kCal/kWh, and specific fuel consumption was 0.29 SM^3/kWh. This operative gross station heat rate is higher than the design value. Low operative gross station heat rate is desirable which reflects higher thermal efficiency and lower specific fuel consumption. There are six GT installed module wise using natural gas as fuel. Each module consists of two numbers of gas turbines. The design efficiency of the gas turbines is 97%, whereas the efficiency of the gas turbines lies in between 77.0 and 79.6%. It is found that the heat transfer effectiveness of all six numbers waste heat recovery boiler lies in between 72.5 and 74.8%. There are three numbers of steam turbine generators with 30 MW each. Each steam turbine generator is supported by two waste heat recovery boilers. The efficiency of these steam turbines lies in between 25.5 and 27.8%. The condenser is the most important component of turbine cycle that affects the turbine heat rate. There are three numbers of steam condensers at AGBPP. The design heat transfer effectiveness of steam condenser is

Table 1 Module-wise rating of gas turbine and steam turbine

Module	GT/ST generator unit	Steam generating unit	Rating at base load (MW)
I	Gas turbine 1	WHRB 1	33.66
	Gas turbine 2	WHRB 2	33.66
	Steam turbine 1	WHRB 1 and WHRB 2	30.00
II	Gas turbine 3	WHRB 3	33.66
	Gas turbine 4	WHRB 4	33.66
	Steam turbine 2	WHRB 3 and WHRB 4	30.00
III	Gas turbine 5	WHRB 5	35.01
	Gas turbine 6	WHRB 6	35.01
	Steam turbine 3	WHRB 5 and WHRB 6	30.00

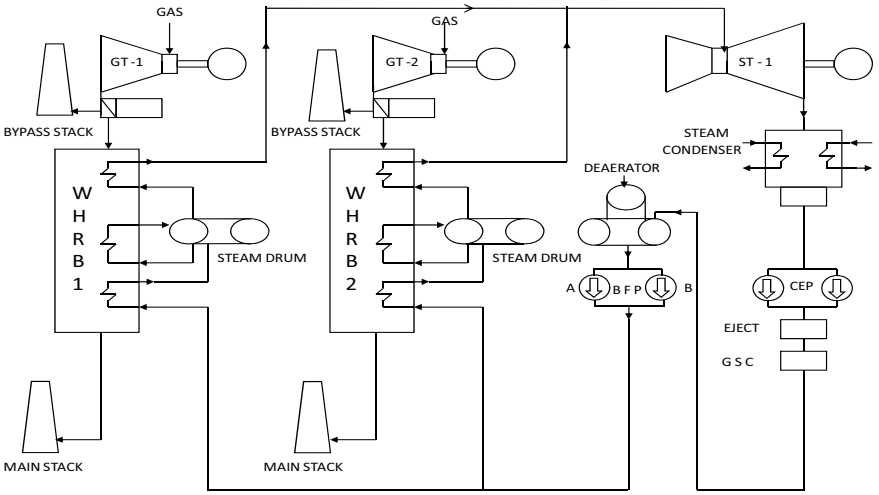

Fig. 2 Typical module overview

given as 60%, and as-run values are found in between 51.3 and 56.8%. The cooling tower effectiveness has been found in the range of 51.1 to 57.9% by conducting as-run trial on parameters like cooling water inlet and outlet temperature, air dry bulb and wet bulb temperature, etc. The evaporation loss from cooling tower is found in the range of 559–679 m^3/h. There are six numbers of boilers feed pumps that are used for waste heat recovery boilers, out of which three numbers remain standby during the study. There are six numbers of pumps used for condensate extraction, out of which three number of pumps are used in operation and other three remain standby. The design efficiency of the pump is 63%, and as-run values show that the condensate extraction pump efficiency lies in between 56 and 60%. The circulating water pumps pump efficiency lies in between 64 and 66%, whereas the design efficiency of the pump is much higher.

Agartala Gas Turbine Power Plant (AGTPP) with an installed capacity of 84 MW consists of four numbers of gas turbine units operated in an open cycle mode. The ratings of each unit are presented in Table 2. The efficiency of all four gas turbine compressor are estimated by conducting an as-run trial and found that it is lies in between 82.4 and 83.2%. The efficiency of all four gas turbine compressor are

Table 2 Rating of GT units at AGTPP

Generator unit	Rating at base load (MW)
Gas turbine 1	21.34
Gas turbine 2	21.01
Gas turbine 3	21.01
Gas turbine 4	21.01
Total	84.37

calculated and found that it is in between 84.2 and 84.7%. It is observed that the percentage of loading of the cooling tower fan for GTG 1 lies in between 55.8 and 59.36%. Likewise, the percentage of loading of cooling tower fan for GTG 2, GTG 3, and GTG 4 lies in between 50.7 to 55.9%, 58.0 to 59.3%, and 50.5 to 58.0%, respectively.

3 Scope for Energy Conservation

The design efficiency for GT compressors are 84% at 23 ^{0}C base load condition, whereas the as-run efficiency lies between 73.74 and 76.37% in AGBPP. This may be due to high inlet filter pressure drop, high inlet air temperature, cleanliness of the compressor blade, etc. Daily monitoring and reporting of GT compressor parameters and efficiency is a necessary task required for efficiency improvements. Individual gas consumption metering is strongly recommended for enabling performance assessment of GTGs, merit rating, planning, and need-based O & M interventions. Daily monitoring of natural gas GCV is recommended for reporting of heat rate, station performance. Major results for performance improvement include cooling towers.

AGTPP is operated in open cycle mode, where the exhaust flue gas from gas turbine is released to atmosphere at 480–500 °C. This can be converted to combined cycle mode by using waste heat recovery boiler. AGTPP has a generation capacity of 84 MW in open cycle mode of operation, which can be improved up to 126 MW by converting it in to a combined cycle mode. The specific fuel consumption will be reduced from 0.41 SM^3/kWh to 0.27 SM^3/kWh due to this conversion. Station heat rate is an important parameter for improvement of a thermal power plant. The station heat rate of AGTPP is 3753.2kCal/kWh against the CERC target 3500 kcal/kWh. In combined cycle mode of operation, considering specific fuel consumption as 0.27 SM^3/kWh and GCV value same as in open cycle, the station heat rate can be reduced to 2427.8 kcal/kWh. The overall efficiency of AGTPP is 22.9% considering specific fuel consumption as 0.41 SM^3/kWh and station heat rate value 3753.2 kcal/kWh. The overall efficiency of the plant can be improved up to 35.4% by considering specific fuel consumption as 0.27 SM^3/kWh and station heat rate as 2427.8 kcal/kWh.

The auxiliary power consumption in open cycle mode is found to be 12.63 MU, which can be increased up to 29.82 MU annually for combined cycle mode. It is observed that the motor loading of the cooling tower fans for all units is in between 50 and 59%. However, by installing fans of 10 kW instead of existing 15 kW, at least 75% of the motor loading can be achieved. The annual saving for 8000 h will be 480,000 kWh (i.e., 120,000 kWh units wise). The total annual saving including all four units (including three fans in each unit) would be Rs. 1,440,000. The simple payback period for this replacement will be only 3 months. The percentage of motor loading of the cooling tower fans (gas turbine) is 54.5%. It is envisaged that by replacing the 15 kW cooling tower fan motors for the GTG 1 and GTG 3 to 10 kW, annual saving for 8000 h of operation is 80,000 kWh. The simple payback period will be only 3 months. Motor loading of the turbine compartment fans for all units is

Table 3 Comparison between AGBPP, AGTPP, and AGTPP (proposed combined cycle)

Parameter	AGBPP (Combined cycle)	AGTPP (Open cycle)	AGTPP (Proposed combined cycle)
Installed capacity (MW)	291	84	126
Energy generation (MU)	1835.4	644	993.8
Specific fuel consumption (SM^3/kWh)	0.29	0.41	0.27
Station heat rate (kCal/kWh)	2666.1	3753.2	2427.8
Overall efficiency (%)	32.3	22.9	35.4

in between 54 and 55%. It is envisaged that by replacing the 30 kW motors for the GTG 1, GTG 2, GTG 3, and GTG 4 to 20 kW motor, the annual saving for 8000 h of operation will be 320,000 kWh. The simple payback period will be 6 months. A comparison between AGBPP, AGTPP, and proposed AGTPP (combined cycle) is presented in Table 3.

4 Conclusions

Energy performance study has been carried out at Assam Gas Based Power Plant (AGBPP), which is a combined cycle power plant, and Agartala Gas Thermal Power Plant (AGTPP), which is an open cycle mode power plant in this work. The study is based on the as-run performance data, performance guarantee test report, and design data. The various energy saving opportunities are identified in these power plants. Major results for performance improvement in AGBPP include cooling towers and fill replacements to achieve 5–6 °C cooling tower approach, as against over 16 °C cooling tower approach in present situation. It is found that installation of all the energy-saving opportunities will lead to an increase of 3–4 MW generations for each steam turbine module totaling to about 10 MW additional station output. It is observed that converting from open cycle to combined cycle mode in case of AGTPP, 50% additional power can be generated by utilizing the same amount of fuel, i.e., the specific fuel consumption will be reduced from 0.41 SM^3/kWh to 0.27 SM^3/kWh.

References

1. Ministry of Power, Government of India (2020) https://powermin.nic.in/. Accessed on 12 Jun 2020
2. Paul IPS, Kaushik SC, Sabberwal SP (1994) Energy conservation aspects in Indian thermal power stations by technological innovations: experience and prospectives. Heat Recovery CHP 14(6):639–649

3. Abdelaziz EA, Saidur R, Mekhilef S (2011) A review on energy saving strategies in industrial sector. Renew Sust Energy Rev 15(1):150–168
4. Ghosh S (2010) Status of thermal power generation in India-Perspective on capacity generation and carbon dioxide emission. Energ Policy 38:6886–6899
5. Graus WHJ, Voogt M, Worrell E (2007) International comparison of energy efficiency of fossil power generation. Energy Policy 35:3936–3951
6. Kanoglu M, Dincer I (2009) Performance assessment of cogeneration plants. Energy Convers Manage. 50(1):76–81
7. Aguilar FJ, García MT, Trujillo EC, Villanueva JAB, Ojeda FJF (2011) Prediction of performance, energy savings and increase in profitability of two gas turbine steam generator cogeneration plant based on experimental data. Energ 36(2):742–754
8. Shrivastava N, Sharma S, Chauhan K (2012) Efficiency assessment and benchmarking of thermal power plants in India. Energ Policy. 40:159–176
9. Najjar YSH (2001) Efficient use of energy by utilizing gas turbine combined systems. Appl Therm Eng. 21(4):407–438
10. Rahman MM, Ibrahim KT, Abdalla NA (2011) Thermodynamic performance analysis of gas based power plant. Int J Phys Sci. 6(14):3539–3550

Chapter 20
Sensitive Load Management in Captive Power Plant—Aluminium Smelter

J. K. Mohanty, M. K. Panda, M. Das, P. R. Dash, and P. K. Pradhan

Abstract Production of aluminium involves two major stages: refining of bauxite to alumina and smelting of alumina to aluminium. Smelting is a highly energy intensive and sensitive process. Any disruption in power supply to the electrolytic cells leads to stoppage of pot-line operation and damages the cells. Hence, the most important life support system for an aluminium smelter is the continuous supply of reliable power to its' potline. Therefore, are liable power supply system is highly essential to ensure the continuous power supply from both the internal or external sources. So making a balance system among necessary power requirement in smelter and power generation in captive power plant and available capacity in power grid (as external sources) is a challengeable task. Hence, always a robust power network is made available, which operates in a very reliable manner to manage continuous power supply to a mega-aluminium smelter.

Keywords Captive power plant · Aluminium · Smelter · Single-line diagram · Blackout · Black start DG · Condition monitoring

Abbreviations

CBM	Condition-Based Maintenance
CD	Contract Demand
CPP	Captive Power Plant
CTU	Central Transmission Utility
DC	Double Circuit
DG	Diesel Generator
DISCOM	Distribution Company

J. K. Mohanty · P. R. Dash · P. K. Pradhan (✉)
Department of Mechanical Engineering, VSSUT, Burla, Odisha, India
e-mail: prasant2001uce@gmail.com

M. K. Panda · M. Das
Vedanta Limited, Jharsuguda, Odisha, India

S. Mahapatra et al. (eds.), *Advances in Energy Technology*, Advances in Sustainability Science and Technology, https://doi.org/10.1007/978-981-15-8700-9_20

GW	Giga Watt
ICT	Inter-Connecting Transformer
OPTCL	Odisha Power Transmission Corporation Limited
PGCIL	Power Grid Corporation of India Limited
RE	Renewable Energy
SEZ	Special Economic Zone
SLD	Single Line Diagram
SS	Sub-Station
TPP	Thermal Power Plant
TWh	Tera Watt hour
WESCO	Western Electricity Supply Company

1 Introduction

Electricity being the most basic form of energy is easy to generate, transmit, distribute, and use. It is easy to control electricity as a form of energy. There are various means by which electricity can be generated. Thermal power plant is one of them. There has been a requirement of better and more efficient power plants since a couple of decades as the requirement for power is increasing day by day. For a better viability of economy, these power plants have multiplied their level of complexities as a result of the growth in the size and the capacity.

The thermal power plant (or steam power plant) works on the principles of a Rankine cycle. It is a process in which heat is converted into mechanical work. The heat is supplied to convert water into steam. That steam runs the turbine, which is coupled with a generator and the generator produces the electricity [1]. India is the third-largest producer of electricity in the world and thermal power plant contributes about 85% of the power generation [2].

With the generation of 1561 TWh, India is the third-largest producer of electricity, with an installed power capacity crossing 360 GW + as on July 2019. Total installed capacity of Odisha state (in India) is 16,500 MW (Utility Sector is 7500 MW and CPPs are 9000 MW), out of which 16% installed capacity belongs to Hydro (2151 MW) and RE sources (512 MW). Out of this, aluminium companies contribute to 6000 MW capacity (37% of total and 67% of total CPP capacity), whereas iron and steel companies contribute to 2463 MW capacity and others contribute to 500 MW capacity, respectively.

Primary aluminium production involves two major stages: one is refining of bauxite to alumina and second is smelting of alumina to aluminium. Smelting is a highly energy sensitive and energy intensive process which almost accounts to about 85–90% of the total energy consumption. The Hall-Héroult process for aluminium production requires a huge amount of electricity. The worldwide average is 15 kWh per kg of aluminium production. It is worthwhile to mention that about 40% of the input required for aluminium production is electrical energy. Other inputs are 40%

alumina, 16% carbon, and 4% others, respectively. Since aluminium smelting is very energy sensitive, any disruption of power to the electrolytic cells for even three to four hours results to stoppage of pot-line operation as molten metal freeze inside the cells.

2 Importance of Continuous Power Requirement in Aluminium Production Process

As enumerated above, a large amount of electrical energy is required to reduce alumina to aluminium. Hence, aluminium is a power intensive industry and need 24 × 7 steady power with.

- Continuous high DC Current @ 325–350 kilo Amps
- Stable Voltage: 4.2–4.5 V to avoid pot blasts
- Operating at 950–1000 °C

The main operational hazard in aluminium smelting is loss of electrical power while smelting pots are in operational mode. Generally, the pots are operate at a temperature of around 950–1000 °C. The loss of electrical power will eventually cools the pots down and a prolonged loss of power will result in solidification of aluminium in the pots when the pot temperature goes below 700 °C. This phenomenon is known as pot freezing. Once the pot freezes completely, it cannot be put back in service and must be discarded. Occurrence of an electrical fault in one pot may render the entire potline to freeze if corrective actions are not taken in time. In case of occurrence of eventualities like 'tap out' (leakage of molten metal due to failure of shell of the pot), pots must be bypassed, known as 'wedging out'.

Most of the failure results show that once a pot's power supply has been off for more than 3–4 h, recovery becomes difficult as loss of power cools the electrolyte and a restart of the potline becomes impossible, even if the power is restored. Restoration of the frozen pot is not only very expensive but also time consuming as solidified aluminium and electrolyte need to be physically chiseled out of the pot for restoration. At the same time, the lifespan of the pot is also reduced considerably. Hence, the most important life support system for an aluminium smelter is the continuous supply of reliable power to its' Potline. Keeping in view of intense and sensitive power requirement, every aluminium production company makes captive power plant (CPP) (as an internal source) to manage their load. Besides the CPP, aluminium plant requires power from external sources according to the requirement and agreement.

3 Alternative Arrangement for External Power Supply to Enhance the Reliability

There are various arrangements/methods of ensuring reliable power supply for continuous operation of pot lines in an aluminium smelter. Few of these are enumerated as below.

3.1 Contract Demand

The aluminium smelters plants are generally connected to a larger grid network for reliability of operation. This arrangement allows the plants for drawl of a mutually agreed quantum of power from the system at a predetermined tariff to ensure operational flexibility. Normally, this connectivity is based on a contract demand agreement with the distribution companies. Fluctuation of power requirement in smelter on real-time basis is taken care of by such arrangement.

3.2 Emergency Power

Black out is the situation when a power station cannot produce power due to tripping of all the turbines and opening of the grid breaker. Blackout in a thermal power station mainly occurs because of any disturbance in grid connecting the plantand substation and also due to major faults generated by Electrical equipment failures inside the plant premises.

Although the Contract Demand arrangement with the network ensures some cushion and security to the operation, this will not suffice the requirement during black out situations as any excess drawl from the contracted quantum leads to heavy financial penalty. To avoid penalties for Contract Demand violation which gets recorded in the metres, it is to be ensured that the drawl never exceeds the contracted quantum. For mitigating such situations, the plants need to enter into a special agreement with some designated power producers/suppliers to avail the emergency requirements in the shortest possible time.

3.3 Installation of a Blackstart DG

The tolerance for power starvation to the pot-line loads are minimum in large power plants connected to sensitive alumimium smelters. During the events of black outs and longer unavailability of grid support for restarting the generators for normalization, a secondary back up is maintained in the form of black start DG sets. The auxiliary

power for startup of the thermal units is made available by operating these DG sets. Upon getting the auxiliary power from the black start DG, the generator units get started and stabilized sequentially thus restoring power supply to the aluminium smelter.

3.4 Power Purchase Through Indian Energy Exchange (IEX)

Indian Energy Exchange provides a nationwide automated platform for deliverying of electricity with efficient pricing. Currently, there are more than 6500 participants in the exchange to trade electricity (this includes distribution companies, generators and open access consumers). The Aluminium Industry is one of the benefiting open-access consumers. After blackout, whenever normalization process extends for longer period, bulk power can be availed from IEX.

3.5 Composite Islanding and Load Management System (CILMS)

The generators and the loads of the aluminium plant need to work in a balanced way to ensure reliable operation. The generation and the load centres are generally distributed over the entire geographical area of the plant and the respective control rooms are normally situated away from each other. Also the disturbances in the connected grid network need to be kept isolated from the plant system. Hence, disturbances in generation and loads pose a real technical challenge to be coordinated manually.

Controlling and monitoring work of the entire electricity generation, transmission and distribution system usually require a lot of utility specific information and knowledge. Implementation of the CILMS scheme together with a reliable communication network assists operators to handle the disturbances effectively.

The major advantages of CILMS in case of electrical system disturbance in grid and plant.

- Secures load shedding scheme
- Secures generation shedding scheme
- Import/export control
- Islanding and restoration assistance. Islanding is a situation in electrical network, where in the power plant and smelter operate in a balance mode, after getting disconnected from grid due to external disturbance.

3.6 Coal Availability and Ash Evacuation

Most of the smelter plants in India operate with coal-fired captive power plants and the performance of the power plant depends on the quality of coal. Coal is extremely heterogeneous varying widely in its' composition and properties from country to country and mine to mine. The principal impurities are high ash content and sulphur. These impurities which are introduced during mining process affect the combustion process thereby reducing the energy generation and discontinuity in power supply. The generating companies have very little or no control over the quality and quantity of coal supply.

Ash content of coal produced in the country is generally 25–45% whereas average ash content of imported coal varies from 10 to 20%. Indian coal has comparatively higher ash content than imported coal. Low quality coal causes problems as ash interferes in the combustion as high ash content reduces the thermal efficiency of the coal, i.e. ash interferes with combustion and reduces the temperature of the combustion zone. Also higher ash content coal burns slower resulting in reduction in the steam output of the boiler; thus, reducing the power generation or generation variation. Hence, imported coal with higher calorific value is often blended with the Indian coal to minimize the variations for sustained generation with rated capacity.

4 Enhancing the Availability of Own Power Supply System

Besides the above alternative arrangements for external power supply, the CPP needs improvement of its own availability. The availability can be maximized by using proper maintenance technique and strategy.

Continuous generation of electricity of a power plant depends on the higher availability of its components/equipments. Higher availability of the components/equipment is inherently associated with their higher reliability and maintainability. Turbine, generator, feed pump, boiler, and condenser are the major units and components in a thermal power plant. Similarly, overhead lines, transformers, switchgear, control systems, and protections are the components of power transmission system. The maintainability and reliability of these units enhance the reliability and availability of the whole system. The proper maintenance strategy is used to enhance the reliability of the plants.

There are different types of maintenance strategies and techniques[3–6-JSAEM] like

- Breakdown maintenance
- Routine maintenance
- Preventive maintenance
- Condition-based maintenance

4.1 Condition Based Maintenance

Condition-based maintenance(CBM) or condition monitoring is determining the health and condition of equipment, machines and machinery systems by observing, checking, measuring, interpreting, and monitoring certain parameters. CBM provides information on failures before system is going to fail. The typical condition monitoring and fault diagnosis process usually consist of four phases, i.e. (i) Data acquisition, (ii) Features extraction, (iii) Fault trend analysis, (iv) Decision making. There are different CBM techniques; these are Vibration Analysis [7], Noise Analysis [8], Temperature Monitoring [9], Motor Current Signature Analysis [10], Wear Debris Analysis [11], etc.

Thus, an integrated CBM ensures reliable power plant operation with their continued availability for sustained power supply to smelter.

4.2 CBM of Switchyard, Transmission Line

Number of transmission lines run from the generating station to the load centres which are normally located at a distance. The transmission-line towers carry multiple transmission lines and are prone to outages due to lightning and thunder storms. During inclement weather conditions, thunder storms can cause tripping of multiple transmission networks leading to plant outages. Condition-based maintenance of the transmission lines ensure the healthiness of insulators, tower structures, and conductor joints. Manual patrolling is usually carried out along the route of the line to ensure passage clearance. Periodic thermal scanning/thermography of the network ensures that timely remedial measures are taken so that there is no loss of transmission lines.

5 Assured Power Supply in Vedanta Aluminium Limited

Vedanta Limited, Jharsuguda (India) has three units: CPP, smelter plant, and TPP. CPP has capacity of (9 × 135) MW connected to Smeter-1 with a power requirement of 900 MW. Similarly, TPP has capacity of (4 × 600) MW synchronized to Smelter-2 with a load requirement of 2000 MW. The plants possess world class technology supplied by GAMI and Shanghai Electric.

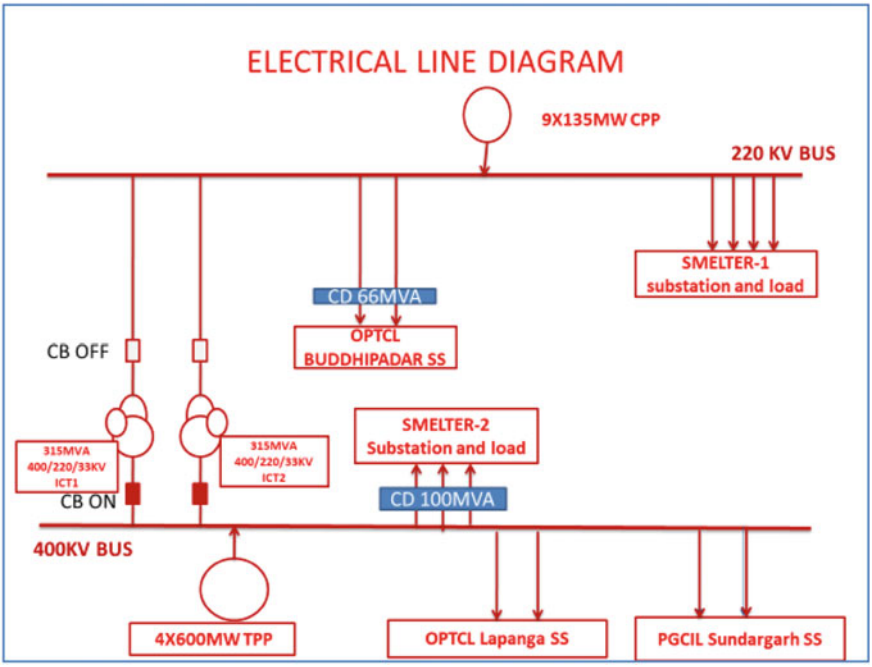

Fig. 1 SLD of grid sub-stations along with power plants and smelters of vedanta limited

5.1 Single-Line Diagram(SLD) of Smelter and Power Plant with Grid Sub-Station and Assurance in Power Reliability

Vedanta limited has adopted the supply network as shown in the single-line diagram (SLD) at Fig. 1. The power supply system can be described as follows.

- Double Circuit (DC) radial transmission line is connected between CPP(9 × 135 MW) switchyard to 220 kV Budhipadar SS under OPTCL. Line capacity is 400 MW on continuous basis. CPPs and Smelter-1 are in synchronized mode with OPTCL system through Budhipadar SS. There is a Contract Demand of 66 MVA with DISCOM WESCO for drawl of power through Budhipadar SS. Power can be availed through Budhipadar SS as per CD or approved open access as and when required during any exigency.
- Power supply from CPP Bus to Smelter-1 is through 04 nos. of dedicated transmission lines for Potline1, Potline2 and its' auxiliaries. Each line capacity is 450 MW on continuous basis.
- Smelter Plant-2 in the SEZ area is connected to a 2400 MW (4 ×600 MW) power plant, out of which 3 × 600 MW units are CPP and 1 × 600 MW unit is an IPP dedicated for the state. The 2400 MW power plant has a dual connectivity/combined bus arrangement, with OPTCL Lapanga substation through a 400 KV DC line and

with the CTU system at Sundargarh PGCIL substation through a dedicated 400 KV DC line backed up by a Contract Demand of 100MVA with WESCO. Line capacity is 600 MW on continuous basis. The 4 × 600 MW units and Smelter-2 are in synchronized mode with both PGCIL and OPTCL systems. This dual connectivity with the robust 400 KV grid system and operation in combined bus logic has ensured that the station does not suffer from a black out situation. Also power can be availed through these SS as per CD or approved open access as and when required during any exigency.

- Apart from the above-mentioned arrangements of the dual connectivity with a total Contract Demand of nearly 170 MVA, there is an agreement with the GRIDCO for drawl of upto 350 MW power from the grid in emergency situations.
- In addition to the stand alone 220 KV and 400 KV substations at the smelters, there is also one 220 KV system in the 2400 MW power plant switchyard with 2 ×315 MVA, 400/220 KV ICTs which has further connectivity with the Smelter-1 220 KV switchyard, with line capacity of 400 MW on continuous basis. This means the TPP and CPP are connected through these 400/220 kV ICTs and the 220 kV Double Circuit Line having length of 5.5 kM. This transmission line was constructed to export power from one unit of TPP as an interim arrangement till the commissioning of 400 kV Vedanta-Meramundali/Lapanga line. Presently, the breakers of these ICTs are kept in OFF condition. Also there is some excess power, available at both of the power stations (1215 and 2400 MW) that can be interchangeably used in both the smelters as per the requirement. Hence, a proposal is under implementation for unification of both the 220 and 400 KV electrical systems of the plant within the regulatory purview for seamless exchange of power between both the units. This will also ensure added power reliability to the complex. To continue power generation during blackout, a black start DG of 36 MVA is also installed.

6 Summary

Metal industries (like aluminium smelter) require bulk power for the metal extraction and manufacturing process. This huge power requirement is generally catered by the captive generation units to minimize the dependency on external power sources. The overall electrical system operates at different voltage levels viz. 220 KV AC, 400 KV AC and 1380 V DC system and the capacities of the plant equipment are large compared to normal loads. To make the balance between power generation in CPP, TPP and power requirement in smelters, continued power availability is a challengeable task. Both generating surplus power and non-availability of power at the time of requirement are huge loss for the organization. To avoid these situations, a systematic model of power system has been made and implemented and it works well.

References

1. Nag PK (2013) In: Engineering thermodynamics, Tata Mc Graw-Hill Education
2. https://www.power-technology.com/features/feature-the-top-10-biggest-thermal-power-plants-in-india/
3. Mohanty AR (2018) Machinery condition monitoring: principles and practices. CRC Press, London
4. Jardine AK, Lin D, Banjevic D (2006) A review on machinery diagnostics and prognostics implementing condition-based maintenance. Mech Syst Signal Process 20(7):1483–1510
5. Mohanty JK, Dash PR, Pradhan PK (2020) FMECA analysis and condition monitoring of critical equipments in super thermal power plant. Int J Syst Assur Eng Manage 1–17https://doi.org/10.1007/s13198-020-00945-4
6. Kim H, Na MG, Heo G (2014) Application of monitoring, diagnosis, and prognosis in thermal performance analysis for nuclear power plants. Nuclear Eng Technol 46(6):737–752
7. Mohanty JK, Adarsh A, Dash PR, Parida K, Pradhan PK (2019) Integrated condition monitoring of large captive power plants and aluminum smelters. Sound Vib 53(5):223–235. https://doi.org/10.32604/sv.2019.07737
8. Collacott RA (1975) Condition monitoring by sound analysis. Non-Destructive Test 8(5):245–248
9. Bagavathiappan S, Lahiri BB, Saravanan T, Philip J, Jayakumar T (2013) Infrared thermography for condition monitoring—a review. Infrared Phys Technol 60:35–55
10. Pradhan PK, Roy SK, Mohanty AR (2019) Detection of broken impeller in submersible pump by estimation of rotational frequency from motor current signal. J Vibr Eng Technol 1–8. https://doi.org/10.1007/s42417-019-00165-6
11. Sugimura J, Takesue M, Yamamoto Y (1998) Wear debris analysis for condition monitoring of gears. Tribol Ser 34:431–442

Chapter 21
Optimal Resource Allocation to Improve Energy Efficiency of Cognitive Radio-Based Vehicular Ad Hoc Network Under Imperfect Sensing

Subrat Kumar Sethi, Arunanshu Mahapatro, and Nabanita Mishra

Abstract The evolution of wireless communication from fourth generation (4G) to fifth generation (5G) is envisioning massive growth in application of vehicular ad hoc network (VANET) based on cognitive radio (CR) technology. In this VANET, fast and efficient spectrum sensing techniques are required to co-exist with heterogenous network. Most of the current applications are done with assuming perfect carrier sensing, but in actual practice, channel sensing is imperfect. We have investigated the performance under imperfect sensing, so as to exactly analyse the key concern of co-existence, i.e. the average/peak transmission power constraints of secondary user (SU) and average interference power constraints of primary user (PU). However, to alleviate these concerns, we need to have optimum resource allocation, to improve the capacity and energy efficiency of this VANET. To solve the resource allocation and power distribution problem, we have investigated two popular cooperative relay transmission schemes such as Decode-and-Forward (DF) and Amplify-and-Forward (AF). Moreover, we have analytically derived the required transmission rates for both AF and DF schemes. In addition to this, we have also develop the new optimal resource allocation strategies for the CR based co-operative relay protocol to improve the capacity and energy efficiency (EE) of the VANET. The MATLAB simulation results are incorporated to validate the correctness of the analysis.

Keywords 4G · 5G · AF · CR · DF · EE · PU · SU · VANET

1 Introduction

The application of CR concept in next-generation wireless communication systems for intelligent network of vehicles has been envisioned as a potential technology towards solving the problem of Intelligent Transportation System (ITS). In VANET frameworks, every vehicle can send messages from vehicle to vehicle (V2V), while

S. K. Sethi (✉) · A. Mahapatro · N. Mishra
Department of Electronics and Telecommunication Engineering, VSSUT, Burla, Odisha, India
e-mail: subrat.sethi@gmail.com

S. Mahapatra et al. (eds.), *Advances in Energy Technology*, Advances in Sustainability Science and Technology, https://doi.org/10.1007/978-981-15-8700-9_21

in vehicle-to-infrastructure (V2I) mode, they interchange messages with roadside units (RSUs). The RSU interfaced with the parent-controlled network and act as a gateway to give administrations to moving vehicles. Due to high mobility and fast changing scenario of high speed vehicles, the RSU gets minimum time for sensing of the signal. The sensing duration has a major role in the overall efficiency of cognitive radio-based VANET network. Practically speaking, various factors such as multipath fading, signal attenuation, noise, and sensing time degrade the spectrum sensing accuracy leading to imperfect sensing. In the light of a limit-based theory test, the error performance criteria of spectrum sensing are false alarm and missed detection. Due to a missed detection, a SU access a primary channel (PC), which may possess interference to the already on-going communication in the PC. Because of false alarm, a SU may lose a chance to opportunistically use the already vacated PC. This error leads to improper distribution of power, which in turn diminishes the total EE of the network. Some of the papers [7, 11] have done analysis to ensure quality-of-service (QoS) to the primary network(PN) by appropriately allocating the resources. To co-exist [12] in the same area of operation, the SU should learn to when to transmit and when to stop. It ought to transmit with a low capacity to limit the impact of debasing execution in the PC and it must stop its transmission when the PU returns at a similar channel. At the point when a PU is identified, SU should quit transmitting over that recurrence band and another channel ought to be allotted [9, 10]. In an underlay network [5], SUs ought to adjust their transmit control so as to control the degree of produced interference. In an overlay network SUs can go about transmission by committing some bit of its capacity to the transmission of the PU signal. Different relay selection systems have been proposed in cognitive radio network (CRN) [5, 8]. Outstanding among other relay transfer technique is AF and DF transferring scheme.

To leverage the above analysis, we have fist derive the expressions for the mean transmitted power for PU and SU. Hence, the data rate is being derived based on AF and DF scheme. We have compared the link capacity obtained by the two cooperative schemes, and show that DF is better than AF. Finally, based on the obtained capacity and mean transmitted power of PU and SU, we have formulated the new modified energy efficiency scheme for the corresponding multi-objective resource allocation problem. Finally, numerical outcomes highlight the significant insights about the performance under different system parameters.

The rest of this paper is arranged as follows. Section 2 highlights the system model and the structure for range detection in a VANET scenario. In Sect. 3, we look at the cost minimization issue and limitations for normal obstruction and presents the optimized resource allocation, ensuring a guaranteed QoS. In Sect. 4, simulation results are provided and discussed. Finally, Sect. 5 highlights the conclusions.

2 System Model

To describe the system model in a realistic way, we have considered a cognitive network-based real-life VANET scenario as shown in Fig. 1. Here, the RSU acts as a cognitive relay, which is used to enhance the overall capacity of the system. The cognitive RSU relay links with the base station using the opportunistic licensed spectrum. These vehicles can be viewed as sender, receiver, and router. As shown in Fig. 1, various entities are included in the model, for example, primary source (PS), primary destination (PD), RSU, vehicles, etc. Let d_1, d_2, d_3, and d_4 denote the distance between PS_1 and RSU_A, RSU_A and PD_1, PS_1 and PD_1, and RSU_A and V_1, respectively. As represented in scenario A, path 1 directly communicating from PS_1 to PD_1 without the use of RSU, but in scenario B, PS_1 sends the data to the PD_1 using the RSU_A via path 2–3. Similarly, in scenario C, vehicle 1 (V_1) is communicating with vehicle 2 (V_2) through vehicle-to-vehicle communication mode (VV) and V_1 is also communicating with the RSU_A through vehicle-to-infrastructure mode (VI). In scenario D, PS_1 sends the data to PD_2 via RSU_A-V_4-RSU_C-PD_2 through both infrastructure to vehicle (IV) mode and VI mode. This data transmission passes through different cognitive phases. All the RSUs have cognitive capability and operate in a decentralized co-operative mode. They proactively search for the available channels and share the status of the channel among each other.

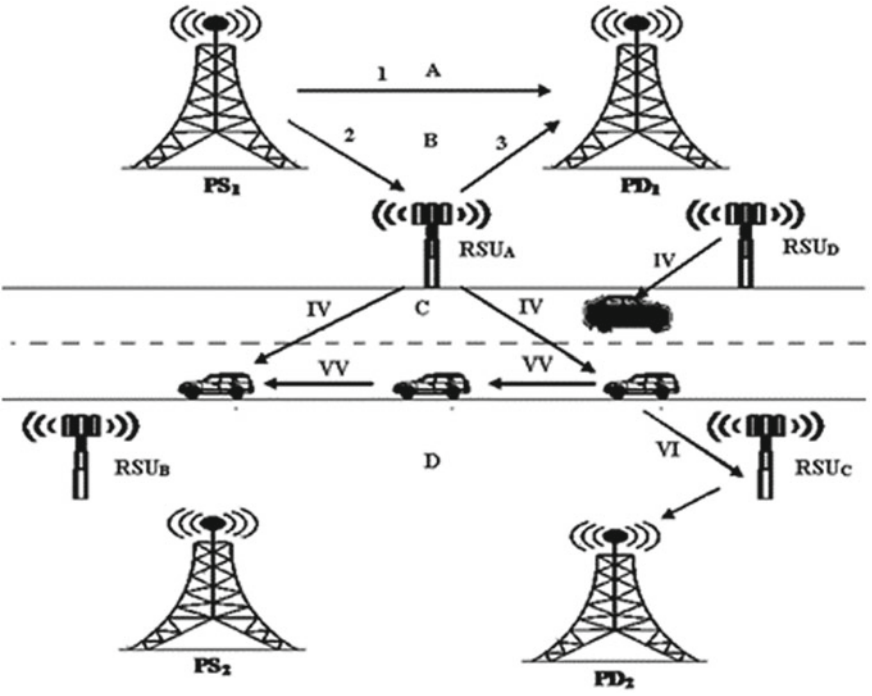

Fig. 1 Cognitive Radio based VANET model

The list of potential channels that are to be searched, may be categorically distributed among all the RSUs, so that at a given time, all the status of the channel may be obtained using minimum attempt, which not only improve the overall capacity of the system but also upgrade the EE of the system. If the PU and SU simultaneously access to verify the availability of a vacant licensed band, sometimes due to sensing error, both user may undergo interference from each other. The detection of a vacant license band can be written as a binary hypothesis test, where the null hypothesis H_0 represents the absence of the PU in the licensed band; hence, a secondary node can access the channel, and H_1 is the alternative hypothesis representing that a PU is transmitting in the pre-licensed band. So, a secondary node cannot transmit. The false alarm probability $\mathbf{f_a}$ and miss detection probability $\mathbf{m_d}$ are the performance criteria of the spectrum sensor, where

$$f_a \triangleq \Pr(D_1|H_0) \tag{1}$$

$$m_d \triangleq \Pr(D_0|H_1) \tag{2}$$

The conditional sensing probabilities under sensing outcome D_j, j $\varepsilon\{0, 1\}$ at the mth band is represented as follows:

$$P_m\left(H_i|D_j\right) = \frac{P_m\left(H_i \cap D_j\right)}{P_m\left(D_j\right)} = \frac{P_m\left(D_j|H_i\right)P_m(H_i)}{P_m\left(D_j\right)} \tag{3}$$

This Eq. 3 is derived from Bayes' rule. Here, $i, j \in \{0, 1\}$, where $P_m(H_i)$ is the probability of the hypothesis H_i and $P_m(D_j)$ is the probability of the sensing outcome D_j for the mth band. The sensing outcomes can be decided by using threshold statistics value, i.e. $\mathbf{Y_m}$, which is noted as follows:

$$Y_m = \sum_{t=1}^{Ts}\sum_{n=0}^{N-1} |R^o_{m,t}[n]|^2, \quad m = 1, \ldots, M \tag{4}$$

where $R^0_{m,t}[n], n = 0, \ldots, N-1$, is the N-point normalized discrete fourier transform of the observed signal in the mth band [1]. The subscript t indicates the index of blocks in each frame. The observed threshold value $\mathbf{Y_m}$ is compared with a predefined threshold value to take the decision of a presence or absence of a vacant license band. Here, we can consider that the SS relay node receives and transmits at the same time in a full duplex mode. Various works are already published reflecting the availability of license band to the SU under different coexisting techniques. But without entering to the details of coexisting methods, we have here characterize the CRN with respect to power, bandwidth, and end-to-end throughput.

Let the transmit power of PU and SU is P_1 and P_2, respectively. The bandwidth of the licensed band is W_1 and bandwidth of cognitive RRs is W_2, respectively. The relationship between bandwidth ratio θ and power ratio φ is specified [2] as follows:

$$\theta = W_2/W_1 \tag{5}$$

$$\varphi = p_2/p_1 \tag{6}$$

Here, we have taken h_{sr}, channel gains from source to RSU (which acts as a relay), h_{rd}, channel gain from relay to destination, and h_{sd} is the channel gain from source to destination, whereas Z_1, Z_2 and $\tilde{Z}$ are zero mean independent white Gaussian noises, whose variance are given by

$$Z_1 = W_1 N_0 \tag{7}$$

$$Z_2 = W_2 N_0 \tag{8}$$

$$\tilde{Z} = W_1 \tilde{N}_0 \tag{9}$$

Here, the power spectral density of noise at the destination is N_0 and power spectral density at relay node is $\tilde{N}_0$. The PS_1 sends the data to the PD_1 via path 1 as shown in Fig. 1. So the SNR for a source and destination pair is as follows:

$$\rho_1 = P_1/N_0 W_1 \tag{10}$$

Similarly, as given in Fig. 1. The RSU_A sends the data to PD_1. So the transmit signal-to-noise ratio from relay to destination is given as:

$$\rho_2 = \rho_1 \varphi/\theta \tag{11}$$

where φ = transmit power ratio between licensed and cognitive RR and θ = bandwidth ratio between licensed and cognitive RS. In addition to this, PS_1 sends the data to the RSU_A via path 2 as shown in Fig. 1. So the SNR from source to relay link is as follows:

$$\rho_3 = \rho_1/\tilde{N}_0 W_1 \tag{12}$$

3 Performance Analysis and Resource Allocation

3.1 Capacity

We have assumed that $N = \{1, 2, \ldots, N-1, N\}$ represent a finite set of SUs. All the SUs are outfitted with CRs that comprise of a reconfigurable transceiver that can tune to a set of continuous frequency bands [4]. The two popular co-operative relay schemes are DF and AF. Through the implementation of DF scheme, at the first time

period, the relay r unravels the signal obtained from source s and in the second period transfers the data to destination d. The receiver end mutually decodes the obtained signal generated from source and relay. Considering that, a relay can completely decipher the source message, the capacity of the cooperative link between source s and destination d in presence of relay r is given by [4]:

$$C_{sdr}^{Df}(f_s, P_s, P_r) = \frac{W}{2} \sum_{f \int fs} \{\log_2\left(1 + \mathrm{SNR}_{sn}^{f}(P_s^f\right) \log_2\left(1 + \mathrm{SNR}_{sd}^{f}(P_s^f\right) + \mathrm{SNR}_{rd}^{f}(P_r^f))\} \tag{13}$$

In the AF scheme, the cooperative relay node r receives the signal from source and only amplifies but not decipher the signal in first time period, and in allotted second time period, it transfers the signal to destination node d. The receiver end jointly deciphers the signal coming from two separate paths, in order to increase the correct detection probability. So the capacity of a cooperative link between source s and destination in AF scheme is given by [4]:

$$c_{sdr}^{AF}(f_s, P_s, P_r) = \frac{w}{2} \sum_{f \varepsilon fs} \log_2\left(1 + \mathrm{SNR}_{sd}^{f}(P_s^f) + \frac{\mathrm{SNR}_{sr}^{f} * P_s^f * \mathrm{SNR}_{rd}^{f} P_r^f}{\mathrm{SNR}_{sr}^{f} * P_s^f + \mathrm{SNR}_{rd}^{f} P_r^f + 1}\right) \tag{14}$$

But in absence of co-operative relaying node, direct transmission takes place in between source s and destination d. Therefore, the capacity is given by

$$C_{SD}^{\mathrm{SNR}}(Fs, Ps) = \sum_{f \varepsilon fs} w * \log_2\left(1 + \mathrm{SNR}_{sd}^{f}\left(r_s^f\right)\right) \tag{15}$$

3.2 Mean Transmitted Power

We studied the improvement issue which amplifies the SU's feasible ergodic limit under various kinds of power distribution imperatives and for various fading channel models. In an underlay spectrum, secondary network (SN) is permitted to coexist with the PN as long as the interference brought about by SU to PU is under a threshold level. We have ascertained the ideal power assignment systems for these enhancement issues. At the beginning of each slot, mean transmitting power [3] for primary user is

$$P_{ps} = \sum_{i=0}^{n} \frac{i E_u P_{Ip}}{T_{\mathrm{p}}} \tag{16}$$

P_{ps} = mean transmitted power for PU, E_U = Amount of joules per unit energy packets, T_{p} = Slot for primary user, T_{s} = Slot for secondary user

$$P_{Ip}(i) = \frac{(\lambda_{ep} T_{\mathrm{p}})^{i} \mathrm{e}^{-t\lambda_{ep} T_{\mathrm{p}}}}{i!} \quad \text{where } i = 0, 1, 2, 3, 4 \ldots n \tag{17}$$

Then, the average transmitting power for SU is as follows

$$P_{ss}(j) = \sum_{j=0}^{n} \frac{j E_U P_{IS}(j)}{T_{\mathrm{s}}} \quad j = 0,\ 1,\ 2 \ldots n \tag{18}$$

$$P_{IS}(j) = \frac{(\lambda_{es} T_{\mathrm{s}})^{j} \mathrm{e}^{-t\lambda_{es} T_{\mathrm{s}}}}{j!} \quad j = 0,\ 1,\ 2 \ldots n \tag{19}$$

3.3 Data Transmission Rate

For the relaying scheme, AF and DF protocols are employed. With reference to Fig. 1, $\mathrm{RSU_A}$ is the secondary source (SS) and $\mathrm{RSU_D}$ is the secondary detector (SD). The channel coefficient of PS and SS is h_1, similarly h_2, h_3, and h_4 respectively be the channel coefficient of, PD and SS, PD and PS, and SD and SS. In the subsequent discussion and analysis, we shall be referred with this convention. Here, for PN and SNs, the calculated transmission rates is as follows

$$R_p = W * \log_2\left(1 + \frac{P_{Ps}|hs|}{W\sigma_d^2}\right) \tag{20}$$

where W = Total allotted licensed spectrum of the PN. But $\boldsymbol{W_1}$ spectrum is allotted to the PN, if R_p exceeds the threshold data rate (R_{th}) [5], and PS sends its data to PD with the help of $\mathrm{RSU_A}$ which is acting as a relay through the path 2–3 as shown in Fig. 1. The SN is allotted with $\boldsymbol{W_2}$ spectrum for its transmission, where $w_1 + w_2 = W$, using DF scheme. Therefore, the data rate for PN is given by

$$R_{PD}^{DF} = W_1 \log_2\left(1 + \frac{P_{ps}|h_3|^2}{W_1\sigma_0^2}\right) \tag{21}$$

The data rate for SN is given by

$$R_{sD}^{DF} = W_2 \log_2\left(1 + \frac{P_{ss}|h_4|^2}{W_1\sigma_0^2}\right) \tag{22}$$

If R_p is below Rth, $\mathrm{RSU_A}$ acts as the relay [3] to assist the primary transmission in a co-operative mode using the AF scheme. Therefore, the data rate of PD using relay assistance is given by:

$$R_{PD}^{AF} = \frac{w_1}{2}\log_2\left[1 + \frac{2P_{ss}P_{ps}|h_1|^2|h_2|^2}{P|h_2|^2 w_1\left(\sigma_{b1}^2 + \sigma_1^2\right) + 4P_{ps}|h_1|^2 w_1\sigma_2^2}\right] \tag{23}$$

The data rate of RSU_D using relay

$$R_{SD}^{AF} = \frac{w_2}{2}\log_2\left(1 + \frac{P_{ss}|h_1|^2}{2w_2\sigma_0^2}\right) \tag{24}$$

3.4 Optimization of Resource Allocation

Our focus is to maximize the energy efficiency by optimally allocating the resource. So we can define the energy efficiency based on AF and Df scheme considering the capacity and transmitted power. The maximum capacity and EE change with respect to different rely locations. As per the discussion [4], the EE is calculated taking the transmitted power in the PC and SC as $\boldsymbol{P_1}$ and $\boldsymbol{P_2}$, respectively.

$$\mathrm{EE}_{\mathrm{DF}} = \frac{c_{\mathrm{SDR}}^{\mathrm{DF}}}{P_1 + \varepsilon P_2} \tag{25}$$

$$\mathrm{EE}_{\mathrm{AF}} = \frac{C_{\mathrm{SDF}}^{\mathrm{AF}}}{P_1 + \varepsilon P_2} \tag{26}$$

$$\mathrm{EE}_{\mathrm{DT}} = \frac{C_{\mathrm{Sd}}^{\mathrm{DIR}}}{P_1 + \varepsilon P_2} \tag{27}$$

The above Eqs. (25, 26, 27) fail to calculate the actual EE in a co-operative scenario. In [4], transmitted power of PU and SU is being taken $\boldsymbol{P_1}$ and $\boldsymbol{P_2}$, respectively, but these are not going to same spatially and temporarily at every node in a dynamic distributed environment. So, to fill the gap, we have taken the average power (Eqs. 16, 17, 18, 19) over the entire activity, which not only reflects the practical approach, but also analytically expresses the superiority of our approach over the existing one. Therefore, the modified and updated energy efficiency is as follows

$$\mathrm{MEE}_{\mathrm{DF}} = \frac{C_{\mathrm{SDR}}^{\mathrm{DF}}}{P_{ps} + \bar{\varepsilon} P_{ss}} \tag{28}$$

$$\mathrm{MEE}_{\mathrm{AF}} = \frac{C_{\mathrm{SDR}}^{\mathrm{AF}}}{P_{ps} + \bar{\varepsilon} P_{ss}} \tag{29}$$

$$\mathrm{MEE}_{\mathrm{DT}} = \frac{C_{\mathrm{SDR}}^{\mathrm{DIR}}}{P_{ps} + \bar{\varepsilon} P_{ss}} \tag{30}$$

4 Simulation Results and Discussion

This segment presents numerical outcomes dependent on our past investigation. Here, some simulation outcomes are presented to confirm the viability of the proposed scheme. Additionally, the inferred investigative outcomes are utilized to reflect upon various parameters effect on the whole system. With reference to Fig. 1, for the AF scheme, the simulation results are depicted in Figs. 2, 6 and 7, which illustrates that, the sum rate first increases with increment of the path 2 distance and afterward it diminishes with increment of path 2 distance, and it accomplishes the maximum value. But for the DF scheme, the simulation outputs are shown in Figs. 3, 4 and 5, which reflect that, when the path 2 increases, and path 4 decreases with reference to Fig. 1, then, the overall sum rate increases. When the path 2 distance increases to a large extent, then, there is loss of connectivity between PS and RSU. The power of PS is more effective in DF scheme and the transmitting distance between SS and PS has a major influence on the total throughput rate. Hence, with increment of distance of path 2, the pass loss between SS and PS increases which results in lower throughput rate.

Figures 8 and 9 show the capacity and EE as functions of bandwidth ratio θ and power ratio φ based on Eq. 5 and Eq. 6. Figure 8 shows that EE increases monotonically with θ, while Fig. 9 shows that the capacity increases monotonically with θ and φ until it reaches a maximum value.

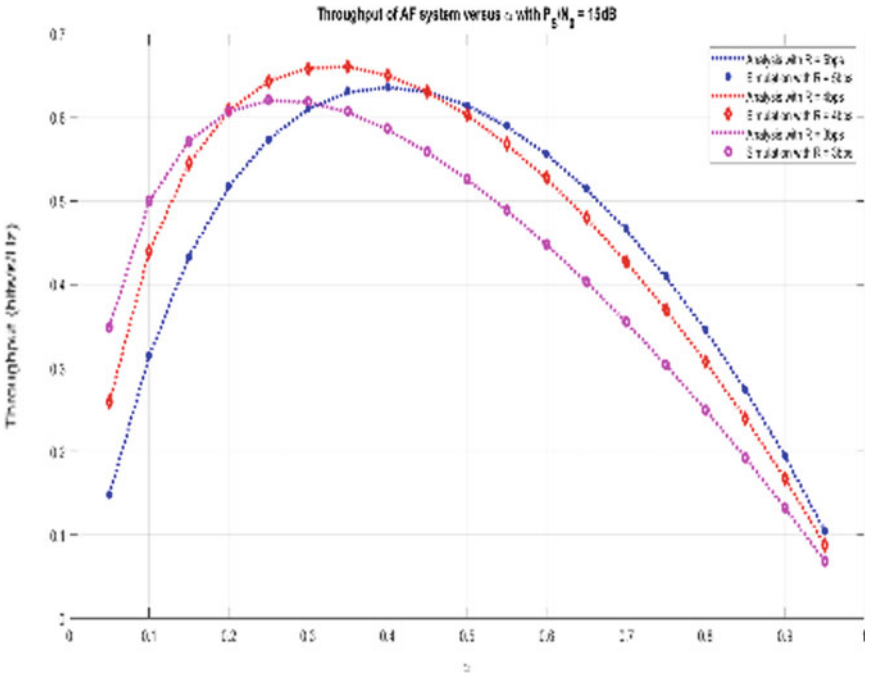

Fig. 2 Throughput of AF system with P_s/N_0 of 15 dB

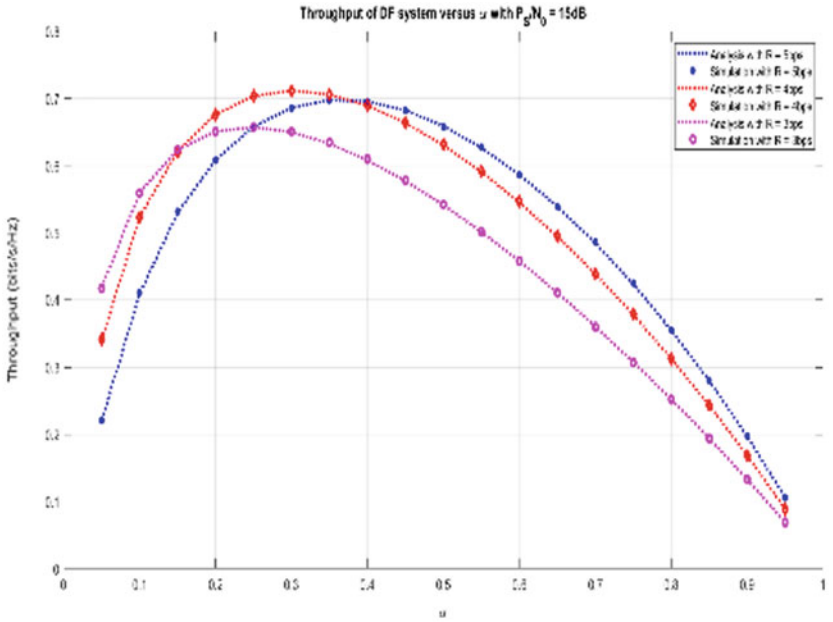

Fig. 3 Throughput of DF system with P_s/N_0 of 15 dB

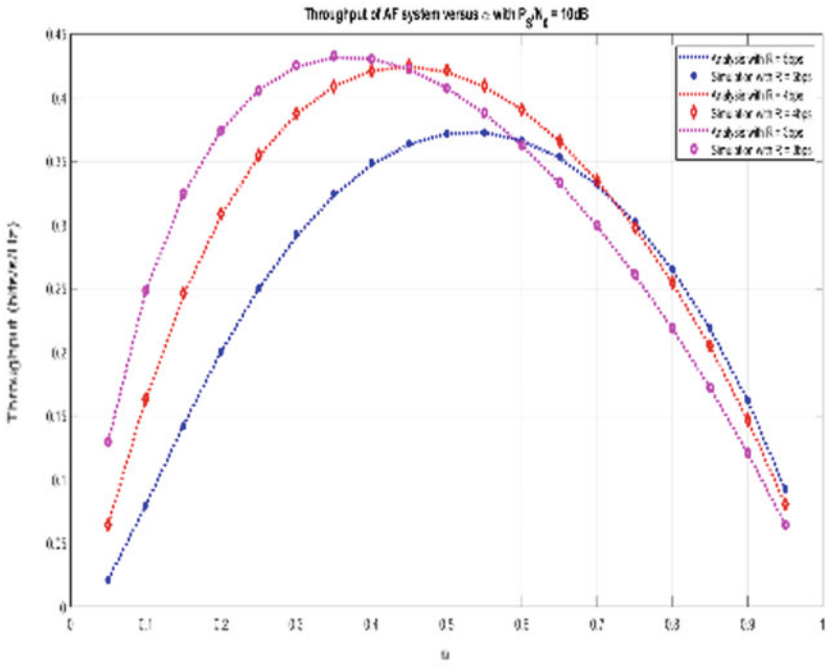

Fig. 4 Throughput of AF system with P_s/N_0 of 10 dB & R of 5 bps, 4 bps, 3bps

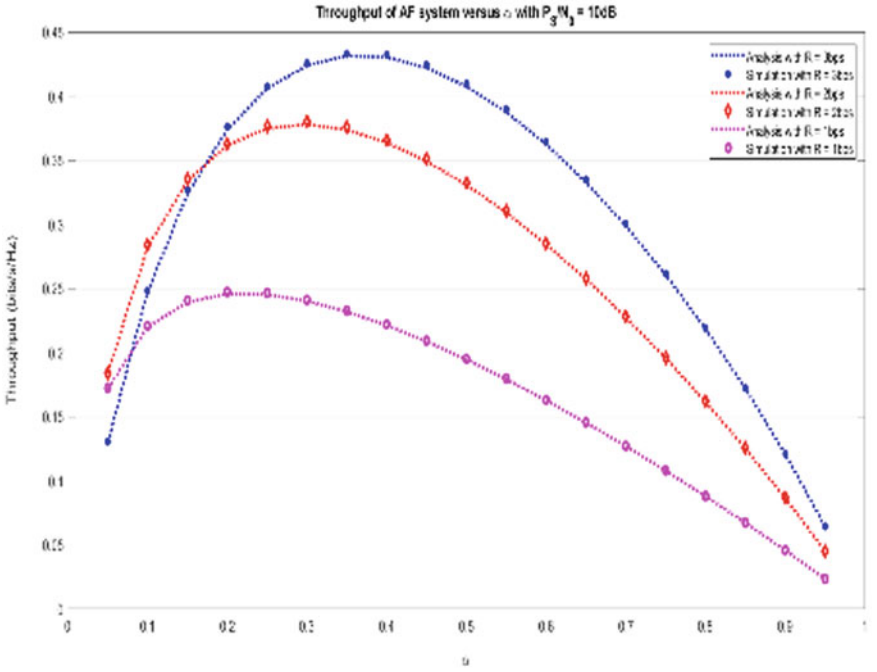

Fig. 5 Throughput of AF system with P_s/N_0 of 10 dB & R of 3 bps, 2 bps, 1bps

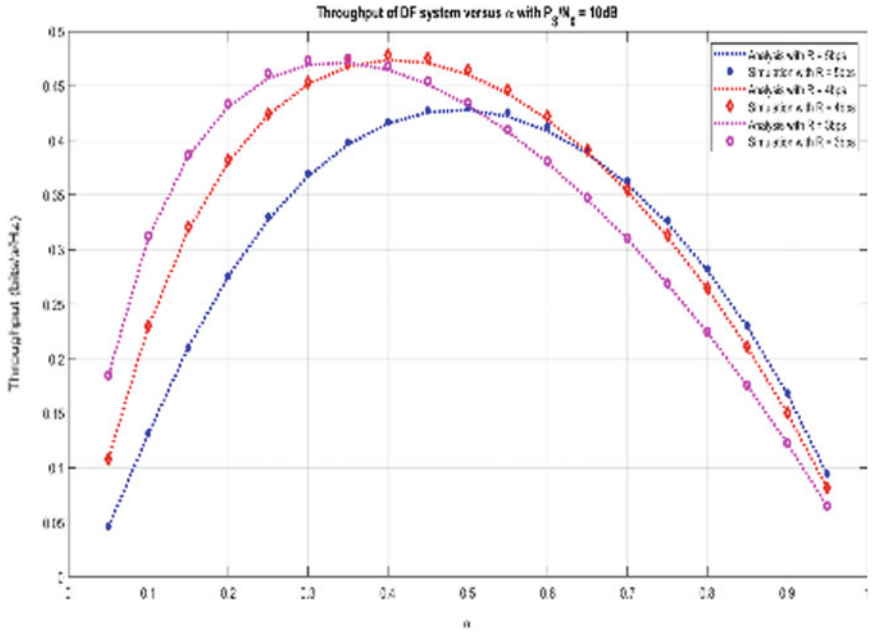

Fig. 6 Throughput of DF system with P_s/N_0 of 10 dB & R of 5 bps, 4 bps, 3bps

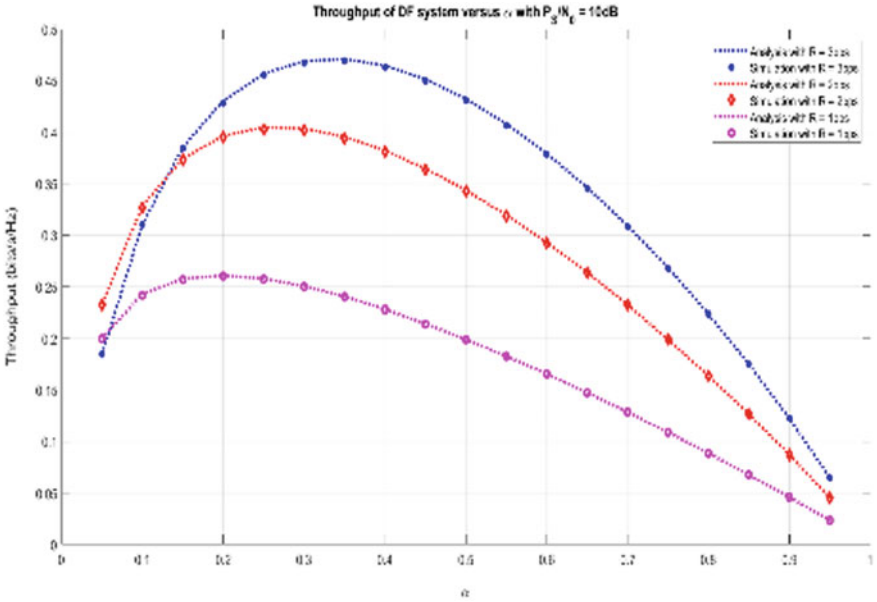

Fig. 7 Throughput of DF system with P_s/N_0 of 10 dB & R of 3 bps, 2 bps, 1bps

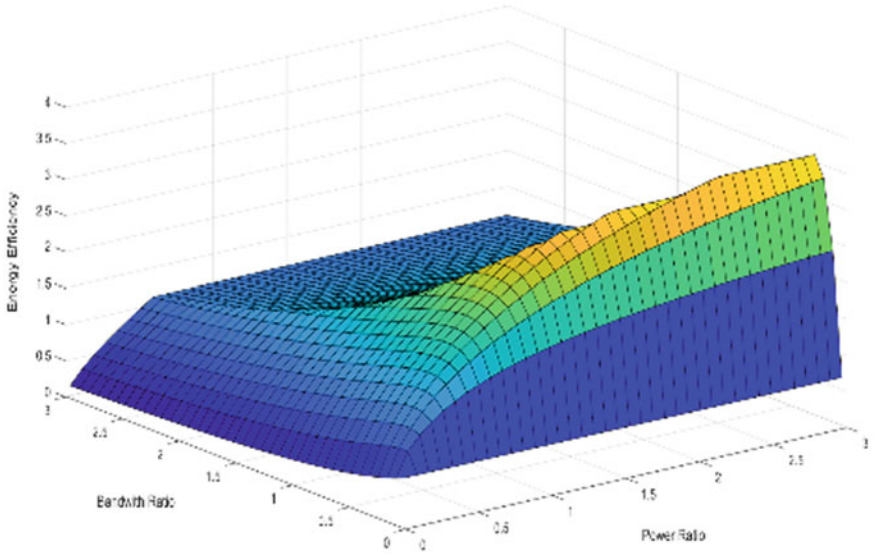

Fig. 8 Energy efficiency versus bandwidth ratio versus power ratio

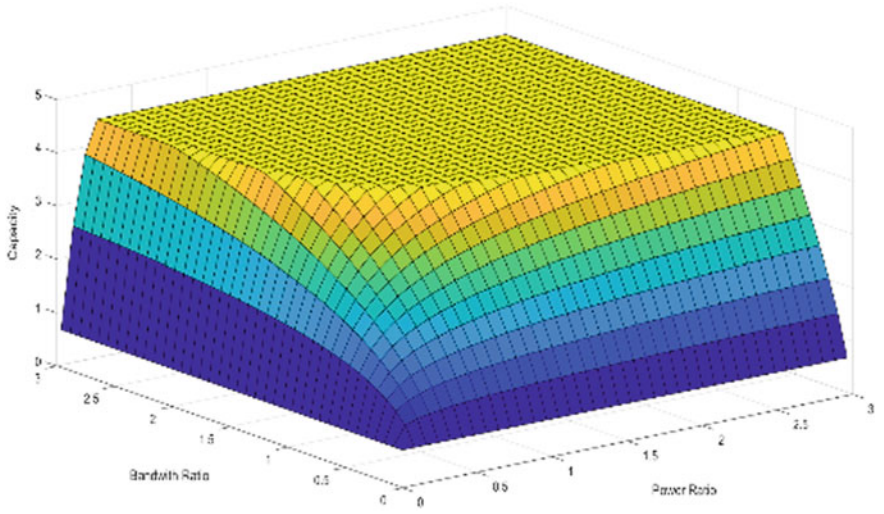

Fig. 9 Capacity versus power ratio versus bandwidth ratio

5 Conclusion

In this paper, we have explored various resource allocation methods in the CRN systems. The numerical representation of data rate for both PN and SN system leads to various relaying schemes, in particular, AF and DF method. We have also verified these numerical outcomes confirming the accuracy of theoretical derivations. In addition to this, the simulation segment shows that the proposed spectrum sharing can accomplish a better transmission rate as compared to the direct transmission with improved energy efficiency. In the end, the simulation outcomes give us important bits of knowledge into the impact of different system parameters on the desired system execution.

References

1. Lim HJ, Seol DY, Im GH (2012) Joint sensing adaptation and resource allocation for cognitive radio with imperfect sensing. IEEE Trans Commun 60(4):1091–1100
2. Hong X, Zheng C, Wang J, Shi J, Wang C-X (2015) Optimal resource allocation and EE-SE trade-off in hybrid cognitive gaussian relay channels. IEEE Trans Wirel Commun 4(8):4170–4181
3. Li Y et al (2019) Bandwidth allocation of cognitive relay networks with energy harvesting for smart grid. J Comput Netw Commun. Article ID 5038963, Apr. 2019
4. Ding L et al (2015) Distributed resource allocation in cognitive and cooperative ad hoc networks through joint routing, relay selection and spectrum allocation. Comput Netw
5. Alnwaimi G, Boujemaa H (2019) Relay selection for broadcast underlay cognitive radio networks using AF and DF relaying. Arab J Sci Eng 44(3):1903–1916

6. Chen Y, Zhao Q, Swami A (2008) Joint design and separation principle for opportunistic spectrum access in the presence of sensing errors. IEEE Trans Inf Theor 54(5):2053–2071
7. Su Z, Hui Y, Yang Q (2017) next generation vehicular networks: a content-centric framework. IEEE Wirel Commun 24(1):60–66
8. Chen Z, Xia B, Liu H (2014) Wireless information and power transfer in two-way amplify-and-forward relaying channels. In: Proceedings of the IEEE Global SIP, Atlanta, GA, USA, Dec 2014
9. Park S, Hong D (2013) Optimal spectrum access for energy harvesting cognitive radio networks. IEEE Trans Wireless Commun 12(12):6166–6179
10. Ding H, Ge J, da Costa DB, Jiang Z (2010) Energy-efficient and low-complexity schemes for uplink cognitive cellular networks. IEEE Commun Lett 14(12):1101–1103
11. Gong X, Vorobyov SA, Tellambura C (2011) Optimal bandwidth and power allocation for sum ergodic capacity under fading channels in cognitive radio networks. IEEE Trans Signal Process 59(4):1814–1826
12. Zame W, Xu J, Schaar M (2014) Cooperative multi-agent learning and coordination for cognitive radio networks. IEEE J Sel Areas Commun 32(3):464–477

Chapter 22
Investigate, Analyze, and Design of Real-Time Problems in the Domain of Power Electronics and Energy Using MATLAB: Review and Application

Bandan Kumar Panigrahi and Ranjan Kumar Jena

Abstract Making a different way of the archetype from classroom teaching to practical-type application-oriented work has been successfully implemented in this research article. This paper aims to reduce the gap between theoretical learning and practical implementation of student in a large prospective. A number of practical oriented real-time problem in the field of power electronics and electrical machines have been simulated in the MATLAB-SIMULINK platform, and the most appropriate outcome has been analyzed in detail. This article also puts light on the development.

Keywords MATLAB-SIMULINK · Power electronics · Electrical machines

1 Introduction

Digital simulation of electrical circuits has found its major impacts in different area of real-time application due to its increase in needs in the research domain. Digital simulation helps the researcher to understand the logic behind the faithful operation of the circuit and also helps to identify the steps required for successful outcome. It is not advised to test the prototype with real voltage and current (in the range of KV and KA) before knowing the real behavior of different circuit components under loading. So, a point-to-point checking and rigorous analysis are required to overcome the component damage, power loss, and assuring the safety prospective measures. Digital simulation helps one to visualize the clear function and connection of different components, before its hardware implementation.

Electrical circuits or prototypes needs to be designed in such a way that it should be able to work efficiently in contingency condition. Digital simulation has the scope

B. K. Panigrahi (✉)
Department of Electrical Engineering, CAPGS, BPUT, Rourkela 769015, India
e-mail: panigrahi91@gmail.com

R. K. Jena
Department of Electrical Engineering, CAPGS, BPUT, Rourkela, India

S. Mahapatra et al. (eds.), *Advances in Energy Technology*, Advances in Sustainability Science and Technology, https://doi.org/10.1007/978-981-15-8700-9_22

to analyze a developed prototype with fault condition, so that implementing that the practical application: measures can be taken out.

1.1 Experiments

Experiment-1

(i) Aim of the Experiment—Simulation of first-order RLC series circuit.

Parameters taken: $r = 100\,\Omega$
$l = 50\,\text{mH}$
$c = 5\,\mu\text{F}$

Simulink Diagram (Fig. 1):
Result (Fig. 2).

(ii) Aim of the Experiment—Simulation of second-order RLC circuit.

Parameters taken: $r = 100\,\Omega$
$l = 50\,\text{mH}$
$c = 5\,\mu\text{F}$

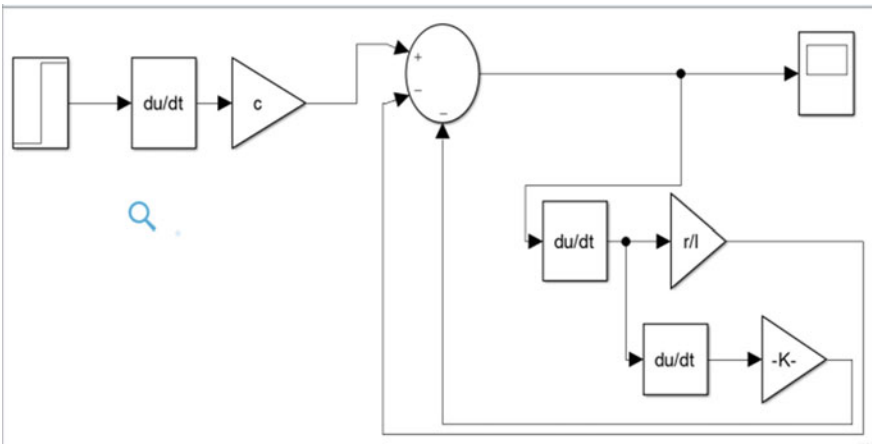

Fig. 1 Simulink model of RLC series circuit

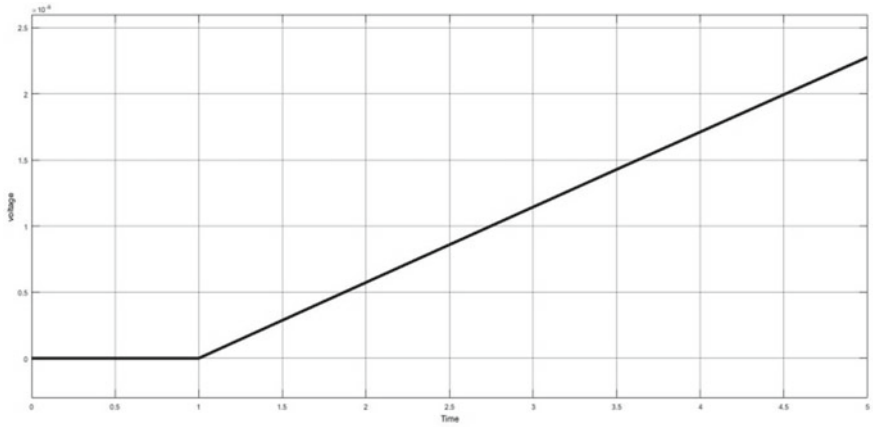

Fig. 2 Plot between voltage versus time. Absisa: time, ordinate: voltage

Simulink Diagram (Fig. 3):
Result (Fig. 4).

(iii) Aim of the Experiment—Simulation of RLC circuit using transfer function.

Parameters taken: $r = 100\,\Omega$
$l = 50\,\text{mH}$

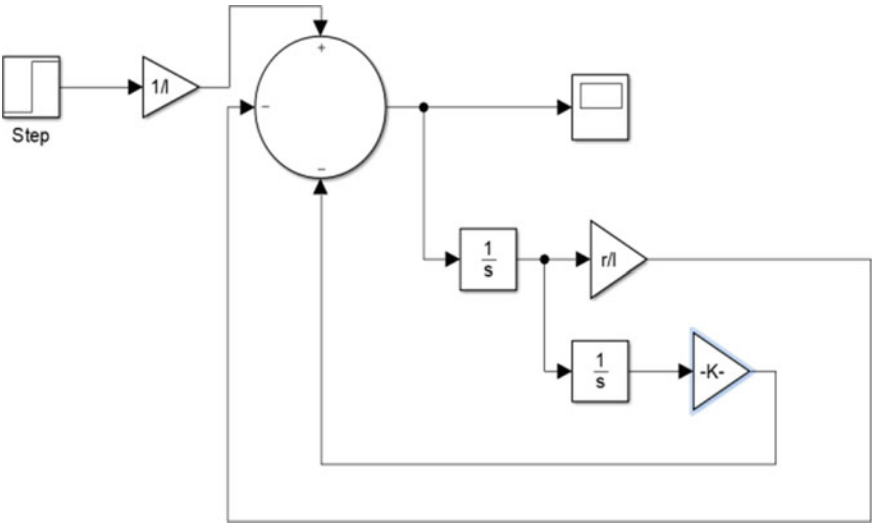

Fig. 3 Simulink model of second-order RLC circuit

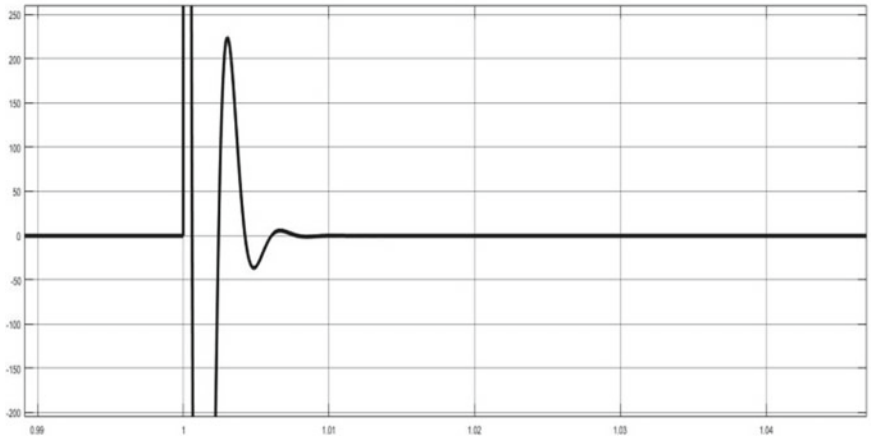

Fig. 4 Plot between voltage versus time. Absisa-time, ordinate-voltage

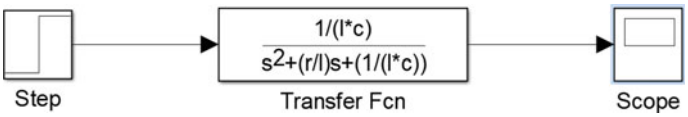

Fig. 5 Simulink model RLC circuit

$$c = 5\,\mu\text{F}$$

Simulink Diagram (Fig. 5):
Result (Fig. 6).

(iv) Aim of the Experiment—Simulation of RLC circuit using state space analysis.

Parameters taken: $A = 6$
$B = 3$
$C = 5$
$D = 1$

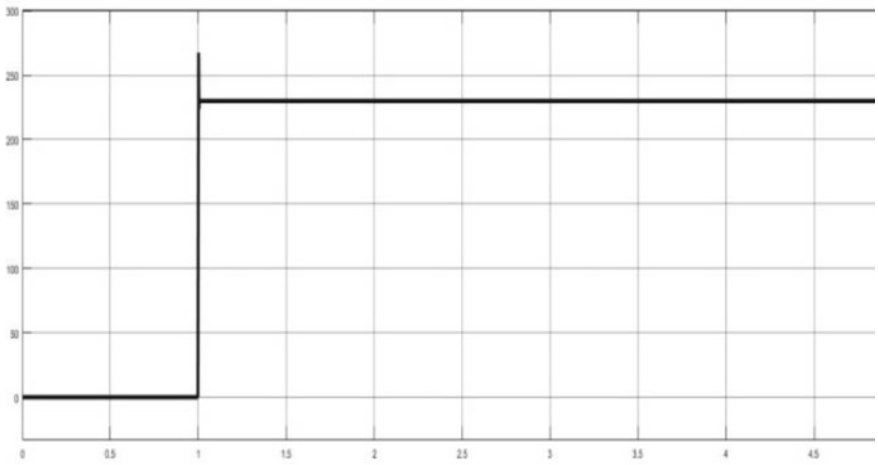

Fig. 6 Plot between voltage versus time. Absisa-time, ordinate-voltage

Simulink Diagram (Fig. 7):
Result (Fig. 8).

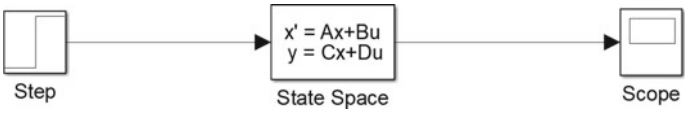

Fig. 7 Simulink model of RLC circuit

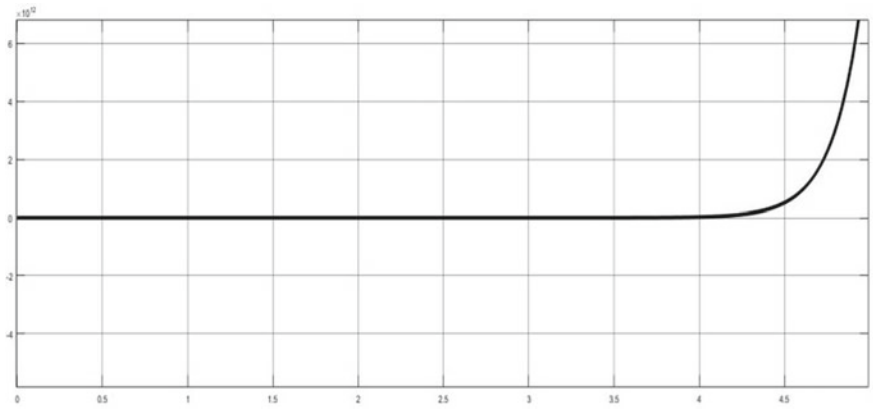

Fig. 8 Plot between voltage versus time. Absisa-time, ordinate-voltage

Experiment-2

(i) Aim of the Experiment—Simulation of open loop control of a DC motor using transfer function with different value of control parameter.

Simulink Diagram (Fig. 9):
Result (Fig. 10):

(ii) Aim of the Experiment—Simulation of open loop control of a DC motor using transfer function.

Simulink Diagram (Fig. 11):
Result (Figs. 12 and 13).

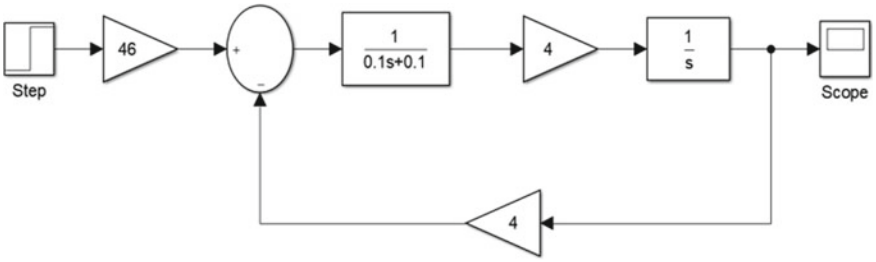

Fig. 9 Simulation model of open loop control of DC motor

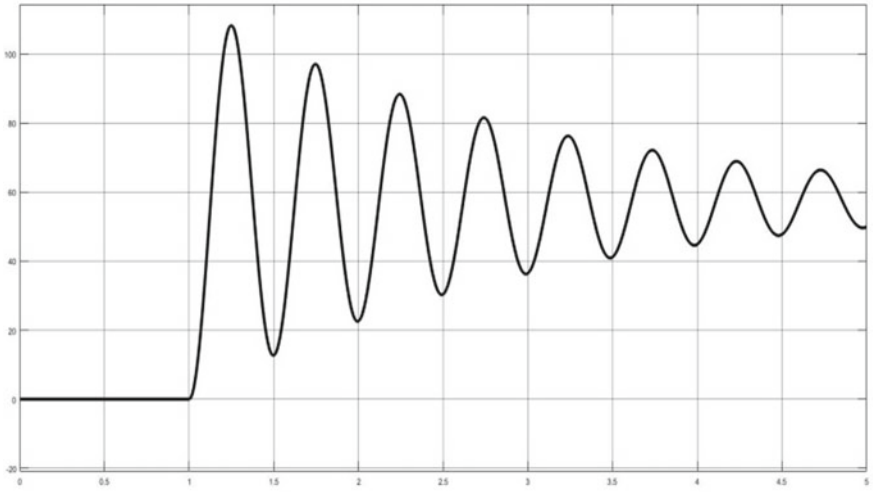

Fig. 10 Plot between voltage versus time. Absisa-time, ordinate-current

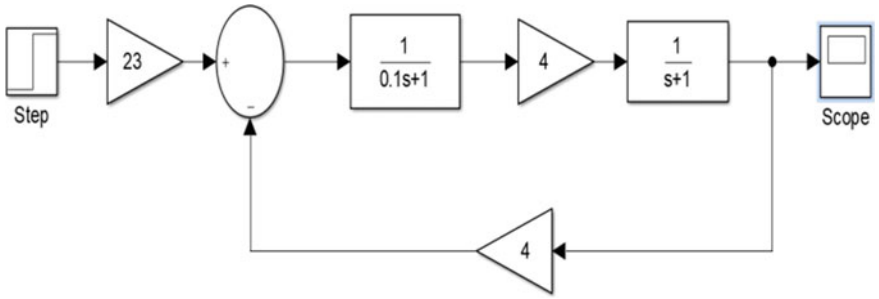

Fig. 11 Simulation model open loop control of DC motor

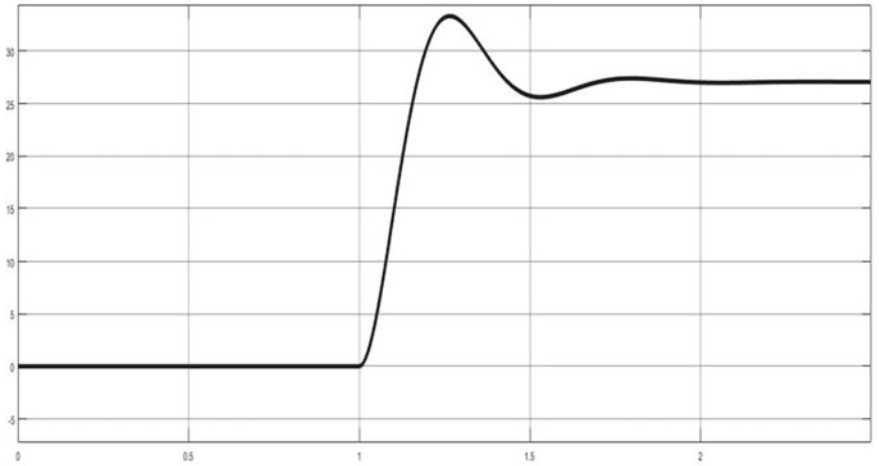

Fig. 12 Plot between voltage versus time. Absisa-time, ordinate-current

(iii) Aim of the Experiment—Simulation of open loop control of a DC motor using transfer function.

Simulink Diagram (Fig. 14):
Result (Fig. 15).

Experiment-3

(i) Aim of the Experiment—Simulation of close loop control of a DC motor using transfer function. (Armature current control)

Simulink Diagram (Fig. 16):
Result (Fig. 17):

(ii) Aim of the Experiment—Simulation of close loop control of a DC motor using transfer function with step sequence. (implementation of armature current and torque control)

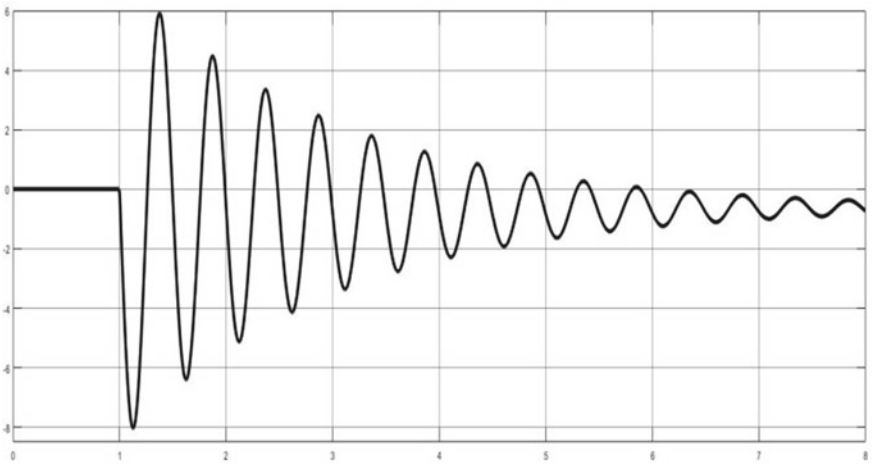

Fig. 13 Plot between voltage versus time. Absisa-time, ordinate-current

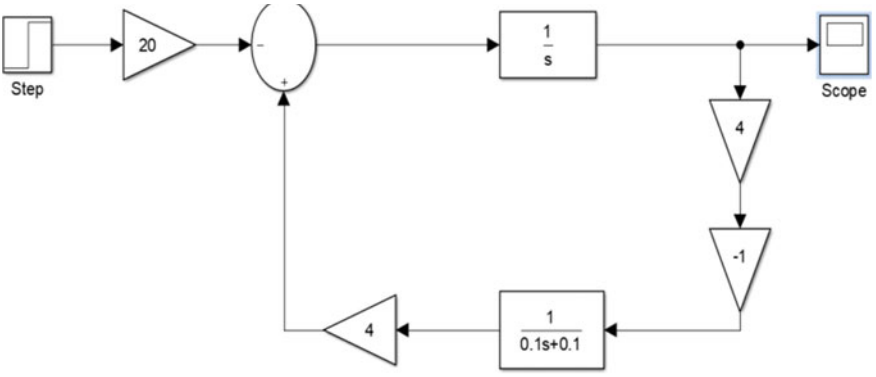

Fig. 14 Simulation diagram open loop control of DC motor

Simulink Diagram (Fig. 18):
Result (Figs. 19 and 20):

(iii) Aim of the Experiment—Simulation of close loop control of a DC motor using transfer function with repeating sequence (implementation of armature current and torque control).

Simulink Diagram (Fig. 21):
Result (Figs. 22 and 23).

Experiment-4

Aim of the Experiment—Simulation of boost converter.
Simulink Diagram (Fig. 24):

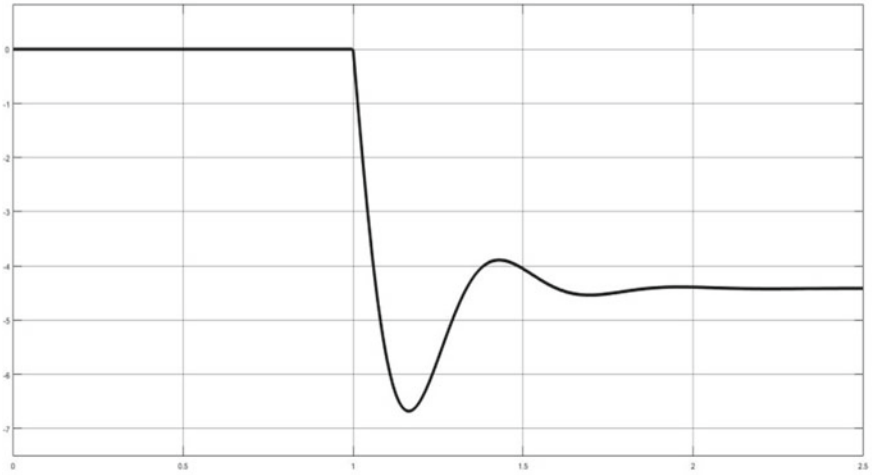

Fig. 15 Plot between voltage versus time. Absisa-time, ordinate-current

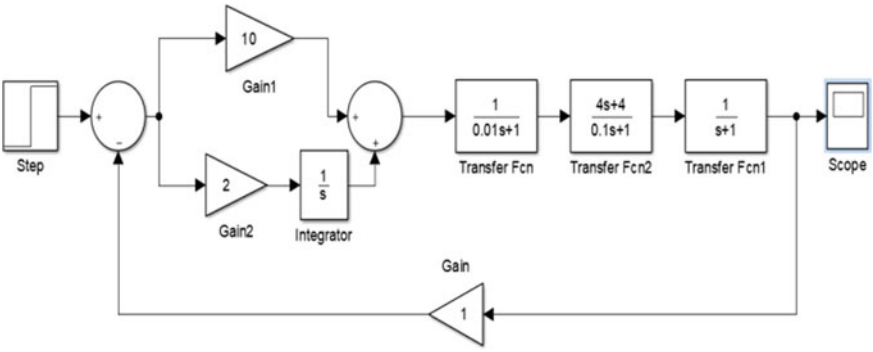

Fig. 16 Simulation model of close loop control of DC motor

Result (Figs. 25, 26, 27).

Experiment-5

Aim of the Experiment—Simulation of CUK converter.

Simulink Diagram (Fig. 28):

Result (Fig. 29).

Experiment-6

(i) Aim of the Experiment—Simulation of unipolar pulse-width modulation (PWM) voltage source inverter.

Simulink Diagram (Fig. 30):

Result (Figs. 31 and 32):

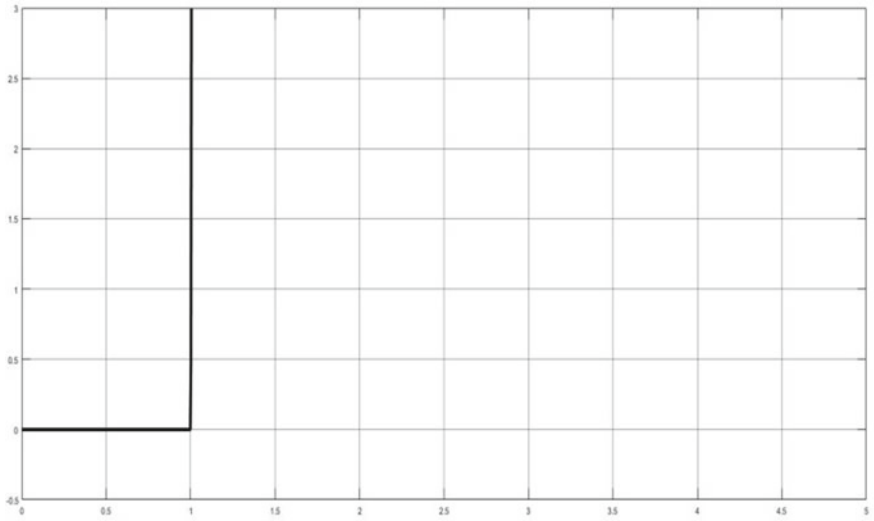

Fig. 17 Plot between voltage versus time. Absisa-time, ordinate-voltage

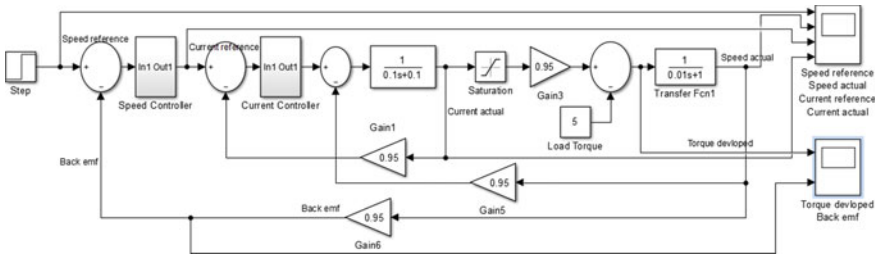

Fig. 18 Simulink model close loop control of DC motor

(ii) Aim of the Experiment—Simulation of unipolar pulse-width modulation(PWM) voltage source inverter.

Simulink Diagram (Fig. 33):
Result (Fig. 34).

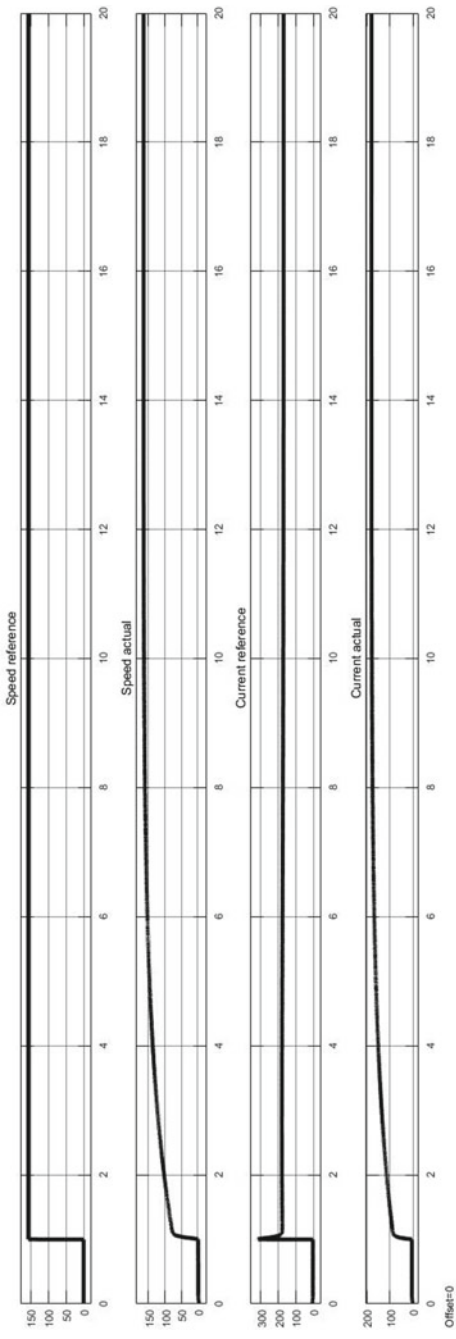

Fig. 19 Simulated waveform of actual speed and current with reference value

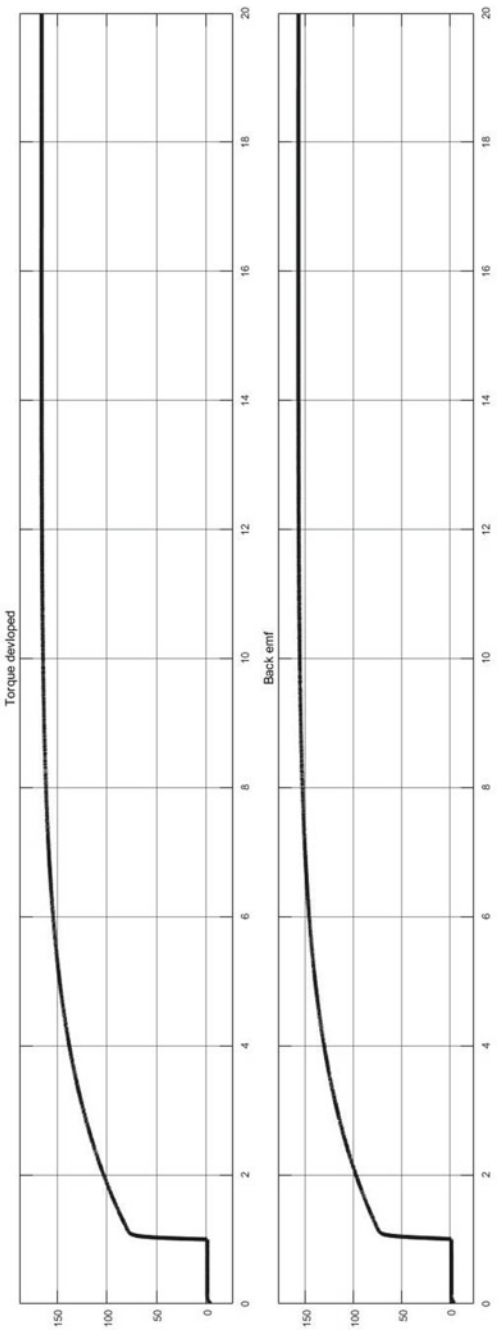

Fig. 20 Simulated waveform of torque and back emf

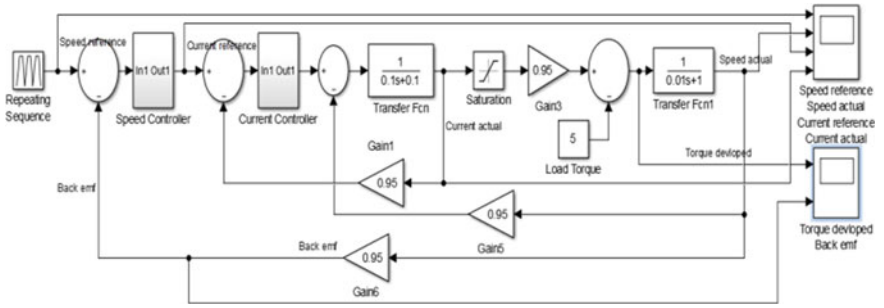

Fig. 21 Simulink model close loop control of DC motor

Experiment-7

Aim of the Experiment—Simulation of design of flux estimator of three-phase induction motor.

Simulink Diagram (Fig. 35):

Result:

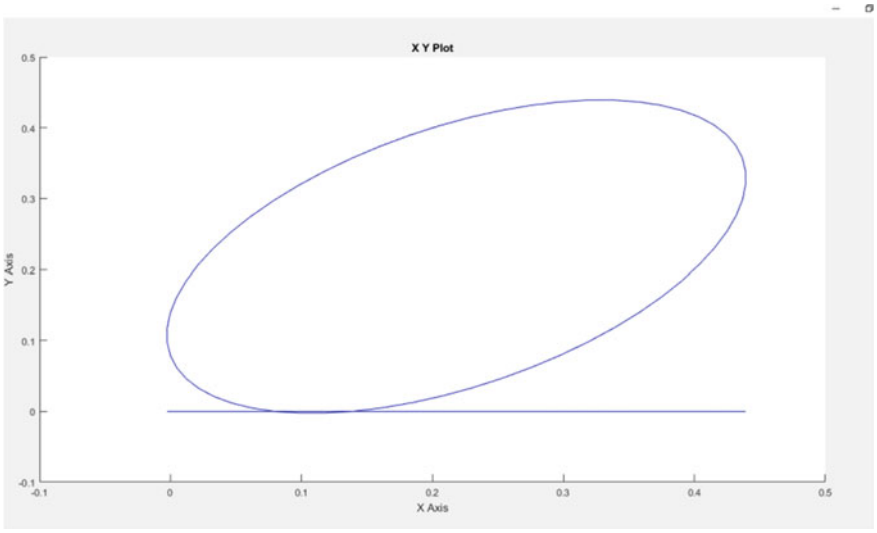

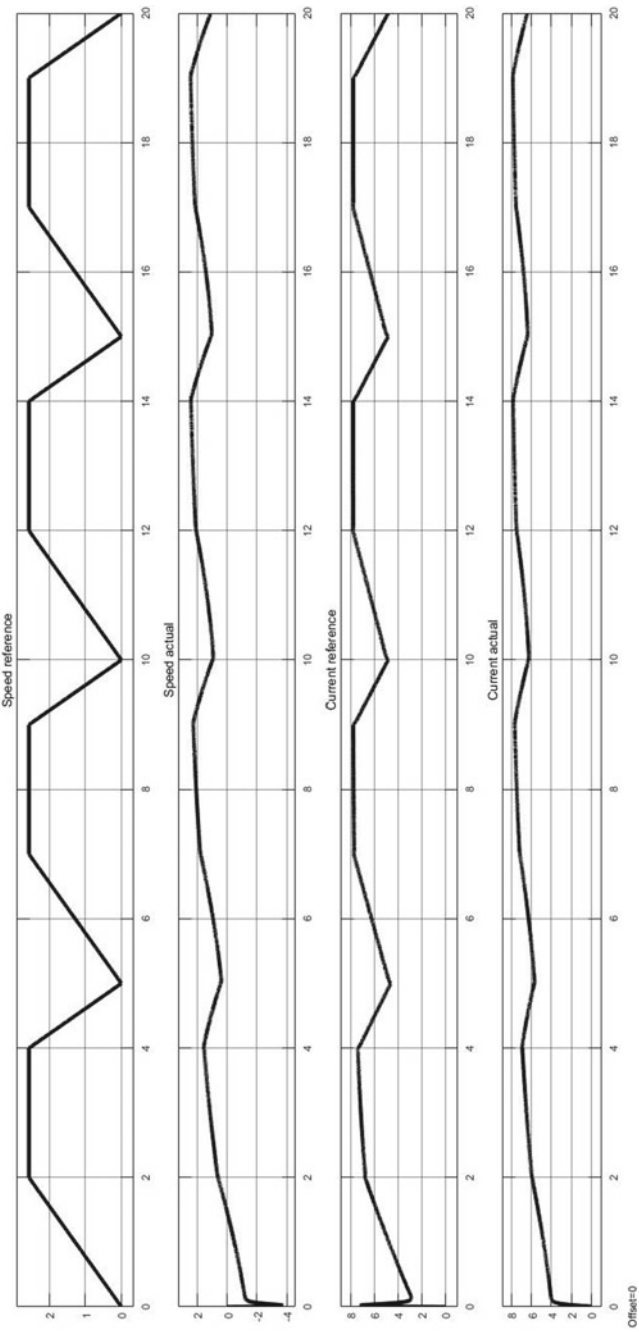

Fig. 22 Simulated waveform of actual speed and current with reference value

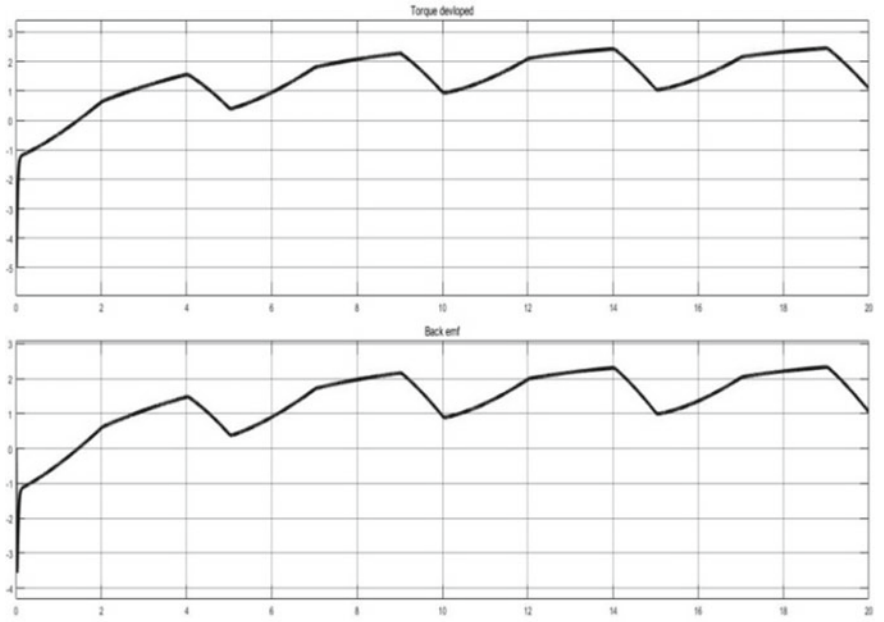

Fig. 23 Simulated waveform of torque and back emf

Experiment-10(ii)

Aim of the Experiment—Simulation of design of flux estimator of three-phase induction motor.

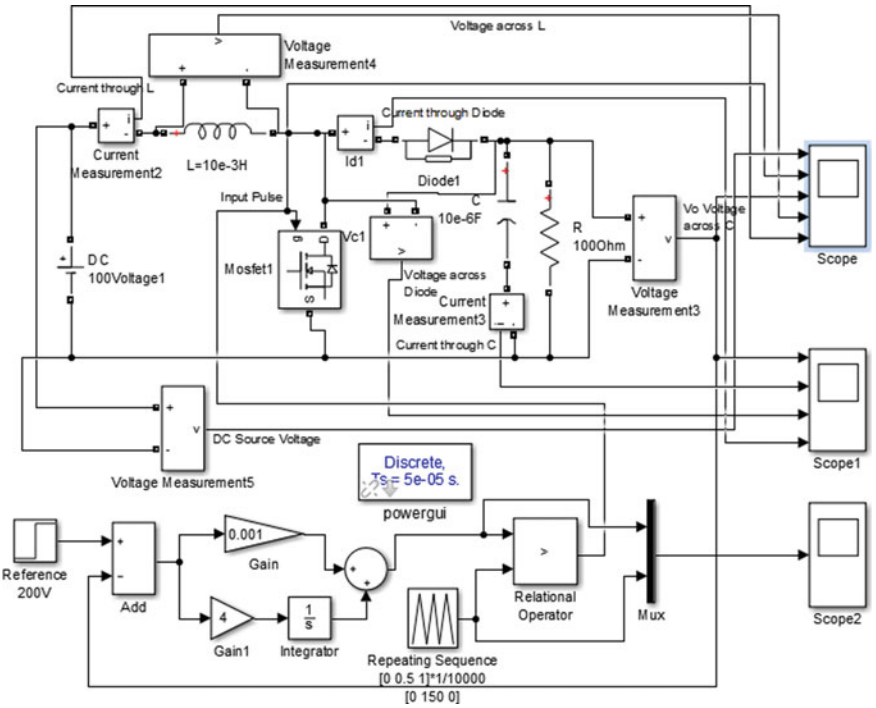

Fig. 24 Simulink model of DC-DC boost converter

Simulink Diagram:

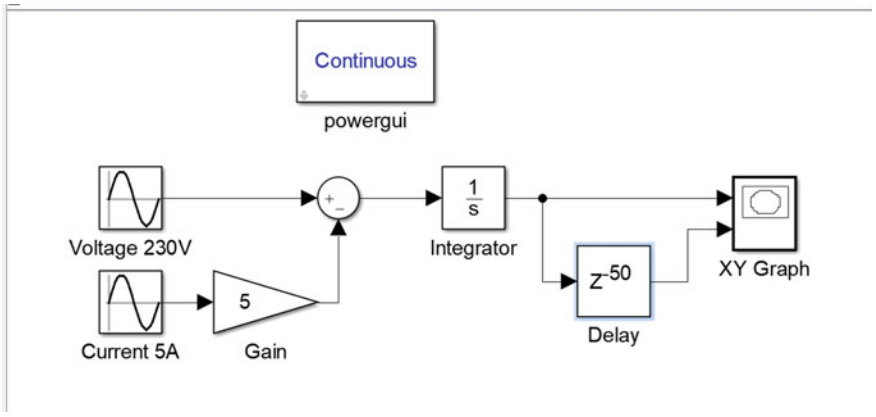

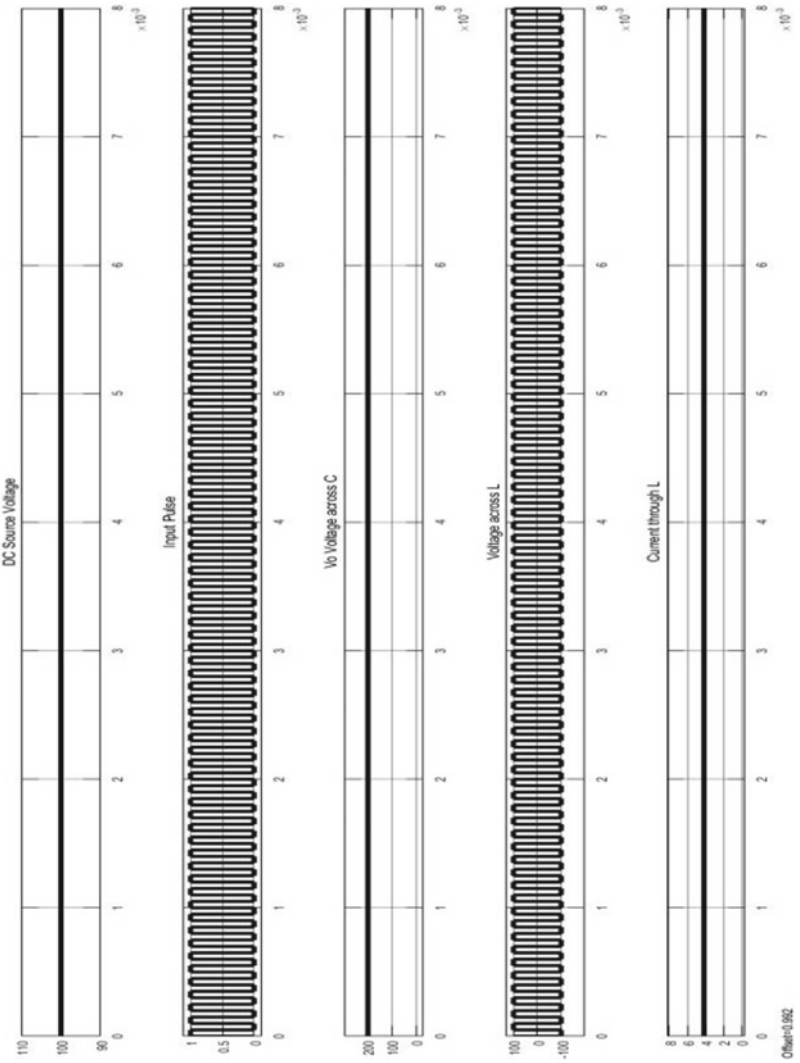

Fig. 25 Simulated waveform of V_o, V_l, V_c, V_s, I_l, and pulse

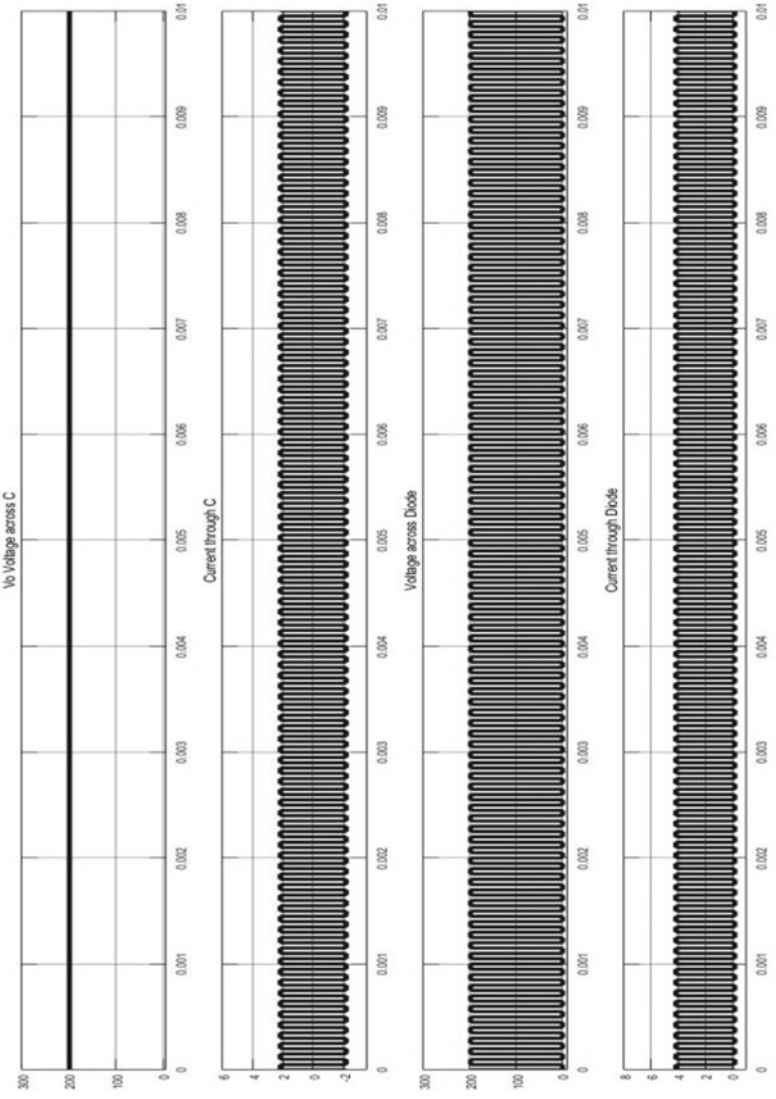

Fig. 26 Simulated waveform of V_c, I_c, V_d, I_d

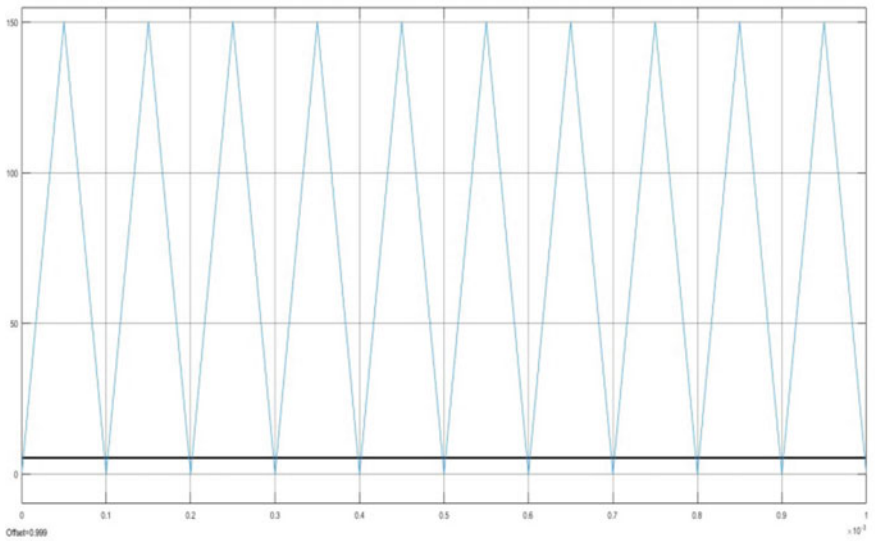

Fig. 27 Simulated waveform of gating pulse in PWM

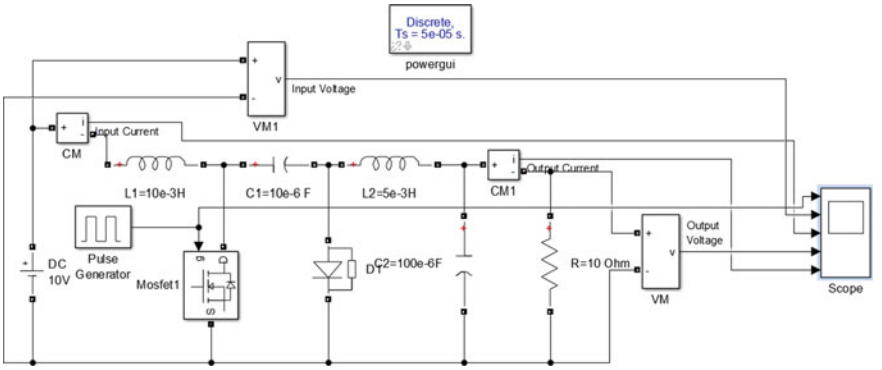

Fig. 28 Simulink model of DC-DC CUK converter

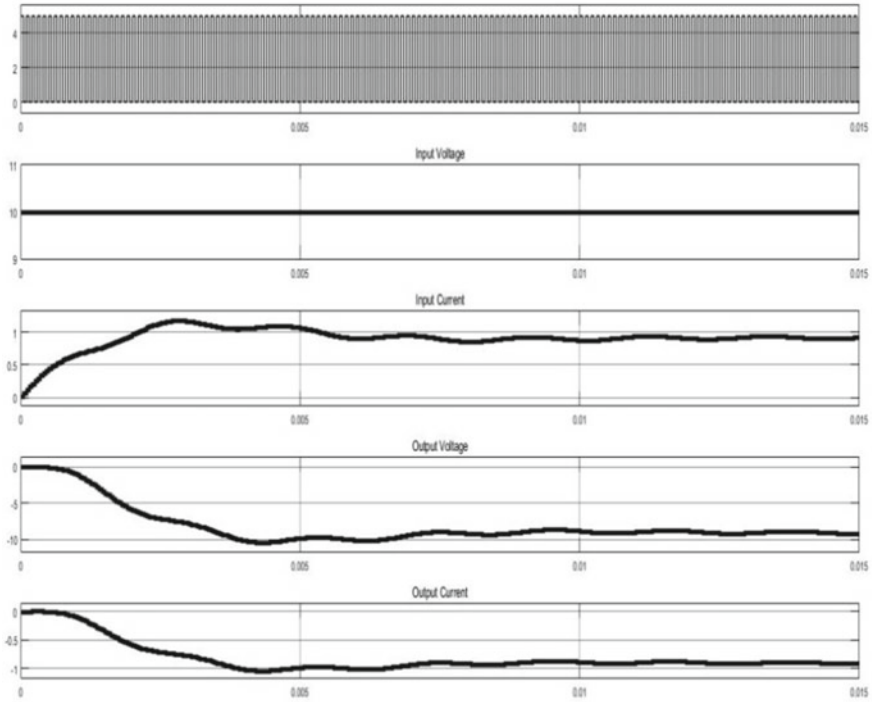

Fig. 29 Simulated waveform of V_s, I_s, V_o, I_o, and pulse

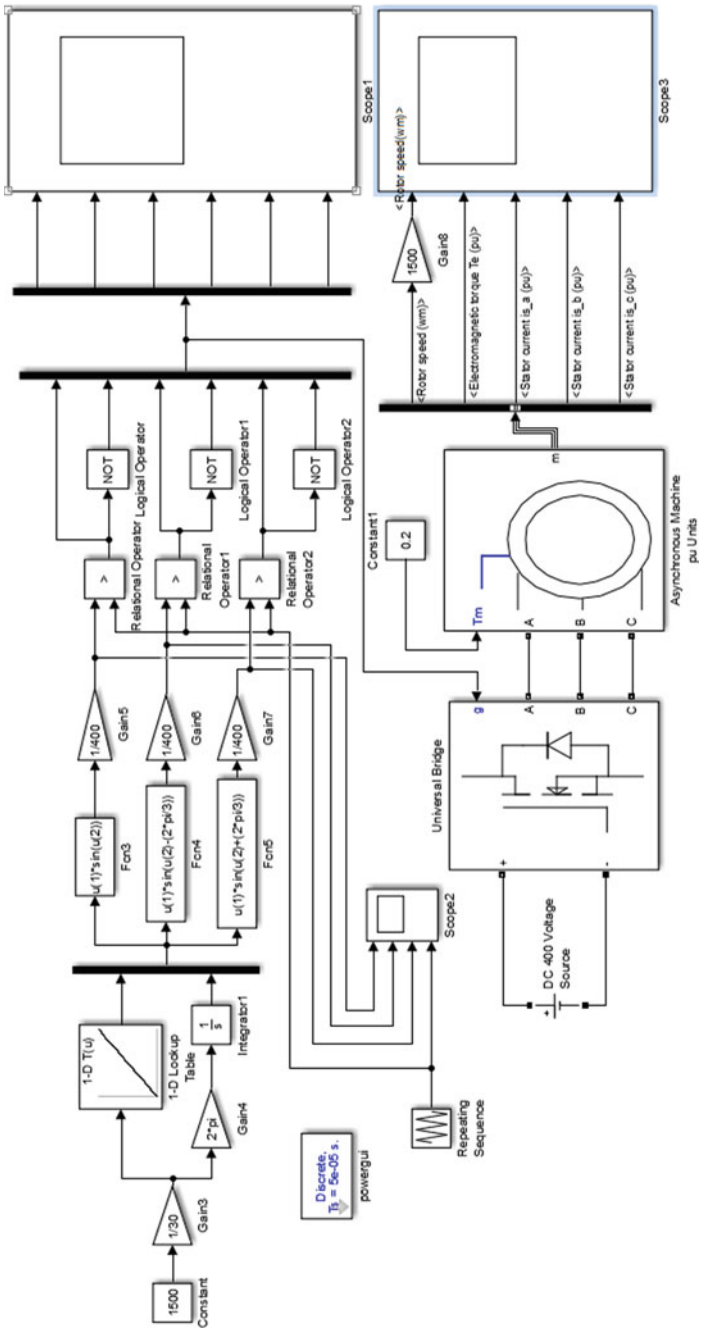

Fig. 30 Simulink model of unipolar pulse-width modulation (PWM) voltage source inverter

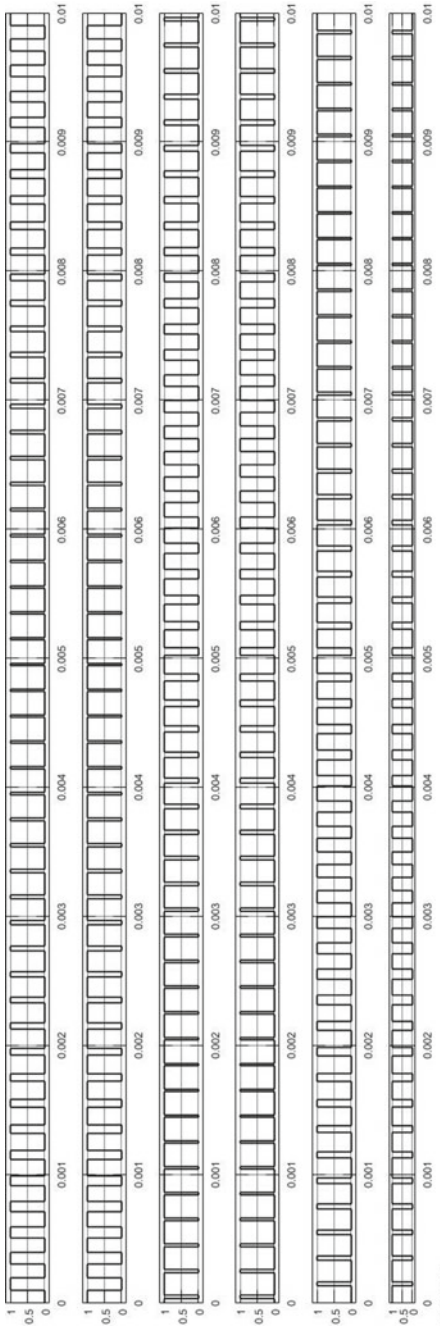

Fig. 31 Simulated waveform of three-phase current and voltage pulses

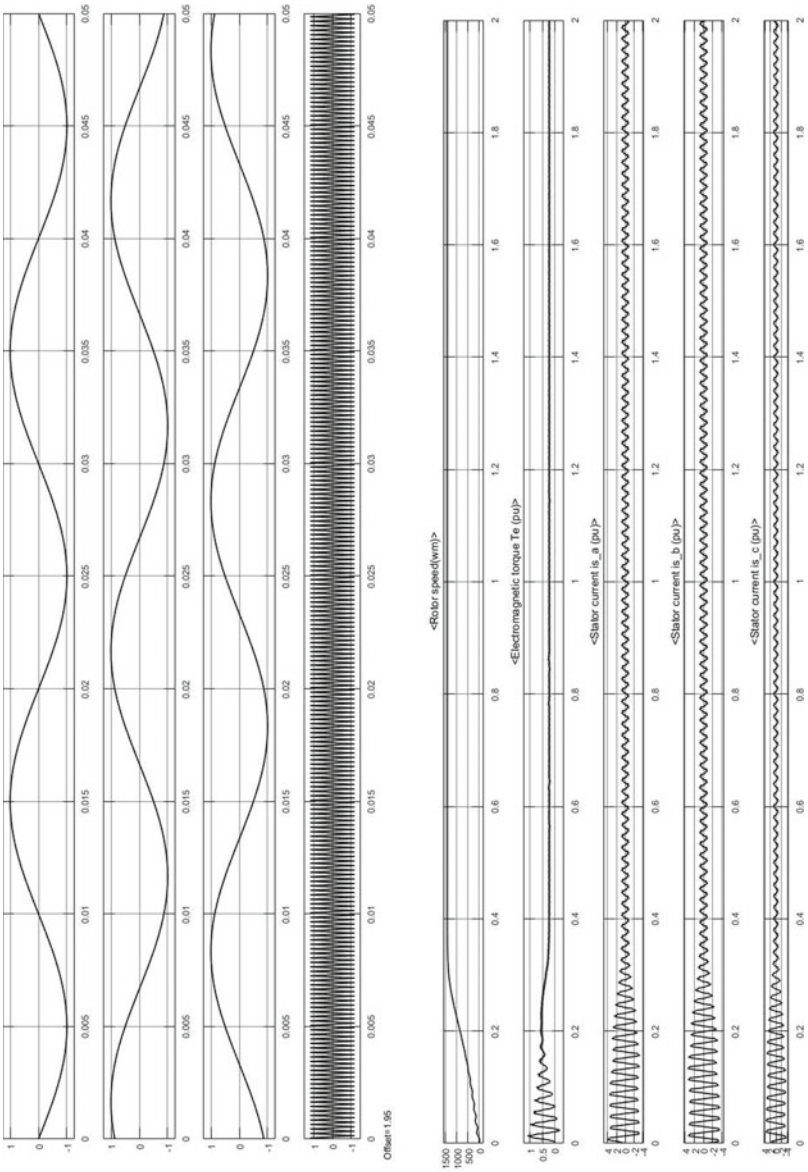

Fig. 32 Simulated waveform of N_r, T_e, I_s (in three phase)

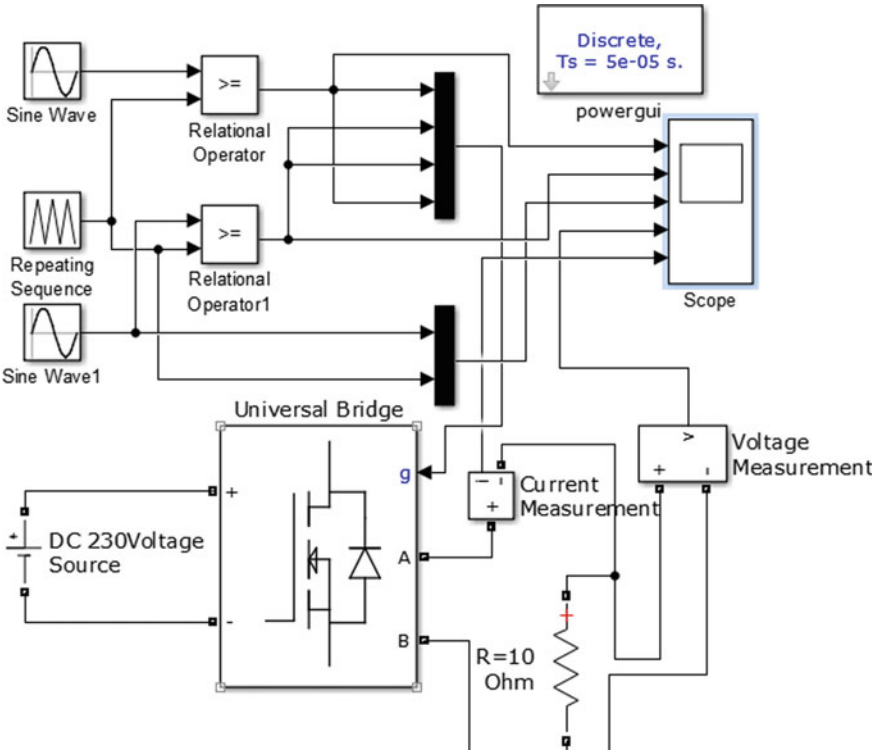

Fig. 33 Simulink model of unipolar pulse-width modulation (PWM) voltage source inverter

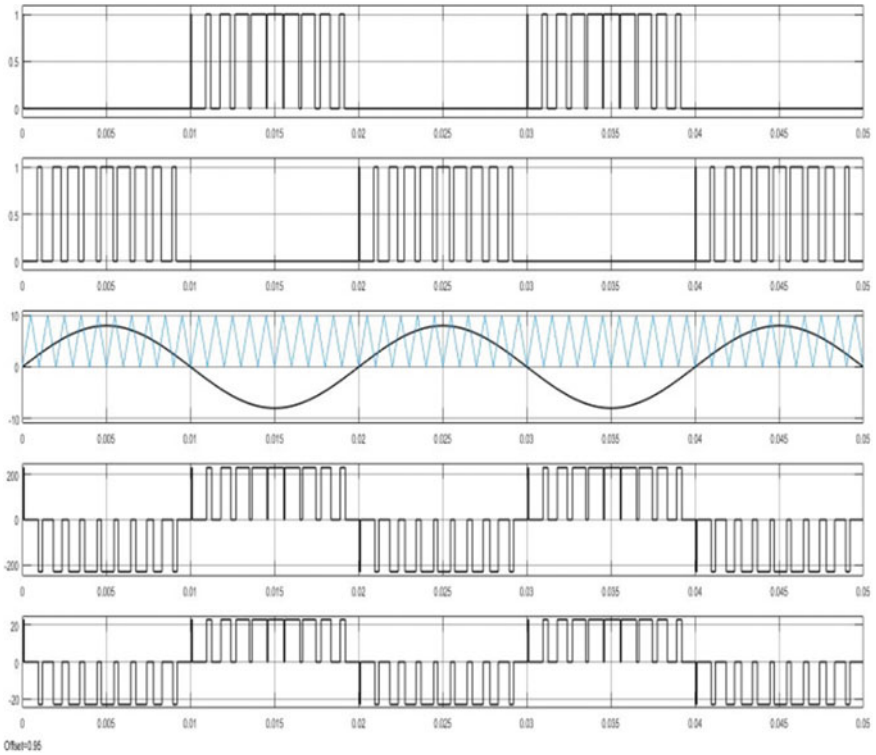

Fig. 34 Simulated waveform of V_o and I_o of three-phase VSI

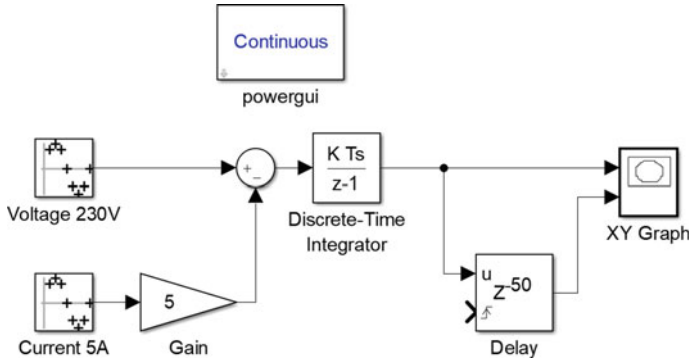

Fig. 35 Simulink model of three-phase flux estimator

Result:

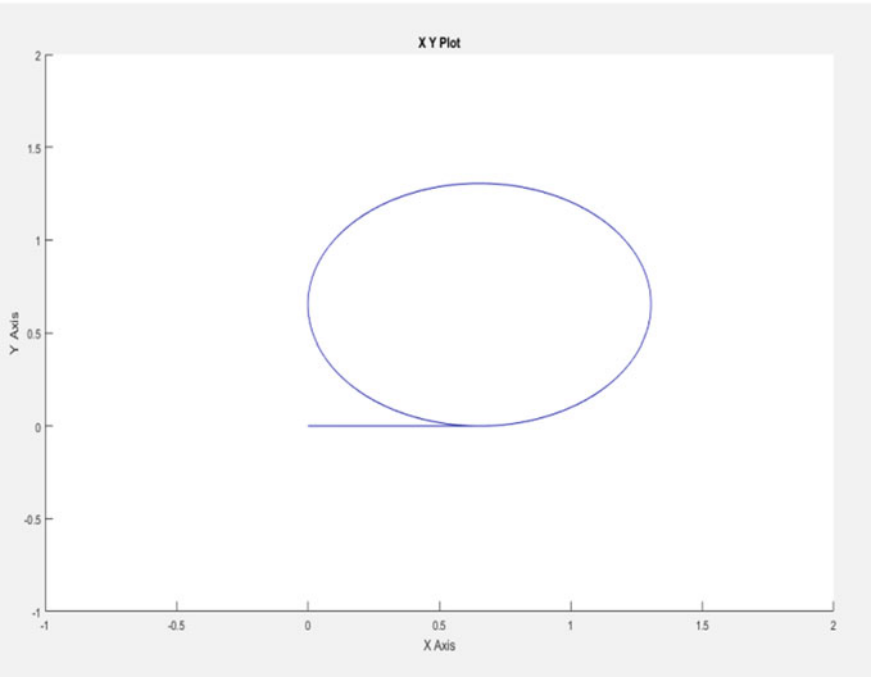

Experiment-11(i)

Aim of the Experiment—Simulation of 3-phase flux control of induction motor.

Simulink Diagram:

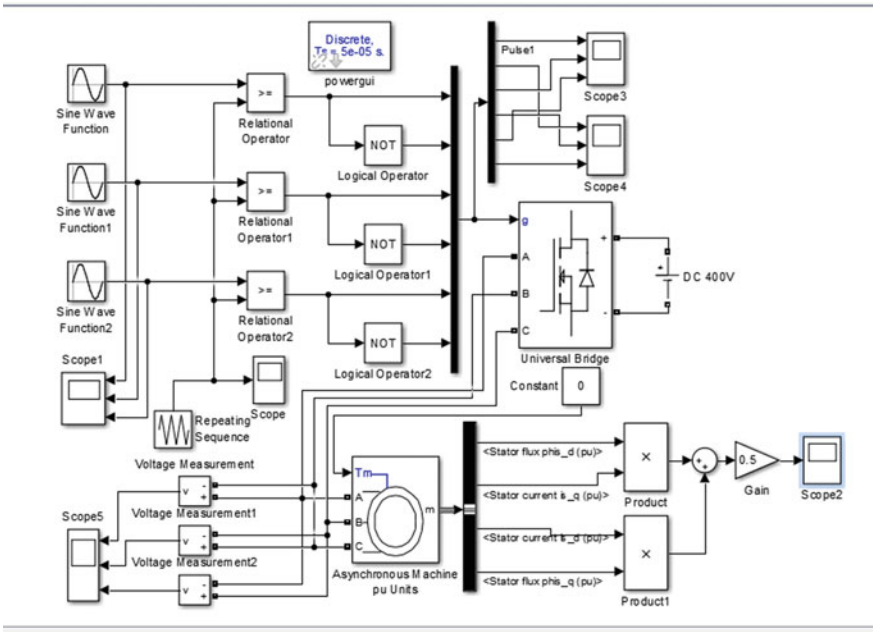

Result:

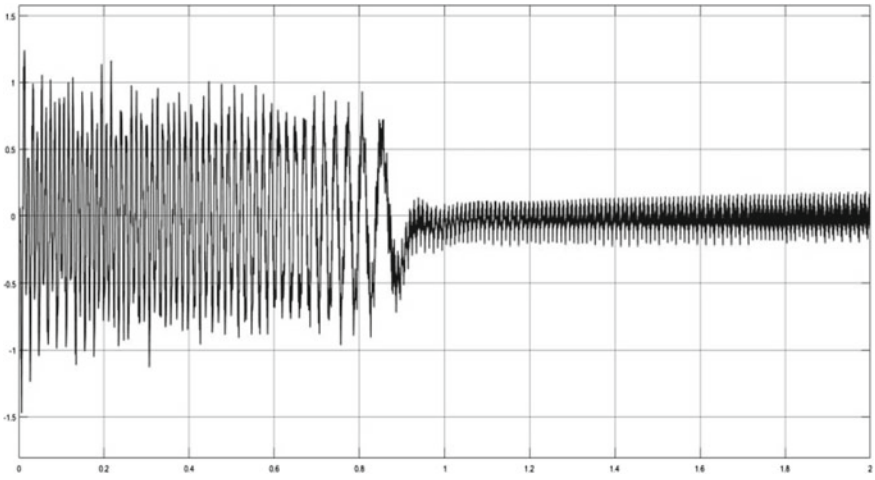

Experiment-11(ii)

Aim of the Experiment—Simulation of three-phase flux control of induction motor (close loop).

Simulink Diagram:

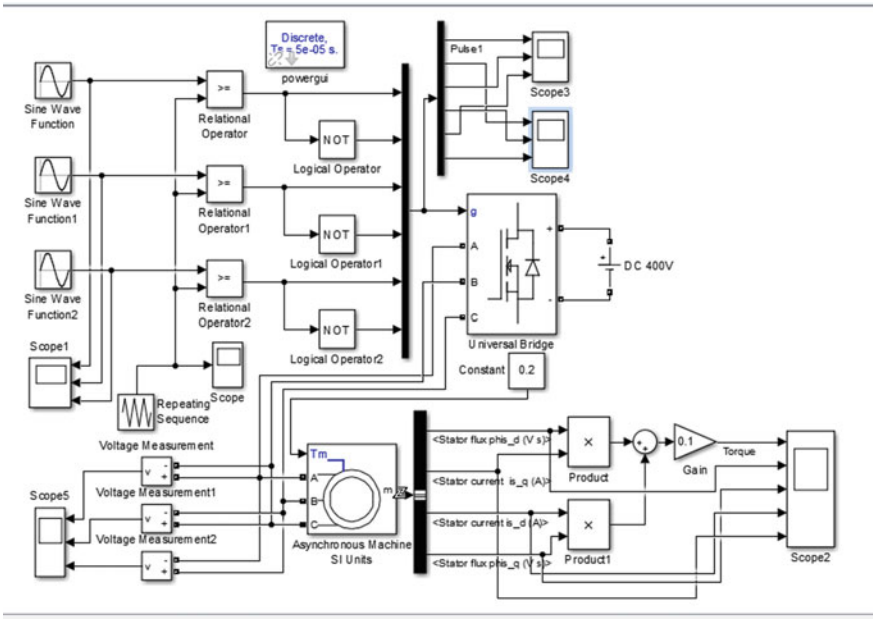

Result:

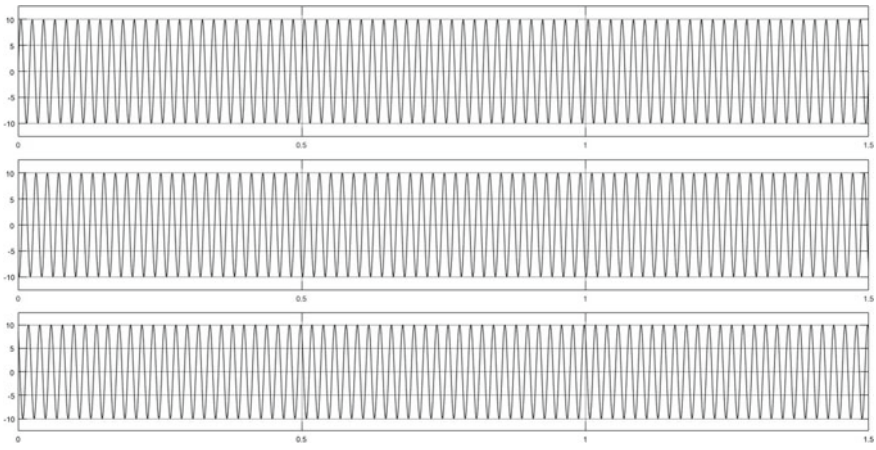

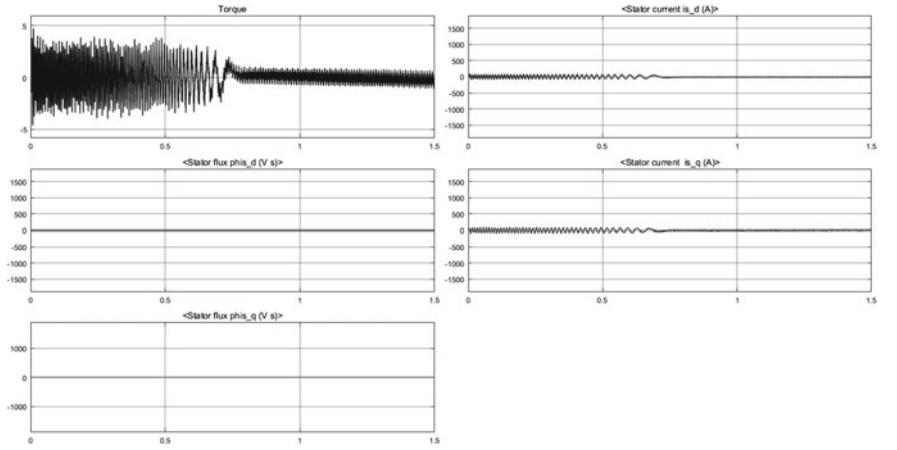
Torque
<Stator current is_d (A)>
<Stator flux phis_d (V s)>
<Stator current is_q (A)>
<Stator flux phis_q (V s)>

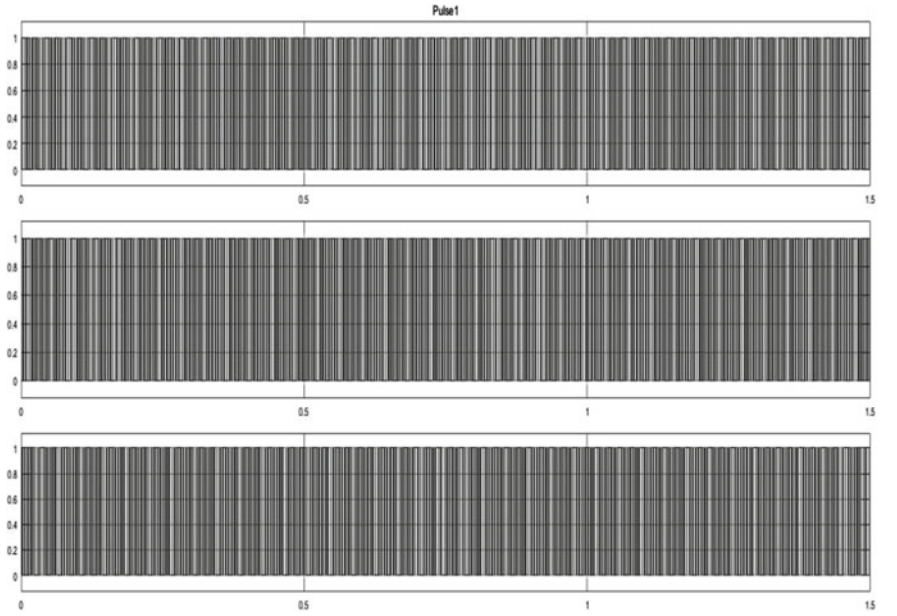
Pulse1

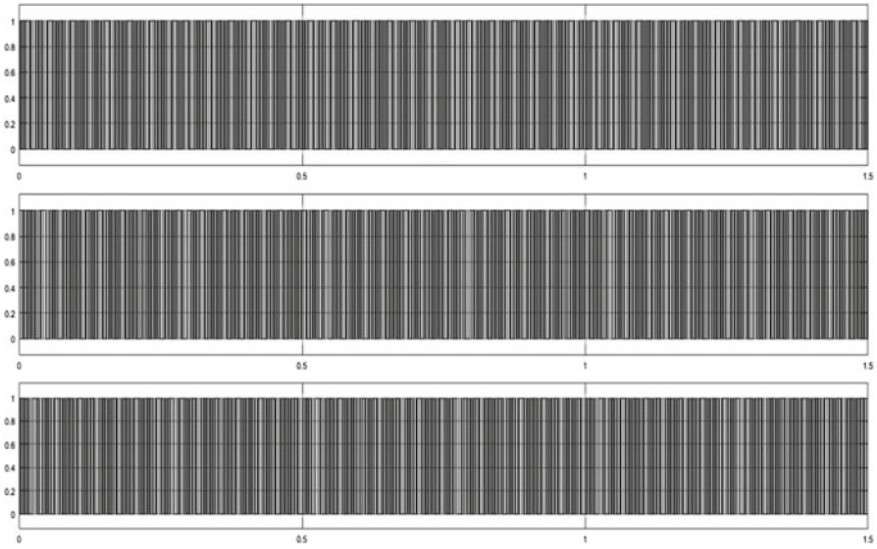

2 Conclusion

This paper successfully implements the idea of different methods such as transfer function methods, state space analysis, and variable supply. Highly efficient controllers such as PI controller and robust control methods such as armature voltage control, flux control, and flux estimation are implemented in digital domain in this paper. A justifiable waveform analysis of different experiments (in the field of the power system and power electronics) has been done. This intensifies and also paved a way for application of power electronics in the field of energy technology.

References

1. Macbahi H, Ba-Razzouk A, Xu J, Cheriti A, Rajagopalan V (1998) Numerical simulation in power electronics using the MATLAB-SIMULINK program. In: IEEE conference proceedings, IEEE Canadian conference on electrical and computer engineering (Cat. No.98TH8341), vol 2. Waterloo, Ontario, Canada 1998. pp 473–476
2. Zhao T, Wang Q (2005) Application of MATLAB/SIMULINK and PSPICE simulation in teaching power electronics and electric drive system, 2005. In: International conference on electrical machines and systems, Nanjing, 2005, vol 3, pp 2037–2041
3. Path D, ChandrasekaranA (1997) A novel approach to the design and implementation of a power electronics simulation software package. In: Proceedings the twenty-ninth southeastern symposium on system theory, Cookeville, TN, USA, 1997, pp 473–476

4. Orts S, Segui S, Gimeno FJ, Alcaniz M, Masot R (2004) Modelling and simulation of three phase power active compensator with Matlab/Simulink, 2004. In: IEEE, 35th annual power electronics specialists conference (IEEE Cat. No. 04CH37551), Aachen, Germany, vol 4, 2004, pp 3182–3187
5. Sybille G, Le-Huy H (2000) Digital simulation of power systems and power electronics using the MATLAB/Simulink Power System Blockset, 2000. In: IEEE conference proceedings power engineering society winter meeting. (Cat. No.00CH37077), Singapore, 2000, vol 4, pp 2973–2981
6. Athaide D, Qin J, Zou Y (2019) MATLAB/Simulink-based electromagnetic transient-transient stability hybrid simulation for electric power systems with converter interfaced generation, 2019. In: IEEE, conference proceedings, texas power and energy conference (TPEC), College Station, TX, USA, 2019, pp 1–6
7. Zhao T, Wang Q (2005) Application of MATLAB/SIMULINK and PSPICE simulation in teaching power electronics and electric drive system, 2005. In: International conference on electrical machines and systems, Nanjing, 2005, vol 3, pp 2037–2041
8. Linzen D, De Doncker RW (2002) Simulation of power losses with MATLAB/ Simulink using advanced power device models, 2002. In: IEEE Workshop on Computers in Power Electronics, 2002, Proceedings. Mayaguez, Puerto Rico, USA, 2002, pp 71–75
9. Yusivar F (2018) State space event based model for simulation of power electronics system, 2018. In: 4th international conference on nano electronics research and education (ICNERE), Hamamatsu, Japan, 2018, pp 1–4
10. Martins LS, Costa D, Martins JF, Pires VF (2009) Modeling for computer simulation as a tool for the teaching of transient power systems. In: 2009, International conference on power engineering, energy and electrical drives, Lisbon, 2009, pp 629–634
11. Qiong C, Zhilin D, Li L (2012) Implementation of virtual laboratory of power electronics based on Matlab and LABVIEW, 2012. In: 7th international conference on computer science & education (ICCSE), Melbourne, VIC 2012, pp 1539–1544

Chapter 23
Combined Frequency and Voltage Control of a Multi-area Renewable-Based Interrelated Power Structure

Subhranshu Sekhar Pati, Saroj Kumar Mishra, and Anshuman Panda

Abstract This article investigates combined automatic load frequency control (ALFC) and automatic voltage regulator (AVR) in an interrelated area multi-power source with the integration of thermal, solar thermal plant (SHP), and small hydro plant (SHP). Requisite physical nonlinearities of an actual running plant are reflected in plants taken under consideration. A maiden effort has been made to integrate the multistage controller in combined frequency and voltage regulation. An operative optimization procedure titled as Jaya algorithm has engaged for tuning of controller parameters. A step load of 1% is applied to the system to simulate a real time environment. Various controllers such as Two-Degree-of-Freedom-Proportional-Integral-Derivative (TDOFPID) controller and PID controller with filter (nPID) have been incorporated in the system to verify the system response with that of the multistage controller. The dynamic interaction of the optimization algorithm with the proposed controller arrangement demonstrates noteworthy enhancement on the response over TDOPID and nPID controller.

Keywords Frequency and voltage control · Jaya algorithm · Multistage controller · Solar thermal plant · Small hydro plant

1 Introduction

In today's world, the supply of uninterrupted and reliable power from a highly interconnected complex power system is the primary concern. Stable and reliable power is indicated by its constituent components like frequency, voltage level, and tie-line exchange power which should lie within the predetermined limits subjected to disturbances in the complex scheme [1]. To retain constancy in frequency and voltage level in power system, ALFC and AVR loop is used. In general, a cross-coupling mechanism is present between ALFC and AVR loop as AVR loop operates rapidly than the ALFC. Thus, it is advisable to include the cross-coupling mechanism in

S. S. Pati · S. K. Mishra (✉) · A. Panda
Department of Electrical Engineering, IIIT Bhubaneswar, Bhubaneswar, Odisha 751003, India
e-mail: saroj@iiit-bh.ac.in

S. Mahapatra et al. (eds.), *Advances in Energy Technology*, Advances in Sustainability Science and Technology, https://doi.org/10.1007/978-981-15-8700-9_23

the system modeling for better analysis purpose with a combined ALFC-AVR loop in the system. It is observed from the past literature that most of the papers focus either ALFC or AVR loop in an interconnected power structure [2]. More often, the cross-coupling mechanism is not incorporated in these papers. Still, some of the researchers analyzed both frequency control and voltage level, but the research is carried out in the traditional environment. A combined ALFC-AVR loop in a single area, as well as two area network, had been presented by multiple researchers. Two-area hydel-thermal interconnected power network without concerning nonlinearities like boiler dynamics and governor dead band is analyzed by various researchers [3, 4]. With the advancement of time, diverse researchers attempted to study the collective ALFC-AVR scheme for three-area interrelated system. Hence, the analysis of combined frequency control and voltage is limited to simply a conventional interrelated power system environment. With the progress of time, the traditional power structure has been transmuted into a restructured domain. Moreover, different renewable power sources, a communication mechanism, and distributed generations are also included in power network so as to the realization of a truly smart grid [5, 6]. The integration of renewable sources mainly solar-based power plant has received increased engrossment owing to its widespread benefits than the fossil fuel burning plant. Furthermore, the quick exhaustion of traditional coal-based power unit and increased climate change due to global warming made renewable energy-based power sources a prime energy producer in the power system. The profile of solar plant increased multifold times across the globe. It has the potential to power up the whole world without using any fossil fuel-based power sources. There are numerous research articles available which present the detailed design modeling of solar power plant [7–10].

STP has a collector that normally has a wide area, so that it focuses the sunlight into a particular place where heat-absorbing medium is present. This medium collects heat from solar irradiance and converts water into steam which is used for electricity generation. The STP modeling used in this article is addressed in detail by Pati et al. [10]. Power generation from SHP units can be huge but yet untapped in most of the countries in particular developing areas like India. Its technology is now rapidly developed and already proves its effectiveness and efficient controlling thus significantly contribute to energy harvesting. Still, there is considerable research gap that needs to be further addressed. SHP can serve a small locality or industry whose rated power must not exceed 20 MW. It can serve as a standalone mode or grid-connected mode with other renewable-based power plant there by implementing idea of a microgrid. The diverse researcher proposed SHP application as controlling flow of water through the multiple pipe or conduit for managing dump load. Furthermore, the dynamic transfer function model of SHP plant for a multiple area network is a challenging task [8].

The primary objective of designing a controller is to uphold the frequency deviation and terminal voltage level inside the desired limit even though the application of large disturbances. It is reported by past literature that a different type of secondary controllers like classical controller such as proportional plus integral plus derivative (PID) controller, fractional-order-based controller, i.e., FOPID controller, or

fuzzy-rule-based controller is used. Moreover, these regulators are incorporated in the study of an individual ALFC system and AVR loop. However, the application of a multistage controller in the study of combined ALFC-AVR loop is still limited. Hence, authors decided to use a multistage controller in this study for controlling both frequency deviation and voltage level. Dash et al. proposed a cascaded PI-PID controller and used it for frequency regulation [7]. Pati et al. presented a new version of multistage controller, i.e., (PD) − (1 + PI) controller, and used in the multi-area system for controlling only the frequency deviation. This type of controller integration in combined frequency and voltage regulation is still limited [10]. For the successful operation of an effective controller, its parameters are tuned through an application of an optimization algorithm. There are several optimization algorithms used by several researchers in past literature. Some of those are flower pollination algorithm, teaching–learning algorithm, whale algorithm, and Jaya algorithm [2–12]. Owing to less computation time with minimum hindrance in the tuning process, the Jaya algorithm received increased attention in recent times.

2 System Modeling

In this study, two equal area of combined frequency and voltage regulation models are included for analysis. Each area consists of thermal, solar-based sources and SHP as a power generating sources are considered. The dynamic transfer function and its associated parameters of thermal, STP, and SHP are taken for investigation in this study that is reported by literature [10].

The complete test model of the combined ALFC loop is presented in Fig. 1 with transfer function. The frequency of the power system controlled through the ALFC mechanism which checks out the active power mismatch. With the rise of active power, the frequency will also rise. Consequently, the internal electromotive force (E) of the generating unit will eventually rise which in line the terminal voltage level. The relationship of the above can be addressed by the following equation, where n and f are the speed and field current, respectively [8, 9].

$$E \alpha n i_f \tag{1}$$

The change of terminal voltage (V) will take care of the AVR loop and can be stated by Eq. 2.

$$P_e = \frac{|V||E|}{X_s} \sin \delta \tag{2}$$

The AVR loop operates faster than the ALFC loop and has a much greater impact on the ALFC mechanism. But no such effect of ALFC over AVR loop is observed. There are certain cross-coupling coefficients like K_1, K_2, K_3, and K_4 that are involved in AVR modeling. The generalized diagram of AVR is shown in Fig. 2. Out of these

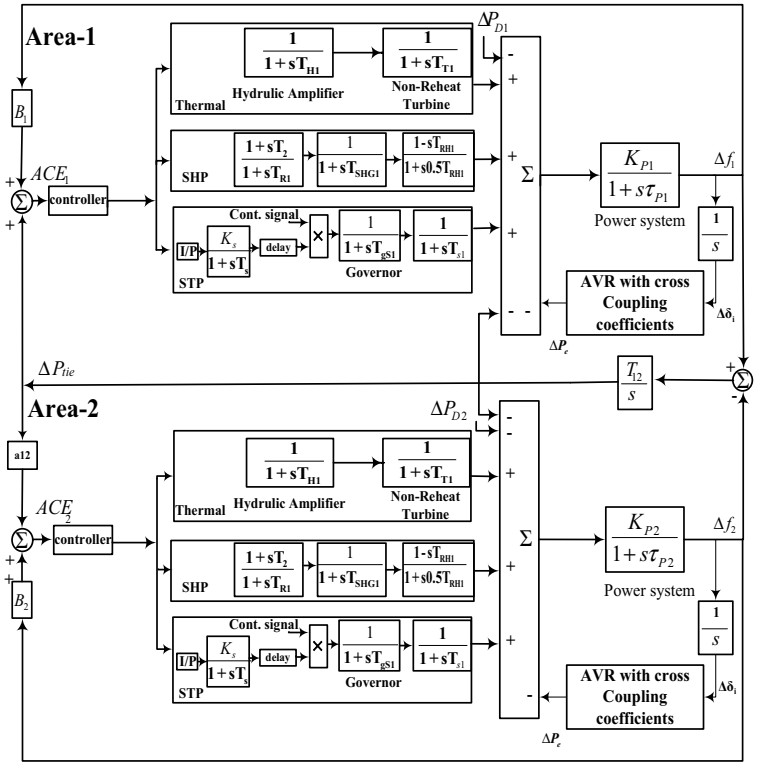

Fig. 1 Test model under consideration

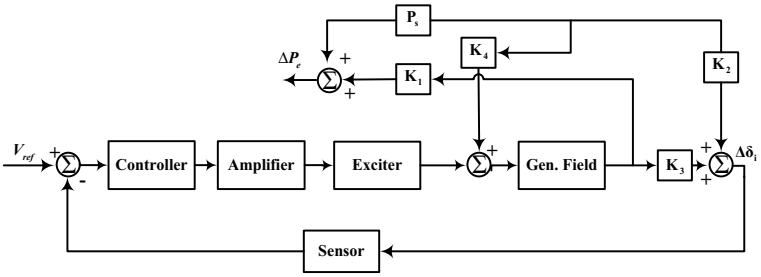

Fig. 2 Generalized structure of AVR loop

coefficients, the values of K_1, K_3, and K_4 are always positive. However, the value of K_2 is either positive or negative depending upon system impedances [1].

In AVR loop, an amplifier is operated by the following equation.

$$\Delta X_a = \frac{K_a}{1 + sT_a} \Delta V \tag{3}$$

Similarly, the characteristics of the exciter and generator field can be expressed by Eqs. 4 and 5.

$$\Delta X_e = \frac{K_e}{1 + sT_e} \Delta X_a \tag{4}$$

$$\Delta X_g = \frac{K_g}{1 + sT_{g\,a}} \tag{5}$$

The sensor used in the AVR loop obeys the following equation, where K_a, K_e, K_g, and K_s are the gain constants and T_a, T_e, T_g, and T_s are the time constants.

$$\Delta V_r = \frac{K_s}{1 + sT_s} \Delta V \tag{6}$$

3 Controller Structure

To maintain system stability, the design of an efficient controller is necessary. It is observed that most of the literature considered the PID controller as a controlling agent [4–6]. Although the PID controller structure is simple to implement, simplest and easily optimized, it cannot produce an improved result in a particular transient and steady state when the system is highly complex and multiple energy resources are integrated [5, 6].

Furthermore, with an increment of proportional gain which reduces steady-stare error which in turn deteriorates the response at transient state. The high value of proportional gain also slows down the system response. To overcome such a scenario, an efficient multistage controller is considered in this study. The multistage controller has two stage. In first stage, proportional plus derivative (PD) controller is considered, whereas in the second stage, proportional plus integral term with a constant, i.e., (1 + PI) controller, is considered. The generalized structure of multistage controller is presented in Fig. 3. The transfer function model of such an arrangement is depicted in Eq. 7.

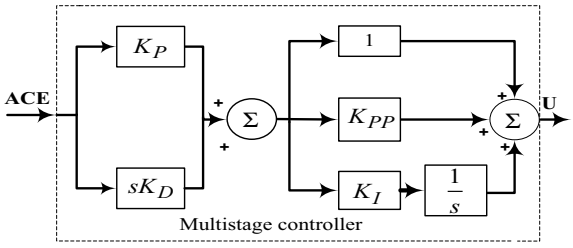

Fig. 3 Proposed controller arrangement

$$\text{T. Fmultistage} = (K_P + sK_D) \times (1 + K_{PP} + K_I/s) \tag{7}$$

The main idea of designing such a controller structure is to dive the controlling action into two parts, i.e., the first stage takes care of the transient state, and the second part controls the steady state. It gives improved results during the continuous load disturbances [10]. Also, it has a greater number of tuning parameters. Hence, it is easy to maintain system stability subjected to time-varying load disturbances. To tune the controller parameters, generally, an objective function is involved [11, 12]. In this study, integral time-multiplied absolute error (ITAE) is considered which is also depicted in the following equation, where t sim represents simulation time and Δf_1 and Δf_2 are the frequency abnormality in area 1 & 2 correspondingly. Similarly, ΔP_{tie} is the incremental change of power in tie line. Jaya algorithm is applied for optimization of regulator parameters.

$$J_{\text{ITAE}} = \int_0^{t_{\text{sim}}} (|\Delta f_1| + |\Delta f_2| + |\Delta P_{\text{tie12}}|) t \, \mathrm{d}t \tag{8}$$

4 Optimization Technique

Optimizing a powerful and constraint-based nonlinear controller is a tedious and monotonous task when optimized manually using Ziegler & Nichols method. In a complex power system model involving different nonlinearities and constraints to be satisfied, novel optimization algorithms are applied to locate optimized data set of controller parameters. Jaya algorithm is a metaheuristic algorithm proposed by Rao et al. [13] in 2016 that is a simple optimization algorithm which is more successful than new heuristic algorithms in recpect to its simple implementation and fewer numbers of iterations taken to meet the ideal solution. The principle behind the algorithm is that the movement of the obtained solution in each iteration should be toward the optimal solution and not to move to worst solution. In another similar type of metaheuristic optimization algorithm teaching-learning-based optimization algorithm (TLBO), the algorithm is first trained to catch the optimized values, and then, the algorithm is used to resolve the ALFC-AVR problem; but in Jaya algorithm, there is no teaching process, rather it learns to find the optimized values on its own. This helps in improving computational efficiency and reduces the memory utilized in algorithm execution [13]. Let P is the size of population or the number of candidate solutions ($i = 1, 2, 3, \ldots P$) which is equivalent to the quantity of regulator parameters to be optimized and Q be the number of decision variables ($j = 1, 2, 3, \ldots Q$) for each controller parameters which stores the values obtained for each controller parameters during every iteration, and finally, it is used to find the optimum values at the end of the optimization process. At the termination of each kth iteration, the optimum solution is denoted as $X\text{best}K$, and the worst solution is denoted as $X\text{worst}K$. During

the Kth iteration if Xi, jK is the worth of the jth decision state for ith population element, then Xi, jK is updated as below equation [14].

$$Xi, jK = Xi, jK + \mu 1,\ jK(Xj,\ \text{best}K - |Xi, jK|) - \mu 2,\ jK(Xj,\ \text{worst}\ K - |Xi, jK|) \tag{9}$$

where Xj, best$K$ and Xj, worst$K$ are the optimal solution value and worst solution value obtained for jth decision variable, respectively. $\mu 1$ and $\mu 2$ are two randomly value which lie in the range 0–1. The updated value of Xi, jK participates in the subsequent iteration, and the procedure is reiterated till the global solution is reached.

5 Result Analysis

In this study, multi-area renewable-based multi-source interrelated system has been taken into account. Jaya optimized multistage controller has incorporated in the combined frequency and voltage regulation process.

As the system network is highly complex, the classical controller cannot produce an efficient result. So multistage controller, in this case, provides a better response than the other conventional controller structure. The upper and lower limit of the controller parameter used in this literature is +3 to −3, the gain value of the projected controller structure is presented in Table 1.

To check the system stability, a step load of 1% is applied to the area-1. The response derived with the application of the step load shown in Fig. 4. From the figure, it can be inferred that the suggested multistage controller proves its superiority with regards to peak over and undershoot then the FOPID controller and nPID controller. Similarly, the settling time is much less in the event of multistage controller. Moreover, the proposed controller also produced an enhanced result of voltage regulation in AVR loop. The graphical demonstration of the voltage outcome derived from the test system with the proposed controller with that of TDFOPID and nPID controller is shown in Fig. 5.

Table 1 Controller parameters

Controller/optimization technique		Controller parameters				Obj. fun (ITAE × 10^{-3})
		K_P	K_D	K_{PP}	K_I	
Area-1	PD − (1 + PI): Jaya	2.184	1.481	2.151	2.136	1.5494
Area-2	PD − (1 + PI): Jaya	1.994	1.719	2.916	2.434	

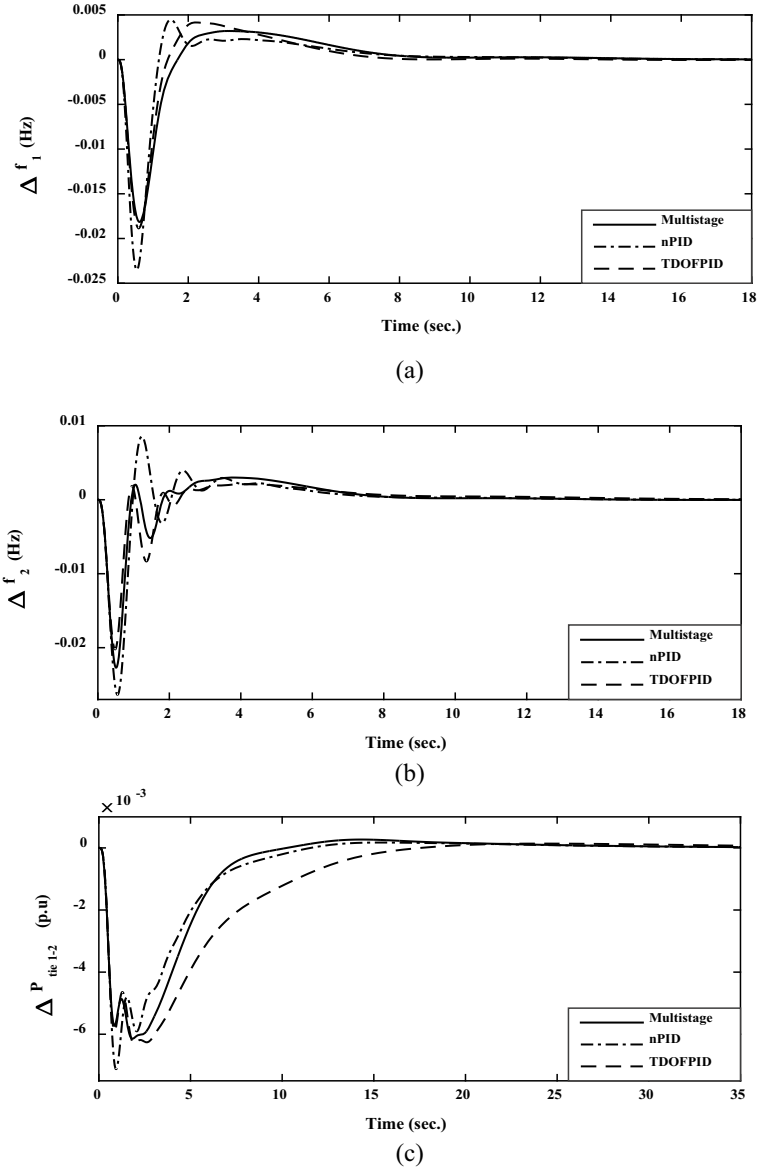

Fig. 4 Graphical abnormality of frequency in **a** area-1, **b** area-2, and **c** tie-line power variation

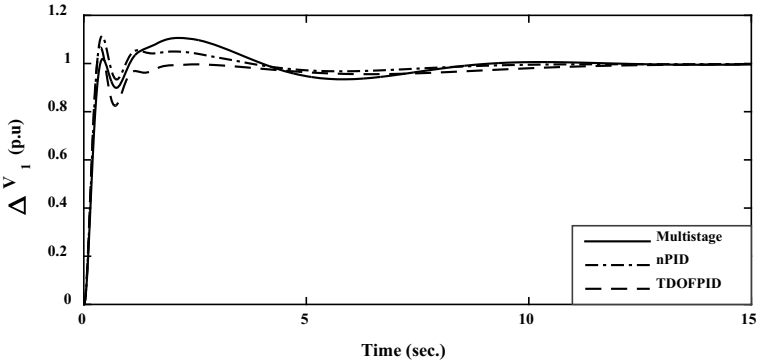

Fig. 5 Terminal voltage variation of the test system

6 Conclusion

In this study, an interrelated multi-area varied energy management structure has been investigated. Diverse renewable-based power generation unit like STP and SHP is integrated successfully in each area. For control of frequency and voltage, a multistage controller is employed. The multistage controller frequency deviates in ALFC system, and at the same time, it also regulates the voltage in AVR loop. The multistage controller shows not only improved result in both transient and steady state but also maintained system stability with the change in load disturbances. For a better understanding of the efficient controller mechanism, results derived from the proposed controller is equated with other recently used controller structure. Out of all controller arrangements, multistage controller shows significantly improved response in respect of overshoot, undershoot, and settling time. With the application of the Jaya optimization technique, the tuning process becomes more efficient and effective as it does not comprise tuning algorithm-related factors. It is observed with repeated application of multiple step load perturbation, the controller parameters show better stability and do not require any updating in optimization.

References

1. Elgerd OL (2000) Electric energy systems theory—an introduction, 2nd edn. Tata McGraw Hill, New Delhi
2. Chandrakala KRM, Vijay A, Balamurugan S (2016) Simulated annealing based optimal frequency and terminal voltage control of multi-source multi area system. Int J Electr Power Energy Syst 78:823–829
3. Rahman A, Saikia LC, Sinha N (2016) AGC of dish-Stirling solar thermal integrated thermal system with biogeography based optimised three degree of freedom PID controller. IET Renew Power Gener 10(8):1161–1170

4. Rajbongshi R, Saikia LC (2017) Combined control of voltage and frequency of multi-area multisource system incorporating solar thermal power plant using LSA optimised classical controllers. IET Gener Transm Distrib 11(10):2489–2498
5. Doolla S, Bhatti TS (2006) Load frequency control of an isolated small-hydro power plant with reduced dump load. IEEE Trans Power Syst 21(4):1912–1919
6. Saha A, Saikia LC (2019) Renewable energy source-based multiarea AGC system with integration of EV utilizing cascade controller considering time delay. Int Trans Electr Energy Syst 29(1):2646
7. Dash P, Saikia LC, Sinha N (2015) Automatic generation control of multi area thermal system using Bat algorithm optimized PD–PID cascade controller. Int J Electr Power Energy Syst 68:364–372
8. Pati SS, Mishra SK (2020) Contribution of energy storage technologies in load frequency control—a review. Int J Renew Energy Res 10(2):871–891
9. Mishra SK, Pati SS (2020) A solar-hydro based frequency regulation in two-area power system incorporating unified power flow control, smart intelligent computing and applications, vol 159. Springer, Singapore. https://doi.org/10.1007/978-981-13-9282-5_46
10. Pati SS, Mishra SK (2019) A PSO based modified multistage controller for automatic generation control with integrating renewable sources and FACT device. Int J Renew Energy Res (IJRER) 9(2):673–683
11. Rajbongshi R, Saikia LC (2017) Combined voltage and frequency control of a multi-area multisource system incorporating dish-stirling solar thermal and HVDC link. IET Renew Power Gener 12(3):323–334
12. Pati SS, Mishra SK (2020) Automatic generation control of a wind turbine integrated hydro-thermal plant with redox flow batteries for 2-area interconnected power system. Smart intelligent computing and applications, vol 159. Springer, Singapore. doi: https://doi.org/10.1007/978-981-13-9282-5_39
13. Rao RV (2016) Jaya: a simple and new optimization algorithm for solving constrained and unconstrained optimization problems. Int J Ind Eng Comput 7:19–34
14. Rao RV, Saroj A (2017) A self-adaptive multi-population based Jaya algorithm for engineering optimization. Swarm Evolut Comput 37:1–26

Author Index

S. Mahapatra et al. (eds.), *Advances in Energy Technology*, Advances in Sustainability Science and Technology, https://doi.org/10.1007/978-981-15-8700-9